



Thèse

2020

Open Access

This version of the publication is provided by the author(s) and made available in accordance with the copyright holder(s).

Interplay of chemical doping, crystal structure and magnetism in oxygen non-stoichiometric $\text{Nd}_{2-x}\text{Sr}_x\text{NiO}_{4+\delta}$

Maity, Sumit Ranjan

How to cite

MAITY, Sumit Ranjan. Interplay of chemical doping, crystal structure and magnetism in oxygen non-stoichiometric $\text{Nd}_{2-x}\text{Sr}_x\text{NiO}_{4+\delta}$. Doctoral Thesis, 2020. doi: 10.13097/archive-ouverte/unige:131881

This publication URL: <https://archive-ouverte.unige.ch/unige:131881>

Publication DOI: [10.13097/archive-ouverte/unige:131881](https://doi.org/10.13097/archive-ouverte/unige:131881)

UNIVERSITÉ DE GENÈVE
Section de Physique
Department of Quantum Matter Physics

FACULTÉ DES SCIENCES
Professeur Ch. Rüegg

Interplay of chemical doping, crystal structure and magnetism in oxygen non-stoichiometric $\text{Nd}_{2-x}\text{Sr}_x\text{NiO}_{4+\delta}$

THÈSE

*présenté à la Faculté des Sciences de l'Université de Genève
pour obtenir le grade de docteur ès Sciences, mention Physique*

par

Sumit Ranjan Maity

de
Suqian (India)

Thèse N° 5432

GENÈVE
Atelier de reproduction de la Section de Physique
2020



**UNIVERSITÉ
DE GENÈVE**

FACULTÉ DES SCIENCES

DOCTORAT ÈS SCIENCES, MENTION PHYSIQUE

Thèse de Monsieur Sumit Ranjan MAITY

intitulée :

«Interplay of Chemical Doping, Crystal Structure and Magnetism in Oxygen Non-Stoichiometric $\text{Nd}_{2-x}\text{Sr}_x\text{NiO}_{4+\delta}$ »

La Faculté des sciences, sur le préavis de Monsieur C. RÜEGG, professeur titulaire et directeur de thèse (Département de physique de la matière quantique), Monsieur L. KELLER, docteur et codirecteur de thèse (Laboratory for neutron scattering and imaging, Villigen, Switzerland), Monsieur E. GIANNINI, docteur (Département de physique de la matière quantique), Monsieur P. WERNER, professeur (Institut Charles Gerhardt, Centre national de la recherche scientifique, École nationale supérieure de chimie de Montpellier, Université de Montpellier, France) et Monsieur M. JANOSCHEK (Neutron und Muon Instrumentation, Paul Scherrer Institut, Villigen, Suisse), autorise l'impression de la présente thèse, sans exprimer d'opinion sur les propositions qui y sont énoncées.

Genève, le 17 janvier 2020

Thèse - 5432 -

Le Décanat

N.B. - La thèse doit porter la déclaration précédente et remplir les conditions énumérées dans les "Informations relatives aux thèses de doctorat à l'Université de Genève".

Abstract

The fundamental understanding of the microscopic origin of oxygen diffusion mechanism is essential in order to design and optimize new oxygen ion conductors with oxygen mobility close to room temperature. This is extremely important for a variety of technological applications such as oxygen membranes, cathodes and electrolytes in solid oxide fuel cells, and sensors or catalysts. In this regard, the $\text{RE}_2\text{NiO}_{4+\delta}$ (RE: La, Pr, Nd) system emerged as promising candidates showing oxygen mobility at under electric potential close at ambient conditions. This surprising behavior raises questions regarding the microscopic oxygen diffusion pathways in these classes of materials at temperatures close to 300 K.

In this work, combining single crystal neutron diffraction investigations with sophisticated data treatment with maximum entropy method for Sr and O-doped $\text{Nd}_2\text{NiO}_{4+\delta}$ single crystals, we have shown strong delocalization of apical oxygen atoms specifically towards the nearest oxygen interstitial sites. Such delocalization of apical oxygen atoms is strongly anharmonic in nature and related to specific low energy local structural distortions induced by the excess oxygens. Such structural distortions yield highly disordered $\text{O}_{\text{int}}\text{-(O}_{\text{ap}})_4$ tetrahedra, which are prerequisites to trigger oxygen mobility close to room temperature. The subsequent oxygen diffusion mechanism is closely related to the “phonon assisted diffusion mechanism”, as originally demonstrated for oxygen deficient $\text{AFeO}_{2.5}$ (A: Sr, Ca) Brownmillerites, provides an atomistic description of non-classical oxygen diffusion process in non-stoichiometric oxides at low temperature.

In addition to the promising oxygen mobility at ambient temperature, $\text{Nd}_{2-x}\text{Sr}_x\text{NiO}_{4+\delta}$ phases also show ordering of excess oxygen atoms, spins and charge below room temperature. Neutron diffraction studies demonstrate a complicated 3D ordering schemes of excess oxygen atoms in O-doped single crystals ($\delta \sim 0.1, 0.23$) at room temperature. However, such behavior is absent for Sr-doped phases in which $\delta \leq 0.1$. A commensurate antiferromagnetic spin order in $\delta \sim 0.1$ single crystal is found with $T_N = 53$ K with a weak ferromagnetic component perpendicular to the NiO_2 planes. The weak ferromagnetism can be explained by strong DM interactions. Below T_N , the intensity of superstructure reflections related to 3D ordering of excess oxygen atoms are largely increased which illustrates the presence of a spin-lattice coupling in $\text{Nd}_2\text{NiO}_{4.1}$. In contrast, an incommensurate magnetic order is observed in $\delta \sim 0.23$ single crystal with $T_N = 150$ K. The observed incommensurate magnetic phase is different from the usual stripe type magnetic order observed in isoelectronic Sr-doped $\text{Nd}_{1.5}\text{Sr}_{0.5}\text{NiO}_{4+\delta}$ single crystal. Thus, this work indicates a strong connection between excess oxygen and spin ordering in oxygen doped $\text{Nd}_2\text{NiO}_{4+\delta}$ single crystals.

Résumé

La compréhension fondamentale de l'origine microscopique du mécanisme de diffusion de l'oxygène est essentielle pour la conception et l'optimisation de nouveaux conducteurs à base d'oxygène avec une mobilité de ce dernier proche de la température ambiante. Ceci est extrêmement important pour diverses applications technologiques telles que les membranes à oxygène, les cathodes et les électrolytes dans les piles à combustible à oxyde solide, ainsi que les capteurs ou encore les catalyseurs. À cet égard, le système $\text{RE}_2\text{NiO}_{4+\delta}$ (RE: La, Pr, Nd) s'est avéré être un candidat prometteur affichant une mobilité de l'oxygène aux conditions ambiantes dans une réaction électrochimique. Ce comportement surprenant soulève des questions sur les réels mécanismes de transport microscopiques dans ces classes de matériaux à des températures aussi basses que 300 K.

Dans ce travail, combinant des études de diffraction de neutronique sur monocristaux avec un traitement de données sophistiqué basée sur une méthode d'entropie maximale pour les monocristaux $\text{Nd}_2\text{NiO}_{4+\delta}$ dopés Sr et O, nous avons montré une forte délocalisation des atomes d'oxygène apicaux spécifiquement vers les sites interstitiels d'oxygène les plus proches. Cette délocalisation d'atomes d'oxygène apicaux est de nature fortement anharmonique et liée à des distorsions structurelles spécifiques de basse énergie induites par la sur-stœchiométrie en oxygène. De telles distorsions structurelles produisent des tétraèdres $\text{O}_{\text{int}}(\text{O}_{\text{ap}})_4$ très désordonnés, qui sont des conditions préalables pour déclencher la mobilité de l'oxygène à proximité de la température ambiante. Le mécanisme ultérieur, étroitement lié au «mécanisme de diffusion assisté par phonon», tel que démontré à l'origine pour les Brownmillerites $\text{AFeO}_{2.5}$ (A: Sr, Ca) déficientes en oxygène, fournit une base complète pour décrire à l'échelle atomique la diffusion non classique de l'oxygène dans ces oxydes non stœchiométriques.

Outre la prometteuse mobilité de l'oxygène à la température ambiante, les phases $\text{Nd}_{2-x}\text{Sr}_x\text{NiO}_{4+\delta}$ affichent également un ordre des atomes d'oxygène, des spins et des charges en excès en dessous de la température ambiante. Les études de diffraction neutronique démontrent un schéma d'ordre 3D complexe des atomes d'oxygène en excès dans des monocristaux dopés en O ($\delta \sim 0.1, 0.23$) à la température ambiante. Cependant, un tel comportement est absent pour les phases dopées au Sr dans lesquelles $\delta \leq 0.1$. Un ordre antiferromagnétique commensurable des spins dans un monocristal de $\delta \sim 0,1$ est trouvé avec $T_N = 53$ K ainsi qu'une composante ferromagnétique faible perpendiculaire aux plans NiO_2 . Le faible ferromagnétisme peut être expliqué par de fortes interactions de DM. En dessous de T_N , l'intensité des réflexions de la superstructure liée à la mise en ordre 3D des atomes d'oxygène en excès est largement augmentée, ce qui illustre la présence d'un couplage spin-réseau dans $\text{Nd}_2\text{NiO}_{4.1}$. En revanche,

un ordre magnétique incommensurable est observé dans le monocristal $\delta \sim 0.23$ avec $T_N = 150$ K. La phase magnétique incommensurable observée est différente de l'ordre magnétique habituel du type bande observé dans le monocristal iso-électronique dopé au Sr $\text{Nd}_{1.5}\text{Sr}_{0.5}\text{NiO}_{4+\delta}$. Ainsi, ces travaux indiquent un lien étroit entre l'oxygène en excès et l'ordre de spin dans les monocristaux de $\text{Nd}_2\text{NiO}_{4+\delta}$ dopés à l'oxygène.

Contents

Abstract	i
Résumé	iii
Chapter 1 Oxide-ion conductors	11
1.1. General introduction	11
1.2. Applications	13
1.3. Problems to be addressed	14
1.4. Achievements	18
Chapter 2 Introduction: Structure and properties of $RE_2NiO_{4+\delta}$	21
2.1. Structure and properties of non-stoichiometric oxides	21
2.2. Ordering of excess oxygen atoms	31
2.3. Oxygen migration in $RE_2NiO_{4+\delta}$	35
2.4. Spin and charge ordering in $RE_{2-x}Sr_xNiO_{4+\delta}$	42
Chapter 3 Theory and Instrumentation	51
3.1. Basic theory of diffraction	51
3.2. Instrumentation	58
3.3. Maximum Entropy Method (MEM)	66
Chapter 4 Synthesis and characterizations of poly- and single crystals of $Nd_{(2-x)}Sr_xNiO_{4+\delta}$	71
4.1. Polycrystalline sample preparation	71
4.2. Single crystal growth	73
4.3. Characterizations	76
4.4. Conclusions	85
Chapter 5 Crystal structure, excess oxygen ordering and magnetic properties of moderately oxygen-doped $Nd_2NiO_{4+\delta}$ ($\delta = 0.11$)	87
5.1. Crystal structure as a function of temperature	87
5.2. Macroscopic magnetization	94
5.3. Magnetic structure	98
5.4. Excess oxygen ordering	102
5.5. Apical oxygen disorder	109
5.6. Conclusions	114
Chapter 6 Modulated crystal structure, oxygen disorder, and incommensurate magnetic order in $Nd_2NiO_{4.23}$	117
6.1. Structural evolution with temperature	118
6.2. Ordering of excess oxygens	122
6.3. Apical oxygen disorder	124
6.4. Magnetic susceptibility	130
6.5. Incommensurate magnetic order	132
6.6. Conclusions	144

Chapter 7	<i>Investigations on crystal structure and magnetic properties of Sr-doped $Nd_{2-x}Sr_xNiO_{4+\delta}$</i>	147
7.1.	Structural phase diagram of $Nd_{2-x}Sr_xNiO_{4+\delta}$	148
7.2.	Excess oxygen ordering and apical oxygen disorder	156
7.3.	Macroscopic magnetization	159
7.4.	Specific heat	162
7.5.	Spin and charge ordering in $Nd_{1.5}Sr_{0.5}NiO_{4+\delta}$	164
7.6.	Conclusions	174
Chapter 8	<i>Conclusions and Outlook</i>	177
8.1.	Conclusions	177
8.2.	Outlook	180
Appendix A	<i>Properties of selected ions and stability of the $RE_{2-x}Sr_xNiO_{4+\delta}$ family</i>	185
Appendix B	<i>Group theoretical analyses of possible magnetic structures</i>	186
Appendix C	<i>Twinning in as-grown $Nd_2NiO_{4+\delta}$ single crystal</i>	192
Appendix D	<i>Point charge calculations of crystal field levels of Nd^{3+} with Mcphase</i>	195
References		207
Acknowledgements		216
Curriculum Vitae		218

Chapter 1

Oxide-ion conductors

One of the biggest problem of our current generation is global warming that is taking place mainly due to emission of greenhouse gasses like CO₂. During the past century, global surface temperatures have increased at a rate near 0.6°C/century which is large enough to melt different glaciers across the world. New technologies are being developed worldwide to reduce the emissions of these greenhouse gases. One of such efficient and environmental-friendly energy technologies is the solid-oxide fuel cell (SOFC). SOFC is a device which efficiently converts chemical energy to electrical energy using abundant and inexpensive natural gasses, permitting overall less emission of greenhouse gasses. Fuel cell consists of three components; a cathode, a solid electrolyte and an anode. Fuel cells use “reduction-oxidation” reactions through which electrons are transferred from one fuel to the other to produce electricity¹. Principally, air is reduced into depleted air in the cathode. Resulting O²⁻ ions diffuse through the solid electrolyte and reach to the anode where fuel materials like H₂, CH₄ get oxidized and resulting electrons flow through the outer load that produces electricity. However, high temperature (1000-1300 K) is required for most of these electrochemical reactions to occur. Thus, problems still remain with regard to cost and durability of such devices. A decrease in the operating temperature to below ~ 800 K is essential to overcome these problems. However, lowering down the operating temperature largely affects the efficiency of these devices, particularly the oxygen diffusion coefficient of cell components. Consequently, in this thesis work, a concerted research effort is devoted to understand the microscopic oxygen diffusion mechanism occurring in layered rare earth nickelates close to room temperature for further designing and tailoring of oxygen ion conductors for cathodes and electrolytes in SOFCs.

1.1. General introduction

Oxide-ion conductors are solid oxides that contain large number of mobile oxide ions. In these materials, current flow occurs by the movement of these oxide ions through the crystal lattice. In general at elevated temperatures, this movement is a result of *hopping processes* in which oxide ions move from one crystal lattice site to a nearest vacant crystal lattice site by overcoming an energy barrier E_a . The oxide-ion conductivity is given by the Arrhenius equation of the form²

$$\sigma_a = (A/T)\exp(-E_a/kT), \quad (1.1)$$

where E_a is the activation energy, T is the absolute temperature and k is the Boltzmann constant. The factor A is proportional to the fraction of vacant sites in the lattice. Thus, to design a *good* oxide-ion conductor, it is fundamental to maximize A and minimize E_a . Therefore, for a good oxide-ion conductor, partial occupancy of an energetically equivalent set of oxide-ion lattice sites is essential. Consequently, the oxygen diffusion process is strongly temperature dependent. At high temperatures, in some materials σ_a can approach values close to 100 Siemens per meter (S/m), comparable to the levels of ionic conductivity found in liquid electrolytes. This is clearly a remarkable property of these materials. To understand its origins, different structural considerations need to be considered. The first observation is that these materials contain a large number of unoccupied lattice sites equivalent to those occupied by the oxide ions like in $\text{RE}_2\text{NiO}_{4+\delta}$ as shown in **Fig.1.1**. Secondly, the energy barrier (E_a) involved in the process of migration from one site to the unoccupied equivalent site must be small (< 1 eV). The oxide ions (O^{2-}) are the largest components of the lattice, with an effective ionic radius of 1.4 Å. At first sight, the migration energy barrier for oxygen diffusion seems to be difficult to overcome. Intuitively, it would be expected that the smaller and lighter cations would be more likely to have higher mobility in the lattice and, hence, carry the current. However, in very special crystal structures with large number of vacant sites, this is not the case and the heavier O^{2-} ions migrate in the electric field. It is thus clear from these facts that the materials displaying high oxide ion conductivity must have highly unusual crystal structures with partially occupied oxygen sites. Hence, the number of materials that exhibit high oxide ion mobility is relatively small.

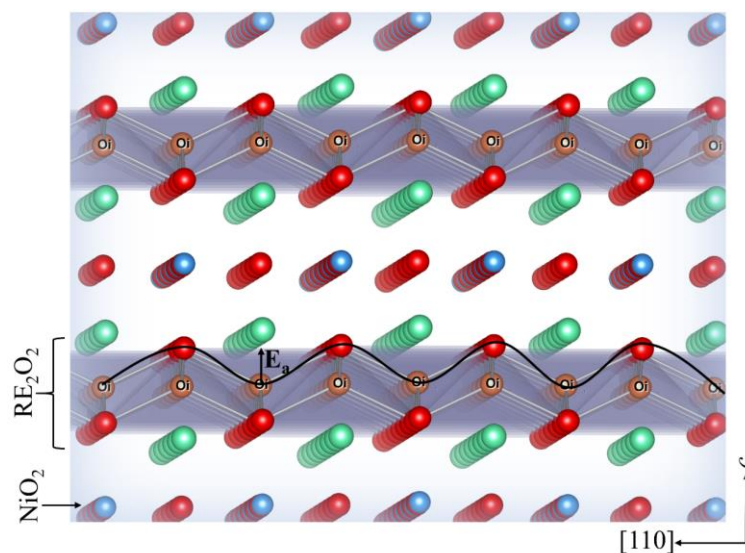


Figure 1.1 | Layered crystal structure of oxygen over-stoichiometric $\text{RE}_2\text{NiO}_{4+\delta}$. Green, blue and red balls represent RE (La, Pr and Nd), Ni and oxygen atoms, respectively. These systems contain

large number interstitial sites (orange balls) in which excess oxygens can be incorporated. Only 12.5% interstitial sites can be filled with excess oxygens at most. Interstitial oxygens allow an easy diffusion process from one interstitial site to another nearest vacant interstitial site via the apical oxygen (black thick line) by overcoming the migration energy barrier (E_a).

In order to obtain a material that is a 'pure' oxygen ion conductor i.e. a solid electrolyte, the level of any electronic contribution to the total conductivity should be minimal. This is not easy to achieve. Even very low concentrations of electronic carriers will give rise to a significant electronic component because of the very high mobility of electrons and holes in comparison with the ionic mobilities. Consequently, most oxygen ion conductors are, in fact, mixed ionic conductors (MIEC) and only very few are capable of being classed as pure ionic conductors. This simple picture, however, neglects the fact that most technological applications of these materials are under extreme conditions, where an oxygen partial pressure gradient is either applied or generated across a dense membrane of the material. Under these extreme conditions, many oxides will reduce and the reduction process will liberate electrons and give rise to electronic conductivity. Only very few materials meet the requirements needed to function satisfactorily as an electrolyte in a device such as a solid oxide fuel cell (SOFC) and, hence, the need to search for alternatives with superior properties at low temperature. Therefore, the challenge is to design a solid material that will allow oxide-ion conduction relatively at a low enough temperature to be technically useful.

1.2. Applications

These oxide ion conductors form the basis of many technological devices that have a huge market potential as schematized in **Fig.1.2**. Ionic conductors are used as electrolyte in devices such as SOFCs³⁻⁵ and oxygen separators⁶. Electrolytes are placed as a separator between the air and fuel in SOFC. The mixed conductors are particularly useful, find application as electrodes in both of these devices. Moreover, they can be used alone as dense, highly selective oxygen separation membranes or for partial-oxidation reactions in the production of valuable products from fossil fuels. Moreover, SOFCs are also attracting interests for stationary and mobile applications in powered electric vehicles such as in cars, trucks and military applications⁷.

One of the current goals of the society is to achieve the clean and efficient generation of electrical power from renewable sources by minimizing the emission of both atmospheric pollutants and greenhouse gasses such as CO₂. This is not easily obtainable, but priorities should be given to avoid some of the predicted hazards that cause large-scale climate change. Solid-oxide fuel cells

(SOFCs) have a major role to play in achieving this transition from a high-carbon economy to a low-carbon economy².

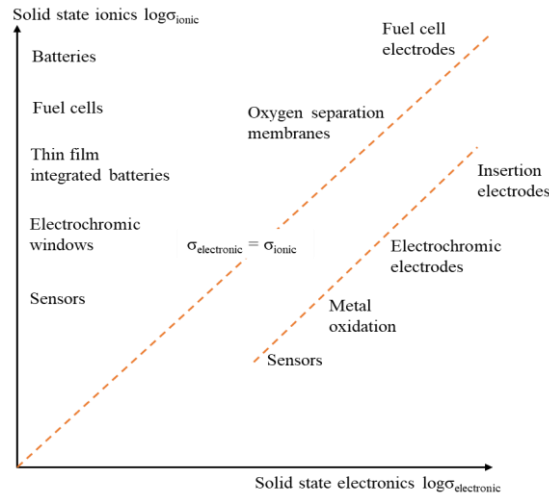


Figure 1.2 | Illustration of technological applications of mixed electronic and ionic conductors.

The figure is taken from reference ⁶.

1.3. Problems to be addressed

The operating temperature of these devices lies at high temperature region (1000-1300 K), and there are materials that work well at these temperatures. However, problems still remain regarding to the cost and the durability of these devices. These challenges have stimulated a drive to lower down the operating temperature to below ~ 800 K (Intermediate temperature (IT) SOFC). However, lowering down the operating temperature strongly affects the efficiency of the SOFCs, particularly the oxygen diffusion coefficient of different cell components. In recent years, a concerted research effort has been devoted in finding new materials for designing and tailoring of new low temperature oxide ion conductors for cathode and electrolyte of IT-SOFCs.

Recent studies have demonstrated that only few materials with layered Brownmillerite^{8,9} and K_2NiF_4 -type crystal structure, in particular $RE_2MO_{4+\delta}$ ($RE = La, Pr, Nd$ and $M = Ni, Cu, Co$) compounds⁹⁻¹³, show strongly anisotropic oxygen mobility in the intermediate temperature range. These materials possess either large number of point defects in terms of regular vacant lattice sites (in case of Brownmillerite compounds) or excess oxygen atoms in the interstitial sites (for K_2NiF_4 phases). Furthermore, these materials could reversibly be oxidized or reduced at room temperature with gentle electrochemical methods. The oxygen intercalation can reach up to $\delta = 0.25$, in particular for $Pr_2NiO_{4+\delta}$ and $Nd_2NiO_{4+\delta}$ compounds^{14,15}. Experimentally determined oxygen diffusion coefficient (D^*) of $Nd_2NiO_{4.25}$ phase is shown in **Fig. 1.3** both for single and

polycrystalline samples. It is found that D^* is strongly anisotropic¹⁶ even in the high-temperature regime, being about three orders of magnitude higher in the (a - b) plane than along the c -axis. The oxygen diffusion process in the high-temperature regime is usually described by the Arrhenius law as shown in **Eq. 1.1**. However, in the low-temperature regime, the diffusion process is non-classical and cannot be explained by such thermally activated stochastic hopping processes^{17,18}.

In this regards, for Brownmillerite compounds, a phonon-assisted oxygen diffusion mechanism was proposed for the description of the non-classical oxygen diffusion process on a microscopic scale⁸, relying on specific low-energy phonon modes, triggering and amplifying oxygen diffusion at low-temperature. This dynamically triggered diffusion process leads to an easy migration of the oxide ions into the open vacancy channels and vice versa. Similarly, for K_2NiF_4 -type materials, numerous studies^{17,19} have revealed an intimate connection between low energy phonon modes and oxygen diffusion mechanism at low temperatures. An *interstitialcy diffusion* mechanism is proposed from *ab-initio* molecular dynamical simulations²⁰⁻²⁴, occurring through the interstitial-apical oxygen-vacant interstitials network. A remarkable behavior observed for these materials is the pinning of interstitial oxygen atoms to the lattice, giving rise to superstructure reflections related to 1D or 3D long-range ordering of excess oxygens^{18,25-29}. Neutron diffraction studies revealed disc-shaped delocalization of apical oxygen atoms in $Nd_2NiO_{4.25}$ and $Pr_2NiO_{4.25}$ at room temperature as shown in **Fig. 1.4**. Such a delocalization of apical oxygen atoms provides a quasi-continuous shallow energy diffusion pathway between apical and vacant interstitial oxygen sites. The amount of the delocalization largely depends on both the rare earth element and the excess oxygen content δ . These large displacement amplitudes are considered to be-at least partially-of dynamical origin, which would be consistent with the proposed phonon assisted diffusion mechanism, already activated at very moderate temperatures. The delocalization of apical oxygen atoms is essential and directly correlated with the oxygen mobility at low temperatures since it draws the apical oxygen atoms closer to the vacant interstitial sites, thus reducing the effective diffusion pathway and lowering the energy barrier required to activate the diffusion event.

While the phonon-assisted mechanism provides an explanation of low temperature oxygen mobility on a microscopic scale for Brownmillerite oxides, many uncertainties still remain concerning its application to the $RE_2NiO_{4+\delta}$ phases. These compounds show non-classical oxygen diffusion at moderate temperatures, down to the ambient under the electric potential. They exhibit a similar set of structures, characterized by the coherent tilting pattern of MO_6 octahedra, and the long-range ordering of excess oxygen atoms in the interstitial sites and their associated defective clusters as discussed in more details in **chapter 2**. In this work, our particular aim is to investigate experimentally, using neutron and x-ray diffraction techniques, the structural phase

diagram of these complex systems as a function δ to determine how the correlation of interstitial oxygen defects with the lattice activate the oxide ion diffusion at low-intermediate temperature regime. Furthermore, compare these results with already reported results from *ab-initio* calculations in order to extend the understanding of fast oxygen diffusion in solid oxides *via* lattice instabilities and dynamically triggered internal interfaces.

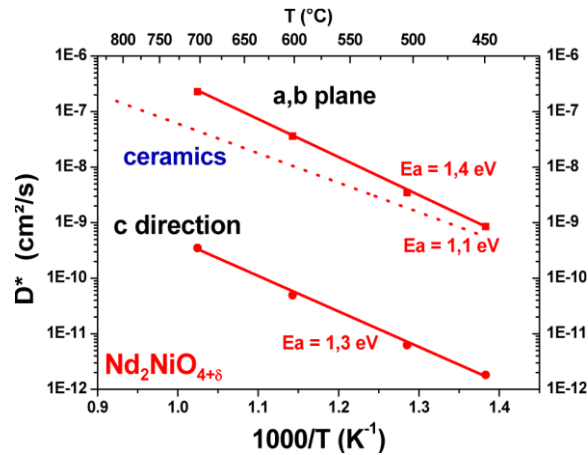


Figure 1.3 | Experimentally determined oxygen diffusion coefficient (D^*) as a function of temperature. Measurements were performed on an oriented single crystal (solid line) and on a polycrystalline sample (dashed line) of $\text{Nd}_2\text{NiO}_{4+\delta}$ with $\delta \sim 0.25$ in the intermediate temperature range. A linear fit was made to extract the activation energy according to the Arrhenius law. The figure is taken from reference¹⁶.

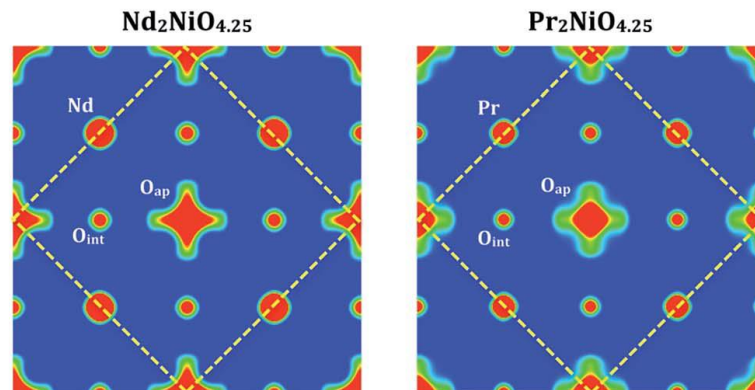


Figure 1.4 | Nuclear scattering densities of apical (O_{ap}), interstitial (O_{int}) and rare earth (Nd and Pr) atoms in $\text{Nd}_2\text{NiO}_{4.25}$ and $\text{Pr}_2\text{NiO}_{4.25}$, obtained with single crystal neutron diffraction data with MEM analysis at ambient temperature. $2a \times 2b$ projection of the $I4/mmm$ unit cell (the F-centered cell is outlined by yellow dashed bars) in $0.1 \leq z \leq 0.3$. The figure is taken from reference¹⁸.

In addition to the complex interplay of crystal structure and oxygen mobility as a function of temperature and the oxygen content (δ), numerous studies have also shown electronic and magnetic complexities in the $\text{RE}_2\text{MO}_{4+\delta}$ family, including high-temperature superconductivity^{30,31}, stripe spin and charge ordering³²⁻³⁵, orbital ordering and electronic phase separation³⁶. Oxygen doping or partially replacing RE^{3+} ions with Sr^{2+} ions, inject holes inside the NiO_2 planes. On cooling, these holes segregate into an ordered array of parallel regions separating the antiferromagnetic (AFM) spin order as a domain boundary, known as a stripe/checkerboard ordered state, as shown in **Fig.1.5**. In this stripe ordered state, with respect to the pseudo-tetragonal cell, the spin order is described by a modulation vector; $\mathbf{Q}_{\text{so}} = \mathbf{Q}_{\text{AF}} \pm (\epsilon, 0, 0)$, where $\mathbf{Q}_{\text{AF}} = (1, 0, 0)$ is the commensurate antiferromagnetic wave vector found for undoped compounds, and the charge ordering is characterized by a modulation vector $\mathbf{Q}_{\text{co}} = (2\epsilon, 0, 0)$ ³⁵. The incommensurability, $\epsilon \approx n_{\text{h}} = 2\delta$, changes almost linearly with the doped hole concentration $n_{\text{h}} < 1/2$ ³⁷. Oxygen interstitials ordering leads to the ordered deformation of NiO_2 planes, which provides a modulated potential that can pin the charge stripes to the lattice. Therefore, the amount of interstitials and its ordering state both play a crucial role on the nature of the spin and charge orderings appearing at low temperature.

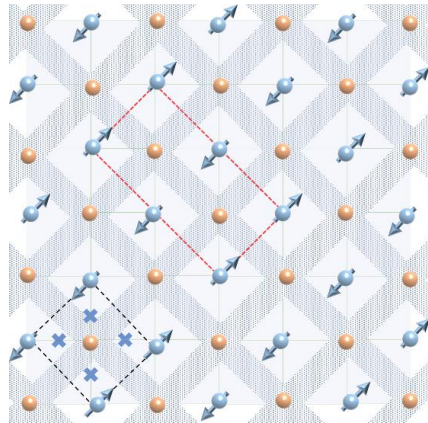


Figure 1.5 | Idealized sketch of the commensurate charge and spin ordering in the NiO_2 plane for $\text{Nd}_{1.5}\text{Sr}_{0.5}\text{NiO}_{4.0}$ with $\epsilon = 0.5$. Blue spheres denote Ni^{2+} sites and yellow spheres designate Ni^{3+} sites with holes. Black and red squares represent the F-type structural unit cell and the magnetic unit cell, respectively.

Wochner et.al.³⁵ proposed that the charge correlations are fluctuating about an average ordered configuration determined by the ordering of interstitials. Moreover, the temperature dependence of ϵ demonstrates coupling of charge stripes with the underlying crystal lattice and the occurrence of the rational fraction of ϵ is the result of a competition of two length scales, one associated with the ideal spin-charge order and the other associated with the modulation of the lattice potential due to the ordering of interstitials³⁵. Moreover, a direct relationship exists

between the modulation vectors of the charge stripes in the NiO₂ planes and the interstitial ordering along one direction of the lattice. It was also proposed that the charge ordering and interstitials ordering appears at the same temperature in La₂NiO_{4.125}³⁸.

Until now, La-based Ruddlesden-Popper (RP) nickelates are vastly studied, compared to the iso-structural (Pr/Nd)₂NiO_{4+ δ} phases, owing to their structural similarity with La-based high-T_c cuprates. Because of this, experimental investigations are performed on Sr-doped compounds or restricted to the moderately oxygen-doped region, as La-based compounds can intercalate excess oxygens only up to $\delta \sim 0.15$. The stripe type spin and charge ordering schemes are already well established for Sr-doped compounds and moderately oxygen doped La₂NiO_{4+ δ} compounds. Our present work focuses on the Nd₂NiO_{4+ δ} system in which the oxygen intercalation can reach up to $\delta \sim 0.25$, allowing to investigate electronic properties in the moderate-to-high oxygen doped regime. Therefore, in this work, we explore the magnetic phase diagram of Nd₂NiO_{4+ δ} compounds with $\delta \sim 0.23$ and 0.12 , in the temperature range of 2-300 K. We compare our findings with Sr-doped compounds which are electronically equivalent to the oxygen doped systems i.e. the hole concentration is similar in both type of compounds.

1.4. Achievements

The subtle modifications in the crystal structure and magnetic properties are studied as a function of oxygen content (δ) and Sr-doping in Ruddlesden-Popper K₂NiF₄-type nickelates at different temperatures, employing poly-and single crystal X-ray and neutron diffraction techniques.

We reveal strong anisotropic thermal displacements of apical oxygen atoms toward nearest vacant interstitial sites, 3-4 times larger in the *ab*-plane compared to the *c*-axis. The modulus of thermal displacement parameters are largely increased on an absolute scale with the excess oxygen content δ . In addition, diffuse type systematic anharmonic local displacements, induced by oxygen interstitials, of the apical oxygen atoms are observed. Such delocalization of apical oxygen atoms is essential and directly correlated with the oxygen mobility at low temperatures since it takes the apical oxygen atoms closer to the vacant interstitial sites, thus effectively reducing the diffusion pathway and lowering the energy barrier required to activate the diffusion process. Such anharmonic behavior of the apical oxygens is interpreted to be an important prerequisite for oxygen mobility at low temperature within the framework of phonon assisted oxygen diffusion in K₂NiF₄ oxides, as previously demonstrated for Brownmillerites. Excess oxygen atoms at interstitial sites show a repulsive O_{int}-O_{ap} interaction, leading to a symmetrical increase of the O_{int}(O_{ap})₄ tetrahedra, while the O_{int}-O_{ap} distance reaches 2.76 Å, instead of 2.15 Å when

taking into account the average structure. For the moderately doped phase, oxygen diffusion along the [110]-direction involves important local distortions of the respective tetrahedral sites, resembling to a successively in- and exhaling behavior of the involved occupied and empty tetrahedra along the diffusion pathway. It is evident that such a mechanism is far away from a rigid $O_{\text{int}}(O_{\text{ap}})_4$ configuration but that the associated structural changes of the tetrahedral sites that considerably reduce the oxygen mobility in the $P4_2/ncm$ phase of $\text{Nd}_2\text{NiO}_{4.12}$, compared to the fully disordered non-stoichiometric $\text{Nd}_2\text{NiO}_{4.23}$ phase, where all tetrahedra become dynamically activated and structurally equivalent. Therefore, in this work, we have experimentally found that the concept of phonon-assisted diffusion activated by strong thermal displacements of apical oxygen atoms, related to specific low energy phonons, is equally applicable for K_2NiF_4 structures. These findings not only offer a new dimension to design and to tune fast oxygen ion conductors in solids, but also allows understanding the low temperature solid-state reactivity with a special accent on the reversible battery systems.

With single crystal neutron diffraction studies, we show that the moderately oxygen doped phase is antiferromagnetically ordered below 53 K with the magnetic propagation vector (100) with a weak ferromagnetic component along the c -axis. The weak ferromagnetic component is related to the cooperative tilts of NiO_6 octahedron and successfully described by the Dzyaloshinskii-Moriya interaction (DM). Furthermore, we could evidence 3D ordering of excess oxygen atoms even at room temperature, which is unusual for such a low oxygen doping concentration at which 1D ordering was previously proposed. Moreover, we have found that with the appearance of the antiferromagnetic order at 53 K, the intensity of oxygen superstructure reflections are largely increased, suggesting a strong coupling between the crystal lattice and spin ordering. In comparison, a different 3D incommensurate order of excess oxygen atoms is found for the $\text{Nd}_2\text{NiO}_{4.23}$ phase. In addition, an incommensurate magnetic order is observed below 150 K, which is characterized by magnetic satellites at $(h \pm \epsilon, 0, l/2)$ with h and l being odd integer numbers and the magnetic incommensurability, $\epsilon \sim 0.36$. The observed magnetic phase behave substantially different from that of a stripe ordered phase as evidenced for electronically equivalent $\text{Nd}_{1.5}\text{Sr}_{0.5}\text{NiO}_4$ compound. With spectroscopic techniques, it was previously proposed that doped holes injected by Sr-substitution and oxygen doping have similar effects on the electronic structure of the compound. However, our findings of two different magnetic ground states for two electronically equivalent compounds achieved by oxygen doping and Sr-substitution hint at a complex charge transfer mechanism in nickelates.

Chapter 2

Introduction: Structure and properties of $\text{RE}_2\text{NiO}_{4+\delta}$

$\text{RE}_2\text{MO}_{4+\delta}$ compositions display rich structural phase diagram as a function of the excess oxygen content δ and the temperature, showing complex long-range ordering of excess oxygen atoms in oxygen over-stoichiometric phases, non-classical oxygen mobility in the room- and moderate-temperature regimes for some compositions, and exciting electronic and magnetic properties. This chapter summarizes the state-of-the-art knowledge of the $\text{RE}_2\text{MO}_{4+\delta}$ materials, in particular the $\text{Nd}_2\text{NiO}_{4+\delta}$ system.

The **section 2.1** focuses on the structure and properties of perovskites and its derivatives. Different structural distortions, structural phase diagram, and excess oxygen ordering found for $\text{Nd}_2\text{NiO}_{4+\delta}$ compound and other materials of the $\text{RE}_2\text{MO}_{4+\delta}$ family are summarized. The **section 2.2** is dedicated to theoretical calculations and experimental investigations performed on $\text{RE}_2\text{MO}_{4+\delta}$ phases to characterize the oxygen diffusion mechanism, pathway, and coefficients as a function of temperature. At last, the **section 2.3** reviews the complex magnetic and electronic behavior observed at low temperature in hole doped $\text{RE}_2\text{MO}_{4+\delta}$ compounds.

2.1. Structure and properties of non-stoichiometric oxides

2.1.1. Perovskites and its derivatives

The general formula of the perovskite structure is AMO_3 where A and M are the cations. Perovskite type structure can be described as a 3D cubic network of corner sharing MO_6 octahedrons with the larger A cations occupying every site created by eight MO_6 octahedra. This designates *twelve-fold* oxygen coordination for the larger A cation and a *six-fold* oxygen coordination for the smaller M site cation. Perovskite type oxides are well known as the oxygen stoichiometry can be varied by the substitutions of A or M cations. Depending on the oxygen stoichiometry and the size of the substituted cations, the structure is distorted from the ideal perovskite structure. These distortions can be described by these following mechanisms: distortions of the octahedra, cation

displacements within the octahedra and tilting of the octahedra. The distortion in the octahedra can be described by a key parameter called Goldschmidt tolerance factor; t and it can be described by the following equation³⁹:

$$t = \frac{r_A + r_O}{\sqrt{2}(r_A + r_M)} \quad (2.1)$$

where r_A and r_M are the ionic radius of A and B cations, respectively, and r_O is the ionic radius of the oxygen atoms. The stability of the perovskite structures can be defined by the tolerance factor (t) which is used to quantify the internal strain as a function of ionic radii or as a function of inter-atomic bond lengths. The structural strain is minimal if the value of t is one, and consequently, the structure is ideal cubic. For $t < 1$, the crystal structure is tetragonal or orthorhombic and for $t > 1$, the structural symmetry is hexagonal. Experimentally it is observed that perovskite structures become unstable for a value of $t < 0.86$, and the atomic arrangement adopts a layered configuration. The t value of a perovskite structure changes as a function of the thermodynamic conditions (temperature or pressure) that lead to various phase transitions. Interesting physical properties emerge from these structural changes like ferroelasticity in $SrTiO_3$ ⁴⁰, ferroelectricity in $BaTiO_3$ ⁴¹, ferromagnetism in $YTiO_3$ ⁴², piezoelectricity and pyroelectricity in PZT ($PbZr_xTi_{1-x}O_3$)⁴³, etc.

Fig. 2.1 presents a schematic to obtain different structural phases from the ABO_3 framework. Among them, Ruddlesden-Popper (RP) $A_{n+1}M_nO_{3n+1}$ can be derived by inserting the intergrowths of AMO_3 perovskite blocks with AO rock-salt layers⁴⁴. The chemical formula of these layered perovskites can also be expressed as $(AO)(AMO_3)_n$. Thus, the crystallographic structure can be described by n consecutive AMO_3 perovskite blocks interspersed between AO-type rock-salt layers along the crystallographic c -axis. In these compounds, A is usually a rare earth metal ion (e.g. La, Pr, Nd) and M is a transition metal ion (e.g. Co, Ni and Cu), and n is a positive integer number. Therefore, the ideal perovskite structure corresponds to $n = \infty$ and the K_2NiF_4 structure corresponds to $n = 1$. An ideal cubic perovskite structure is shown in **Fig. 2.2(a)** with $Pm\bar{3}m$ space group. **Fig. 2.2** shows different higher order RP-type crystal structures with $n = 1, 2, 3$. In K_2NiF_4 structure, each NiO_6 octahedral layer is interspersed between two slabs of rock salt AO layer. This gives the structure a highly anisotropic nature since the thickness of the perovskite layers is minimal, giving rise to corner sharing octahedra that are not interconnected between the layers. The ideal structure of this series is simple tetragonal, but orthorhombic distortions have been observed due to the tilting of the octahedra and a variations of the oxygen non-stoichiometry. This class of compounds is particularly interesting since they exhibit a wide range of exciting chemical, structural and physical properties as a function of doping on the A site, M site and/or

with excess oxygen doping. In terms of the Goldschmidt tolerance factor (t), the K_2NiF_4 structure is only stable for $0.86 < t < 1$. In **appendix A**, we show the structural stability of the $RE_{2-x}Sr_xNiO_{4+\delta}$ compounds based on the tolerance factor calculation.

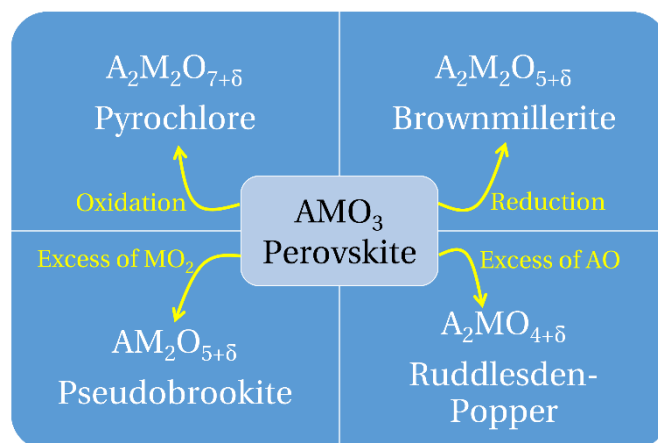


Figure 2.1 | Different structural phases related to AMO_3 perovskites.

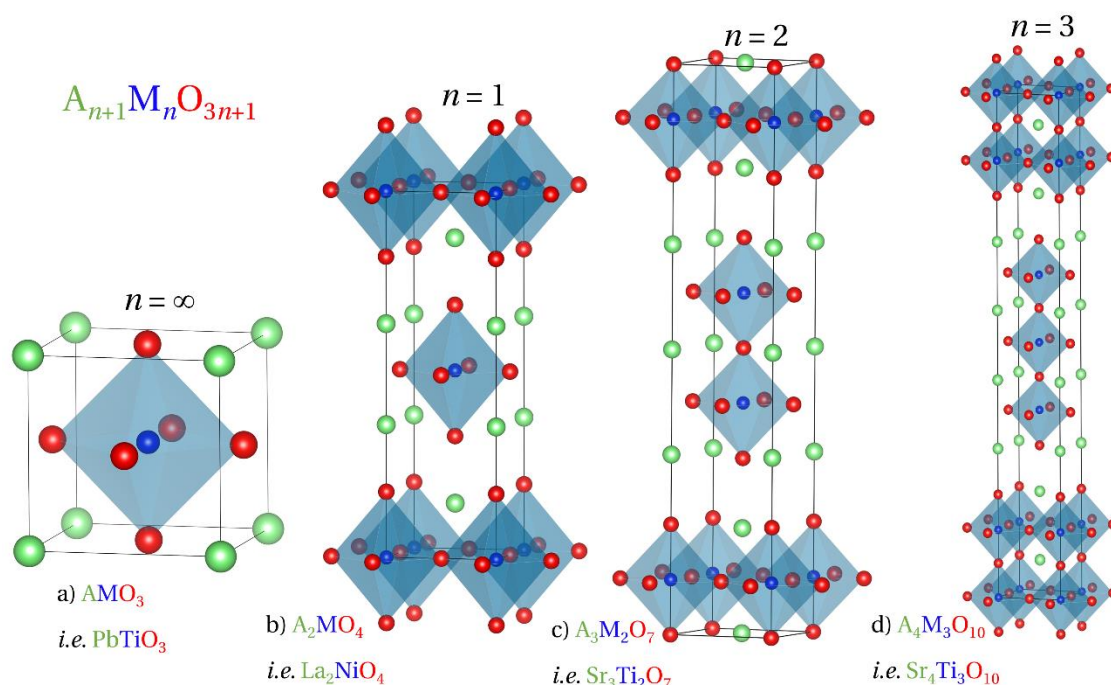


Figure 2.2 | Schemes of the Ruddlesden-Popper series of layered oxides (a) $n = \infty$, equivalent to ideal perovskite, (b) $n = 1$, (c) $n = 2$, and (d) of $n = 3$.

2.1.2. Crystal structure and phase diagram of $RE_2NiO_{4+\delta}$

Since the discovery of high temperature cuprate superconductors by Bednorz and Müller⁴⁵, there has been considerable efforts devoted in understanding of the interplay of the crystal structure and physical properties of rare earth transition metal oxides. Among the RP-type oxides, large number of research works have been carried out especially on the $RE_2NiO_{4+\delta}$ system owing to their structural similarity with $La_{2-x}Sr_xCuO_4$, the system in which first superconductivity was discovered. The crystal structure of the stoichiometric $RE_2MO_{4.0}$ phase can be described as alternate stacking of $RENiO_3$ perovskite blocks and rock salt REO layers along the crystallographic c -axis as shown in **Fig. 2.3**. The NiO_6 octahedrons share corners in the ab -plane forming a 2D network, which is responsible for various interesting anisotropic physical properties. The ideal crystal structure can be described in the tetragonal $I4/mmm$ space-group, which is generally observed only at high-temperature (e.g. at 770 K for $La_2NiO_{4.0}$ ⁴⁶, at 1500 K for $Pr_2NiO_{4.0}$ ⁴⁷ and at 1900 K for $Nd_2NiO_{4.0}$ ⁴⁸). The ideal tetragonal high temperature crystal structure is symbolized as “HTT”, also can be expressed in the unconventional $F4/mmm$ space group in order to obtain a better comparison between the structural parameters of the different phases as a function of temperature as shown in **Fig. 2.3**. Structural strain in the stoichiometric phase exists due to lattice mismatch between REO and NiO_2 layers below the phase transition temperature ($T_{HTT-LTO}$). Generally, the *REO layer is in the extensional strain and NiO_2 layer feels a compressional strain.* The structural strain is released by the canting of NiO_6 octahedra about the a -axis such that the direction of canting alternates between the nearest neighbors in the basal plane. Neighboring octahedrons in the (100) planes are contra-rotated, whereas those in the (010) planes are co-rotated⁴⁹. The crystal structure of these stoichiometric compounds at room temperature can be fully described by the orthorhombic $Bmab$ space group, known as low temperature orthorhombic “LTO” as shown in the **Fig. 2.4**. With decreasing temperature, larger lattice mismatch appears, consequently, another phase transition occurs at $T_{LTO-LTT}$ (80 K for $La_2NiO_{4.0}$ ⁴⁶, 125 K for $Pr_2NiO_{4.0}$ ⁴⁷, 130 K for $Nd_2NiO_{4.0}$ ⁵⁰) from the orthorhombic phase to another tetragonal $P4_2/ncm$ phase, known as the low temperature tetragonal “LTT”. In the LTT phase, the structure is characterized by an octahedron tilting about the [110]-direction in the basal plane, such that in plane nearest neighbors are contra-rotated. The rotation axis alternates between [110] and $[1\bar{1}0]$ directions along the c -axis⁴⁹. The LTT type crystal structure corresponds to the $P4_2/ncm$ space group is shown in **Fig. 2.5**. However, there are reports that the crystal structure below $T_{LTO-LTT}$ can also be described by another orthorhombic space group $Pccn$, known as the low temperature less orthorhombic “LTLO” phase. In this case, the tilt axis of the NiO_6 octahedron is in between [100] and [110] directions⁵¹. The orthorhombic $Pccn$ structure can be described by the vector sum of two previously described symmetries i.e. the structures in $Bmab$ and the $P4_2/ncm$ space group. The Rietveld refinements of neutron powder diffraction data cannot distinguish between LTT

and LTLO phase as both refinements provide similar results within the experimental error⁵⁰. The distortion associated to these symmetries (except the HTT phase) involve the systematic tilting of NiO_6 octahedron about a fixed crystallographic axis parallel to the basal plane. Thus, these symmetries are characterized by the long-range order of octahedron tilting. Therefore, they give rise to systematic superstructure reflections in the diffraction pattern compared to the HTT phase⁵¹.

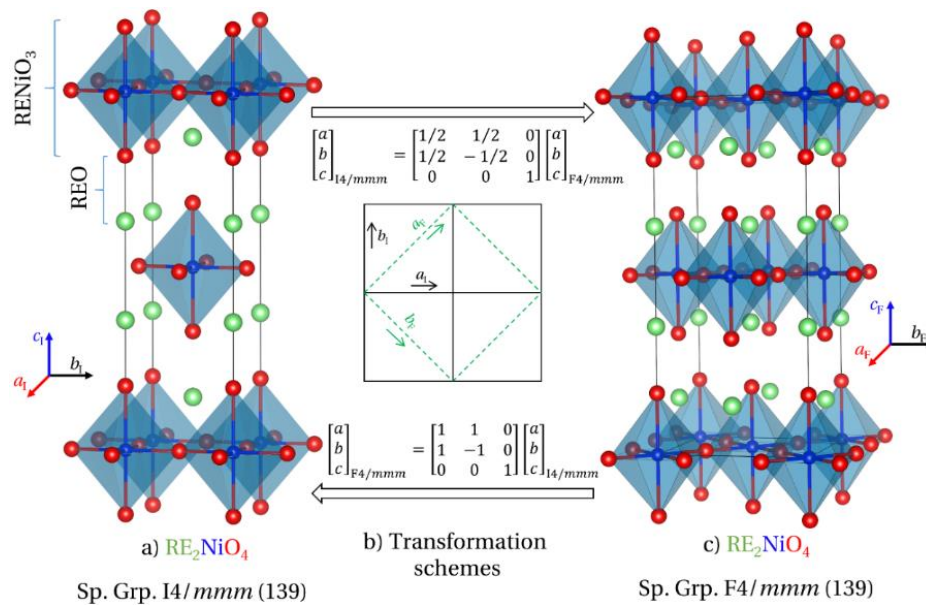


Figure 2.3 | High temperature crystal structure of $Nd_2NiO_{4+\delta}$ in $I4/mmm$ and $F4/mmm$ space groups. Transformation matrices are shown from I-cell to F-cell and vice versa.

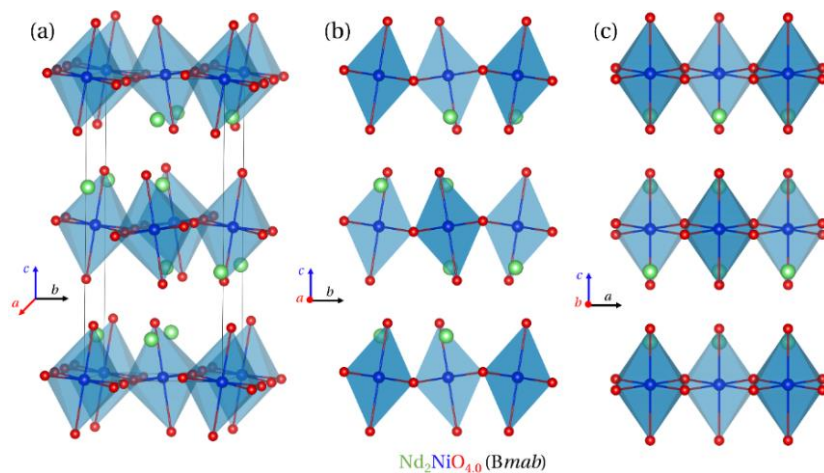


Figure 2.4 | The LTO phase of $Nd_2NiO_{4.0}$ with orthorhombic $Bmab$ space group. Different projections are shown, illustrating the NiO_6 octahedron tilt pattern around the a -axis.

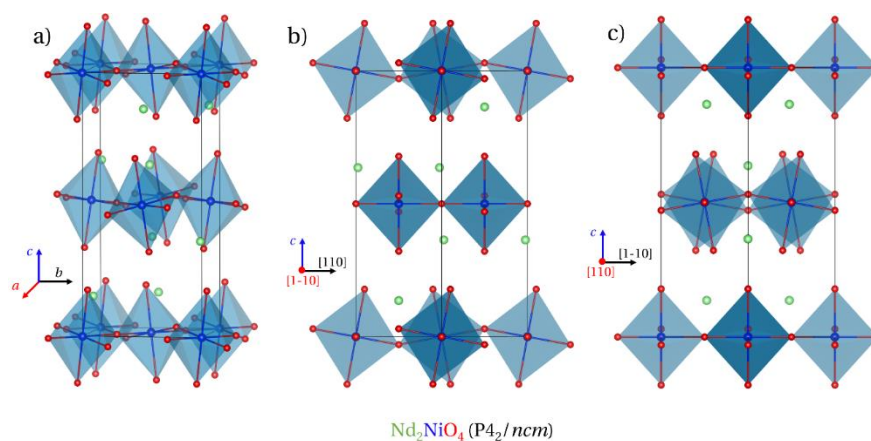


Figure 2.5 | The LTT crystal structure of $Nd_2NiO_{4.0}$ with tetragonal $P4_2/ncm$ space group. Different projections are shown, illustrating the NiO_6 octahedron tilt pattern around the $[110]$ -axis.

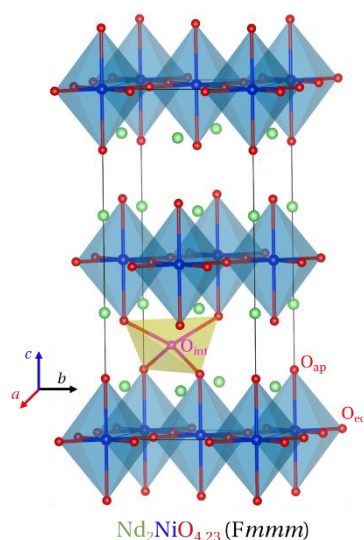


Figure 2.6 | Orthorhombic average crystal structure (LTO') of $Nd_2NiO_{4.23}$ with $Fmmm$ space group. On average one interstitial oxygen is present in the structure, thus one tetrahedron out of eight is occupied as shown by yellow polyhedron.

The structures derived from the high temperature parent $I4/mmm$ space group by condensation of the soft phonon mode with wave vector corresponding to the X point ($\frac{1}{2} \frac{1}{2} 0$) of the Brillouin zone (BZ). This leads to several possible structures with different symmetries which are in accordance with the Landau theory of phase transition⁴⁶. This can be described in terms of an *order parameter* associated with octahedral canting soft modes. The order parameter is two-dimensional (2D) which has two components η_1 and η_2 owing to the degeneracy of the X -point. If one of the components of the soft modes condenses with cooling, the resulting structural symmetry is $Bmab$. If both the components condense together ($\eta_1 = \eta_2 \neq 0$) with cooling, the structural symmetry is tetragonal $P4_2/ncm$. A third possibility exists when $\eta_1 \neq \eta_2 \neq 0$ resulting in an orthorhombic structure intermediate between $Bmab$ and $P4_2/ncm$ with the space group $Pccn$.

The Wyckoff sites and corresponding atomic positions in $RE_2NiO_{4.0}$ compounds with the above-mentioned space groups are given in **table 2.1**. **Fig. 2.7** shows the displacements of apical and equatorial oxygen atoms with respect to the HTT phase to obtain the orthorhombic $Bmab$ or tetragonal $P4_2/ncm$ structures. The less symmetric space group $Pccn$ is a subgroup of all the others. $Bmab$ and $P4_2/ncm$ are both subgroups of the parent $F4/mmm$, but $P4_2/ncm$ is not a subgroup of $Bmab$. Powder diffraction experiments have shown that the structural transition from HTT-LTO is a second order transition⁴⁶ in contrast to the first order LTO-LTT/LTLO structural transition. However, these systems do not possess a HTT-LTT/LTLO structural transition.

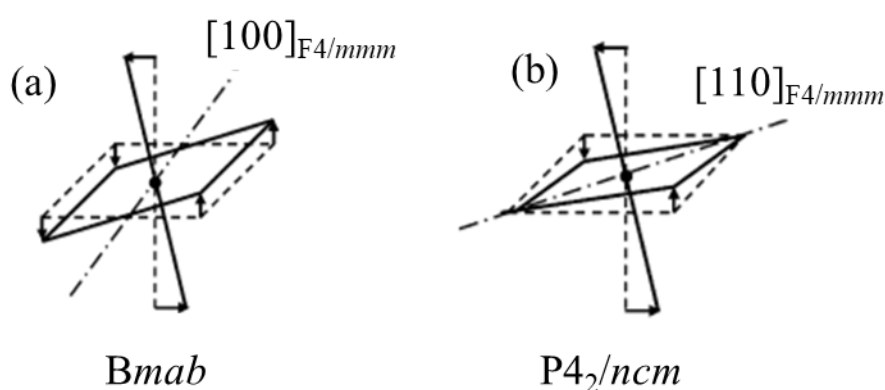


Figure 2.7 | Tilting of NiO_6 octahedron and movements (shown by arrows) of apical and equatorial oxygen atoms to obtain (a) $Bmab$ and (b) $P4_2/ncm$ structures with respect to the undistorted F-type HTT unit cell (dashed line). The figure is taken from reference⁵².

Table 2.1 | Positions occupied by atoms in $RE_2NiO_{4.0}$ compounds in space groups $F4/mmm$, $Bmab$, $P4_2/ncm$ and $Pccn$. The table is based on reference⁴⁶.

Atoms	$F4/mmm$	$Bmab$	$P4_2/ncm$	$Pccn$
RE	$8e$ $4mm$	$0\ 0\ z$ $8f$ $m..$	$0\ y\ z$ $4a$ $0\ 0\ 0$ $2/m..$	$8e$ $x\ x\ z$ 1
Ni	$4a$ $4/mmm$	$0\ 0\ 0$ $4a$ $2/m..$	$0\ 0\ 0$ $4d$ $..2/m$	$4a$ $0\ 0\ 0$ $\bar{1}$
O_{ap}	$8e$ $4mm$	$0\ 0\ z$ $8f$ $m..$	$0\ y\ z$ $8i$ $..m$	$8e$ $x\ y\ z$ 1
O_{eq1}	$8c$ mmm	$\frac{1}{4}\ \frac{1}{4}\ 0$ $8e$ $..2$	$\frac{1}{4}\ \frac{1}{4}\ z$ $4e$ $2..mm$	$4c$ $\frac{1}{4}\ \frac{1}{4}\ z$ $..2$
O_{eq2}			$4a$ $2..22$	$4a$ $\frac{1}{4}\ \frac{3}{4}\ z$ $..2$

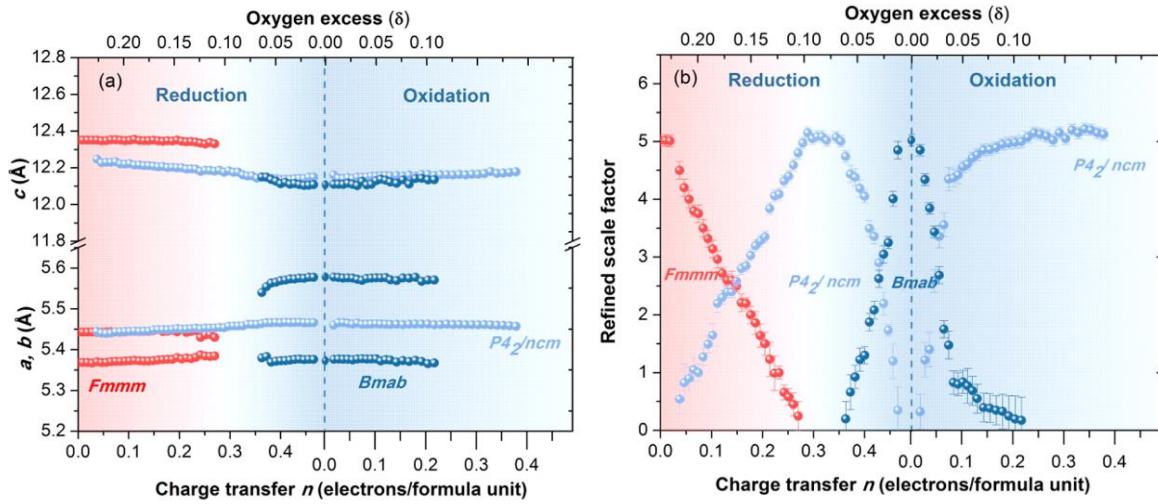
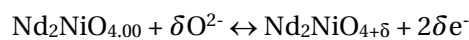


Figure 2.8 | Variation of different structural parameters as a function of δ in $Nd_2NiO_{4+\delta}$ at 300 K. (a) Evolution of a , b , and c lattice parameters and (b) the refined scale factor as a function of δ thus the charge transfer n , obtained from neutron powder diffraction data. Red, light blue and dark blue symbols denote the starting LTO' phase, the intermediate LTT phase, and the stoichiometric LTO phase respectively. The figure is taken from reference¹⁴.

The structural strain in the stoichiometric compound can be released by two different ways: partially replacing RE^{3+} ions with smaller cations which leads to well defined stoichiometric phases, stable with temperature, as Sr-doped $RE_{2-x}Sr_xNiO_{4.0}$; and excess oxygen doping, which leads to $RE_2NiO_{4+\delta}$ phases with adjustable oxygen over stoichiometry even at low-temperature. The additional oxygen content δ can be specifically tuned in between 0 and 0.25. The structural strain is released partially with doping; consequently, a disorder is introduced in the long-range tilting pattern of NiO_6 octahedron. When the disorder is present and correlation length of NiO_6 octahedron tilting is short ranged, the resulting average structure can successfully described by another low temperature orthorhombic phase (LTO') with $Fmmm$ space group symmetry⁵¹. The structural phase diagram obtained for the $Nd_2NiO_{4+\delta}$ system as a function of δ has been reported recently by Ceretti et.al¹⁴. The structural phase diagram is obtained by in-situ electrochemical oxidation and reduction of the as-prepared polycrystalline $Nd_2NiO_{4.24}$ compound. The electrochemical reaction process can formally be described as



The intercalation of excess oxygen atoms is directly related to the charge transfer (n) due to doubly negative O^{2-} ions. Thus, the charge transfer can be expressed by a simple relation as $\delta = 2n \text{ e/f.u.}$ Therefore, an intercalation of $\delta = 0.24$ oxygen atoms corresponds to a charge transfer of about 0.48 e/f.u. The structural phase diagram obtained by Ceretti et.al¹⁴ for $Nd_2NiO_{4+\delta}$ at

ambient temperature with this diffraction study is shown in **Fig.2.8**. Principally, three distinct phases were observed as a function of δ : (i) the starting LTO' phase (though a subtle monoclinic distortion was observed with high-resolution x-ray powder diffraction measurements⁵³), (ii) the tetragonal LTT phase for the intermediate stoichiometry, and (iii) the LTO phase for fully reduced and stoichiometric $Nd_2NiO_{4.0}$. For the $Nd_2NiO_{4.24}$ starting phase, additional superstructure reflections were detected in addition to those corresponding to the $Fmmm$ space group. These superstructure reflections are related to the incommensurate ordering of excess oxygen atoms. The intensities of these superstructure reflections are below the detection level of usual laboratory based x-ray powder diffraction studies even with long counting statistics. Therefore, the true crystal structure of the $\delta = 0.24$ compound is much complex and incommensurate while only the average structure (without considering superstructure reflections) can be described by the $Fmmm$ space group. The starting $Nd_2NiO_{4.24}$ and the end $Nd_2NiO_{4.0}$ phases were revealed as line phases since their lattice constants remain constant during the intercalation and deintercalation process while their respective scale factors only vary. The transformation of the $Nd_2NiO_{4.24}$ phase towards the intermediate tetragonal phase goes through a biphasic region. A single-phase region with LTT structure was clearly identified for the excess oxygen content $0.07 \leq \delta \leq 0.10$. It is worth to point out that *no superstructure reflections related to excess oxygen ordering were observed in the neutron diffraction pattern* of the LTT phase implying a commensurate crystal structure of this compound at room temperature. The reduction process below $\delta = 0.07$ proceeds as a two-phase reaction, where the volume fraction of the $Nd_2NiO_{4.07}$ continuously decreases, and the amount of stoichiometric $Nd_2NiO_{4.00}$ increases accordingly. *The reoxidation stops when the LTT phase was reached with stoichiometry $Nd_2NiO_{4.10}$. Consequently, the reoxidation process is not fully reversible even with the same current density as the reduction.*

It is worth to compare the RT-phase diagram of the $Nd_2NiO_{4+\delta}$ system obtained with thermally prepared samples^{54,55} as the oxygen diffusion kinetics largely depend on the temperature. In these samples, δ was precisely tuned by high temperature annealing using different reductive gas atmospheres. The phase diagram obtained by Ishikawa et al.⁵⁵ with powder x-ray diffraction measurements is shown in **Fig. 2.9**. It was found that the system belongs to a single-phase region with LTO' phase with space group symmetry $Fmmm$ for $0.15 \leq \delta \leq 0.25$. However, three different orthorhombic phases (O^I , O^{II} and O^{IV}) were distinguished depending on the variations of their lattice parameters, cell volume and structural strain as function of δ . A phase coexistence region comprised of LTLO + LTO' phases is evidenced for $0.10 \leq \delta \leq 0.15$ region. However, for $0.067 \leq \delta \leq 0.10$ region, a slight deviation from the tetragonal LTT phase is reported and the orthorhombic LTLO phase is identified which is in strong contrast to the neutron powder diffraction study on the electrochemically prepared sample. Therefore, a possible effect of the sample synthesis technique might exist on the observed discrepancies related to the moderately doped phase.

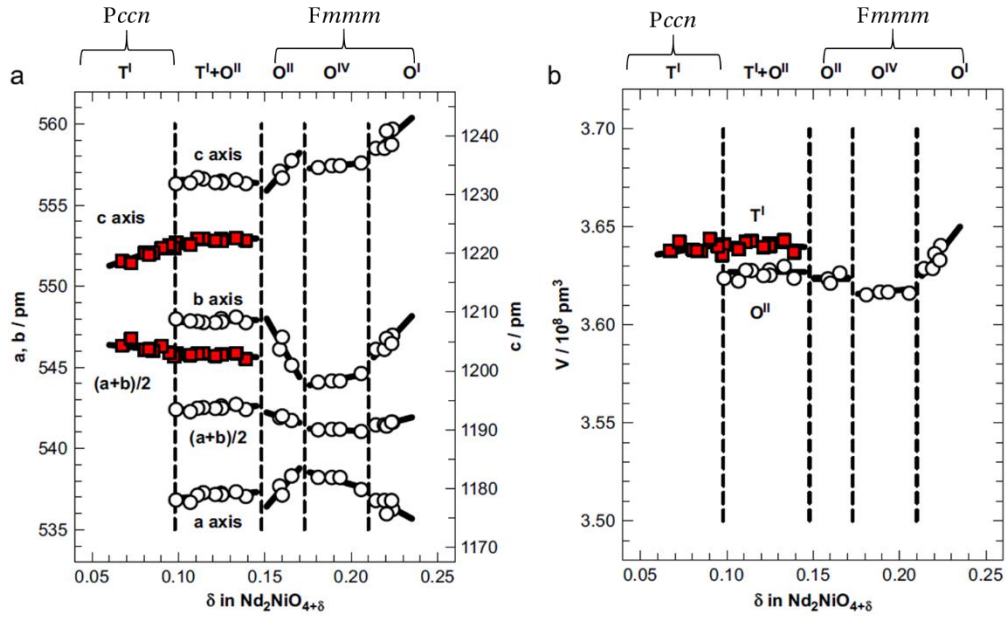


Figure 2.9 | Variation of different unit cell parameters with δ in $Nd_2NiO_{4+\delta}$ at room temperature. (a) Cell parameters and (b) the cell volume corresponding to the different phases at different δ . In the plots different unit cell abbreviations are as following: O^I : orthorhombic-I (space group $Fmmm$: LTO \checkmark); O^{II} : orthorhombic-II (space group $Fmmm$: LTO \checkmark); O^{IV} : orthorhombic-IV (space group $Fmmm$: LTO \checkmark); T^I : quasi-tetragonal-I (space group $Pccn$: LTLO). The figure is taken from reference⁵⁵.

In the other way, substitution of RE^{3+} ions with smaller Sr^{2+} ions appears to be random i.e. Sr^{2+} ions randomly replace rare earth cations in the regular lattice sites and has a relatively weak effect on the lattice. In contrast, in case of oxygen doping, excess oxygen atoms take regular interstitial sites inside the RE_2O_2 bilayer and introduce disorder in the long-range tilting pattern of NiO_6 octahedrons. Furthermore, in case of O-doped system, the excess oxygen atoms become mobile at high temperature in comparison to the Sr-doped system in which random positions of dopants are fixed at relatively high temperature. The Sr-doped system allows a continuous variation of the hole concentration. In contrast, ordered single phases only occur at particular values of δ for O-doped systems, and phase separation occurs for an arbitrary value of δ ³⁵. However, Sr doping prevents the development of long-range stripe order due to chemical disorder introduced by dopants. The x - T structural phase diagram reported by Hücker et al.⁵⁶ is shown in **Fig.2.10** for oxygen stoichiometric $La_{2-x}Sr_xNiO_4$ system. The HTT phase becomes stable at or below room temperature for a Sr-doping concentration $x \sim 0.21$. For a lower Sr-doping concentration with $0.05 \leq x \leq 0.2$, a similar structural transition sequence, similar to the undoped $RE_2NiO_{4.0}$ system, from HTT to LTO to LTT is observed as a function of temperature. However, the transition temperatures are largely decreased with Sr-doping. Furthermore, the LTLO phase is observed at lower Sr-concentration with $x < 0.05$. Similar structural transition sequence is also observed for

Pr^{3+} and Nd^{3+} systems. However, the phase boundary of HTT/LTO transition shifts toward higher x and T with respect to La^{3+} system owing to smaller ionic radii of the former two ions. Moreover, the LTT phase is extended to $x = 0.33$ at low temperature in case of Pr and Nd-based systems whereas the LTT/LTO phase transition is already suppressed at $x \sim 0.2$ for La-based compounds.

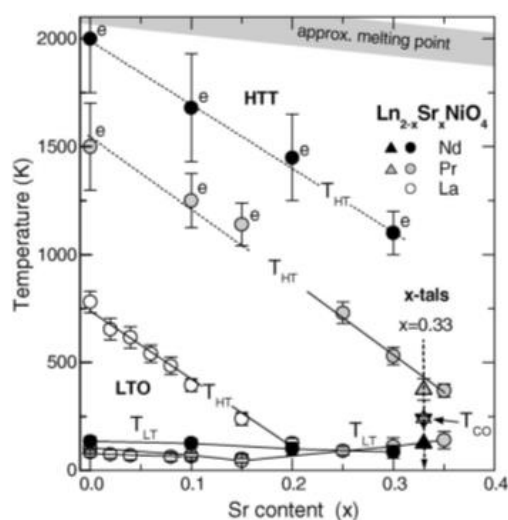


Figure 2.10 | Schematic representation of x - T phase diagram of different $Ln_{2-x}Sr_xNiO_4$ systems.

Data points are obtained from x-ray powder diffraction studies on polycrystalline samples. “e” symbols represent data points obtained from linear extrapolations of experimental data up to 800 K. Triangular symbols marks data points for $x = 0.33$ single crystals. The figure is taken from reference⁵⁶.

2.2. Ordering of excess oxygen atoms

The excess oxygen content δ in $RE_2MO_{4+\delta}$ strongly depends on RE^{3+} and the transition metal (M^{2+}/M^{3+}) ions. $La_2NiO_{4+\delta}$ or $La_2CuO_{4+\delta}$ can incorporate only a limited amount of excess oxygen δ while $(Nd,Pr)_2NiO_{4+\delta}$ or $La_2CoO_{4+\delta}$ can adapt up to $\delta = 0.25$ ^{18,57}. Neutron and synchrotron diffraction experiments have evidenced that the diffraction pattern of these high- δ phases show numerous incommensurate or commensurate satellite peaks, corresponding to the complex long-range ordering of excess oxygen atoms in interstitial sites. Long-range ordering of excess oxygens develops at $\delta \geq 0.03$ in $La_2NiO_{4+\delta}$ as new superstructure reflections appear in the diffraction pattern. The presence of superstructure reflections in the $0.03 \leq \delta \leq 0.11$ region can be explained by a 1D model similar to the staging behavior previously observed for halogens or alkalis intercalated into graphite²⁷. Apical oxygens, in the LTO phase, are displaced along the [010] direction since NiO_6 octahedrons are tilted around the [100] axis and equatorial oxygens are displaced perpendicular to the NiO_2 plane. Nearest-neighbor octahedrons are contra-rotated since equatorial oxygens bridging them. In this way, the structural distortion moves throughout

the NiO₂ plane. In the oxygen non-stoichiometric LTO phase, excess oxygens occupy interstitial sites inside the (REO)₂ bilayer. These interstitial sites are tetrahedral sites coordinated by four RE³⁺ ions and four apical oxygen atoms. Such an arrangement leads to Coulomb repulsion between the interstitial and nearest four apical oxygens. If the repulsion of interstitials displaces apical oxygens along the [010] direction of LTO phase, this tilt would then transmit within the plane and perpendicular to the planes. Thus, the interstitial layer creates an antiphase domain boundary since excess oxygens induce a reversal of the usual LTO tilt pattern. Such tilting pattern in the intercalated phase creates an array of energetically favorable interstitial positions, whereas none exists in the normal LTO phase as shown in **Fig. 2.11(a)** and **(b)**. Hence, if an interstitial site is occupied by an excess oxygen in a particular layer, it will create favorable positions for other oxygen atoms to occupy the same layer. However, the Coulomb repulsion between oxygen interstitials will restrict the amount of interstitials inside a particular layer, and thus on the distance between the intercalated layers along the *c*-axis. For the description of such a tilting pattern, Tranquada et.al. adopted the notion used for "staging" in intercalated graphite²⁷. In this model, a stage-*n* ordering is described by the repetition of an oxygen interstitial layer after *n* NiO₂ planes. Schematic representations for *n* = 2, 3 and 4 are illustrated in **Fig. 2.12** as illustrated by Tranquada et al.²⁷. Extinction condition in the pure LTO phase allows superlattice peaks of (*0kl*) type with *k* odd, *l* even and not equal to zero. For the oxygen intercalated LTO phase with stage-*n* ordering, the superlattice peaks are expected to appear at (*0, k, l ± 1/n*) with *k* odd and *l* even (including zero). However, due to defects and imperfect ordering, actual superlattice peaks barely occur at these positions. The "intercalated LTO" does not mean that the correct space group for the staged structure is *Bmab*. Rather, it indicates that LTO type octahedron tilting pattern exists between two interstitial layers. **Fig. 2.11(c)** and **Fig. 2.11(d)** show the displacement pattern of the apical oxygen atoms just below and above an interstitial layer at *z* = 0.25 in the oxygen intercalated LTT phase as illustrated by Tranquada et al.²⁷. In the LTT phase, apical oxygens are displaced diagonally from the interstitial sites. Tranquada et.al. proposed two different scenarios for the interstitial oxygen position and related displacement for apical oxygen atoms²⁷. In the first scenario as shown in **Fig. 2.11(c)**, apical oxygens with extra local displacement might accommodate isolated interstitials. In the LTT tilt pattern, only half of the equatorial oxygens sitting along a diagonal are displaced perpendicular to the NiO₂ plane. Thus, it is possible to flip the tilts of a diagonal row of octahedra without disturbing the neighboring rows. Such a defect creates favorable positions for excess oxygens in which all-neighboring apical oxygens are displaced radially away from the interstitial site. This scenario is schematized in **Fig. 2.11(d)**. In any case, until now, superstructure reflections characterizing such a coherent tilt pattern due to added oxygens were not detected in the intercalated LTT phase²⁷.

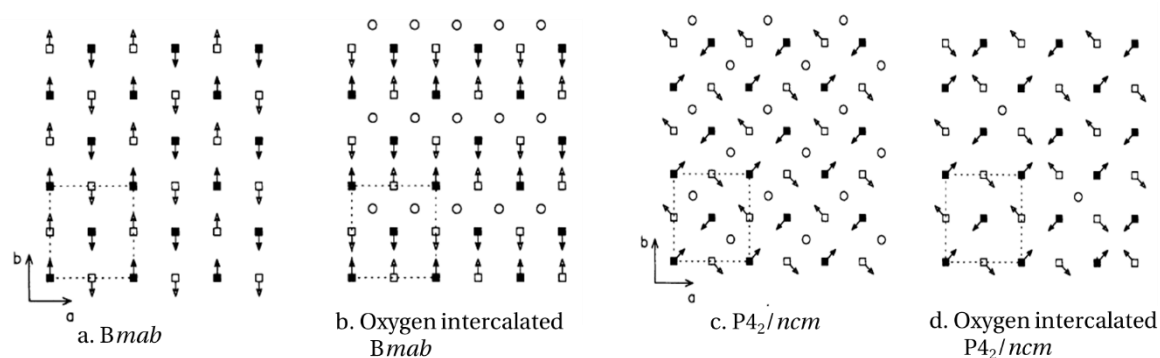


Figure 2.11 | Displacement patterns of apical oxygen atoms in normal and oxygen intercalated LTO ($Bmab$) and LTT ($P4_2/ncm$) phases. Open and solid squares represent the apical oxygens just above and below an interstitial layer, respectively. Small arrows indicate the directions of oxygen displacements, and the dotted lines represent the chemical unit cell. The open circles indicate interstitial oxygens. The figure is taken from reference²⁷.

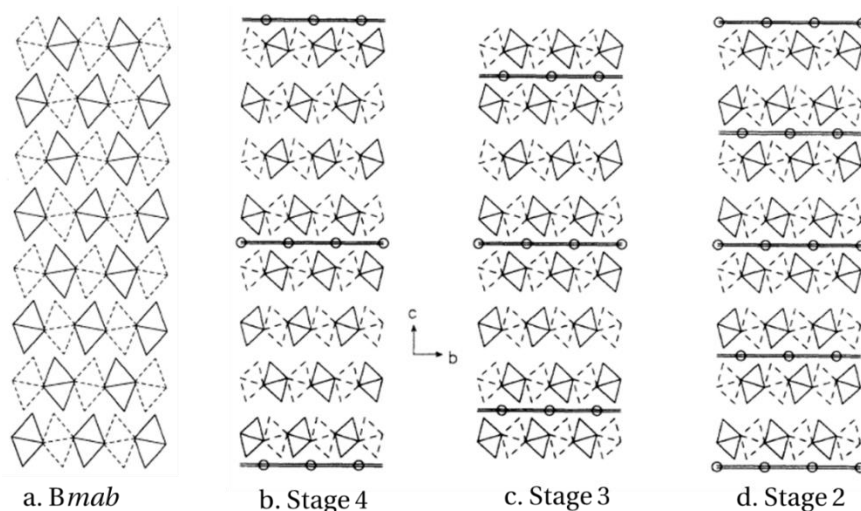


Figure 2.12 | The a -axis projections of the crystal structures showing NiO_6 octahedron tilting pattern for undoped and oxygen doped $RE_2NiO_{4+\delta}$ phases. The crystal structure of (a) undoped LTO phase, (b) stage-4, (c) stage-3, and (d) stage-2 structure. The double triangles represent NiO_6 octahedra. Octahedrons represented by dashed lines are displaced by $a/2$ with respect to the octahedra drawn with solid lines. Thus, dashed octahedrons are out of the plane of the paper. Open circles show the positions of oxygen interstitials. Thick solid lines represent the interstitial layer. The figure is taken from reference²⁷.

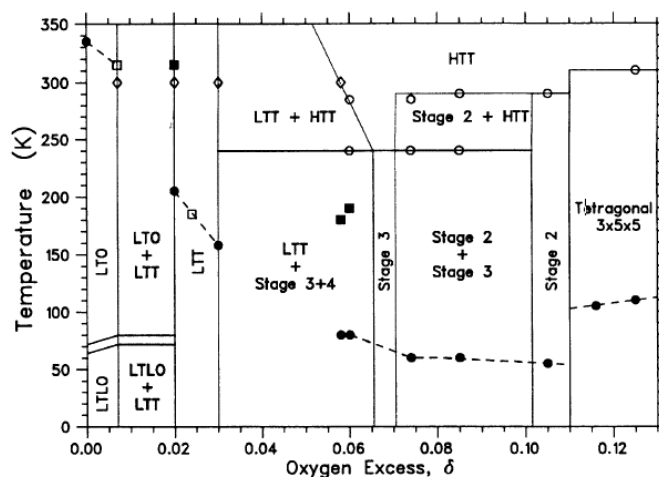


Figure 2.13 | The δ - T phase diagram of $La_2NiO_{4+\delta}$. Solid circles and solid squares denote Neel temperatures of the primary phase and secondary phases while open squares indicate these transitions translated to the appropriate values of δ . The interstitial oxygens are ordered three dimensionally for $0.11 \leq \delta \leq 0.13$ with simultaneous ordering of spins and holes. The figure is taken from reference²⁷.

The structural δ - T phase diagram of $La_2NiO_{4+\delta}$ obtained by Tranquada et al.²⁷ is shown in **Fig. 2.13**. 1D ordering of excess oxygen atoms is evidenced for $0.03 \leq \delta \leq 0.11$ with neutron diffraction study. At $\delta = 0.105$, a stage-2 order is observed. With increasing oxygen concentration, the next stage order is expected to be $n = 1$. Instead, at $\delta = 0.125$, 3D ordering of excess oxygen atoms is evidenced with superstructure peaks related to $q_1 = (1/3, 0, 1)$ and $q_2 = (0, 4/5, 4/5)$, which indicate that the positions of the interstitials are correlated when the amount of intercalated interstitials is larger. The ordering of oxygen interstitials below 310 K is characterized by a unit cell of dimension $3a \times 5b \times 5c$ and corresponds to an ideal excess oxygen content of $\delta = 2/15$ per formula unit. Quantitative analysis of superstructure reflections shown that scattered intensity comes from the displacements of apical oxygen and La atoms in the lattice. Interestingly, it was found that the charge ordering appears and the magnetic order abruptly changes from commensurate to incommensurate near $\delta = 0.11$, where the ordering of the oxygen interstitials also changes from 1D to 3D²⁷. Furthermore, electron diffraction studies on the higher oxygen doped compounds with $\delta \sim 0.25$ show much complicated superstructure reflections and ordering pattern of oxygen interstitials^{26,28}. Hiroi et.al. found two types of homologous series of superstructures for samples containing excess oxygens. These superstructure reflections were indexed with supercells of type $2a \times ka \times lc$ ($k, l = n$ or $2n$ depending upon n ; the most frequently observed sets were $k/2 = l/2 = n = 2$ and $k = l/2 = n = 3$) and $\sqrt{2}a \times p\sqrt{2}a \times qc$ (most frequently $p = 2$ and $q = 1$), where $a \times a \times c$ corresponds to the $I4/mmm$ type cell²⁸. Phases with discrete oxygen contents of $La_2NiO_{4+\delta}$ with $\delta = 0, \dots, 1/8, 1/6, 1/4$ were proposed. However, contradictory observations are reported for $Nd_2NiO_{4.25}$ and $La_2CoO_{4.14}$ compounds at RT. **Fig. 2.14(a)** shows the reconstructed $(hk4)$ plane of

the $Nd_2NiO_{4.25}$ compound obtained with neutron diffraction¹⁸. Strong contributions of incommensurate reflections corresponding to the 3D ordering of excess oxygen atoms became evident in addition to the basic reflections. These superstructure reflections on the $(hk0)$ plane were indexed with wave vectors $q_3 = (0.4378, -0.2302, 0)$ and $q_4 = (0.4378, 0.2302, 0)$. Intensities of these superstructure reflections reach more than 5% compared to the basic reflections, suggesting strong structural modulations. A similar scheme of the incommensurate structure was recently reported for $La_2CoO_{4.14}$ with synchrotron x-ray diffraction study at RT as shown in **Fig. 2.14(b)**²⁵, underlying the more general character of complex excess oxygen ordering in K_2NiF_4 -type oxides as a function of δ . In this case, the superstructure peaks were indexed with $q_5 = (0.85, 0.53, 0)$ (blue) and $q_6 = (0.85, -0.53, 0)$ (red) incommensurate vectors.

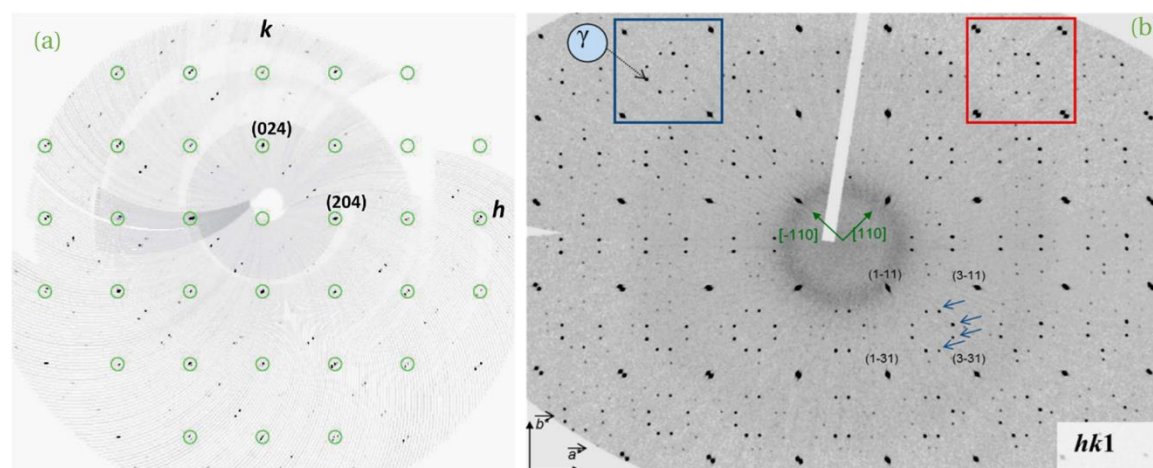


Figure 2.14 | Reconstructed reciprocal planes obtained with x-ray and neutron diffraction data showing strong structural modulations due to excess oxygen ordering in $RE_2MO_{4+\delta}$. (a) $(hk4)$ -plane of twice twinned $Nd_2NiO_{4.25}$ single crystal at RT obtained by neutron diffraction. The incommensurate superstructure reflections corresponding to ordering of interstitials were indexed with 2D modulation vectors q_3 and q_4 with respect to F-type basic reflections (green circles). (b) $(hk1)$ reciprocal plane of $La_2CoO_{4.14}$ at RT with x-ray diffraction. Few oxygen superstructure reflections are indicated by blue arrows. One first order reflection is marked as γ . Figures are taken from references¹⁸ and²⁵.

2.3. Oxygen migration in $RE_2NiO_{4+\delta}$

Highly anisotropic oxygen ion conductivity in K_2NiF_4 type oxides have made them appropriate candidates for cathodes and electrolytes in solid-state electrochemical devices. In solids, ionic transport highly depends on the crystal chemistry as well as on the interaction of the oxygen ions with the crystal lattice. A large number of concerted theoretical and experimental works have been devoted to understand the microscopic origin of this remarkable physical property, but still

some debates are present about the nature of the migration species and diffusion pathways inside the crystal lattice. This is of critical importance to design and tailor new materials for low temperature oxygen ion conductors. There are two different approaches used to simulate the oxygen diffusion process in RE₂MO_{4+δ}. In the first process, DFT based atomistic calculations are performed to estimate the formation energy of defects involved in the diffusion process, and estimate the potential energy barrier on a known diffusion pathway. Such calculations are generally performed on small structural models with few hundred atoms, and at T = 0 K. In The second approach with MD simulations, structural evolution is traced as a function of time, in order to find diffusion pathways and estimate the macroscopic diffusion coefficients. MD simulations are generally performed on structural models containing several thousand atoms at a set temperature and different classical potential models are used to approximate electronic interactions between atoms.

Table 2.2 | Various compensation mechanisms for excess oxygens and their activation energies in La₂NiO_{4+δ}. The following table is taken from reference⁵⁸.

	Compensation mechanism	Energy/eV	
		Isolated defects	Clustered defects
A	$3\text{La}_2\text{O}_3 \rightarrow 2\text{La}_{\text{Ni}}^{\bullet} + \text{O}_i^{\bullet} + 4\text{La}_{\text{La}}^{\times} + 8\text{O}_{\text{O}}^{\times}$	11.44	7.89
B	$3\text{La}_2\text{O}_3 + 1/2\text{O}_2 \rightarrow 2\text{La}_{\text{Ni}}^{\bullet} + 2\text{O}_i^{\bullet} + 4\text{La}_{\text{La}}^{\times} + 8\text{O}_{\text{O}}^{\times}$	4.93	4.08
C	$1/2\text{O}_2 + \text{O}_{\text{O}}^{\times} \rightarrow 2\text{O}_i^{\bullet} + \text{V}_{\text{O}}^{\bullet\bullet}$	-1.96	—
D	$1/2\text{O}_2 + \text{O}_{\text{O}}^{\times} \rightarrow \text{O}_i^{\bullet} + \text{O}_{\text{O}}^{\bullet}$	-3.99	-5.00
E	$1/2\text{O}_2 + 2\text{O}_{\text{O}}^{\times} \rightarrow \text{O}_i^{\bullet} + 2\text{O}_{\text{O}}^{\bullet}$	-1.48	-6.28
F	$1/2\text{O}_2 + \text{Ni}_{\text{Ni}}^{\times} \rightarrow \text{O}_i^{\bullet} + \text{Ni}_{\text{Ni}}^{\bullet}$	-6.57	-6.87
G	$1/2\text{O}_2 + 2\text{Ni}_{\text{Ni}}^{\times} \rightarrow \text{O}_i^{\bullet} + 2\text{Ni}_{\text{Ni}}^{\bullet}$	-6.63	-7.56
H	$1/2\text{O}_2 + \text{Ni}_{\text{Ni}}^{\times} + \text{O}_{\text{O}}^{\times} \rightarrow \text{O}_i^{\bullet} + \text{Ni}_{\text{Ni}}^{\bullet} + \text{O}_{\text{O}}^{\bullet}$	-3.58	-7.92

In recent years, classical MD simulations have been used to calculate macroscopic diffusion coefficients as well the nature of the mobile ion, thus the electronic structure, electron transfer and oxygen migration mechanisms. L. Minerveni et.al⁵⁸ estimated various defects and their activation energies for oxygen doped La₂NiO_{4+δ} as shown in **Table 2.2**. Thus, the incorporation of excess oxygens in the lattice is compensated either by Ni³⁺ ions or by combined Ni³⁺ and O²⁻ or O⁻ ions. These results suggest that when defects are isolated, true for very small values of δ, the charge compensating holes will reside on the Ni sites, as the reactions F and G exhibit the lowest energies. At larger values of δ, when defect clustering becomes more likely, holes may reside on a mixture of both nickel and oxygen sites, as the reactions G and H are lowest (*cf.* **Table 2.2**). In all such cases, the holes will be in the NiO₂ planes rather than the La₂O₂ planes and the oxygen interstitial ions may be either O⁻ or O²⁻. MD simulations at high temperature of RE₂MO_{4+δ} phases show that the major diffusion mechanism is an interstitialcy process²⁰. This is described as a two-step diffusion process as schematized in **Fig. 2.15**. In the first step, the interstitial oxygen atom

pushes one of the four nearest apical oxygens to a neighboring vacant interstitial site. In the next step, the interstitial oxygen occupies the vacant apical site and so on. Thus, the interstitialcy diffusion dominantly occurs inside the RE_2O_2 bilayers and it is significantly less in the direction perpendicular to the rock-salt layers or along the crystallographic c -axis. Such kind of migration mechanism microscopically explains the origin of anisotropic oxygen ion mobility observed in these materials. The cumulative trajectory obtained from MD calculations can be used to observe oxygen diffusion pathway associated with the interstitialcy mechanism. Simulated trajectory pattern is shown in **Fig. 2.16(a)** for $Pr_2NiO_{4+\delta}$ along with the nuclear density map obtained MEM analysis of powder neutron diffraction data on a Pr_2NiO_4 -based oxide (**Fig. 2.16(b)**)²⁴. In **Figure 2.16(c)**, the evolution of the oxygen diffusion coefficient is plotted as a function δ in $Pr_2NiO_{4+\delta}$ simulated at $T = 1100$ K. Interestingly, the diffusivity rapidly increases with the introduction of excess oxygen content approximately up to $\delta \sim 0.02$, and then surprisingly remains constant up to $\delta \sim 0.23$ ²⁴.

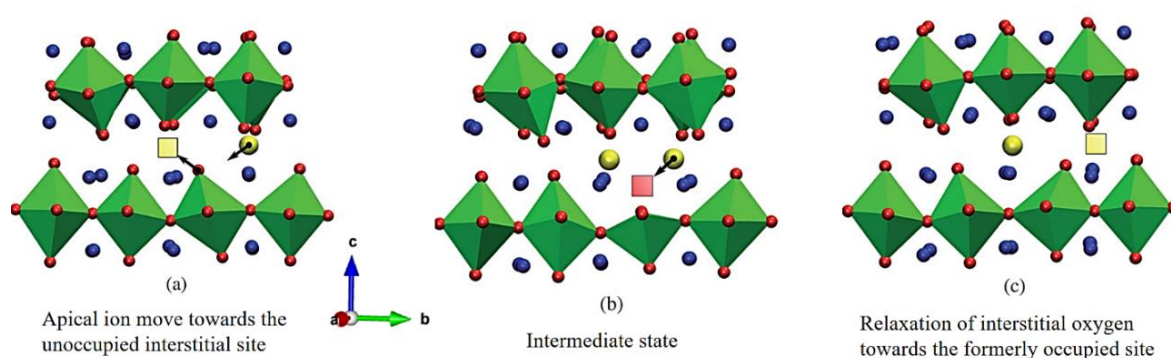


Figure 2.15 | Schematic representation of different steps associated to the interstitialcy mechanism. MD simulations were performed at 900 K for $La_2NiO_{4.09}$. NiO_6 octahedrons are shown in green. Blue, red and yellow spheres represent La^{3+} ions, oxygen atoms and interstitial oxide ions, respectively. Red and yellow squares represent the vacant apical and interstitial sites relevant to the diffusion process, respectively. The figure is taken from reference²⁰.

The importance of the atomistic simulations is substantial in identifying the microscopic diffusion process in $RE_2MO_{4+\delta}$ and for the description of oxygen diffusion coefficient at high-temperature. However, most calculations are performed using a classical approach at high-temperature on the parent HTT phase with random distribution of oxygen interstitials. This scenario is largely different from the low temperature (close to room temperature) regime where ordering of excess oxygen occurs and different complex structural phases are observed related to the cooperative tilting of NiO_6 octahedrons. The oxygen mobility in the room and moderate temperature range is described by a phonon-assisted diffusion, which was originally proposed for oxygen deficient $Sr/CaFeO_{2.5}$ Brownmillerites from a combined study of inelastic neutron

scattering and DFT calculations. This also could be extended to the $RE_2MO_{4+\delta}$ compounds and related materials²⁴.

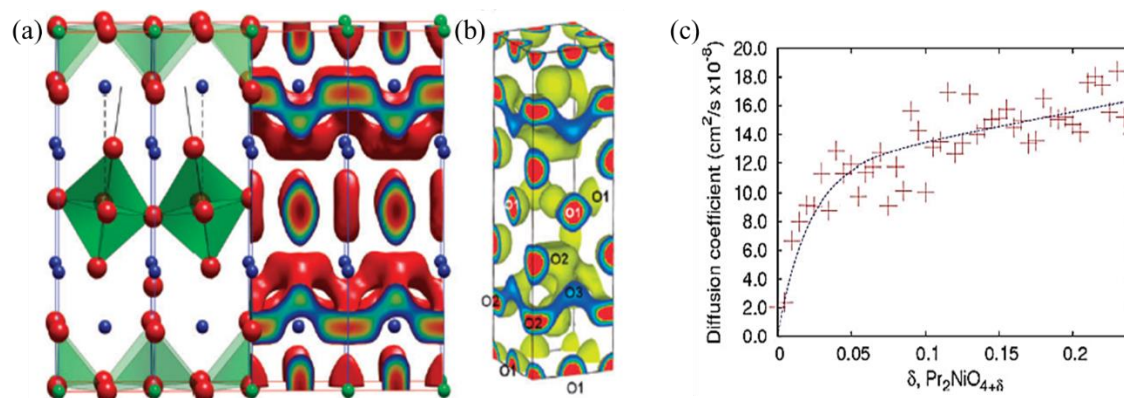


Figure 2.16 | (a) The crystal structure of $Pr_2NiO_{4+\delta}$ and MD simulated trajectory of apical and interstitial oxygens at 1100 K and $\delta = 0.09875$, (b) Nuclear scattering densities of different atoms obtained with MEM analysis from powder neutron diffraction data, and (c) oxygen diffusion coefficient of $Pr_2NiO_{4+\delta}$ as a function of δ . Figures are taken from ²⁴.

Brownmillerite compounds with chemical formula $ABO_{2.5}$ can be treated as oxygen deficient perovskites. The crystal structure of these compounds composed of alternating corner shared octahedral (BO_6) and tetrahedral (BO_4) layers and 1D oxygen vacancy channels inside the tetrahedral layers. Two orientations of the tetrahedral chains are possible, termed as right handed (R) and left handed chains (L). The ground state energies of the R and L chains are similar thus allowing an easy switching of the rotation direction⁸. Depending on the arrangement of these chains and their stacking of along the b -axis i.e. along the stacking axis, the crystal structure is described either in ordered space-groups as $Pnma$ and $I2mb$ or in partially disordered space-group $Imma$, as represented in **Fig. 2.17(a)** for $SrFeO_{2.5}$. Paulus et al.⁸ have recently proposed an oxygen migration mechanism for $SrFeO_{2.5}$ involving low energy phonon modes and dynamic fluctuations of FeO_4 tetrahedral chains on a picosecond time scale. These low energy phonon modes are determined by the movements of iron and apical oxygens along the b -axis and proposed to be important prerequisites for oxide ion migration close to room temperature for Brownmillerites. The apical oxygen atoms, which connect the neighboring octahedron and tetrahedron, exhibit strong thermal displacements that can take the apical oxygen into the vacancy channel inside the tetrahedral layer. The local arrangement during the migration is thus changed from a configuration octahedron-tetrahedron (**Fig. 2.17(b)**) to a configuration square pyramid-reoriented tetrahedron (**Fig. 2.17(c)**). The shallow potential for the migration process of apical oxygens is determined by the Fe-O bond length along the b -axis. While the oxygen

migration is already realized for $SrFeO_{2.5}$ at room temperature (RT), strongly reduced oxygen mobility in isostructural $CaFeO_{2.5}$ at RT strongly depends on the shorter stacking axis and the crystal structure with ordered tetrahedral layers (space group $Pnma$). Therefore, the oxygen migration in $CaFeO_{2.5}$ requires higher temperatures to reach comparable diffusing properties as in $SrFeO_{2.5}$.

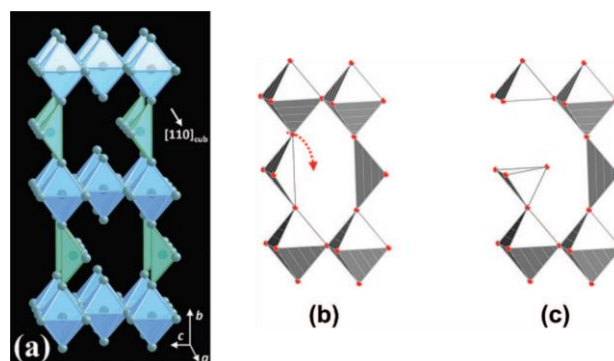


Figure 2.17 | (a) Schematic representation of the Brownmillerite crystal structure in $Imma$ space group of $SrFeO_{2.5}$. The structure consists of 1D oxygen vacancy channels along the $[110]$ -direction with respect to the cubic perovskite phase. FeO_6 octahedrons and FeO_4 tetrahedrons are represented with blue and green colors, respectively. Steps for the oxygen diffusion process from an apical site to the tetrahedral layer are shown in (b) and (c). Figures are taken from the reference⁸.

Oxygen migration in $RE_2NiO_{4+\delta}$ compounds occurs through the regular interstitial lattice sites as confirmed by DFT calculations⁵⁹. Moreover, in these compounds, apical oxygen atoms show strong thermal displacements as confirmed by previous high-resolution neutron diffraction experiments^{14,18,19,25,57,60}. These displacements are also related to the low energy phonon modes. Positional recurrence maps (PRMs) have been calculated for apical oxygen atoms from molecular dynamics trajectories at different temperatures for $Nd_2NiO_{4+\delta}$ phases as shown in **Fig. 2.18** by Piovano et al.⁵⁹. They look similar to nuclear density maps obtained with MEM analysis of single crystal neutron diffraction data by Ceretti et.al¹⁴ as shown in **Fig. 2.19** for $Pr_2NiO_{4.09}$ ¹⁴. However, only dynamical contribution from the displacements of apical oxygen atoms is considered in PRM. As shown in **Fig. 2.18**, the $\delta = 0$ phase restricts any diffusion process on a 40 ps timescale due to freezing of NiO_6 octahedrons with the LTO type tilt pattern at low temperature. Thus, all the apical oxygen atoms are strongly localized at low temperature. However, high temperatures enable the delocalization of the apical oxygen atoms and free rotations of the NiO_6 octahedra for the LTO phase. Corresponding change of the tilt pattern from $[010]$ to $[110]$ direction favors apical oxygen diffusion. As shown in the middle and lower part of **Fig. 2.18**, the oxygen diffusion is triggered by the presence of excess oxygen atoms in interstitial sites already at low temperature

due to change in lattice dynamics. The interstitial oxygens can diffuse only to the nearest apical oxygen in the [110] direction related to the specific NiO_6 octahedron tilt scheme in which apical oxygen comes closer to the nearest interstitial site. At HT, interstitial oxygen has enough thermal energy to hop to any possible next neighboring apical oxygen site. At 1070 K, the patterns look almost isotropic meaning that apical oxygen atoms are freed from the octahedra and do behave independently. This corresponds well to the HT average representation in which all the octahedrons are dynamically disordered. DFT calculations and neutron scattering investigations showed that the displacement of apical oxygen atoms are related to the specific low energy phonon modes as shown in **Fig. 2.20(a)** and **(b)** in which generalized phonon density of states are plotted at RT¹⁷. The states with apical oxygen displacements mainly along the [100] direction correspond to feature A, while the feature B corresponds to those along the [110]-direction. The octahedral modes in particular the stretching of NiO_6 octahedrons along the c -axis represent the feature C. Therefore, the observed changes as a function of δ indicate a decrease of spectral weight for vibrational modes with displacement pattern along the [100] direction and a concomitant increase for the modes with displacement pattern along the [110] direction. Moreover, the change of the tilt pattern from [100] to [110] favors the displacement of the apical oxygen atoms into the rock-salt layer, which activates the diffusion process. However, with increasing temperature, the influence of these anisotropic displacement modes become less important and completely disappears at high-temperature where the stochastic hopping process dominates. This has been experimentally at 1073 K by Perrichon et al.¹⁷ as shown in **Fig. 2.20(c)**.

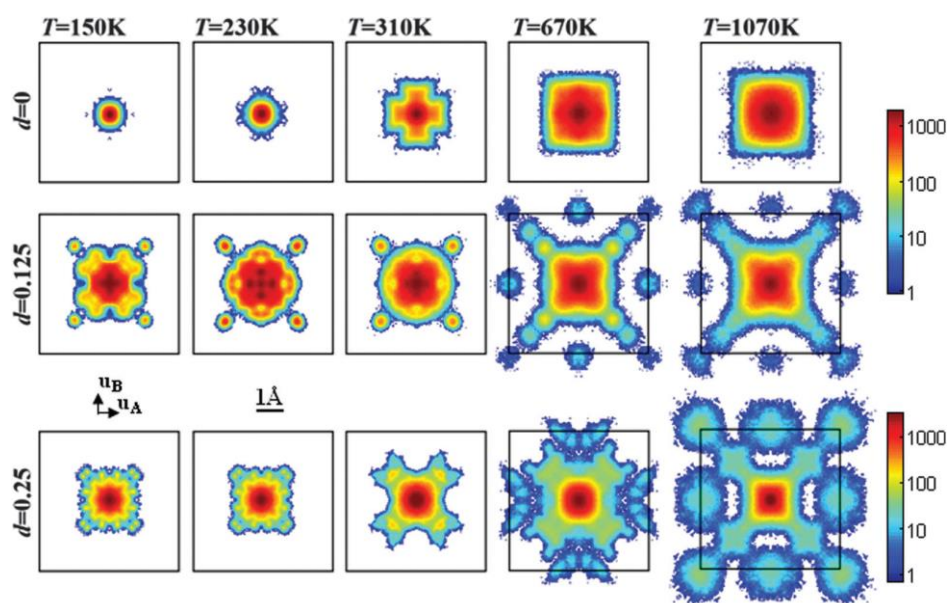


Figure 2.18 | Positional recurrence maps (PRM) showing the cumulative trajectory of apical oxygen atoms on a 40 ps time scale. MD simulations were performed at $T = 150, 230, 310, 670$ and 1070 K for $Nd_2NiO_{4+\delta}$ with $\delta = 0, 0.125$ and 0.25 . Each map is cut in space to the conventional F-cell (black border). Figure is taken from the reference⁵⁹.

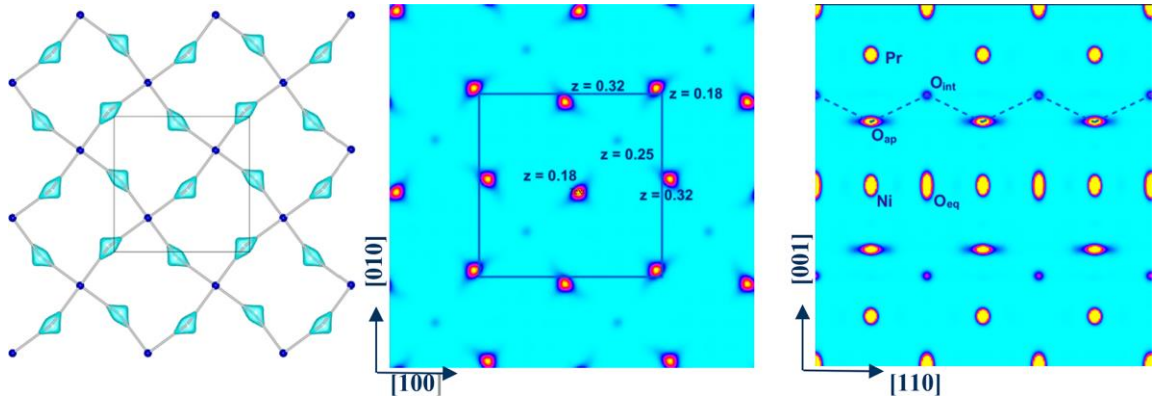


Figure 2.19 | Reconstructed isosurface of apical oxygen atoms in $Pr_2NiO_{4.09}$ obtained from single crystal neutron diffraction data with MEM analysis. Left: isosurfaces of the apical oxygen atoms (green) tetrahedrally coordinated by O_{int} atoms (blue). Middle: projection of the nuclear densities for $0.16 \leq z \leq 0.34$; the F unit cell is outlined. Right: $[110]$ - $[001]$ projection cut along the $[1-10]$ direction with the integration thickness $\Delta(x, x) = 0.07$ showing the oxygen diffusion pathway along the $[110]$ direction, outlined with a blue dashed line. Figure is taken from the reference¹⁴.

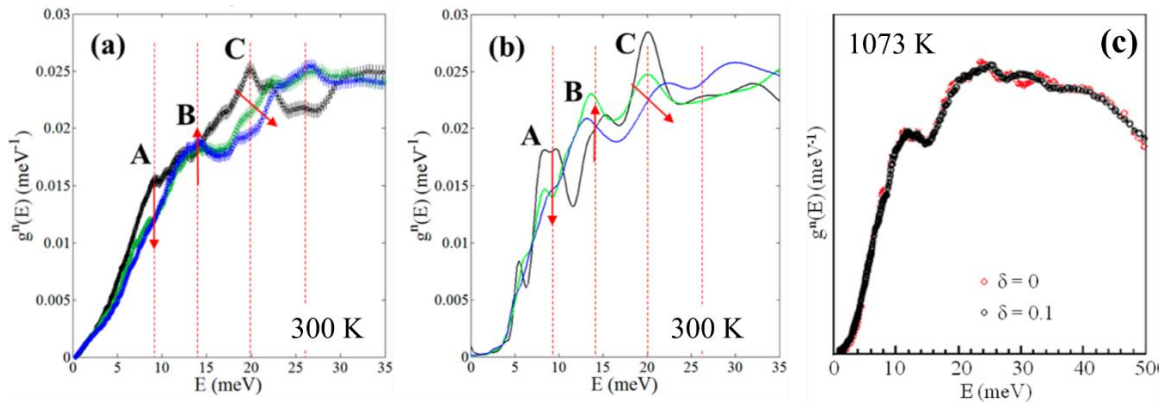


Figure 2.20 | Generalized phonon density of states of $Nd_2NiO_{4+\delta}$. (a) Experimental data measured at 310 K, (b) *ab-initio* MD calculated vibrational density of states with $\delta = 0$ (black), 0.1 (green), and 0.25 (blue) and (c) experimental data at 1073 K with $\delta = 0$ (red) and 0.1 (black). Figures are taken from the reference¹⁷.

In summary, combination of neutron scattering measurements and *ab-initio* DFT calculations confirm a dynamically triggered oxygen diffusion process that enable to explain the enhanced mobility at RT in a partially filled lattice. The diffusion process is coupled with the low energy phonon modes directly related to the different structural instabilities. Yet there are few fundamental differences between the experimental results and theoretical investigations. This is primarily due to the difference between the real crystal structures and the structural models used in simulations. Exact crystal structures are used for calculations. This means that partial occupancy of an oxygen site is not possible. In $RE_2MO_{4+\delta}$ compounds, interstitials induce local structural distortions. Therefore, the structural symmetry used in the calculations are higher than

the true symmetry of the real structure. Furthermore, only a few inequivalent atoms can be simulated with atomistic calculations due to limited computing power. This means that incommensurate phases of $RE_2MO_{4+\delta}$ compounds with higher δ are difficult to simulate. Due to these two major limitations, simulated results from atomistic calculations are only valid in which the used structural model closely define the real crystal structure.

2.4. Spin and charge ordering in $RE_{2-x}Sr_xNiO_{4+\delta}$

The magnetic structures of the $Nd_2NiO_{4+\delta}$ phases were determined by Carvajal et.al.⁵⁰ with neutron powder diffraction study. In the LTO phase of $\delta = 0$, Ni^{2+} ions show antiferromagnetic ordering with $T_N = 320$ K and propagation vector $\mathbf{k} = (1\ 0\ 0)$ with spins lying parallel to the propagation vector, i.e. along the a -axis. The magnetic structure can be described by the Shubnikov space group $B_p mab'$ as shown in **Fig. 2.21 (a)**. The LTO-LTT structural transition at 130 K largely modifies the magnetic structure. In the LTT phase, Ni^{2+} spins are oriented parallel to the $[110]$ direction with a weak ferromagnetic component along the c -axis, and the magnetic structure can be best described either by the Shubnikov $Pc'c'n$ or $P4_2/nc'm'$ space group as presented in **Fig. 2.21 (b)**. The polarization of the Nd^{3+} ions starts at a temperature as high as 70 K and the cooperative ordering of Nd^{3+} ions takes place at $T_N = 8$ K. However, the magnetic structure after and before the Nd^{3+} ordering belongs to the same magnetic space group. *Fully oxidized samples of $Nd_2NiO_{4+\delta}$ ($\delta \sim 0.23$) do not show any static magnetic order down to 1.5 K.* Moreover, the partially oxidized samples with $\delta = 0.04$ were shown to similar magnetic behavior as stoichiometric ones.

The RE_2NiO_4 based systems are structurally similar to the La-based HTc cuprates. Besides having the similar structure, undoped RE_2NiO_4 are also antiferromagnetic insulators. However, the optical gap is twice in La_2NiO_4 (4 eV) compared to the La_2CuO_4 (2 eV)⁶¹. When these compounds are doped with holes either by substituting RE^{3+} with Sr^{2+} (that is x) or by doping excess oxygens (that is δ), the nominal hole concentration per transition metal site per formula unit is given by $n_h = x + 2\delta$. The holes tend to reside in the MO_2 layers ($M = Ni, Cu$), and have a strong O-2p character, although there is larger hybridization with the metal 3d states in the Ni case^{62,63}. Furthermore, in the insulating state, each Ni ion has two missing 3d electrons, which combine to give total spin $S = 1$. On the other hand, Cu^{2+} has a single hole that gives $S = 1/2$.

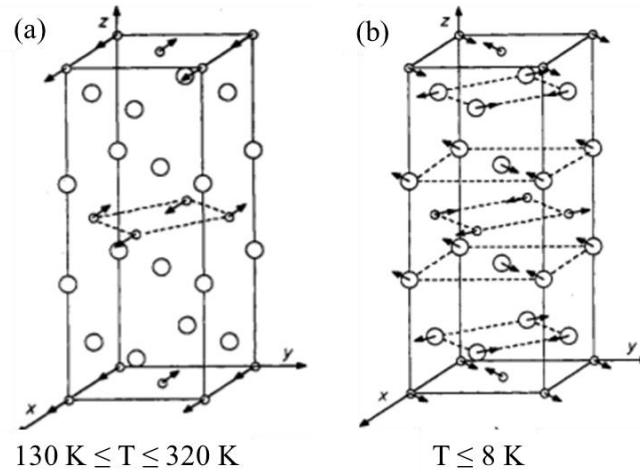


Figure 2.21 | Refined magnetic structures of Nd_2NiO_4 . (a) Schematic representation of the magnetic structure in the LTO phase of Nd_2NiO_4 and (b) the magnetic structure of Nd_2NiO_4 in the LTT phase below 8 K. Small circles denote Ni^{2+} ions and big circles represent Nd^{3+} ions. Oxygen atoms are not shown. Figures are taken from the reference⁵⁰.

The antiferromagnetic order for the stoichiometric phase is characterized by the wave vector $\mathbf{Q}_{AF} = (1, 0, 0)$. In oxygen-doped $La_2NiO_{4+\delta}$, neutron diffraction studies have shown that this commensurate order is preserved for $\delta \leq 0.11$ ²⁷, with the T_N decreasing from 335 K at $\delta = 0$ to 50 K at $\delta = 0.105$. However, the commensurate magnetic peak splits into four symmetrically displaced peaks characterized by the wave vectors $\mathbf{Q}_{so} = \mathbf{Q}_{AF} \pm (\epsilon, 0, 0)/(0, \epsilon, 0)$ for $\delta = 0.125$ ³². Theoretical analyses have shown that an *antiphase domain model* could explain the observed splitting⁶⁴. A possible explanation for the occurrence of antiferromagnetic antiphase domains is given by numerous mean-field analyses of the single band Hubbard model^{65–67}. These calculations indicated that the competition between the kinetic energy of the dopant-induced holes and the potential energy of the spins could cause the holes to collect in domain walls that separate essentially undoped antiferromagnetic regions. While the single-band Hubbard model is more appropriate for describing the behavior in a CuO_2 plane, analysis of a multi-band Hubbard model by Zaanen and Littlewood⁶⁷, shows that similar results should apply to the nickelates. However, in the nickelates, an enhanced electron-phonon coupling (compared to the cuprates) is expected to stabilize domain wall structures. The ordering can be described as a “stripe phase,” in which the holes segregate into an ordered array of parallel regions separating the antiferromagnetic (AFM) spin order as a domain boundary. From the neutron diffraction data³² as visualized in **Fig. 2.22(a)**, it was found that diagonal stripes (45° to the Ni-O_{eq}-Ni bond) are formed in case of nickelates whereas horizontal/vertical stripes (parallel to the Ni-O_{eq}-Ni bond) are evidenced in case of iso-structural cuprates⁶⁸. An idealized model of the spin and charge order is shown for $La_2NiO_{4+\delta}$ with $\delta = 0.25$ in **Fig. 2.22(b)** and for $La_2CuO_{4+\delta}$ with $\delta = 0.125$ in **Fig. 2.22(c)**. The period of the charge order is half that of the spins, so that scattering from the

charge or, rather, from the atomic displacements associated with the charge modulation will emerge as superlattice peaks with a splitting characterized by $2\epsilon = 0.5$ for this case. The neutron diffraction results for ϵ , the inverse of the magnetic period, as a function of hole concentration, n_h are summarized in **Fig. 2.22(d)**³⁷. The general trend is $\epsilon \sim n_h$ which is consistent with having one hole per Ni site along a domain wall. This corresponds to half-filling of the conduction band associated with a 1D charge stripe. Such a condition is unstable with respect to a Peierls distortion, which would introduce a small energy gap thus explaining the experimentally observed insulating behavior of the nickelates up to $n_h = 0.9$ -1^{69,70}. A stripe region is formed for $0 \leq x < 0.5$ as depicted in **Fig. 2.23(a)** and a checkerboard pattern is expected for $x \geq 0.5$, in which each Ni^{3+} layer alternates with each Ni^{2+} layer as drawn in **Fig. 2.23(b)**⁷¹. A representative of neutron diffraction scan is shown in **Fig. 2.24** for the stripe ordered phase of $La_2NiO_{4.126}$ below $T_N = 110$ K³⁴. The incommensurate magnetic peaks appear at $(0, 2n+1\pm\epsilon, 2m)$ and/or $(2n+1\pm\epsilon, 0, 2m)$ where m and n denote integers and $\epsilon \sim 0.275$.

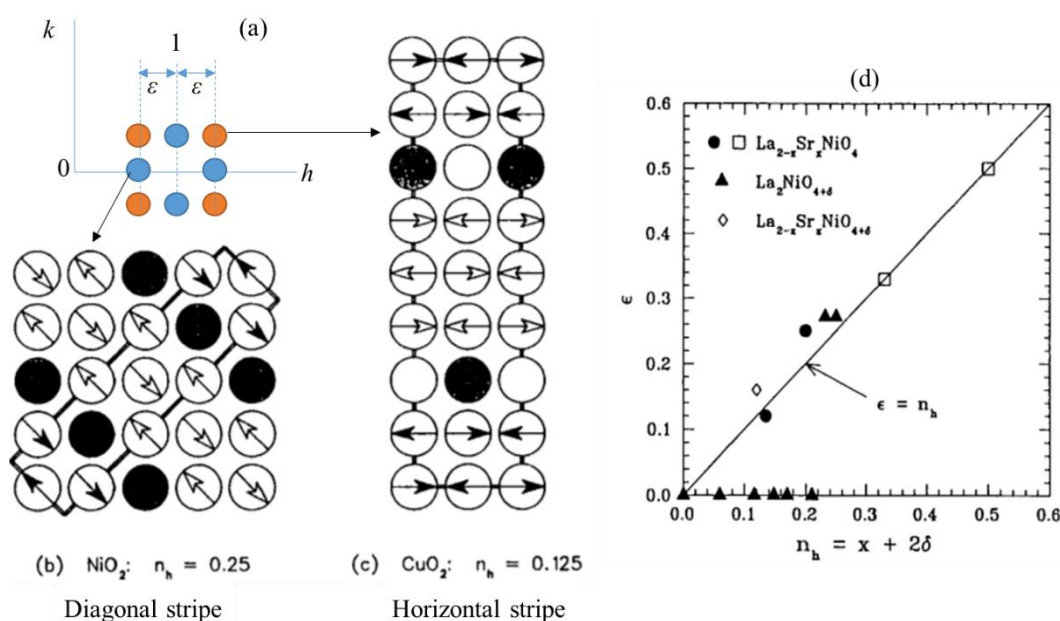


Figure 2.22 | Incommensurate magnetism in hole doped $RE_2NiO_{4+\delta}$ and $RE_2CuO_{4+\delta}$. (a) Sketch of the $(hk0)$ reciprocal plane showing the positions of the magnetic peaks observed in hole-doped $La_2NiO_{4+\delta}$ (blue circles) and $La_2CuO_{4+\delta}$ (yellow circles). (b) Idealized spin and charge stripe patterns within an NiO_2 plane in hole doped $La_2NiO_{4+\delta}$ with a hole density of $n_h = 1/4$. (c) Proposed stripe pattern in a CuO_2 plane of hole-doped La_2CuO_4 with $n_h = 1/8$. Only the metal atoms are represented. Arrows indicate the orientation of magnetic moments on metal atoms, which are locally antiparallel. The spin direction rotates by 180° (relative to a simple antiferromagnetic structure) on crossing a domain wall. The doubled lines outline the magnetic unit cell in each case. Holes (filled circles) are located at the anti-phase domain boundaries. (d)

Variation of the incommensurability ϵ with the hole concentration n_h in hole-doped $La_{2-x}Sr_xNiO_{4+\delta}$. Figures are adapted from the reference⁶¹.

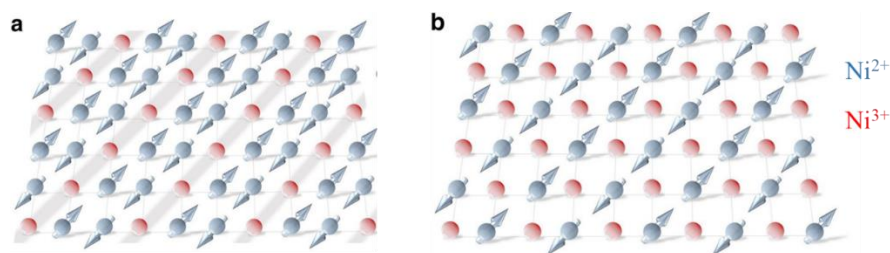


Figure 2.23 | Example of stripe and checkerboard spin and charge order in $La_{2-x}Sr_xNiO_4$. (a) Stripe for $x = 1/3$ and (b) checkerboard order for $x = 1/2$. The arrows represent magnetic moments on Ni^{2+} ions and the red spheres denote hole sites with Ni^{3+} ions. Figures are taken from the reference⁷².

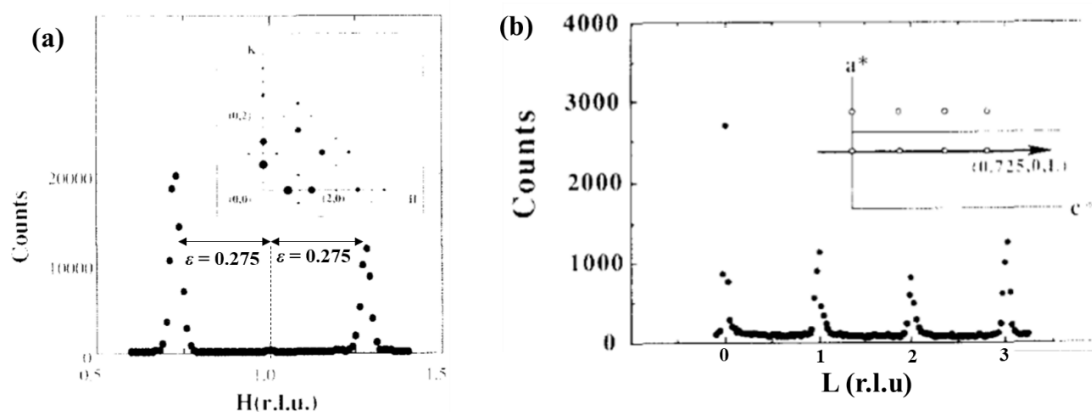


Figure 2.24 | Neutron diffraction spectrum of $La_2NiO_{4.126}$ below $T_N = 110$ K. (a) The scan along $[1, 0, 0]$ direction in the $(hk0)$ plane. The inset shows the intensity distribution of the magnetic Bragg peaks. (b) The scan along the reciprocal l -direction on the incommensurate position along $[0.725, 0, l]$. Figures were taken from the reference³⁴.

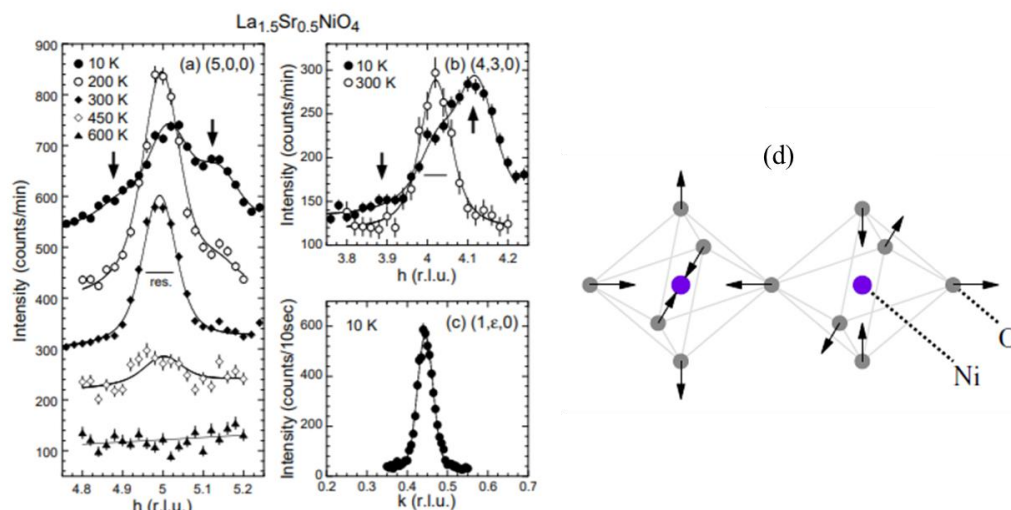


Figure 2.25 | Charge ordering in $La_{1.5}Sr_{0.5}NiO_4$. Temperature dependences of checkerboard charge order peaks at (a) (5, 0, 0) and (b) (4, 3, 0). (c) Profile of a stripe spin order peak at (1, 0.44, 0) at 10 K. Horizontal bars in the panel (a) and (b) present the instrumental resolutions (FWHM). (d) Breathing mode distortion of the NiO_6 octahedra in the checkerboard-type charge-ordered state. Arrows indicate the displacement directions of O^{2-} ions. Figures are taken from references⁷³ and⁷⁴.

An interesting charge ordering scheme is reported with a hole concentration of $n_h = 0.5$ for $La_{1.5}Sr_{0.5}NiO_4$ with neutron diffraction⁷³. A rearrangement of the charge ordering pattern was observed with temperature as shown in **Fig. 2.25(a)** and **(b)**. With decreasing temperature, a checkerboard-type charge order is formed below $T_{CO}^C \sim 480$ K, which is taken over by the stripe-type charge order with an incommensurability twice as large as that of the spin order below $T_{CO}^{IC} \sim 180$ K as confirmed by stripe magnetic peak in **Fig. 2.25(c)**. When the CB-type charge order is formed, it induces a so-called “breathing mode”-type periodic distortion of oxygen atoms of NiO_6 octahedron, as depicted in the **Fig. 2.25(d)**⁷⁴. Such displacements of oxygen atoms reduces the crystal symmetry, thus allowing reflections like (5, 0, 0) and (4, 3, 0) which are actually forbidden in the K_2NiF_4 -type structure (HTT). Superlattice reflections of the CB-type charge order are also observed for the $x = 0.6$ and 0.7 samples. In case of cuprates, the pinning of charge stripes with the underlying lattice is observed in the LTT phase of $La_{1.48}Nd_{0.4}Sr_{0.12}CuO_4$ ⁷⁵. It was understood in terms of tilting of the CuO_6 octahedra as shown in **Fig. 2.26 (a)** and **(b)**, where displacements of the equatorial oxygen atoms are presented. The distortions clearly form diagonal stripes in the LTO structure in which charge stripes are purely dynamical, whereas in the LTT phase the pattern is horizontal at $z = 0$, rotating by 90° in the neighboring layers. In general, 3D stacking of parallel charge stripes structure occurs in a staggered fashion in neighboring layers to minimize the Coulomb energy as demonstrated in **Fig. 2.26 (c)**. However, if the charge and spin correlations are pinned by the structural distortions in the LTT phase, then will rotate by 90° from one layer to

the next, as illustrated in **Fig. 2.26 (d)**, which was indeed observed by neutron diffraction⁷⁵. In case of oxygen doped samples, ordering of interstitial oxygen atoms occur close to the RT and the ordered arrangement leads to the ordered deformation of NiO_2 planes, which provides a modulated potential that also can pin the charge stripes to the lattice. Therefore, the amount of interstitials and its ordering state both should also play a crucial role on the nature of the spin and charge orderings appearing at low temperature in nickelates. It was proposed that the charge correlations are fluctuating about an average ordered configuration determined by the ordering of interstitials³⁵. An interesting scenario is observed for $La_2NiO_{4+\delta}$ phases, in which incommensurate magnetic order and charge order appears at δ where interstitial order changes from 1D to 3D³⁸. The temperature dependence of ϵ demonstrates that the charge stripes are coupled to the lattice and the occurrence of the rational fraction of ϵ is the result of a competition of two length scales, one associated with the ideal spin-charge order and the other associated with the modulation of the lattice potential due to the ordering of interstitials. Moreover, a direct relationship exists between the modulation vectors of the charge order in the NiO_2 planes and the 3D interstitial ordering along one direction of the lattice³⁵. However, no diffraction study has been conducted addressing the spin and charge ordering for the most over-stoichiometric $RE_2NiO_{4+\delta}$ phases with $\delta \sim 0.25$ where a different type of 3D ordering of interstitials is observed as discussed in **section 2.2**. Furthermore, no studies were undertaken for the moderately oxygen doped $(Pr/Nd)_2NiO_{4+\delta}$ phases where a single LTT phase exists similar to the cuprates. In this work, we have undertaken these concerns and explored magnetic properties of $Nd_2NiO_{4+\delta}$ phases with $\delta \sim 0.12$ (LTT) and 0.23 (LTO') in the temperature range of 2-300 K.

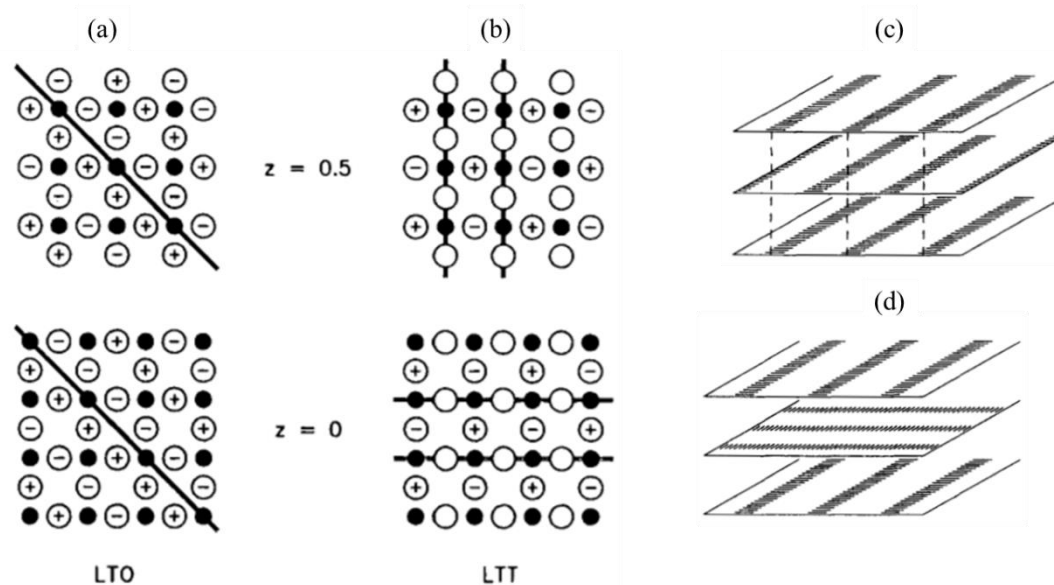


Figure 2.26 | Equatorial oxygen displacements in the (a) LTO and (b) LTT structures. Open (solid) circles represent oxygen (Ni) atoms. The equatorial oxygen atoms are displaced from the plane (+ or -) by coherent tilting of NiO_6 around a tilt axis indicated by the thick lines. Stacking of

charge stripes along the c -axis. (c) Staggering of charge stripes in the nickelates to minimize the Coulomb energy. (d) Rotation of charge stripes orientation by 90° from layer to layer in case of the LTT structure. Figures are taken from the reference⁶¹.

Theory and Instrumentation

The current chapter provides the basic theory of X-ray and neutron diffraction techniques, which are essential to understand experimental results described in the following chapters. Moreover, an overview of different instruments that were used in this work is presented.

In **section 3.1**, the basic theory of x-ray and neutron diffraction is summarized and theoretical background of the spherical neutron polarimetry is presented. In **section 3.2**, various powder and single crystal X-ray and neutron diffractometers are introduced. Subsequently, the basic idea of a triple axis spectrometer is introduced. In **section 3.3**, a detailed description of the maximum entropy method is provided for model free reconstruction of nuclear and electron densities from single crystal and powder diffraction data.

3.1. Basic theory of diffraction

X-ray and neutron diffraction are two important experimental tools used for the analyses of crystalline materials. X-rays are electromagnetic waves and interact with electron clouds of atoms. In contrast, neutrons interact with point like atomic nuclei. Therefore, neutron diffraction is similar to and yet different from the x-ray diffraction. The crystal structure can be described as a sum of lattice planes constructed by ordered arrangement of point-like atoms. The diffracted waves from the lattice planes exhibit interference phenomena. Lattice planes are defined by Miller indices (hkl) , representing their intersection with the crystallographic a , b and c -axes. Diffraction occurs when a geometrical condition known as Bragg's law is fulfilled⁷⁶, as represented by **Eq. (3.1)** and **Fig. 3.1(a)**, where d_{hkl} is the interplanar spacing, θ is the diffraction angle represented by the incident beam and the lattice plane, n is an integer number, and λ is the wavelength of the monochromatic beam. The spatial arrangement and intensity of diffracted waves provides information on the interplane distance d_{hkl} , hence the cell parameters, and crystal structure of the investigated compounds.

$$2d\sin\theta = n\lambda \quad (3.1)$$

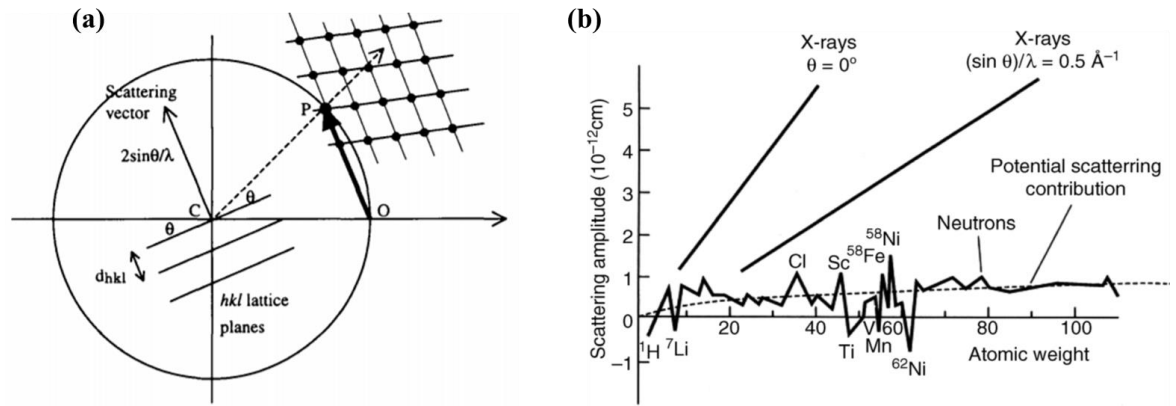


Figure 3.1 | (a) The Ewald sphere and the reciprocal lattice illustrating the requirement to fulfil the Bragg's law for diffraction and (b) Coherent scattering length distribution of atoms for x-rays and neutrons. Figures are taken from references⁷⁷ and ⁷⁸.

Scattered intensities of diffracted beams are related to the Fourier transform of $\rho(x, y, z)$ defined by density of electrons and nuclei in the crystal. The Fourier transform of $\rho(x, y, z)$ is known as structure factor and represented by $F(h, k, l)$. The mathematical expression for nuclear or electronic density in a crystal in terms of structure factors, $F(h, k, l)$ is given by **Eq. (3.2)**.⁷⁹

$$\rho(x, y, z) = \sum_{h,k,l} F(h, k, l) \exp\{-2\pi i(hx + ky + lz)\} \quad (3.2)$$

where the summation runs over the Miller indices and x, y, z are the fractional coordinates representing atomic positions in the unit cell in terms of unit cell parameters a, b and c , respectively. However, it is not possible to obtain $\rho(x, y, z)$ directly from the observed diffraction intensities, because of the crystallographic phase problem where only the amplitudes of the $F(h, k, l)$ can be determined experimentally. The structure factor $F(h, k, l)$ is given by **Eq. (3.3)**.⁸⁰

$$F(h, k, l) = \sum_{\text{atom } i} a_i b_i W_i \exp\{2\pi i(hx_i + ky_i + lz_i)\} \quad (3.3)$$

where a_i is the atomic site occupancy, b_i is the scattering length, and W_i is the Debye–Waller factor, and the summation runs over n atoms in the crystallographic unit cell. According to kinematical theory of diffraction, the intensity $I(h, k, l)$ is given by⁷⁷

$$I(h, k, l) \propto I_0 k \lambda^2 V_c / V^2 |F(h, k, l)|^2 \quad (3.4)$$

where I_0 is the incident flux, V_c is the volume of the crystal and V is the unit cell volume. Neutrons are scattered from the atomic nuclei, which are tiny and 10^{-4} times smaller than atomic radius. The scattering length does not fall off with the scattering angle for neutron scattering as the atomic form factor in the case of x-rays. Although, neutrons are uncharged, they carry a spin, and therefore interact with magnetic moments. Therefore, neutron diffraction is used to study the magnetic structure of a material. However, the magnetic form factor falls off rapidly with the scattering angle. Due to different nature of the form factors for x-rays and neutrons, neutron diffraction has added advantages over x-rays in studies where light atoms like hydrogen or lithium must be located, or where isotopic substitutions may be of interest. Furthermore, as neutrons interact with the nucleus, neutron diffraction provides an accurate estimation of the mean atomic position in contrast to the x-ray diffraction in which an average atomic position is obtained at the centroid of its electron density cloud.

The atomic-displacement parameters (ADP's) are an important piece of information resulting from the structure analysis as displacement of atoms from their average positions affect the intensities of Bragg peaks in an exponential manner. The mean square displacements of atoms are only one of numerous kinds of disorder present in the crystalline materials. The ADP's derived from neutron diffraction are naturally lacking all complications from the electron clouds, and therefore, neutron diffraction is the primary technique to measure reliable ADP's. The insertion of ADP's into the structural model occurs in terms of Debye-Waller factor. The Debye-Waller factor W_i takes into account the reduction in the diffracted intensity due to displacements of the atoms from its average position that causes an overspread of the scattering density. The **Eq. (3.5)** shows the isotropic approximation for Debye-Waller factor⁷⁷:

$$W_i = \exp\left(-\frac{U_i Q^2}{2}\right) = \exp\left\{-8\pi^2 U_i \left(\frac{\sin^2 \theta}{\lambda^2}\right)\right\} \quad (3.5)$$

U_i is the atomic mean square ADP's. The Debye-Waller factor with anisotropic thermal displacement parameters is given by⁷⁷

$$W_i = \exp\{-2\pi^2(U_{11}a^{*2}h^2 + U_{22}b^{*2}k^2 + U_{33}c^{*2}l^2 + 2U_{12}a^*b^*hk + 2U_{23}b^*c^*kl + 2U_{13}a^*c^*hl)\} \quad (3.6)$$

Where a^* , b^* and c^* are reciprocal lattice vectors.

An important concept in the neutron scattering is the scattering cross section. The total scattering cross section represents the probability that a neutron will be scattered. A mathematical definition of the total cross section is given by⁸¹

$$\sigma_{total} = \frac{N_1}{\phi} \quad (3.7)$$

where ϕ is the incident neutron flux defined by the number of incident neutrons per unit time and unit area. N_1 is the total number of neutrons scattered per unit time. The differential cross section is the probability that a neutron will be scattered within a given solid angle, and can be defined as

$$\frac{d\sigma}{d\Omega} = \frac{N_2}{\phi d\Omega} \quad (3.8)$$

where θ, φ are the polar angles, with the polar axis taken as the direction of the incident neutron beam and N_2 is the total number of neutrons scattered per unit time into solid angle $d\Omega$ in the direction θ and φ . The double differential cross section is the probability that a neutron will be scattered within a given solid angle and have an energy within a certain range. This can be expressed as

$$\frac{d^2\sigma}{d\Omega dE} = \frac{N_3}{\phi d\Omega dE} \quad (3.9)$$

where N_3 is the total number of neutrons scattered per unit time into a solid angle $d\Omega$ in the direction θ and φ with the energy range between E and $E + dE$. The cross sections for nuclear, magnetic, inelastic and polarized neutron scattering can be obtained from first principles using quantum mechanics. This requires the knowledge of the initial and final quantum states of the system and the knowledge of the transition probability between these two states.

The neutron scattering cross section for a nuclear Bragg reflection is

$$\frac{d\sigma}{d\Omega} = N \frac{2\pi^3}{V_0} |F(h, k, l)|^2 \quad (3.10)$$

where N is the total number of unit cells of the crystal, V_0 the unit cell volume and $F(h, k, l)$ is the structure factor for nuclear scattering, given by **Eq. (3.3)**. For unpolarized neutron scattering, the differential cross section for a magnetic Bragg reflection occurring with the wave vector Q is

$$\frac{d\sigma}{d\Omega} = N_m \frac{2\pi^3}{V_{0m}} \left(\frac{\gamma r_0}{2}\right)^2 \sum_{\alpha\beta} \langle (\delta_{\alpha,\beta} - \widehat{Q}_\alpha \widehat{Q}_\beta) F^\alpha(Q) F^{\beta*}(Q) \rangle \quad (3.11)$$

where N_m is the number of magnetic unit cells in the crystal, V_{0m} is the volume of the magnetic unit cell, $\gamma = 1.91$ is the gyromagnetic ratio, $r_0 = 2.8 \times 10^{-15}$ m is the classical electron radius⁸¹. The summation over α, β is the summation over the Cartesian co-ordinates $x; y; z$, with δ being the Kronecker delta, * represents the complex conjugate and $Q, F^\alpha(Q)$ are the alpha components of the scattering wave vector and the magnetic unit cell structure factor respectively. The components of the magnetic structure factor are given by⁸¹

$$F^\alpha(Q) = \sum_j q_j \mu_j^\alpha f_j^\alpha(Q) \exp(i \cdot Q \cdot r_j) \exp(-W_j) \quad (3.12)$$

where the summation j runs over all the magnetic atoms in the unit cell, μ_j^α is the α -component of the magnetic moment of the j -th atom, and $f_j^\alpha(Q)$ is the α -component of the magnetic form factor of the j -th atom. q_j is the magnetic interaction vector, define by⁸¹

$$q_j = \widehat{Q}(\widehat{Q} \cdot \widehat{\mu}_j) - \widehat{\mu}_j \quad (3.13)$$

The polarization of a neutron beam corresponds to a vector, which is the sum of the individual neutron polarizations. Its modulus takes values between zero for an unpolarized beam to one for a fully polarized beam. Assuming an initial polarization P_i , the final polarization P_f and the partial differential cross-section can conveniently be written for nuclear and magnetic scattering as^{82,83}

$$\begin{aligned} \left(\frac{d^2\sigma}{d\Omega dE_f}\right) \mathbf{P}_f &= C_p \frac{k_f}{k_i} \{ \mathbf{P}_i \langle NN^\dagger \rangle_\omega + \langle \mathbf{M}_\perp (\mathbf{P}_i \cdot \mathbf{M}_\perp^\dagger) \rangle_\omega + \langle \mathbf{M}_\perp^\dagger (\mathbf{P}_i \cdot \mathbf{M}_\perp) \rangle_\omega - \langle \mathbf{P}_i (\mathbf{M}_\perp^\dagger \cdot \mathbf{M}_\perp) \rangle_\omega \\ &+ \langle N \mathbf{M}_\perp^\dagger \rangle_\omega + \langle N^\dagger \mathbf{M}_\perp \rangle_\omega + i \mathbf{P}_i \times (\langle N \mathbf{M}_\perp^\dagger \rangle_\omega - \langle N^\dagger \mathbf{M}_\perp \rangle_\omega) \\ &+ i \langle \mathbf{M}_\perp \times \mathbf{M}_\perp^\dagger \rangle_\omega \} \end{aligned} \quad (3.14)$$

$$\begin{aligned} \left(\frac{d^2\sigma}{d\Omega dE_f}\right) &= C_\sigma \frac{k_f}{k_i} \{ \langle NN^\dagger \rangle_\omega + \langle \mathbf{M}_\perp \cdot \mathbf{M}_\perp^\dagger \rangle_\omega - \langle \mathbf{P}_i (\mathbf{M}_\perp^\dagger \cdot \mathbf{M}_\perp) \rangle_\omega + \mathbf{P}_i \\ &\times (\langle N \mathbf{M}_\perp^\dagger \rangle_\omega + \langle N^\dagger \mathbf{M}_\perp \rangle_\omega) - i \mathbf{P}_i \langle \mathbf{M}_\perp \times \mathbf{M}_\perp^\dagger \rangle_\omega \} \end{aligned} \quad (3.15)$$

Where C_p and C_σ are scale factors. The angular brackets explicitly represent

$$\langle AB^\dagger \rangle_\omega = \frac{1}{2\pi\hbar} \int_{-\infty}^{\infty} dt e^{-i\omega t} \langle A(\mathbf{Q}, 0) B^\dagger(\mathbf{Q}, t) \rangle \quad (3.16)$$

which corresponds to space and time Fourier transforms of the thermal average of A and B. In **Eqs. (3.14-15)**, N relates to the nuclear scattering and \mathbf{M}_\perp relates to the magnetic scattering from moments perpendicular to the momentum transfers. The first term in **Eq. (3.14)** shows the nuclear contribution, which does not change the initial polarization. Next three terms correspond to the non-chiral magnetic contribution, which modifies the initial polarization. Then next three terms are the interference between the nuclear and magnetic scattering. Depending on the phase between the nuclear and magnetic scattering, these terms can generate a polarization, independent of the initial polarization, and/or rotate the initial polarization around \mathbf{M}_\perp . The last term corresponds to the chiral magnetic term, which generates a polarization along Q, independent of the initial neutron polarization.

In case of spherical neutron polarimetry, the **Eq. (3.14)** can be written in a matrix form as⁸⁴

$$\sigma P_f = \sigma \bar{P} P_i + \sigma P'' \quad (3.17)$$

Where σ is the partial differential cross section. The coordinates in neutron polarimetry generally defined such that x -axis is parallel to the momentum transfer Q, y -axis is perpendicular to the x -axis and lying in the horizontal scattering plane and the z -axis is perpendicular to the horizontal scattering plane. In this coordinate system, the magnetic vector $\mathbf{M}_\perp = (0, M_\perp^y, M_\perp^z)$. The first term in **Eq. (3.17)** corresponds to a rotation of the initial polarization by the matrix \bar{P} , given by⁸⁴

$$\sigma \bar{P} = \begin{pmatrix} \sigma_N - \sigma_{M_y} - \sigma_{M_z} & i\sigma_{I_z} & -i\sigma_{I_y} \\ -i\sigma_{I_z} & \sigma_N + \sigma_{M_y} - \sigma_{M_z} & \sigma_{M_{mix}} \\ i\sigma_{I_y} & \sigma_{M_{mix}} & \sigma_N - \sigma_{M_y} + \sigma_{M_z} \end{pmatrix} \quad (3.18)$$

The second term is the polarization P'' created by the sample, given by

$$\sigma P'' = \begin{pmatrix} \sigma_C \\ \sigma_{R_y} \\ \sigma_{R_z} \end{pmatrix} \quad (3.19)$$

The different cross-sections used in these matrices are presented in **Table 3.1**. In spherical neutron polarimetry, the cross sections which are generally measured experimentally are $\sigma_{\alpha\beta}^{\pm\pm}$, where α and β are indices for x, y, z -axis and the signs + and - indicate the direction along the relevant axis. The indices α and β indicate the initial and final polarization, respectively. The chiral term and the real part of the NMI terms in **Eq. (3.18)** can be evaluated by

$$\sigma_C = \frac{\sigma_{xx}^{-+} - \sigma_{xx}^{+-}}{2|\mathbf{P}_i|} \quad (3.20)$$

$$\sigma_{R\alpha} = \frac{\sigma_{\alpha\alpha}^{++} - \sigma_{xx}^{--}}{2|\mathbf{P}_i|} \quad (3.21)$$

If these terms can be neglected, i.e. $P'' = 0$, the elements of the rotation matrix \bar{P} are given by

$$\bar{P}_{\alpha\beta} = \frac{\sigma_{\alpha\beta}^{++} - \sigma_{\alpha\beta}^{-+}}{\sigma_{\alpha\beta}^{++} + \sigma_{\alpha\beta}^{-+}} \quad (3.22)$$

Spherical neutron polarimetry experiments were performed with MuPAD (Mu-metal polarization analysis device) on TASP at SINQ, PSI^{84,85}. The principal of this device is to provide a chamber with zero magnetic field. With the MuPAD, mu-metal shields external magnetic fields. The incident neutron polarization is rotated to point along any direction relative to Q . The zero field chamber guarantees that this polarization is kept and that only the sample can change the beam polarization. This is especially important to be able to measure transverse components of the polarization. In contrast, in the longitudinal polarization analysis setup, the Helmholtz coils generates a small magnetic field at the sample position and transverse components are rapidly depolarized. In spherical polarimetry, the polarization of scattered beam is rotated again to select with the analyzer the final polarization to be measured. In this way, all the cross-sections $\sigma_{\alpha\beta}^{\pm\pm}$ can be measured, allowing separating the different nuclear and magnetic contributions presented in **Table 3.1**.

Table 3.1 | Definition of cross-section terms in **Eqs. (3.18-19)**. The table is taken from the reference⁸⁴.

Description	Cross-section terms
Nuclear term	$\sigma_N = \langle NN^\dagger \rangle_\omega$
α -component of non-chiral magnetic term	$\sigma_{M_\alpha} = \langle M_\perp^\alpha \cdot \mathbf{M}_\perp^{\alpha\dagger} \rangle_\omega$
Mixed yz non-chiral magnetic term	$\sigma_{M_{mix}} = \langle M_\perp^y \cdot \mathbf{M}_\perp^{z\dagger} \rangle_\omega + \langle M_\perp^z \cdot \mathbf{M}_\perp^{y\dagger} \rangle_\omega$
Chiral magnetic term	$\sigma_C = i(\langle M_\perp^y \cdot \mathbf{M}_\perp^{z\dagger} \rangle_\omega - \langle M_\perp^z \cdot \mathbf{M}_\perp^{y\dagger} \rangle_\omega)$
Real part of the NMI term	$\sigma_{R\alpha} = \langle N \mathbf{M}_\perp^{\alpha\dagger} \rangle_\omega + \langle N^\dagger M_\perp^\alpha \rangle_\omega$
Imaginary part of the NMI term	$\sigma_{I\alpha} = \langle N \mathbf{M}_\perp^{\alpha\dagger} \rangle_\omega - \langle N^\dagger M_\perp^\alpha \rangle_\omega$

3.2. Instrumentation

3.2.1. X-ray and Neutron powder diffraction

There are two experimental procedures (i.e. single crystal and powder diffraction) for conducting a diffraction experiment with monochromatic x-ray and neutron beam. In the conventional method of powder diffraction, a monochromatic x-ray or neutron beam is selected by a crystal monochromator. Ideally, a powder sample consists of a very large number of small crystallites that are randomly oriented. A small proportion of these crystallites will be in the correct orientation for satisfying the Bragg's law for diffraction by the (hkl) planes. Consequently, the intensity $I(2\theta)$ of the scattered beam from the sample is measured as a function of the scattering angle 2θ . The experimental plot of $I(2\theta)$ versus 2θ shows a series of diffraction peaks whose positions along the 2θ axis are determined by the Bragg's law, thus by unit cell parameters.

In this work, x-ray powder diffraction measurements were performed for with lab based high-resolution Bruker D8 ADVANCE x-ray diffractometer installed at the Laboratory for Scientific Developments and Novel Materials (LDM) at PSI. The diffractometer operates in the Bragg-Brentano geometry and uses $\text{CuK}\alpha_{1-2}$ radiation. The instrument is equipped with a LynxEye point detector. Diffraction patterns were collected by placing a small amount of powder sample (usually mixed with acetone) on a silicon substrate that gives a low featureless background. Powder patterns were usually collected over 4-6 h in the 2θ range of 10-130° with 0.02 step size. This laboratory based x-ray diffraction patterns were treated with Rietveld analysis for qualitative phase analysis of as-synthesized powder and single crystal samples.

Synchrotron x-ray powder diffraction (SXRPD) measurements were performed at different temperatures in between 5 and 300 K at the Material Sciences (MS) beamline X04SA at the Swiss light source (SLS), Paul Scherrer Institute (PSI), Switzerland⁸⁶. Measurements were performed with a nominal photon energy of 17.5 keV. In order to accurately determine the wavelength of the x-rays ($\lambda = 0.6208(1) \text{ \AA}$) and the instrument profile parameters, the standard LaB_6 powder (NIST) was also measured under the identical experimental condition. Data were collected in the range of $3^\circ \leq 2\theta \leq 120^\circ$ with an intrinsic step size of 0.0036° . Samples were filled into a thin glass capillary of 0.3 mm diameter and horizontally inserted to a Janis Cryostat for the measurements. For high temperature measurements, a hot air blower was used to access the temperature range of 300-900 K. During the data collection, the sample was continuously rotated to reduce the effect of preferred orientation and profile shape dependence. The powder diffraction patterns were treated with Rietveld analysis using the FullProf suite program⁸⁷ to solve the crystal structure and for analysis of structural phase transitions.

Powder neutron diffraction measurements were carried out on the thermal neutron diffractometer HRPT at SINQ, PSI (**Fig. 3.2(a)**)⁸⁸ and on the cold neutron diffractometer DMC at SINQ, PSI (**Fig. 3.2(b)**)^{89,90} for crystal and magnetic structure analysis. The multidetector diffractometer HRPT is designed as flexible instrument for efficient powder neutron diffraction studies⁹¹. By means of primary collimators, a secondary slit system and by appropriate choice of the sample diameter, resolution ($\delta d/d < 0.001$) and intensity can be optimized. Due to the use of a large position sensitive (PSD) ³He detector, simultaneous measurements are possible within a scattering angle range of 160 degrees with angular step size of 0.1°. In this work, a short neutron wavelength $\lambda = 1.494 \text{ \AA}$ [Ge (533), $2\theta_M=120^\circ$] was used for data collection in high intensity (HI)-medium resolution (MR) mode. With this setup, high quality powder data sets were recorded up to high momentum transfers [$\sin\theta/\lambda = 0.66 \text{ \AA}^{-1}$], yielding excellent resolution for structural analysis, especially thermal displacement factors for light oxygen atoms. Approximately 5 g sample was filled inside a vanadium can with inner diameter of 6 mm for powder diffraction measurements and placed inside a ³He cryostat for low temperature measurements in the range of 1.5-300 K. For high temperature characterization, powder samples were filled inside a steel can and placed inside a tantalum furnace to access the temperature range of 300-1400 K.

For magnetic structure analysis, the cold neutron powder diffractometer DMC is used⁹⁰. It is located at a cold neutron guide in the SINQ experimental hall. The instrument is equipped with a large position sensitive BF₃ detector covering a scattering angle of 90° with wavelengths in the range of 2.3 -5 Å can be accessible. The oscillating radial collimator system suppresses peaks from the sample environment and optimized shielding offers very low instrumental background, thus offering high signal-to-noise ratio. This is particularly useful for determining integrated intensities of weak superstructure peaks with high precision having structural and/or magnetic origin, and thus complements the thermal neutron diffractometer HRPT. Furthermore, DMC offers single crystal diffraction measurements by reciprocal plane mapping. In this mode, a pre-oriented single crystal sample is mounted on top of a thin aluminium pin (usually with varnish glue for low temperature measurements and a ceramic glue for high temperature measurements) and the desired horizontal reciprocal plane is mapped out by rotating the single crystal sample around its zone axis. This is particularly useful to locate weak superstructure peaks or diffuse scattering in the reciprocal space. In this thesis work, DMC was used in both powder diffraction and single crystal diffraction modes. For all measurements, a wavelength of 2.4586 Å was used allowing accessing a reciprocal space up to a momentum transfer [$\sin\theta/\lambda$] 0.33 Å⁻¹. The (*hk0*) and (*h0l*) reciprocal planes were mapped at different temperatures in the temperature range of 2-450 K. The reciprocal planes were reconstructed from raw data with TVtueb program or Matlab code⁹². Typical single crystal measurements were performed on ~ 200 mg single crystals over 6-8 h with 0.2° step size.

Fig. 3.2 presents schematic illustrations of these two powder diffractometers. The ‘white’ neutron beam from the reactor passes through a collimator in the reactor shield, and a particular wavelength is then selected by Bragg reflection from a crystal monochromator. The monochromatic beam interacts with the sample and then diffracts into the large detector.

Powder neutron and x-ray diffraction techniques are very powerful tools for determining crystal and magnetic structures with Rietveld analysis. Growing large and high-quality single crystals for some materials is difficult or even impossible, in such cases powder diffraction has important advantages. Moreover, powder diffraction methods also have the advantages for their wide applicability and generally allow a much more rapid data collection. However, one of the major disadvantage of the powder method comes from the limited amount of information accessible from a diffraction pattern, which generally sets an upper limit on the complexity of structures that can be satisfactorily treated. Furthermore, in the powder method, information related to each diffraction plane is lost due to overlap of several reflections, particularly at high Q . Additionally, inevitable problems such as peak broadening and asymmetry related to the different grain sizes cannot be discarded with powder diffraction. These problems create difficulties for crystal/magnetic structure refinements with powder data, and often lead to incorrect structural and thermal parameters.

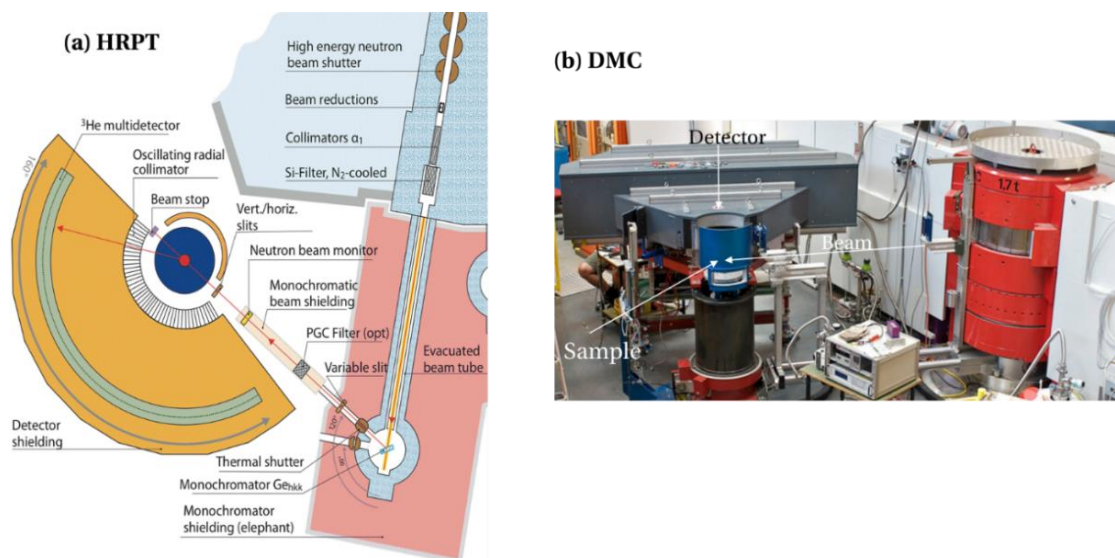


Figure 3.2 | Schematic layout of (a) thermal neutron powder diffractometer HRPT and (b) cold neutron powder diffractometer DMC at SINQ, PSI. Figures are taken from references ⁹¹ and ⁹⁰.

3.2.2. Single crystal neutron diffractometer

In single crystal diffraction, we extract the intensity in reciprocal space. The 3D nature of diffraction pattern means that much of the reciprocal space has to be accessed to measure the full diffraction pattern. However, due to the symmetry, measuring a section of the reciprocal space allows most of the data collection. The four-circle diffractometer is the standard instrument used for single crystal diffraction experiments at constant wavelength with a single detector. The diffracted intensity of each reflection in the reciprocal space is measured by rotating the single crystal and the detector. **Fig. 3.3(a)** is a schematic diagram of a four-circle diffractometer⁸⁰. The three circles ϕ , χ and ω constitute an Eulerian cradle for orienting the crystal, and the independent fourth circle (2θ) is employed to rotate the detector in the horizontal plane. The crystal is mounted on a goniometer head attached to the ϕ circle; the ϕ circle rotates about the χ -axis, and the combined ϕ - χ assembly rotates about the vertical ω -axis, which is coaxial with the 2θ -axis. The (hkl) reflections are measured by bringing the diffraction vectors \mathbf{Q} into the horizontal plane and at an angle $90^\circ - \theta_B$ to the incident beam. By scanning the diffraction vector \mathbf{Q} in small steps and at constant rate through the Ewald sphere, and by summing the neutron counts, which are recorded at each step, the integrated intensity I_{hkl} is measured. This scan can be carried out by rotating the crystal about the ω -axis, either with the detector fixed (ω -scan) or with the detector rotating about the 2θ -axis at twice the angular velocity of the ω -axis ($\omega/2\theta$ or $\theta/2\theta$ scan) as shown in **Fig. 3.3(b)**⁷⁷. In this work, three different single crystal neutron diffractometers were used, namely ZEBRA⁹³ at SINQ, PSI, and HEiDi⁹⁴ at MLZ, FRM II and D9⁹⁵ at ILL. ZEBRA is a single crystal neutron diffractometer equipped with a single detector. The instrument uses thermal neutrons allowing short (1.18 Å) and long (2.32 Å) wavelengths, for applications in crystallography and magnetism in the field of materials science, multiferroics, and highly correlated electron systems. In this thesis work, for the crystal structure analysis, the short wavelength was used to access a large reciprocal space ($\sin\theta/\lambda \sim 0.75 \text{ \AA}^{-1}$) while the long wavelength was used for magnetic structure analysis ($\sin\theta/\lambda \sim 0.37 \text{ \AA}^{-1}$). Low temperature measurements were performed by mounting the single crystal sample on top of an aluminium pin and inserting it inside a closed cycle cryostat (CCR3) to access the temperature range of 4-300 K.

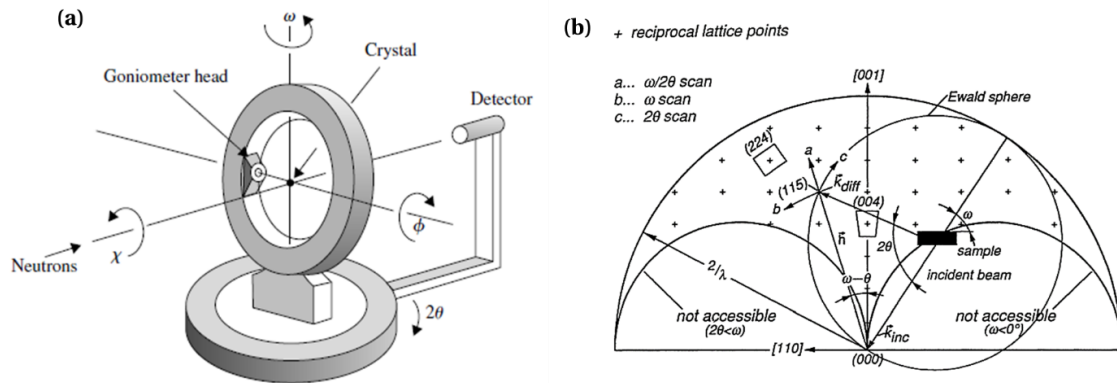


Figure 3.3 | (a) Schematic representation of four circle single crystal diffractometer and (b) Ewald sphere reconstruction of reciprocal space showing different scans performed during single crystal diffraction experiments. Figures are taken from references⁸⁰ and⁷⁷.

HEiDi is a single crystal diffractometer at the neutron source Heinz Maier-Leibnitz (FRM II). The instrument is equipped a single detector and uses hot neutrons, allowing to access very short wavelengths ($0.55 \text{ \AA} < \lambda < 1.2 \text{ \AA}$). Diffraction experiments profit from a shorter wavelength by getting access to a larger Q space to focus on structural details, especially ADP's. Moreover, use of short wavelength reduces the extinction and absorption effects of large and perfect single crystals. For measurements on HEiDi, a monochromatic beam of wavelength $\lambda = 0.793 \text{ \AA}$ was selected with a Ge(422) monochromator, which allows data collection up to high momentum transfers ($\sin\theta/\lambda \sim 0.9 \text{ \AA}^{-1}$), yielding excellent resolution. A standard ^3He cryostat was used for the low temperature measurements while a specially designed optical furnace was used for high temperature measurement in high vacuum (10^{-3} mbar).

The diffractometer D9 uses hot neutrons and is equipped with a small 2D detector, particularly useful for studies of satellites and twinning. The instrument is used for precise and accurate measurements of Bragg intensities up to very high momentum transfer. The resolution allows routine measurement of extended data sets for the detailed study of atomic and thermal disorder. A Cu crystal is used as a monochromator in transmission geometry using the (220) planes. In this thesis work, high temperature measurements were performed on D9 to study the structural transition and thermal disorder of oxygen atoms using a monochromatic beam of wavelength $\lambda = 0.837 \text{ \AA}$ accessing a large reciprocal space up to high momentum transfer ($\sin\theta/\lambda \sim 0.9 \text{ \AA}^{-1}$). For high temperature measurements, a hot gas blower was used to access the temperature range of 300-1000 K.

The basic working principle of the single crystal diffractometers ZEBRA and D9 is presented in **Fig. 3.4(a)** and **3.4(b)**, respectively. The main instrumental components being the monochromator, the diffractometer and the detector. The monochromator creates a

monochromatic beam via Bragg scattering from a crystal plane with suitable lattice spacing, which is scattered off at the sample position, and detected at the detector counter. For data collection with a monochromatic beam, structure factors are related to the measured intensities by the following equation⁷⁷:

$$I_{hkl} = \text{scale factor} \times A_{\theta} \times E_{hkl} \times L_{\theta} \times P_{\theta} \times |F_{hkl}|^2 \quad (3.23)$$

Where A_{θ} , E_{hkl} , P_{θ} and L_{θ} are absorption, Extinction, Polarization, and Lorentz corrections to the integrated intensity as discussed in the following.

- a. **Absorption correction:** The absorption effect of the incident beam from the sample is defined by the Beer-Lambert law: $I = I_0 \exp(-\mu x)$. The linear absorption coefficient (μ) is an isotropic property of the material and depends on the wavelength. Therefore, it is necessary to measure the sample size along all directions to correct the biased intensities due to the different path lengths traversed by the diffracted beam.
- b. **Extinction correction:** Extinction correction is defined by the reduction in intensity of the final diffracted beam due to repeated reflections from several crystalline domains inside the crystal. However, these domains are not perfectly aligned to each other, instead they have a mosaic spread. The extinction effect depends on two main factors, the radii of these crystalline domains, and the angular spread in their orientation within the crystal. There are two different type extinction effects depending on the orientations of these crystalline domains. When the particle size is the dominant effect i.e. small particle size and large mosaic spread, the extinction effect is termed as type I. In contrast, when the mosaic distribution is dominant i.e. for large particle size and small mosaic spread, the extinction effect is termed as type II. Both the angular distribution of orientations and the distributions of particle size can be parameterized by either Gaussian or Lorentzian models and used during data refinement.
- c. **Polarization correction:** If a radiation is 'monochromatized' by reflection from a crystal, it will be partially polarized, and the two parts of the beam will be of unequal intensity. The intensity of reflection then depends on the angular relations between the original, the reflected, and the scattered beams. The polarization factor then becomes $(1 + A \cos^2 2\theta) / (1 + A)$, where $A = \cos^2 2\theta_M$ and θ_M is the Bragg angle of the monochromator crystal.
- d. **Lorentz correction:** The Lorentz factor takes into account two different geometrical effects and it has two components. The first component is owing to the finite size of reciprocal lattice

points is proportional to $1/\sin\theta$ and the second component is finite thickness of the Ewald's sphere is directly proportional to $1/\sin2\theta$.

Polarization and Lorentz corrections to the single crystal data are usually done with the diffractometer software. In contrast, the absorption correction depends on the material under study and needs to be done manually during the refinement. The model for extinction correction largely depends on the crystal geometry and therefore, proper extinction correction needs to be applied during least-square refinements to obtain correct positional and thermal parameters.

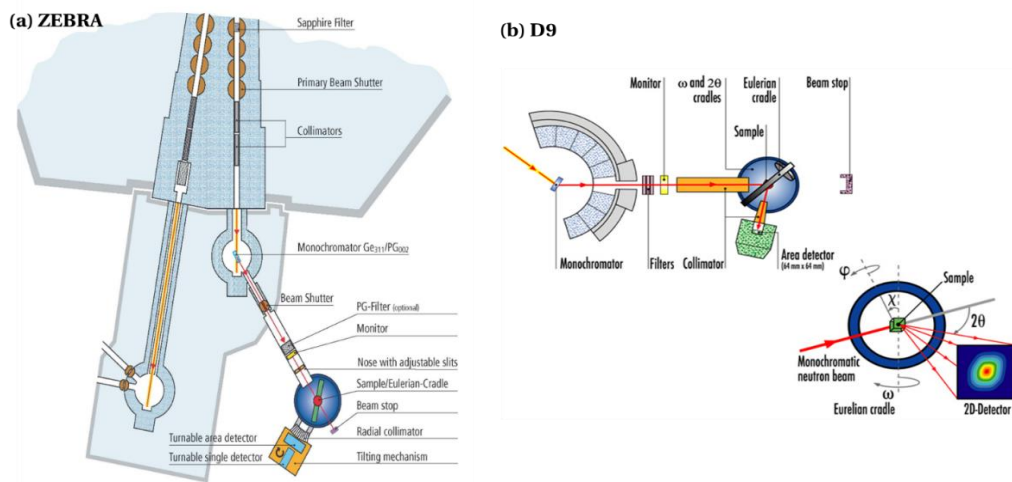


Figure 3.4 | Basic layout of (a) single crystal thermal neutron diffractometer ZEBRA at SINQ, PSI and (b) hot neutron single crystal diffractometer D9 at ILL. Figures are taken from references⁹³ and⁹⁵.

3.2.3. Triple axis spectrometers (TAS)

The triple axis spectrometer is the most commonly used type of instrument for studying excitations in materials, although they are used in elastic mode in this work to study the static magnetic order. **Fig. 3.5** shows a basic layout of a triple axis spectrometer (TAS), with the three main components being the monochromator, the sample position and the analyzer. The monochromator creates a monochromatic beam, which is scattered off the oriented sample at the sample position, and the analyzer is used to examine the neutrons, which have been scattered off the sample in the desired manner for the scan selected. Spherical neutron polarimetry experiments were performed with MuPAD (Mu-metal polarization analysis device) on TASP⁸⁵⁸⁴ at SINQ, PSI. The principal of this device is to provide a chamber with zero magnetic field. With the MuPAD, mu-metal shields external magnetic fields. The incident neutron polarization is rotated to point along any direction relative to Q . The zero field chamber guarantees that this polarization is kept and that only the sample can change the beam polarization. This is especially

important to be able to measure transverse components of the polarization. In contrast, in the longitudinal polarization analysis setup, the Helmholtz coils generates a small magnetic field at the sample position and transverse components are rapidly depolarized. In spherical polarimetry, the polarization of scattered beam is rotated again to select with the analyzer the final polarization to be measured. In this way, all the cross-sections $\sigma_{\alpha\beta}^{\pm\pm}$ can be measured, allowing separating the different nuclear and magnetic contributions presented in **Table 3.1**.

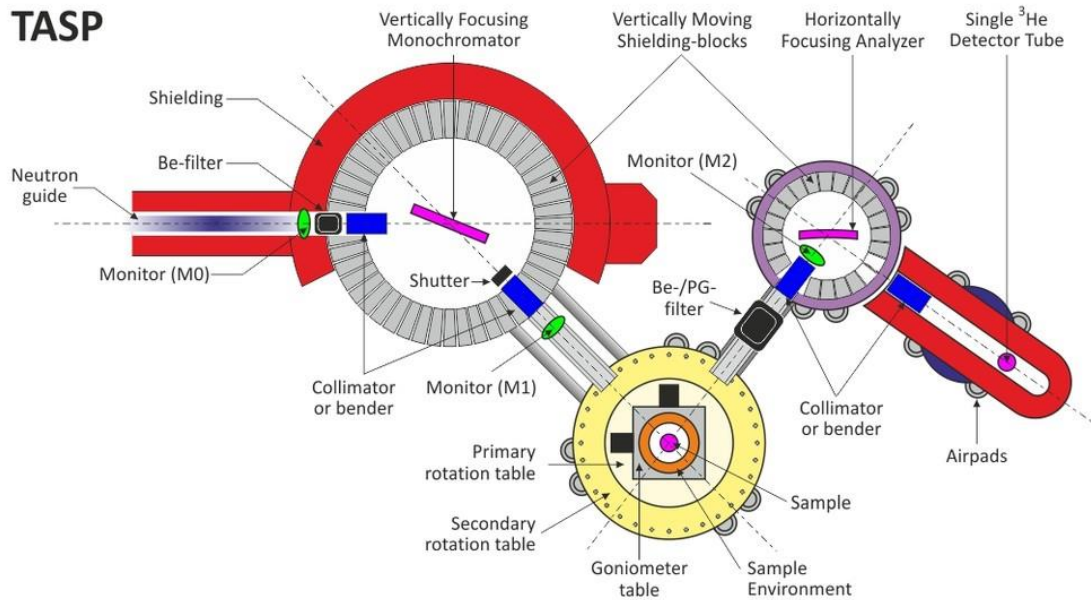


Figure 3.5 | Basic layout of triple axis spectrometer TASP with cold neutrons at SINQ, PSI. The figure is taken from reference⁸⁵.

3.2.4. Physical Properties Measurement System (PPMS) and Magnetic properties Measurement System (MPMS)

Bulk properties of powder and single crystal samples were measured using magnetic properties measurement system (MPMS, Quantum design) and physical properties measurement system (PPMS) at LDM, PSI.

Physical Property Measurement System (PPMS) is a flexible instrument that can be used to measure large number of physical properties of bulk and thin film samples. The main components of PPMS consist of a dewar with the superconducting magnet, a pump to evacuate the sample chamber, a power source and a lock-in amplifier. The measurements are generally performed in the temperature range 1.8-400 K with applied magnetic fields up to 9 T. In principle,

ACMS (AC Measurement System) and VSM (Vibrating Sample Magnetometer) options are used to record magnetic characteristics of a sample. In the ACMS option, DC magnetization is measured by attaching the sample to a thin rigid rod and moved through superconducting coils. The induced voltage is recorded through the detection coil. This setup provides very good sensitivity of about 10^{-6} emu. In this work, isothermal magnetization measurements were performed using PPMS as a function of applied magnetic field with decreasing fields from 9 T.

The PPMS can also be used to measure the heat capacity of a sample at constant pressure. In the heat capacity measurement, a known amount of heat is applied to a sample (approximately 15 mg of pellet) at constant power for a fixed time, and then this heating period is followed by a cooling period of the same duration. A thermometer is attached to the bottom side of the sample stage to measure the change in the temperature during the heating and cooling process. A thin layer of grease was used to mount the sample to the platform to provide thermal contact. The sample puck is sealed with a cap that acts as a radiation shield and placed inside the chamber under high vacuum ($<10^{-3}$ mbar). Before the measurement with the sample, the heat capacity of the puck with the grease was measured separately.

The main components of a MPMS system includes a superconducting magnet that generates large magnetic fields, a superconducting detection coil that couples inductively to the sample, a Superconducting Quantum Interference Device (SQUID) connected to the detection coil, a superconducting magnetic shield surrounding the SQUID. The main advantage of the MPMS system comes from the use of superconducting detection coils instead of the classical Ohmic conductor. During a measurement, a sample is moved through the superconducting detection coils located at the center of the magnet and outside the sample chamber. When the sample moves through the coils, an electric current is induced in the detection coils by the magnetic moment of the sample. Any variation in magnetic flux in the detection coils produces a change in the persistent current in the detection circuit, which is proportional to the change in magnetic flux. The variation in the current in the detection coils produces corresponding change in the SQUID output voltage, which is proportional to the magnetic moment of the sample. The SQUID offers much higher sensitivity (10^{-7} emu) than conventional magnetometers. In this work, DC magnetic susceptibility (both zero-field-cooled and field-cooled) measurements are performed on powder samples and pre-oriented single crystals as a function of temperature during the slow heating of the sample from 2-320 K with a small applied magnetic field.

3.3. Maximum Entropy Method (MEM)

The maximum entropy method (MEM) is a very powerful tool for accurate structure analysis in terms of electron and nuclear density distribution^{96,97}. MEM offers the analyses of diffraction data without any assumptions based on the structural model. Most of the computing software for MEM analysis such as DYSNOMIA⁹⁸ follows the Collins's theory since actual electron or nuclear density is explicitly formulated in this theory rather than the normalized density. The entropy (S) expression according to the Collins's formalism can be written as⁹⁶:

$$S = - \sum_r \rho'(r) \ln [\rho'(r)/\tau'(r)] \quad (3.24)$$

The probability $\rho'(r)$ and prior probability $\tau'(r)$ are related to the actual electron or nuclear density by following expressions

$$\rho'(r) = \frac{\rho(r)}{\sum_r \rho(r)}, \quad \tau'(r) = \frac{\tau(r)}{\sum_r \tau(r)} \quad (3.25)$$

where $\rho(r)$ is the actual electron or nuclear density at a certain pixel r and $\tau(r)$ is the prior density for $\rho(r)$. The given information comes from constraint relations related to the phase-known and phase-unknown structure factors.

$$C_1 = \frac{\left(\frac{1}{N_1}\right) \sum_k |F_{calc}(k) - F_{obs}(k)|^2}{\sigma^2(k)} \quad (3.26)$$

$$C_2 = \frac{\left(\frac{1}{N_2}\right) \sum_k ||F_{calc}(k)| - |F_{obs}(k)||^2}{\sigma^2(k)}$$

where N_1 and N_2 are the number of reflections for phase-known and phase-unknown structure factors, respectively. $F_{obs}(k)$ is the observed structure factor for reflection k , $\sigma(k)$ is the standard deviation of $F_{obs}(k)$, and $F_{cal}(k)$ is the calculated structure factor given as

$$F_{cal}(k) = V \sum_r \rho(r) \exp(-2\pi i \mathbf{r} \cdot \mathbf{k}) \quad (3.27)$$

where V is the unit-cell volume. The expected value for C_1 and C_2 is 1. The sum in the **eq. (3.26)** are taken over all the reflections for which the phase-known and phase-unknown structure-factors data are experimentally available. In the process of maximizing the information entropy (S), Lagrange's method of undetermined multipliers are used to constrain C_1 and C_2 to be unity. Then we have

$$Q(\lambda_1, \lambda_2) = - \sum_r \rho(r) \ln [\rho(r)/\tau(r)] - (\lambda_1/2)C_1 - (\lambda_2/2)C_2 \quad (3.28)$$

where λ_1 and λ_2 are Lagrange multipliers. By setting $\partial Q(\lambda_1, \lambda_2)/\partial \rho(r) = 0$ and using some approximations,

$$\begin{aligned} \rho(r) = & \exp [\ln \tau(r) + \frac{\Lambda_1}{N_1} \sum \left[\frac{1}{\sigma^2(k)} \right] \times \{F_{obs}(k) - F_{calc}(k)\} \exp (-2\pi i \mathbf{k} \cdot \mathbf{r}) \\ & + \left(\frac{\Lambda_2}{N_2} \right) \sum \left[\frac{1}{\sigma^2(k)} \right] \times \{|F_{obs}(k)| \exp [i\varphi(k)] - F_{calc}(k)\} \\ & \times \exp (-2\pi i \mathbf{k} \cdot \mathbf{r}) \end{aligned} \quad (3.29)$$

where $\Lambda_1 = \lambda_1 F_0$ and $\Lambda_2 = \lambda_2 F_0$ and F_0 is equal to the total number of electrons or total scattering length in a unit cell. Since all the structure factors are measured with an appropriate scale factor, this can be done in a straightforward way. When $F_{obs}(k)$, $\sigma(k)$ and λ_i are given, the **eq. (3.29)** determines the MEM electron-density or nuclear density distribution, $\rho_{MEM}(r)$. In general, a numerical approach is applied to obtain the value of $\rho_{MEM}(r)$ by an iterative procedure, starting from a uniform electron density.

There are many cases in crystallography where inverse Fourier transformation is used to generate the electron or nuclear density distribution from structure factor data. Mathematically, to perform a Fourier inversion without any ambiguity, an infinite number of Fourier coefficients are required. However, this is simply not possible experimentally. Hence, Fourier inversion is performed by using a limited number of structure factors that are measured experimentally and ignoring experimental errors. This procedure implicitly means that all the missing/not-measured structure factors are zero. This is a highly biased assumption from MEM perspective. MEM tries to do this by demanding that the map contains as little information as possible, i.e. its entropy is at a maximum, subject to the constraints imposed by the experimental data. This means that whatever information the map contains is demanded by the data and is not there as a by-product of the numerical method or a hidden assumption. It also means that it can make no assumptions at all about the missing information and so produces as unbiased an estimate of the true map as possible⁹⁹. In addition, in MEM analysis, no series termination errors occur and yield a high-resolution density distribution even from the limited number of structure factors. The main disadvantage of MEM is to locate missing atoms with low occupancies and to reconstruct their correct densities.

Dysnomia is a computer program, which is used in this work for MEM analysis of powder and single crystal neutron diffraction data in 0th-order single-pixel approximation⁹⁸. It uses the linear

combination of the generalized F and G constraints and arbitrary weighting scheme based on the lattice plane spacing. The program *Dysnomia* can run with the combination of refinement program *JANA*¹⁰⁰, as *JANA* generates the input files for further MEM analysis with *DYSNOMIA*. *Dysnomia* accepts two different types of input files; (i) *.fos*: for powder diffraction data (ii) *.mem*: for single crystal diffraction data. In addition, it accepts *.prf* file, which contains all conditions of MEM calculations, can be generated after the first run of MEM calculation. To perform an MEM calculation, the unit cell is divided into 2^n grids along the crystallographic axes; a , b , c . Grid numbers along the axes should be selected in such a way that symmetry elements such as mirrors, rotation axes, and inversion centers coincide with intersections of grid lines. In addition, the grid numbers must be appropriately set by considering the value of lattice parameters. After MEM calculation, it gives standard output file as *.out* and it generates the 3D voxel data file storing densities in a binary format as *.pgrid* files that were visualized by *VESTA*^{101,102}.

Chapter 4

Synthesis and characterizations of poly-and single crystals of $\text{Nd}_{(2-x)}\text{Sr}_x\text{NiO}_{4+\delta}$

The current chapter introduces various synthesis techniques that were used to grow poly-and single crystal samples of $\text{Nd}_{(2-x)}\text{Sr}_x\text{NiO}_{4+\delta}$ and different characterization methods to analyze the phase purity and oxygen content of as-prepared samples used for my investigations.

Firstly, in the **section 4.1**, we address the solid-state reaction route to obtain high quality powder samples. In the **section 4.2**, we describe the floating zone technique using optical mirror furnace to grow the single crystal of $\text{Nd}_{2-x}\text{Sr}_x\text{NiO}_{4+\delta}$ nickelates. At last, in the **section 4.3**, we discuss experimental results on the quality and phase purity of as-prepared powder and single crystal samples with powder X-ray diffraction measurements at room temperature. The overall oxygen content was determined with thermogravimetric analysis (TGA). In addition, the experimental results on the quality of *as-grown* single crystals are discussed from x-ray Laue diffraction and single crystal neutron diffraction measurements.

4.1. Polycrystalline sample preparation

Polycrystalline samples were synthesized as a first step to obtain high quality starting materials to grow large single crystals of $\text{Nd}_{(2-x)}\text{Sr}_x\text{NiO}_{4+\delta}$ and to obtain powder samples for X-ray and neutron diffraction studies. Conventional solid-state reaction route was used for the synthesis of powder samples at high temperature¹⁰³. In the first step, stoichiometric amount of highly pure Nd_2O_3 , SrCO_3 (in case of Sr-doped samples), and NiO powders, supplied by Sigma Aldrich, were thoroughly mixed and finely ground with an agate mortar and pestle. Powders were mixed in acetone medium to obtain homogeneous admixture of all starting materials. In all cases, Nd_2O_3 powder was pre-annealed at 1173 K for 12 h in air to remove hydroxide traces that appear in presence of water from atmosphere in ambient conditions. Therefore, Nd_2O_3 powders should be stored in a desiccator after pre-annealing. Mixed powders were calcined at 1523 K in alumina crucibles for 12 h. The calcination process was performed in a box furnace with air atmosphere. In the next step, calcined powder materials were again thoroughly mixed and ground, and then pressed into pellets of diameter 6 mm under 10 MPa pressure and then fired at 1523 K for 12 h.

This step was repeated 3-4 times with intermediate grinding and pelletizing. In each step, a representative X-ray diffraction measurement was performed to follow the phase formation process, as shown in **Fig.4.1** for $Nd_{1.5}Sr_{0.5}NiO_{4+\delta}$. The solid-state reaction method can be represented by following two chemical reactions for Sr-free and Sr-doped samples, respectively:

For Sr-free samples: $Nd_2O_3 + NiO + \delta/2 O_2 \rightarrow Nd_2NiO_{4+\delta}$

For Sr-doped samples: $(1-x/2) Nd_2O_3 + x SrCO_3 + NiO + \delta/2 O_2 \rightarrow Nd_{(2-x)}Sr_xNiO_{4+\delta} + CO_2\uparrow$

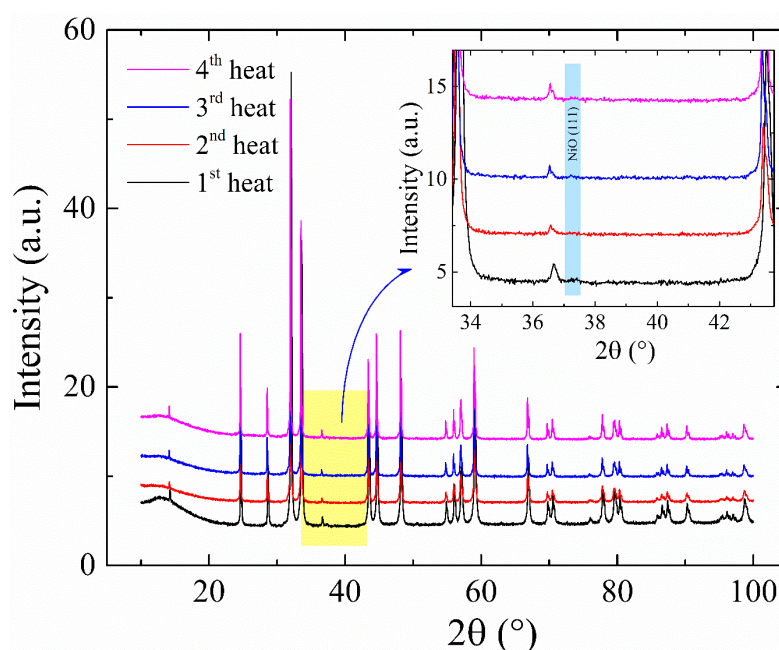


Figure 4.1 | X-ray powder diffraction patterns of $Nd_{1.5}Sr_{0.5}NiO_{4+\delta}$. Powder patterns were collected at room temperature on D8 at LDM, PSI using $CuK_{\alpha 1-2}$ radiation. Measurements were performed at each step of the heat treatment during solid-state synthesis. The inset shows the disappearance of unreacted NiO with repeated heat treatment.

There were few difficulties faced during the synthesis of powder samples. First of all, the use of Nd_2O_3 oxide is delicate because of its tendency to form $Nd(OH)_3$ in ambient conditions. If the Nd_2O_3 powders are not pre-annealed before the synthesis or the atmosphere is not well controlled after the post-annealing, the reactant powders will contain a large amount of hydroxide element. This has a dramatic effect on the final product, since it reduces the expected Nd/Ni ratio and the subsequent excess of Ni will lead to impurities (namely Ni_2O_3 or NiO). The lack of Nd or the excess of Ni may partially stabilize the higher order Ruddlesden popper $Nd_4Ni_3O_{10}$ phase at ambient temperature. Another difficulty during the powder synthesis arises due to partial loss of Ni at high temperatures. Ni also reacts with the alumina crucible to form Al_2NiO_4 spinel that appears on the surface layer of the crucible detectable by its blue color. The subsequent loss of Ni from the powder also modifies the Nd/Ni ratio. This has to be overcome by adding excess amount of Ni in the starting material. Moreover, higher Ni excess must be present

for longer heat treatment. 3% molar excess of Ni has been found to be ideal for the single crystal growth after several trials¹⁰³.

4.2. Single crystal growth

It is essential to grow high quality single crystals of $RE_2NiO_{4+\delta}$ compounds with well-defined stoichiometry to investigate their anisotropic structural and physical properties. Crystal growth of $Nd_{(2-x)}Sr_xNiO_{4+\delta}$ compounds were carried out by floating zone (FZ) method in optical furnace, allowing synthesis of large (centimeter size) and high quality single crystals^{104,105}.

The principle of crystal growth with image furnace is simple as shown in **Fig.4.2(a)**¹⁰⁶. In the first step, a molten zone is formed between the feed and seed rods, and then to connect these two rods *via* the liquid phase. The molten zone is formed by focusing the radiation from halogen lamps into a narrow band between the seed and feed rods. When the zone becomes approximately stable and appropriate conditions are reached, the zone is moved through the cylindrical feed rod. This allows the melt to precipitate on the seed rod. The zone can be moved either by displacing the lamps upward, or by transferring the feed-molten zone-seed rod system downward, depending on the type of apparatus. If the moving rate is adapted together with the thermodynamic conditions, a crystalline phase can be grown on top of the seed rod. In this work, the first option was used to move the molten zone. This technique is crucible free as the zone is formed by contactless heating and is held between the two solid rods by its own surface tension. Thus, contamination coming from the crucible is avoided, which is a major problem in high chemically reactive materials.

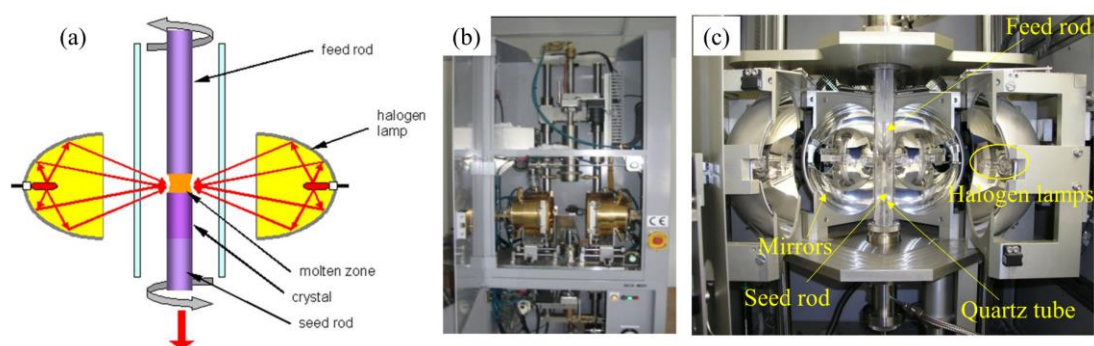


Figure 4.2 | Overview of the floating zone technique for crystal growth. (a) A schematic representation of the floating zone technique. Mirror furnaces that were used to grow the single crystals of $Nd_{(2-x)}Sr_xNiO_{4+\delta}$ systems, (b) with two halogen lamps (model: NEC SC2) at university of Montpellier and (c) with four halogen lamps (model: FZ-T-10000-H-VI-VP) at LDM, PSI. Figures are taken from the reference¹⁰⁷.

In the course of this work, two different mirror furnaces were used. The single crystal growth of $Nd_2NiO_{4+\delta}$ was carried out at the University of Montpellier, France using a two-mirror optical floating zone furnace (NEC SC2, Japan). This apparatus was equipped with two 500 W halogen lamps as a heat source, as shown in **Fig.4.2(b)**. These lamps, are located at the focal point of the mirrors, generate the radiation to heat the substance. The power of halogen lamps are high enough to reach about 2000 K and melt the polycrystalline material. Sr-doped $Nd_{2-x}Sr_xNiO_{4+\delta}$ ($x = 0.25$ and 0.5) single crystals were grown at LDM, PSI with the use of four-mirror crystal growth furnace (model FZ-T-10000-H-VI-VP, CSI Japan), as shown in **Fig.4.2(c)**. However, no experiments were performed on the $x = 0.25$ single crystal, therefore, will not be discussed in this thesis work. The feed and seed rods were prepared by placing highly pure powder samples inside thin rubber tubes. Subsequently, these tubes were compressed under hydrostatic pressure of 400 MPa into rods of length and diameter of about 10 mm and 6 mm, respectively. Final sintering of both rods were performed 1523 K for 12 h in air atmosphere. The seed rod was fixed at the lower shaft and the feed rod was hung from the upper shaft of the furnace. The crystal growth rate was 2-3 mm per hour with the feed and seed rods were counter rotating at 20-35 rotation per minute. All growth process was initiated using a polycrystalline seed rod. Stable crystal growth was found in pure oxygen atmosphere (pure oxygen, 99.99%). Representative photographs of the molten zone are shown in **Fig.4.3** during the crystal growth process of $Nd_{1.5}Sr_{0.5}NiO_{4+\delta}$ compound.

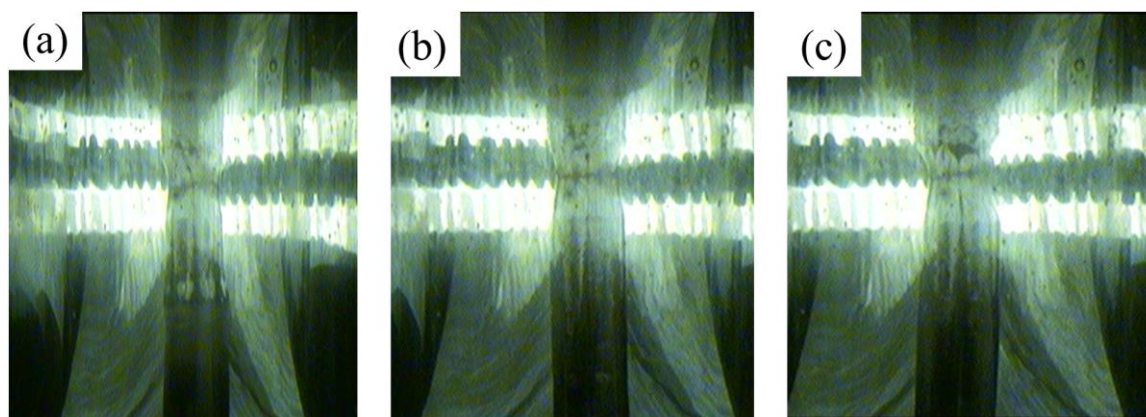


Figure 4.3 | Photographs of the molten zone taken at different time during the crystal growth of $Nd_{1.5}Sr_{0.5}NiO_{4+\delta}$ compound.

There are various experimental parameters to be controlled, which can affect the stability of the molten zone and consequently, the final quality of the grown crystals. They are listed as follows:

- **Chemical homogeneity:** Careful attention must be taken in the preparation of the feed rod. Homogeneity and accurate chemical composition of the feed rod has to be maintained, as impurities may form within the bulk crystal. For example, the presence of unreacted Nd_2O_3

makes the crystal unstable due to its hygroscopic nature and may react with moisture in the air to form hydroxides. The formation of hydroxides increases the volume inside the bulk crystal, which may cause the crystal to disintegrate completely.

- **Structural homogeneity:** The pressing step to prepare the seed and feeds rod are important to ensure that the rods are uniform along its length, mainly in its diameter and density. Excess porosity can lead to bubble formation in the melt, which seriously affect the stability of the molten zone.
- **Gas atmosphere:** Gaseous environment, with which the molten zone is in contact, plays an important role in determining the composition, especially the oxygen content and the type of phase, which is stabilized at the molten zone. Thus, in general, the crystal growth process is performed inside a cylindrical quartz tube into which different inert or active gases can be flown. In addition, the partial pressure of the gases may be controlled individually. Moreover, the amount of different gases is controlled independently by different manometers. Therefore, both the gaseous atmosphere and pressure can be chosen for a successful crystal growth. In general, different oxidizing gases are mixed with a dominant inert gas like Ar or He.
- **Rotation of feed and seed rods:** Rotational speed of both rods are two important parameters to control the stability of the molten zone. Furthermore, counter-rotation of seed and feed rods is fundamental to form a homogeneous molten zone.
- **Temperature control:** The temperature distribution around the molten zone is an important parameter for stable crystal growth. The size and the position of the lamps are two important factors that influence the temperature distribution in the molten zone. Therefore, a small defocusing of the lamps from the focal point of the ellipsoid (~1 mm) strongly changes the heat distribution and the corresponding temperature profile around the molten zone. Therefore, the focal point of the lamps must be systematically checked and corrected prior to the successful crystal growth. The heat distribution around the molten zone not only depends on the size of the filament of the lamps but also to their relative orientation with respect to the system. The melt's temperature can be adjusted by changing the power of the lamps, but it cannot be measured directly. Consequently, the stability of the molten zone is only possible to follow by visual observation with an infrared camera.

- **Growth rate:** The crystal growth rate is a crucial parameter for a stable crystal growth. However, the growth rate is also connected with the absolute temperature of the zone thus with the power of the lamps. Consequently, equilibrium must be achieved by adjusting both the growth rate and the power level. Subsequently, they are kept constant as much as possible during the whole growth process. If the growth rate is higher or the temperature of the molten zone is too low, it will result into shaking of the feed rod that is usually hung with a thin wire from the top. This will displace and partially defocus the feed rod from rightly aligned configuration. Consequently, its temperature will be lower that will solidify the melt very fast. Thus, the power of the lamps should be adjusted as soon as possible, otherwise the melt will drop and rods will be disconnected. Conversely, too high power of the lamps also leads to a drop since the melt will not be sticky enough to hold the liquid anymore.

Photographs of successfully synthesized *as-grown* single crystals of $Nd_2NiO_{4.23}$ and $Nd_{1.5}Sr_{0.5}NiO_{4.05}$ are shown in **Fig.4.4**.



Figure 4.4 | Photographs of as-grown single crystals with floating zone technique. As synthesized single crystals of (a) and (b) $Nd_2NiO_{4.23}$ and (c) $Nd_{1.5}Sr_{0.5}NiO_{4.05}$.

4.3. Characterizations

4.3.1. X-ray powder diffraction

Conventional x-ray powder diffraction experiments were performed at room temperature to follow the crystallization procedure of K_2NiF_4 phase during powder sample preparation of $Nd_{2-x}Sr_xNiO_{4+\delta}$ compounds. XRPD measurements were carried out with a Bruker D8-Advance diffractometer ($CuK_{\alpha 1-\alpha 2}$ radiations) installed at LDM, PSI. The **Fig. 4.1** shows the x-ray diffraction patterns recorded at different intermediate steps during the powder synthesis of $Nd_{1.5}Sr_{0.5}NiO_{4+\delta}$ compound. It was found that the K_2NiF_4 phase was already formed during the first heating. However, few extra peaks from unreacted NiO and Nd_2O_3 were found in the diffraction pattern. Those extra peaks were disappeared and the structural Bragg peaks become sharper due to better crystallization of the powder sample with repeated heating and grinding process, as shown in the inset of **Fig. 4.1**. However, with the repeated heat treatments no significant change in the positions of structural Bragg peaks were observed for the K_2NiF_4 phase.

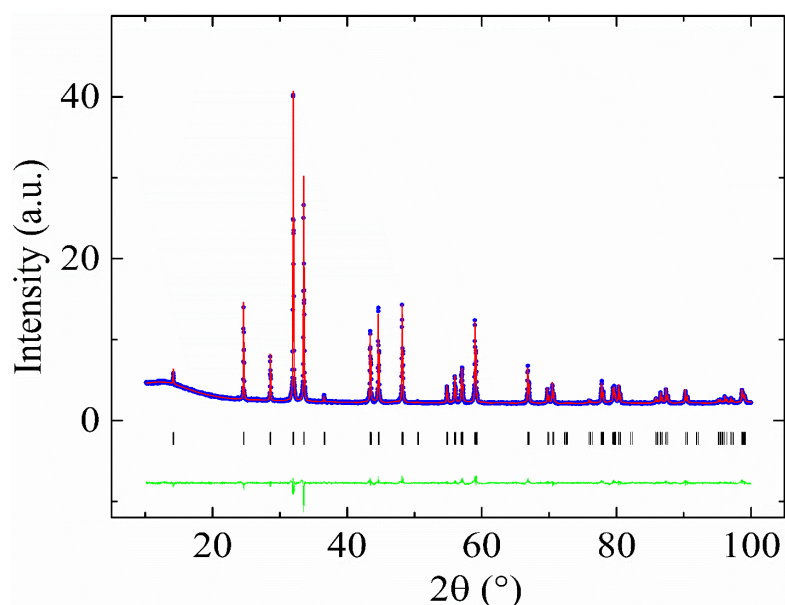


Figure 4.5 | X-ray Powder diffraction pattern of $\text{Nd}_{1.5}\text{Sr}_{0.5}\text{NiO}_{4+\delta}$. Observed (blue circles), calculated (red line), difference patterns (green continuous line) and positions of Bragg reflections (black ticks) resulting from Rietveld analysis of room temperature XRPD data. Data was measured on D8 at LDM, PSI using $\text{CuK}\alpha_{1-2}$ radiation.

Table 4.1 | Refined structural and thermal parameters at room temperature obtained for the $\text{Nd}_{1.5}\text{Sr}_{0.5}\text{NiO}_{4.05}$ compound from x-ray powder diffraction data. Space group: $F4/mmm$. $R_B = 6.7\%$, $R_F = 5.3\%$.

Atoms	x	y	z	$U_{\text{iso}} (\text{\AA}^2)$	Occ.
Nd/Sr	0	0	0.36112(12)	0.01073(3)	0.125
Ni	0	0	0	0.00952(6)	0.0625
O_{ap}	0	0	0.1742(9)	0.0205(3)	0.125
O_{eq}	$\frac{1}{4}$	$\frac{1}{4}$	0	0.0145(3)	0.125

Le-bail and Rietveld refinements of powder data were carried out with the FullProf Suite program. These refinements are only to check the phase purity and crystalline quality of the as prepared powder samples. Therefore, these results are not used to draw any structural interpretations. The first important result of these refinements is the high purity of all as-prepared powder samples, no secondary phase is found, thus no phase separation occurred in all samples; all reflections in the diffraction patterns could be fitted with one single K_2NiF_4 phase. Moreover, sharp nuclear structural Bragg peaks on the diffraction patterns confirm high crystalline quality of all the samples. An excerpt of Rietveld refined XRPD data of $\text{Nd}_{1.5}\text{Sr}_{0.5}\text{NiO}_{4+\delta}$ compound with tetragonal $F4/mmm$ space group is shown in **Fig.4.5** and structural and thermal parameters are reported in **Table 4.1**. The agreement factors of all refinements are good with typical Bragg R-factors $\sim 5\%$ and R_F factors $\sim 3-5\%$. Extracted lattice parameters for all the samples are tabulated in **Table 4.3**.

Table 4.2 | Refined structural and thermal parameters at room temperature obtained from the x-ray powder diffraction data of the $Nd_2NiO_{4.23}$ compound. Space group: $F112/m$. $R_B = 5.3\%$, $R_F = 5.7\%$.

Atoms	x	y	z	$U_{iso} (\text{\AA}^2)$	Occ.
Nd	0	0	0.35951(12)	0.00951(4)	0.5
Ni	0	0	0	0.00634(17)	0.25
O _{ap}	0	0	0.1766(4)	0.0662(16)	0.5
O _{eq1}	1/4	1/4	0	0.026(1)	0.25
O _{eq2}	1/4	3/4	0	0.0148(17)	0.25
O _{int}	1/4	1/4	1/4	0.0148(17)	0.05625

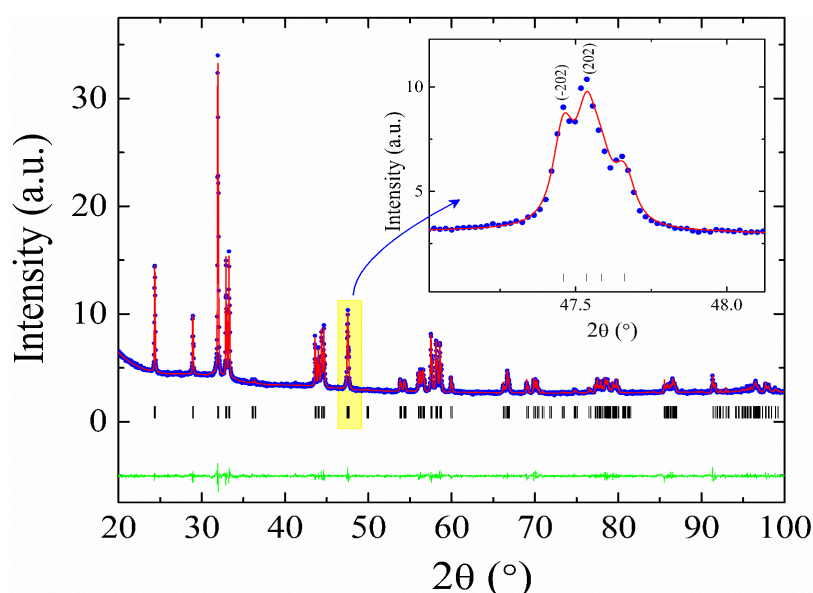


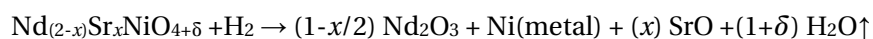
Figure 4.6 | An excerpt of the x-ray diffraction pattern of the as-grown single crystal of $Nd_2NiO_{4.23}$. Observed (blue circles), calculated (red line), difference patterns (green continuous line) and positions of Bragg reflections (black ticks) resulting from Rietveld analysis of room temperature XRPD data. The monoclinic distortion in the crystal structure is evident from the splitting of (220) and (-220) Bragg reflections as shown in the inset. Data was measured on D8 at LDM, PSI using $CuK_{\alpha 1-2}$ radiation.

The quality of as grown single crystals was also checked with powder x-ray diffraction. Small pieces were cut and separated from different cross-sections of the *as-grown* single crystals, then finely ground in a mortar. Powder diffraction measurements were carried at room temperature. An excerpt of the room temperature XRPD pattern of as-grown $Nd_2NiO_{4+\delta}$ crystal is shown in **Fig.4.6**. Rietveld refinements were carried out in the monoclinic $F112/m$ space group with lattice parameters $a = 5.38526(6) \text{ \AA}$, $b = 5.44419(4) \text{ \AA}$, $c = 12.3508(5) \text{ \AA}$, $\alpha = \beta = 90^\circ$ and $\gamma = 90.0784(2)^\circ$. Refined structural and thermal parameters of the monoclinic phase are presented in **Table 4.2**. Extracted lattice parameters correspond to a non-stoichiometric oxygen content according to

previously reported results^{14,103}. X-rays do not allow determining the extra oxygen content precisely. However, it can be estimated from the extracted lattice parameters comparing with previously reported results. The extra oxygen content in the as grown crystal has been determined to be $\delta \sim 0.23$ and it is in accordance with the results of as grown polycrystalline sample.

4.3.2. Thermogravimetric analysis

As-prepared powder samples contain additional oxygens when synthesized in air atmosphere¹⁰³. A more precise value of the average oxygen content in all powder and single crystal samples were determined experimentally with thermogravimetric analysis (TGA) in reductive gas atmosphere at high temperature. TGA analyses were carried out on the NETZSCH Jupiter STA 449C system combined with a ThermoStar Pfeiffer Vacuum mass spectrometer at LDM, PSI. All reduction processes were performed in 5% H₂-95% He gas atmosphere. The chemical reaction representing the reduction process is given by:



In each cases, small amount of powder sample (40-50 mg) was filled inside an alumina crucible and heated from 300 to 1300 K with a rate of 5 K/min. In all cases, a baseline was collected (which is the contribution of the apparatus and the crucible without the sample) in identical atmosphere. After subtracting the baseline, the total loss of weight was measured which is attributed to the departure of excess oxygen. Representative TGA curves of Nd_(2-x)Sr_xNiO_{4+δ} system are illustrated as a function of temperature in **Fig. 4.7**. A common step-like reduction behavior is observed for all the compositions. Several intermediate phases could be stabilized during the reduction process. The composition of these phases are characterized by well-defined broad plateaus in the weight-loss curves. For $x < 0.5$, the reduction mechanism is a two-stage reduction process. For these systems, the first weight loss starts at $T \sim 580\text{-}645$ K (580 K for $x = 0.1$, 602 K for $x = 0.25$ and 645 K for $x = 0.33$) and resulting the stoichiometric phase Nd_{2-x}Sr_xNiO₄. The second and larger loss starts at $T \sim 830\text{-}912$ K (830 K for $x = 0.1$, 877 K for $x = 0.25$ and 912 K for $x = 0.33$), corresponds to full decomposition of the whole phase into $(1 - x/2) \text{Nd}_2\text{O}_3$, $(x) \text{SrO}$ and Ni. From the total weight loss, the excess oxygen content δ is determined to be 0.22(2) for $x = 0$, 0.11(2) for $x = 0.1$, 0.09(2) for $x = 0.25$ and 0.04(2) for $x = 0.33$. However, a continuous weight loss is observed in the reduction process for compositions with $x = 0.5$ and 0.7. The first weight loss starts at 635 K for $x = 0.5$ and at 656 K for $x = 0.7$. A continuous weight loss of 2% and 2.5% occurs for $x = 0.5$ and 0.7 before the final weight loss starts at $T \sim 946$ K and 975 K, respectively. This weight loss is significantly larger compared to the compositions with $x > 0.5$, indicating the formation of an oxygen deficient phase.

From the total weight loss, the oxygen content δ is determined to be 0.04(2) and 0.00(2) for $x = 0.5$ and $x = 0.7$, respectively. It is evident that with increasing Sr-content the amount of δ decreases and the system starts to lose excess oxygens relatively at higher temperatures. These results indicate that the ideal tetragonal K_2NiF_4 type structure becomes stable with higher Sr^{2+} concentration and consequently, concentration of oxygen content for higher Sr-doped compounds. Results of TGA analyses are reported in **Table 4.3**. It can be seen from TGA curves that sample weight slightly increases with increasing temperature between 400 and 700 K even in the reductive atmosphere. This could be explained by the non-reproduction of instrumental baseline with and without the sample, respectively.

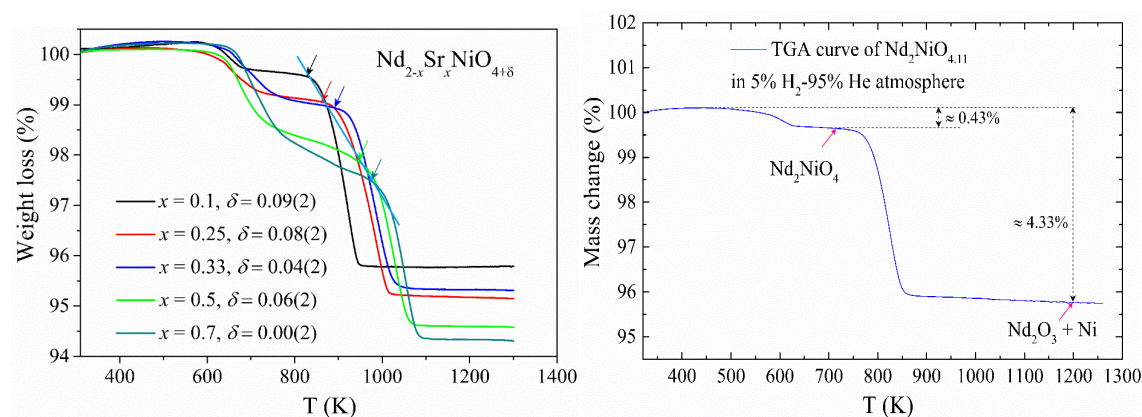


Figure 4.7 | Thermogravimetric analysis of as prepared powder samples of $\text{Nd}_{(2-x)}\text{Sr}_x\text{NiO}_{4+\delta}$ compounds in 95%He-5% H_2 atmosphere. (Left) Sr-doped samples and (right) Sr-free samples.

The excess oxygen content in the as grown $\text{Nd}_2\text{NiO}_{4+\delta}$ sample is found to be 0.23(2). Therefore, a powder and a single crystal sample with intermediate oxygen non-stoichiometry has to be prepared after reduction of the *as-grown* sample. The reduction process can be performed in two different ways i.e. electrochemical reduction process at ambient conditions¹⁴ and at high temperature with appropriate reductive gas medium⁵⁴. In the first approach, it is very hard to produce a large and homogeneous single crystal for neutron diffraction measurements. Therefore, the second approach was undertaken in this work to synthesize the intermediate phase. The optimized reductive atmosphere was found after performing in-situ X-ray powder diffraction experiments at high temperature in controlled gas atmospheres. Two different reductive mediums were tried; mixed $\text{Ar}+\text{H}_2$ gas flow and pure Ar gas flow. In the first case, as shown in the left side figure of **Fig.4.8**, we found that the system start to release the excess oxygen around 300°C at which structural changes start to occur, in accordance with our TGA data. The intermediate phase forms around 330°C. However, the reduction process is so fast that the intermediate phase could not be stabilized at this temperature. In the second case, as shown in the right side figure of **Fig.4.8**, the structural changes start to occur around 450°C and coexistence

of two different phases was observed at 800°C. However, with decreasing temperature, the intermediate phase became stabilized and at room temperature, only the intermediate phase remains. We found that the intermediate phase could be stabilized at 800°C in Ar atmosphere if the reduction process is performed for few hours whereas in-situ diffraction patterns were usually collected only for 30 mins. With these observations, dynamic vacuum (10^{-3} mbar) atmosphere, which is more reductive than Ar, was selected for the reduction process. The reduction process was performed at 800°C K for 24 h to synthesize the reduced phase. TGA analysis of the reduced sample, as presented in the right side figure of **Fig.4.7**, shows the additional oxygen content to be $\sim 0.11(2)$. Rietveld refinement of single crystal neutron diffraction data of the reduced single crystal shows the additional oxygen content $\sim 0.09(1)$. Powder X-ray diffraction measurements confirm the phase purity and good crystalline quality of the reduced samples. The structural symmetry of the reduced phase is found to be tetragonal with $P4_2/ncm$ space group, in accordance with previously reported results on electrochemically prepared samples¹⁴. Refined lattice parameters of the reduced phase is tabulated in **Table 4.3**.

Furthermore, TGA measurement for $Nd_2NiO_{4.23}$ compound was also performed in pure O_2 atmosphere between 300 and 1000 K to correlate the structural changes in this temperature range with the loss of excess oxygen content, as discussed with the powder X-ray and single crystal neutron diffraction measurements in **Chapter 6**.

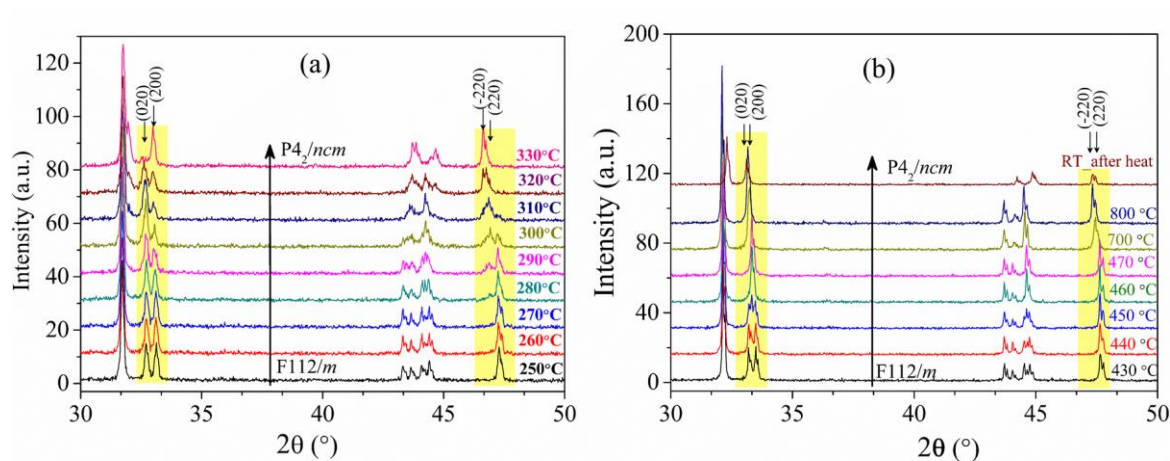


Figure 4.8 | In-situ X-ray diffraction patterns collected during reduction of $Nd_2NiO_{4.23}$ sample.

(a) In mixed Ar-H₂ atmosphere and (b) in pure Ar atmosphere with increasing temperature.

Table 4.3 | Oxygen content obtained with TGA and structural parameters obtained with X-ray diffraction of $Nd_{(2-x)}Sr_xNiO_{4+\delta}$ compounds.

Compound	δ	Space group	Lattice parameters
Nd ₂ NiO _{4+δ} (as-grown powder)	0.23(2)	F112/ <i>m</i>	$a = 5.38140(2) \text{ \AA}$, $b = 5.44047(2) \text{ \AA}$ $c = 12.3434(5) \text{ \AA}$, $\gamma = 90.0743(4)^\circ$
Nd ₂ NiO _{4+δ} (as-grown crystal)	0.23(2)	F112/ <i>m</i>	$a = 5.38526(6) \text{ \AA}$, $b = 5.44419(4) \text{ \AA}$ $c = 12.3508(5) \text{ \AA}$, $\gamma = 90.0784(2)^\circ$
Nd ₂ NiO _{4+δ} (Reduced powder)	0.11(2)	P4 ₂ / <i>ncm</i>	$a = b = 5.46200(2) \text{ \AA}$, $c = 12.20517(9) \text{ \AA}$
Nd ₂ NiO _{4+δ} (Reduced crystal)	0.09(1)	P4 ₂ / <i>ncm</i>	$a = b = 5.4597(5) \text{ \AA}$, $c = 12.2027(4) \text{ \AA}$
Nd _{1.9} Sr _{0.1} NiO _{4+δ}	0.09(2)	Fmmm	$a = 5.36211(5) \text{ \AA}$, $b = 5.419054(5) \text{ \AA}$ $c = 12.3743(1) \text{ \AA}$
Nd _{1.75} Sr _{0.25} NiO _{4+δ}	0.08(2)	F4/ <i>mmm</i>	$a = b = 5.369807(1) \text{ \AA}$, $c = 12.4077(5) \text{ \AA}$
Nd _{1.67} Sr _{0.33} NiO _{4+δ}	0.04(2)	F4/ <i>mmm</i>	$a = b = 5.358741(1) \text{ \AA}$, $c = 12.42639(1) \text{ \AA}$
Nd _{1.5} Sr _{0.5} NiO _{4+δ} (as-grown powder)	0.06(2)	F4/ <i>mmm</i>	$a = b = 5.33957(1) \text{ \AA}$, $c = 12.4840(5) \text{ \AA}$
Nd _{1.5} Sr _{0.5} NiO _{4+δ} (as-grown Crystal)	0.05(2)	F4/ <i>mmm</i>	$a = b = 5.338098(1) \text{ \AA}$, $c = 12.4620(6) \text{ \AA}$
Nd _{1.3} Sr _{0.7} NiO _{4+δ}	0.00(2)	F4/ <i>mmm</i>	$a = b = 5.33717(4) \text{ \AA}$, $c = 12.4441(1) \text{ \AA}$

4.3.3. X-ray Laue diffraction

Crystalline quality of all as-grown single crystals were checked with x-ray Laue diffraction in back scattering geometry. Furthermore, preliminary orientation of single crystals has been carried out for the directional dependent magnetization measurements. The sample has been fixed on a goniometer with the help of wax and placed in front of the x-ray beam. The x-ray beam partially back scattered from the single crystal sample is recorded with CCD cameras from Photonic Science. Laue patterns were recorded with 1-2 minutes of exposure time when the total distance from sample-to-detector was set about 4 cm. Various softwares are available for calculations and treatments of Laue patterns. In this work, Orient Express¹⁰⁸ and QLaue¹⁰⁹ programs were used to determine the principal axis thus the crystal orientation. In this method, first a Laue pattern is recorded for the crystal that is mounted in an arbitrary orientation. Then, one of these softwares were used to calculate Laue patterns using the lattice parameters and space group obtained from XRPD data. Then, the good matching is obtained by superimposing the experimental data with the calculated patterns. **Fig. 4.10(a) and 4.10(b)** respectively shows Laue diffraction patterns recorded for the Nd₂NiO_{4.23} crystal with x-ray beam parallel to the crystallographic [110]-axis and *c*-axis, respectively. Other two photographs in **Fig. 4.10(c) and 4.10(d)** respectively show the Laue

diffraction patterns recorded for the $Nd_{1.5}Sr_{0.5}NiO_{4.05}$ crystal oriented with the a -axis and c -axis collinear to incident x-ray beam. **Fig. 4.10(e) and 4.10(f)** show simulated Laue diffraction patterns with QLaue program for the $Nd_{1.5}Sr_{0.5}NiO_{4.05}$ crystal, confirming the crystallographic orientation of as-grown single crystal with the incoming beam direction. Presence of sharp structural Bragg peaks confirm excellent crystal quality of as-grown single crystals. For the single crystal of $Nd_2NiO_{4.23}$ compound, structural Bragg reflections are splitted into sub-reflections, particularly evident when the c -axis is parallel to the x-ray beam. Such splitting of main structural reflections is due to presence of twin domains inside the single crystal. Quantification of twin volumes is presented in chapter 6. The “star” shape in the Laue pattern as shown in **Fig. 4.10(b) for the $Nd_2NiO_{4+\delta}$** crystal is the characteristic of the orientation in which the c -axis is parallel to the incident beam. The four-fold axis induces this symmetry parallel to the c -axis results such shape of the Laue pattern even though the real symmetry is monoclinic at room temperature (since the monoclinic angle is close to 90° and in-plane lattice parameters are very similar).

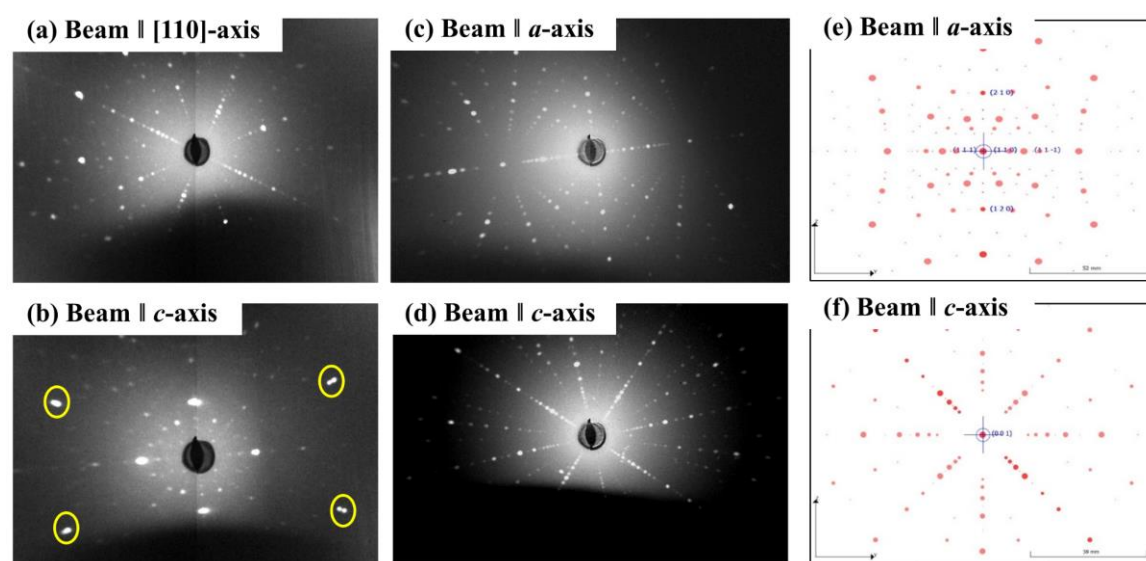


Figure 4.9 | X-ray Laue diffraction patterns obtained for as grown single crystals. (a) and (b) Laue patterns of $Nd_2NiO_{4.23}$, (c) and (d) Laue patterns of as-grown $Nd_{1.5}Sr_{0.5}NiO_{4.05}$ single crystal. Simulated Laue diffraction patterns with QLaue program with X-ray beam parallel to (e) a -axis and (f) c -axis. These simulated patterns are directly comparable with (c) and (d). Circles in (b) show splitted Bragg spots due to twinning in the as grown $Nd_2NiO_{4.23}$ single crystal.

4.3.4. Single crystal neutron diffraction

As X-ray diffraction technique is only limited to the surface of the single crystal, therefore, X-ray Laue patterns do not reflect the crystalline quality of the inner part of mm^3 size crystals. Consequently, preliminary neutron diffraction measurements were performed on ORION ($\lambda =$

2.21 Å)¹¹⁰ and MORPHEUS ($\lambda = 2.5$ and 5 Å)¹¹¹ at SINQ, PSI to perform preliminary experiments regarding the crystalline quality including possible twinning in the as-grown single crystals. Furthermore, these instruments were used to align the single crystals prior to the main diffraction experiments in particular for reciprocal plane mappings on DMC.

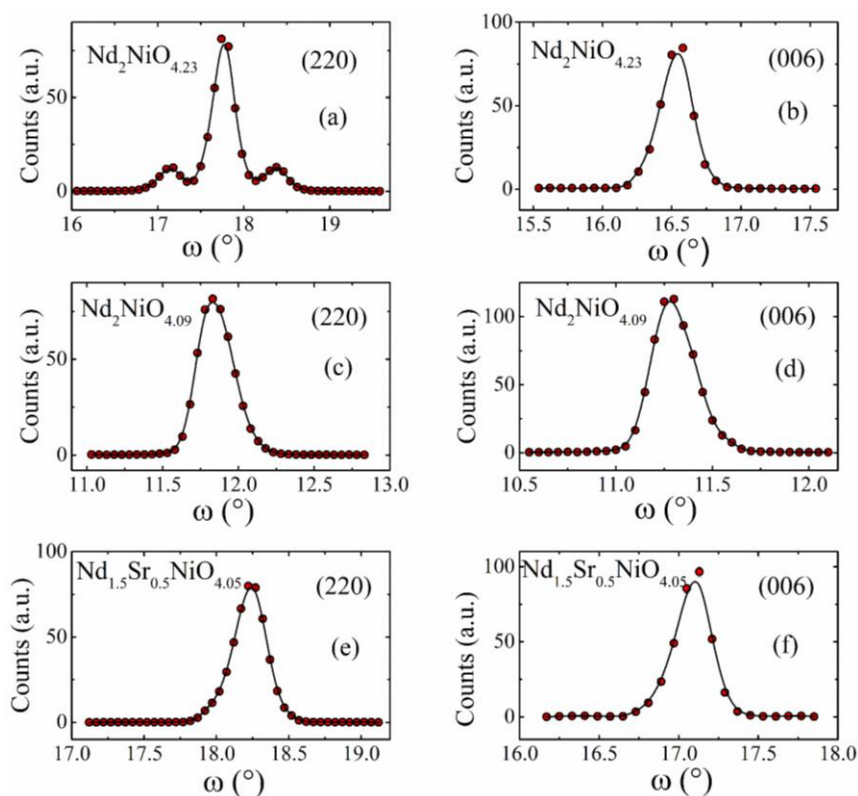


Figure 4.10 | Single crystal neutron diffraction data of as prepared single crystals performed on ω -scan with $(hk0)$ as the scattering plane. (a), (b) measured for $\text{Nd}_2\text{NiO}_{4.23}$ single crystal on ZEBRA ($\lambda = 1.177$ Å) at SINQ, PSI. (c), (d) Measured for $\text{Nd}_2\text{NiO}_{4.09}$ single crystal on HEiDi ($\lambda = 0.793$ Å) at MLZ, FRM II. (e), (f) Measured for as grown $\text{Nd}_{1.5}\text{Sr}_{0.5}\text{NiO}_{4.05}$ single crystal on ZEBRA ($\lambda = 1.177$ Å) at SINQ, PSI.

The information on the crystalline quality and homogeneous distribution of excess oxygen can be inferred from the neutron diffraction profiles of main structural Bragg reflections recorded on the single crystals. For measurements, the crystals were aligned with the c -axis perpendicular to the diffraction plane of the diffractometer. With this orientation, transversal scans (ω -scans) were performed for $(h00)$, $(hh0)$ and $(00l)$ type Bragg reflections. It is found that the full widths at half maximum for all reflections are within or close to the respective instrumental resolution as shown in **Fig. 4.10**. This confirms excellent quality of as-prepared samples. The mosaicity of the as-grown crystals was determined from the rocking curve of e.g. the (006) reflection, which was found to be of the order of 0.2° . The ω -scans for the $(hh0)$ reflections, i.e. the (220) and the

equivalent (-220) reflections, show a different number of twin individuals for the Nd₂NiO_{4+δ} crystals. For Nd₂NiO_{4.23}, the (220) and (-220) reflections were observed to split into three distinct sub-reflections confirming the presence of four twin domains. In contrast, the annealed crystal with reduced stoichiometry Nd₂NiO_{4.09} does not show such splitting, owing to the true tetragonal symmetry (*P4₂/ncm*) at room temperature. Similarly for $x = 0.5$ compound, no twinning is observed, since the symmetry is tetragonal *F4/mmm* at room temperature. The sharp profiles of all (*hh0*) reflections confirm a homogeneous excess oxygen distribution throughout the crystals since any inhomogeneity would show significant profile broadening related to strong changes in the lattice parameters.

4.4. Conclusions

Our high quality powder samples were synthesized with solid-state reaction route at high temperature. Crystalline quality and phase purity of as-synthesized powder samples were investigated by x-ray diffraction measurements. Large and high quality single crystals of Nd_{2-x}Sr_xNiO_{4+δ} ($x = 0$ with $\delta = 0.09, 0.23$ and $x = 0.5$) were successfully synthesized using the floating zone technique in optical mirror furnace. The crystal growth conditions were optimized after several trials in order to obtain large and homogeneous crystals without significant mosaic spread and defects. High crystalline quality of the crystals was checked by x-ray Laue and neutron diffraction measurements.

The major challenge faced during the crystal growth is controlling the (Nd+Sr)/Ni ratio in the final as-grown crystals. Even a small deviation from the ideal cation stoichiometry results in either segregation of NiO or formation of higher order intergrowth phases like Nd₄Ni₃O₁₀. Moreover, an excess of the rare earth metal yields intergrowth phases that lead to rapid disintegration of the crystals already under ambient conditions in air. TGA analyses confirmed the intercalation of extra oxygen atoms in the interstitial sites, which is still the case for higher Sr doping concentrations as is the case for Nd_{1.5}Sr_{0.5}NiO_{4+δ}, where δ is 0.06(2), while for $x = 0.1$, δ is found to reach 0.09(2).

Chapter 5

Crystal structure, excess oxygen ordering and magnetic properties of moderately oxygen-doped $\text{Nd}_2\text{NiO}_{4+\delta}$ ($\delta = 0.11$)

This chapter is dedicated to the LTT phase of $\text{Nd}_2\text{NiO}_{4+\delta}$ with $\delta \sim 0.11$, rendering formally $\frac{1}{4}$ of the Ni-atoms in a three-valent oxidation state. This is not only interesting in terms of related electronic properties and charge transfer, but also with respect to the tetragonal symmetry, which is usually observed for much lower δ only. The influence of δ on the crystal structure, apical oxygen disorder and magnetic properties was investigated by means of synchrotron X-ray powder diffraction, single crystal and neutron powder diffraction studies combined with macroscopic magnetic measurements.

This chapter is structured as follows. In **section 5.1**, experimental results from high-resolution X-ray and neutron powder diffraction measurements are discussed revealing structural changes as a function of temperature. In **section 5.2**, we discuss the magnetic properties of the compound from magnetic susceptibility and isothermal magnetization measurements. The spin structure of the compound is studied by neutron diffraction measurements and summarized in **section 5.3**. In **section 5.4**, the ordering of excess oxygen atoms and its influence on the apical oxygen disorder are presented as a function of temperature from high-resolution single crystal neutron diffraction measurements. The impact of such disorder scenario on low temperature oxygen mobility is drawn from these results. Central results of this chapter are published by S. R. Maity et al. in *Phy. Rev. Mat.* 3, 083604 (2019).

5.1. Crystal structure as a function of temperature

Room temperature X-ray powder diffraction (XRPD) pattern of $\text{Nd}_2\text{NiO}_{4.11}$ collected on a laboratory diffractometer is shown in **Fig. 5.1(a)**. The powder pattern is composed of sharp structural Bragg peaks indicating good crystalline quality of the sample. Additional reflections belonging to the cubic NiO impurity phase ($\sim 0.3\%$) are observed in the diffraction pattern. Le-Bail method has been used to extract the lattice parameters and structural symmetry at room

temperature. Different space groups and their combinations were used to index the experimental diffraction pattern. Tetragonal $P4_2/ncm$ and orthorhombic $Pccn$ structures unambiguously fit the diffraction pattern with lattice parameters $a = b = 5.46200(2)$ Å, $c = 12.20517(9)$ Å at 300 K. Both space groups have similar extinction conditions for Bragg reflections with the only difference comes from the orthorhombic splitting in $Pccn$. With similar in plane a and b lattice parameters, it was impossible to detect such a subtle orthorhombic distortion with laboratory X-ray diffraction. Therefore, additional synchrotron X-ray diffraction measurements were performed to search for orthorhombic splitting of Bragg reflections. No splitting of $(h0l)/(0kl)$ type Bragg reflections was detected down to 5 K (cf. **Fig. 5.1(b)** and its inset) within the high-resolution of our synchrotron data, indicating the LTT-type crystal structure with $P4_2/ncm$ space group in the entire temperature range of 2-300 K. Even if the orthorhombic strain exists in the sample, it is in the order of 5.46×10^{-4} at 300 K.

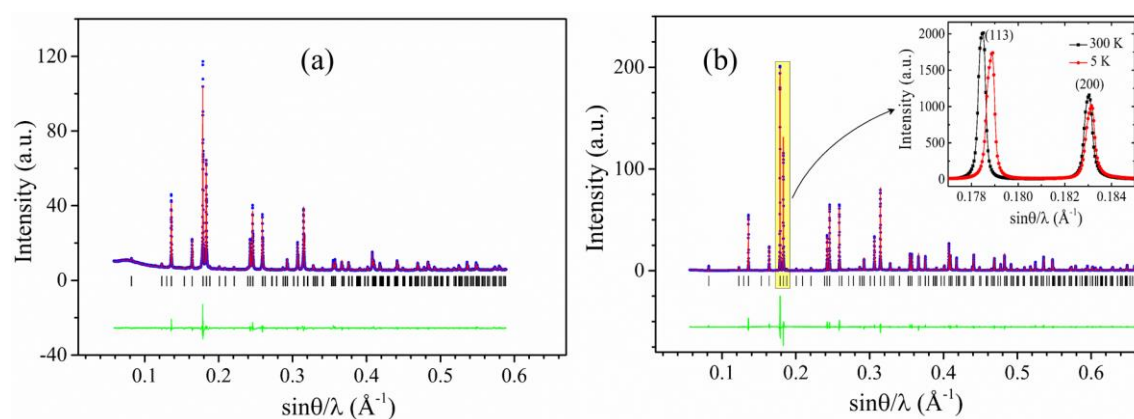


Figure 5.1 | Room temperature X-ray powder diffraction patterns of $\text{Nd}_2\text{NiO}_{4.11}$. Powder patterns were collected on (a) D8 diffractometer and (b) at the MS-X04SA beamline of SLS, PSI. Observed (blue circles), calculated (red line), difference patterns (green continuous line) and positions of Bragg reflections (black ticks) resulting from Rietveld analysis of XRPD data of $\text{Nd}_2\text{NiO}_{4.11}$. [S. R. Maity et al. *Phy. Rev. Mat.* 3, 083604 (2019)].

Structural distortion associated with the LTT-structure involves the systematic rotation of NiO_6 octahedra about $[1, -1, 0]$ -axis with nearest neighbor corner-shared octahedra rotates in opposite direction while the rotation axis is changed to $[110]$ -axis in the neighboring planes. Such distortion scheme is presented in **Fig. 5.2(a)** where it is easily visible that rotation of NiO_6 octahedron allows favorable opening for additional oxygen atoms at $4b/8f$ Wyckoff sites (marked with stars) and but not at $4e$ Wyckoff position. For the determination of the position of excess oxygen atoms in the unit cell, difference Fourier maps were calculated using powder neutron diffraction data since neutrons are highly sensitive to oxygen atoms ($b_{\text{coh}} = 5.803$ Å). Starting structural model for the refinement is taken from reference⁵⁰ as reported for the stoichiometric

Nd₂NiO₄ phase below 130 K. In this model, Nd, Ni, O_{ap}, O_{eq1} and O_{eq2} atoms occupy $8i(x\ x\ z)$, $4d(0\ 0\ 0)$, $8i(x\ x\ z)$, $4a(\frac{3}{4}\ \frac{1}{4}\ 0)$, and $4e(\frac{1}{4}\ \frac{1}{4}\ z)$ Wyckoff sites, respectively. Difference Fourier maps were obtained with and without excess oxygen atoms at those three possible Wyckoff sites and presented in **Fig. 5.2(b)-(e)**. It is uncovered that excess oxygen atoms at $8f(\frac{3}{4}\ \frac{1}{4}\ z = 0.27)$ and $4e(\frac{3}{4}\ \frac{3}{4}\ z = 0.254)$ Wyckoff sites generate pronounced negative intensities around the interstitial position and produces a worse fitting to the observed scattering densities. Best agreement is found with the interstitial oxygen atoms at $4b(\frac{3}{4}\ \frac{1}{4}\ \frac{1}{4})$ Wyckoff site. Therefore, in this oxygen-doped LTT phase, additional oxygen atoms *selectively occupy* the tetrahedral sites with symmetry $\bar{4}$. This result also confirms that the correct structural symmetry of moderately oxygen-doped phase is $P4_2/nm$ and but not $Pccn$ as the required site symmetry of additional oxygen atoms is absent in the later space group. During these refinements, the occupancy of interstitial sites was fixed to the ideal value as determined by TGA. The room temperature synchrotron x-ray powder diffraction (SXRPD) and neutron powder diffraction (NPD) patterns of Nd₂NiO_{4.11} are shown in **Fig. 5.1(b)** and **5.3(a)**, respectively along with the Rietveld refinement profiles with the tetragonal LTT-type structure model. The crystal structure using harmonic displacement factors (probability 85%) is visualized in **Fig. 5.5**. Structural and thermal parameters obtained with Rietveld refinements are summarized in **table 5.1**. Note that, on average only 11% of all $4b$ sites are statistically occupied by interstitial oxygen atoms in Nd₂NiO_{4.11} that approximately corresponds to $\frac{1}{2}$ -oxygen atom per unit cell. In the LTT-structure, the tilt angle α_1 is defined by the angle between the c -axis and the respective shift of the O_{ap}, as presented in **Fig. 5.4(b)**. Extracted values of α_1 at 300 K and 2 K are 9.3° and 9.6°, respectively. For the corresponding LTT structure of stoichiometric Nd₂NiO_{4.0}^{51,112}, the corresponding tilt angle was found to be 10.3° at 2 K. The LTT-type tilt pattern generates two different sets of equatorial oxygen atoms, O_{eq1} atoms at basal plane while O_{eq2} atoms are slightly displaced along the c -axis. Such a displacement of O_{eq2} atoms from the basal plane, further characterized by the angle α_2 , lifts the center of inversion between two in plane magnetic Ni²⁺ ions. This further induces the Dzyaloshinskii-Moriya (DM) interactions between the in-plane Ni spins that induce the spin canting along the c -axis from ab -plane. This spin canting develops a weak ferromagnetic component in the LTT structure of Nd₂NiO_{4.11} below the magnetic ordering temperature as discussed in **section 5.3**. Refined values of α_2 at 300 K and 2 K are 7.7° and 8.4° while for stoichiometric Nd₂NiO_{4.0}, α_2 is found to be 10.5° at 2 K. Strong decrease of these tilt angles indicates that the inclusion of excess oxygens at interstitial sites relaxes partially the inherent structural strain in Nd₂NiO_{4+δ} compounds.

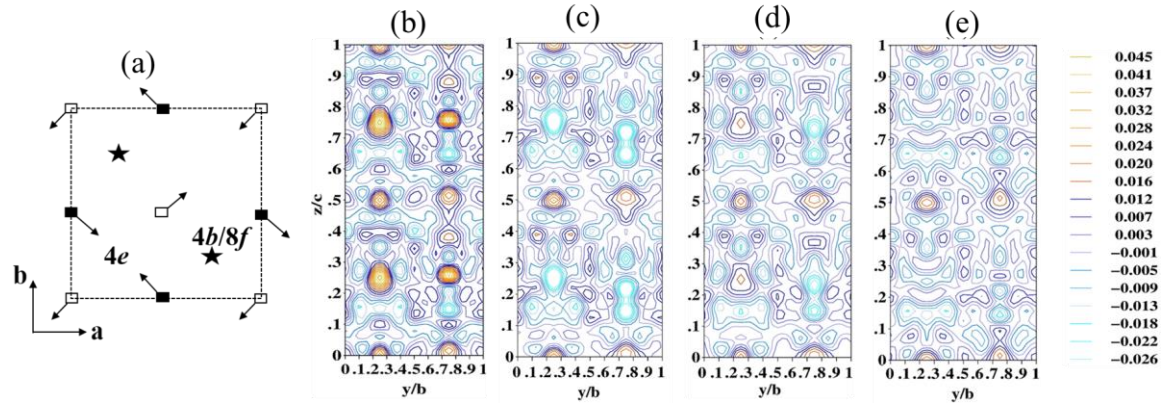


Figure 5.2 | Difference Fourier maps of $\text{Nd}_2\text{NiO}_{4.11}$. (a) Displacement of apical oxygens in $z \sim 0.17$ (open squares) and $z \sim 0.33$ (filled squares) layers in LTT structure allowing favorable $4b$ and $8f$ Wyckoff sites for interstitial oxygen atoms while the site $4e$ is not favored. Difference Fourier maps obtained from neutron powder diffraction data (b) without interstitial oxygen atoms, with interstitials (c) at $4e$ sites, (d) at $8f$ sites and (e) at $4b$ sites. Data were recorded on HRPT ($\lambda = 1.4940(2) \text{ \AA}$)

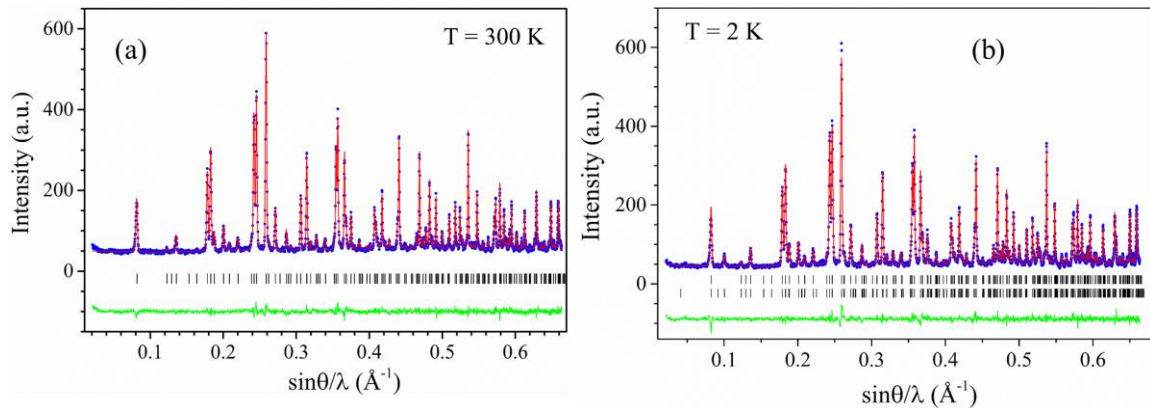


Figure 5.3 | Powder neutron diffraction patterns of $\text{Nd}_2\text{NiO}_{4.23}$. Observed (blue circles), calculated (red line) and difference (green continuous line) patterns resulting from Rietveld analysis of NPD data collected at (a) 300 K and (b) 2 K for $\text{Nd}_2\text{NiO}_{4.11}$ on HRPT ($\lambda = 1.4940(2) \text{ \AA}$), SINQ, PSI. Ticks show the positions of nuclear Bragg reflections. Upper and lower row of ticks show the positions of structural and magnetic reflections, respectively.

Structural refinements reveal anisotropic elongation of NiO_6 octahedrons along the c -axis, a common trend found in K_2NiF_4 oxides, with Ni-O_{ap} to Ni-O_{eq} (average) bond length ratio is close to 1.136 and larger than the value (1.129) found in undoped Nd_2NiO_4 at 300 K. Large anisotropic thermal parameters are found both for equatorial and apical oxygen atoms. Anisotropic thermal ellipsoids of apical oxygen atoms are largely elongated in the ab -plane while anisotropic thermal ellipsoids of both equatorial oxygens show extended components with shifts along the c -axis. Such unusual anisotropic thermal factors are also reported for other oxygen doped K_2NiF_4

nickelates^{14,18}. It is worth mentioning that the presence of excess oxygen atoms in the interstitial sites results into four unreasonable $\text{O}_{\text{int}}\text{-O}_{\text{ap}}$ bond lengths of 2.15 Å. In this way, the shift of the apical oxygen atoms induces a rotation of the $\text{O}_{\text{int}}\text{-O}_{\text{ap}}$ tetrahedra around the c -axis by 9.4°. As further outlined below by maximum entropy method, the short $\text{O}_{\text{int}}\text{-O}_{\text{ap}}$ distances found with Rietveld method in the harmonic approximation do not reveal the real apical site disorder scenario rather corresponds to the averaged structure without considering the local displacements of apical oxygen atoms caused by the steric pressure from oxygen interstitials.

It is at first sight surprising to find the LTT-type structure for $\text{Nd}_2\text{NiO}_{4.11}$ compound, since no significant disorder has been observed in the long-range NiO_6 octahedron-tilting pattern despite a considerable amount of oxygen interstitials. However, a LTT-type tilt pattern was first proposed by DFT calculations in oxygen intercalated $\text{La}_2\text{NiO}_{4.125}$ based on lattice relaxation around the interstitial oxygen ions⁵². Therefore, it is consistent with our present experimental observation. Furthermore, even though excess oxygen atoms selectively occupy the $4b$ Wyckoff site, no superstructure reflections were observed in the x-ray and powder neutron diffraction patterns down to 2 K, indicating the absence of long-range ordering of excess oxygen atoms in the investigated temperature range. This observation is in strong contrast with that reported results for iso-structural $\text{La}_2\text{NiO}_{4+\delta}$ in which 1D ordering of excess oxygen atoms along the c -axis is observed with similar δ values²⁷. Such 1D ordering of interstitials had been described by an antiphase model between the layers with $Bmab$ symmetry as discussed in chapter 2 (*cf.* section 2.2). In the next section, we reveal a complex 3D ordering scheme of excess oxygen atoms in $\text{Nd}_2\text{NiO}_{4.11}$ found with single crystal neutron diffraction data, however, these oxygen ordering superlattice peaks are masked in the powder data.

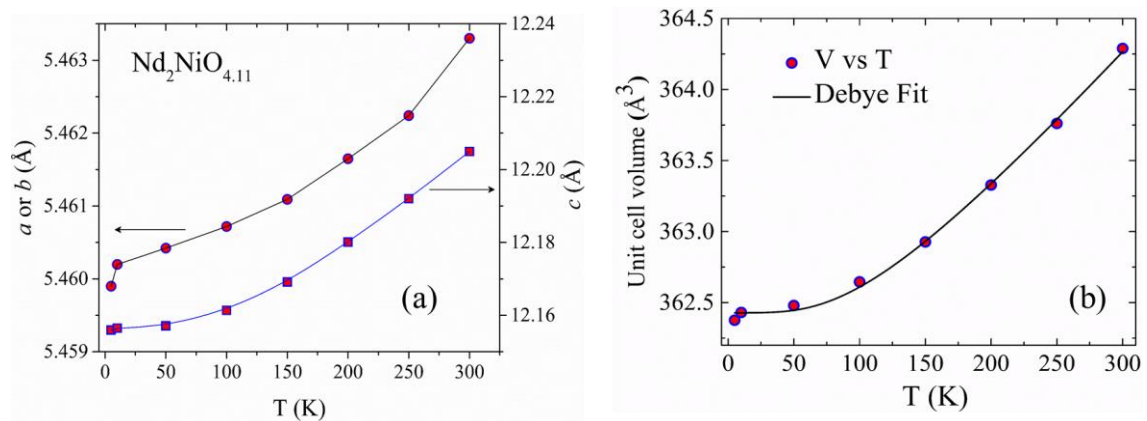


Figure 5.4 | Temperature evolution of various lattice parameters of $\text{Nd}_2\text{NiO}_{4.11}$ extracted from synchrotron x-ray powder diffraction data measured on MS-X04SA ($\lambda = 0.6208(1)$ Å) at SLS, PSI. (a) Evolution of a , b and c -axes with temperature. Solid lines are guide to eyes. (b) Evolution

of tetragonal unit cell volume with temperature of Nd₂NiO_{4.11}. The solid line is a Debye fit to the data following the Eq. (5.1).

Table 5.1 | Refinement results of polycrystalline Nd₂NiO_{4.11} compound in *P4₂/ncm* space group using Rietveld method. Data were collected on HRPT at SINQ, PSI, λ = 1.4940(2) Å up to sinθ_{max}/λ = 0.66 Å⁻¹), Thermal displacement parameters *U*_{ij} in Å². [S. R. Maity et al. Phys. Rev. Mat. 3, 083604 (2019)].

Temperature		300 K	2 K
<i>a</i> = <i>b</i>	(Å)	5.46200(2)	5.45868(1)
<i>c</i>	(Å)	12.20517(9)	12.15376(8)
Ni (0 0 0)	Occ.	1	1
	<i>U</i> _{iso}	0.0072(3)	0.0039(2)
	μ _x = μ _y (μB)	---	0.81(5)
	μ _{total} (μB)	---	1.14(7)
Nd (<i>x x z</i>)	Occ.	2	2
	<i>x</i>	0.9889(3)	0.98731(18)
	<i>z</i>	0.36104(12)	0.36104(9)
	<i>U</i> _{iso}	0.0096(4)	0.0052(2)
	μ _x = μ _y (μB)	---	1.15(3)
	μ _{total} (μB)	---	1.63(5)
O _{ap} (<i>x x z</i>)	Occ.	2.006(7)	2.023(6)
	<i>x</i>	0.0458(4)	0.0473(3)
	<i>z</i>	0.1783(3)	0.1779(2)
	<i>U</i> ₁₁ = <i>U</i> ₂₂	0.0382(14)	0.0335(10)
	<i>U</i> ₃₃	0.0085(11)	0.0133(8)
	<i>U</i> ₁₂	-0.0023(14)	-0.0024(10)
O _{eq1} (¾ ¼ 0)	Occ.	1.01(3)	0.966(20)
	<i>U</i> ₁₁ = <i>U</i> ₂₂	0.0077(16)	0.0100(10)
	<i>U</i> ₃₃	0.041(4)	0.0134(14)
	<i>U</i> ₁₂	0.002(2)	-0.0007(15)
O _{eq2} (¼ ¼ <i>z</i>)	Occ.	0.97(3)	1.021(20)
	<i>z</i>	0.9795(4)	0.9766(3)
	<i>U</i> ₁₁ = <i>U</i> ₂₂	0.0095(16)	0.0085(10)
	<i>U</i> ₃₃	0.0119(19)	0.0108(14)
O _{int} (¾ ¼ ¼)	<i>U</i> ₁₂	-0.001(2)	0.0006(15)
	Occ.	0.11	0.11
	<i>U</i> _{iso}	0.026(6)	0.037(7)
<i>R</i> _p (%)		15.5	12
<i>wR</i> _p (%)		14.2	11.2
<i>R</i> _{Bragg} (%)		2.86	3.45
<i>R</i> _{Magnetic} (%)		---	7.42

Temperature evolution of lattice parameters are obtained from synchrotron XRPD data and plotted in Fig. 5.3(a). As temperature decreases from room temperature to 5 K, *a* and *b* decreases by 0.0034 Å from 5.4633 Å to 5.4599 Å (i.e., by 0.06%) and *c* decreases by 0.0489 Å from 12.2049 Å

to 12.1559 Å (i.e., by 0.4%). Thus, the thermal expansion is highly anisotropic and much pronounced along the c axis than in the ab -plane. Similar anisotropic thermal expansion is also reported for other K_2NiF_4 nickelates [44]. Inset of **Fig. 5.3(b)** shows the temperature dependence of unit cell volume that nearly remains constant in the temperature range of 5-50 K, and then linearly increases with increasing temperature. The solid line represents a fit of the data with a quasi-harmonic Debye model¹¹⁴, which provides the contribution of anharmonic lattice vibration to the thermal expansion.

$$V(T) = V_0 + A \cdot \left(\frac{T}{\Theta_D}\right)^3 \cdot T \int_0^{\Theta_D/T} \frac{x^3}{e^x - 1} dx \quad (5.1)$$

The fitted parameters are $A = \frac{\gamma N k_B}{Y} = 0.0319$ (Å/K) and $\Theta_D = 414.54$ K where γ is the thermodynamic Grüneisen parameter, Y is the bulk modulus, k_B is the Boltzmann constant, Θ_D is the Debye temperature, and N is the number of atoms. The quasi-harmonic Debye model fits well the observed temperature dependence of the unit-cell volume in the 5-300 K temperature regime, indicating the thermal expansion to be mainly dominated by phonon contributions.

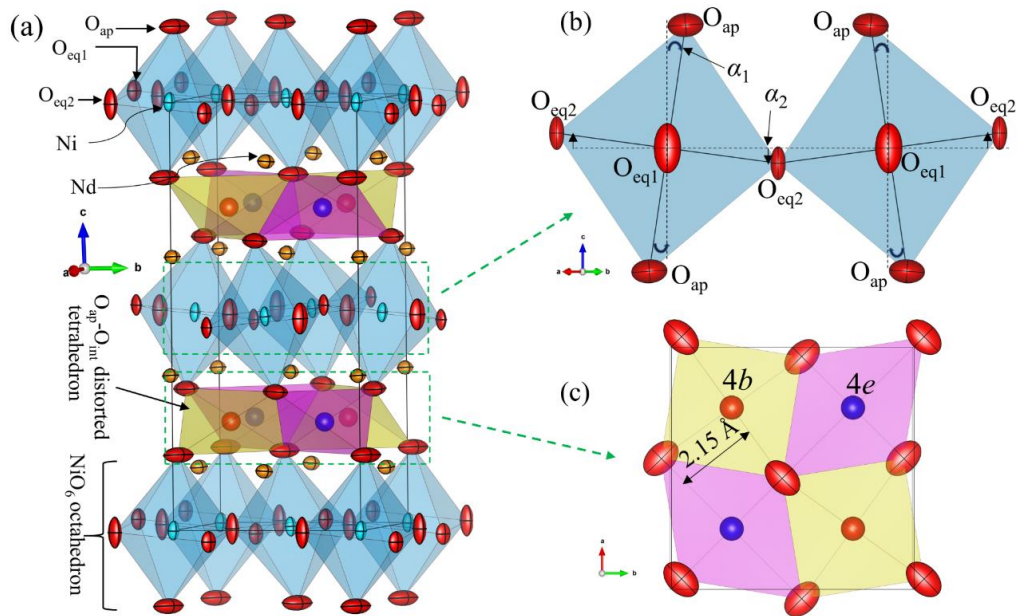


Figure 5.5 | Tetragonal crystal structure of $\text{Nd}_2\text{NiO}_{4.11}$. (a) Perspective view of the tetragonal unit cell in $P4_2/nmc$ space group, showing two distinct tetrahedral sites $4b$ ($3/4, 1/4, 1/4$) (yellow balls) and $4e$ ($1/4, 1/4, z \sim 1/4$) (pink balls) accessible for extra oxygen atoms, while only the $4b$ Wyckoff site with point symmetry $\bar{4}$ is occupied and the $4e$ tetrahedral site with point symmetry $2.mm$ being entirely empty. Note that, on average approximately $1/2$ oxygen atom is present per unit cell

i.e. only 11% of $4b$ sites are filled in Nd₂NiO_{4.11}. (b) [110]/[001] projection of NiO₆ octahedral layer at $z = 0.5$ showing specifically the tilt pattern of NiO₆ octahedron around the [110]-axis. (c) [100]/[010] projection of the two O_{int}(O_{ap})₄ tetrahedra with Wyckoff positions $4b$ and $4e$ illustrating ex- and inhaling behavior of occupied and empty tetrahedrons, respectively.

5.2. Macroscopic magnetization

DC magnetic susceptibility curves were recorded both in zero-field-cooled (ZFC) and field cooled (FC) configurations in the temperature range of 2-320 K with 1 T magnetic field. Inverse magnetic susceptibility curves are presented in **Fig. 5.6(a)**. An anomaly is observed in both curves around the magnetic ordering temperature T_N related to the long-range antiferromagnetic ordering of the Ni-sublattice. The magnetic ordering temperature T_N is found to be 53 K from $d\chi^{-1}/dT$ curve as shown in the inset of **Fig. 5.6(a)**. Thus, additional oxygen doping strongly suppresses T_N as it is reduced from 330 K in Nd₂NiO₄^{115,116} to 53 K in Nd₂NiO_{4.11}. Any evidence corresponding to the long-range magnetic ordering of the Nd-sublattice is not observed in the susceptibility data. However, a broad hump is observed with $T \sim 23$ K in the $d\chi^{-1}/dT$ curve suggesting the onset temperature related to the polarization of Nd³⁺ ions. The temperature dependence of χ^{-1} above 150 K is well represented by the following Curie-Weiss law:

$$\chi(T) = \chi_0 + \frac{C}{T - \theta} \quad (5.2)$$

From the least-square fitting, we extract $\mu_{\text{eff}} = 5.35 \mu_B$, which in complete ionic approximation leads to $\mu_{\text{eff}}(\text{Ni-site}) = 1.46 \mu_B$ taking Nd³⁺ as a free ion ($3.63 \mu_B$) in this temperature range. The reduced value of the effective magnetic moment for the Ni-site is formally due to the presence of either Ni³⁺ ($3d^7$) or Ni ions in $3d^8$ configuration that is ($3d^8\bar{L}$) where \bar{L} is an oxygen 2p hole. The Curie-Weiss temperature of $\theta = -36$ K indicates predominant antiferromagnetic exchange interactions at low temperature in Nd₂NiO_{4.11}. The temperature independent term, χ_0 is found to be 1.3×10^{-3} emu/mol. The temperature independent contribution can be due to a combination of Pauli paramagnetism, Van Vleck paramagnetism, and/or core diamagnetism. As our sample is non-metallic, the Pauli paramagnetic contribution is expected to be very small and the core diamagnetic contribution is estimated to be $\sim -0.1 \times 10^{-3}$ emu. mol⁻¹. Therefore, the temperature independent term is probably dominated by the Van Vleck contribution due to crystal field contribution of Nd³⁺ ions.

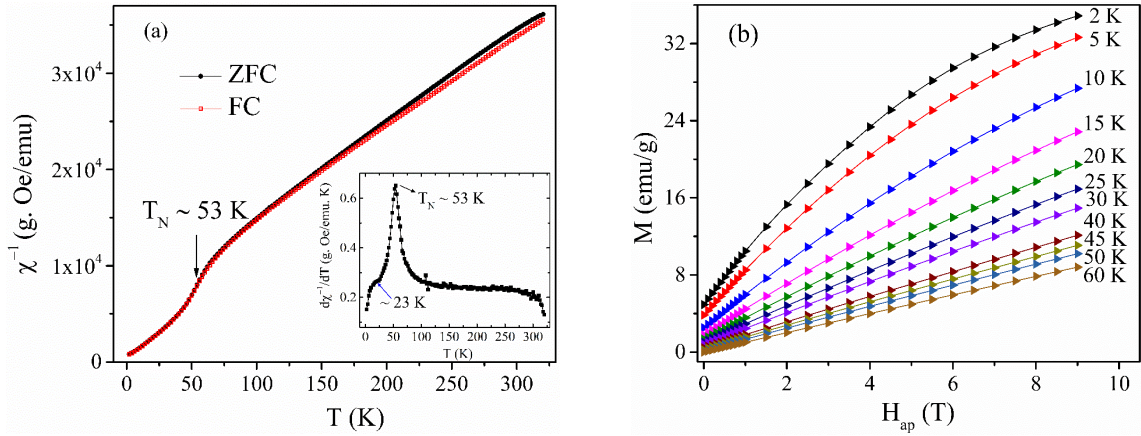


Figure 5.6 | Macroscopic magnetization data of $\text{Nd}_2\text{NiO}_{4.11}$ as a function of temperature and field. (a) Inverse dc magnetic susceptibility curves measured as a function of temperature for the in zero-field cooled (ZFC, black circles) and field cooled (FC, red squares) configurations. The magnetic ordering temperature of the Ni-sublattice is marked with an arrow around 53 K. The inset shows the first order temperature derivative of the inverse magnetic susceptibility data illustrating the magnetic ordering of Ni-sublattice with $T_N \sim 53$ K and the onset temperature of the magnetic contribution of Nd^{3+} ions. (b) Isothermal magnetization curves recorded as a function of applied magnetic field between 0-9 Tesla below 60 K. Note the appearance of a small ferromagnetic component in the magnetization curves below 50 K.

Fig. 5.6(b) shows several isothermal magnetization curves measured between 2 K and 60 K as a function of magnetic field between 0-9 T. In the high-temperature-range ($T \geq 60$ K), magnetization curves have a linear field dependence with no remanence at all, as expected for the paramagnetic region. However, a small spontaneous magnetization starts to appear around 50 K, showing typical features of a weak ferromagnet. No signature of a magnetic field induced magnetic transition was observed at low temperature as found in the undoped sample¹¹⁵. It is worth noting that the M - H curves show no indication of magnetic saturation even at 2 K with 9 T magnetic field and become nonlinear below 10 K possibly due to magnetic contribution of Nd^{3+} . The isothermal magnetization curves (M - H) can be represented by the following equation¹¹⁵:

$$M(H_a, T) = M_0(T) + \chi_{dif}(T)H_a \quad (5.3)$$

Where $\chi_{dif}(T)$ is the high-field differential susceptibility, H_a the applied magnetic field and $M_0(T)$ the extrapolated spontaneous magnetization. Linear fits were made in the 0-3 T region so that the extrapolated spontaneous magnetization is close to the remanence at each temperature. The temperature dependence of $M_0(T)$ is shown in **Fig. 5.7(a)**. $M_0(T)$ starts to depart from zero just below 50 K and smoothly increases down to 25 K followed by a strong increase down to 2 K. Similar behavior of $M_0(T)$ in undoped Nd_2NiO_4 was described by the evolution of the weak

ferromagnetic component of the Ni²⁺ magnetic moments along the *c*-axis¹¹⁵. Furthermore, this weak ferromagnetic component polarizes the Nd³⁺ magnetic moments (through the Nd-Ni interactions), which contribute to the observed increase of the spontaneous magnetization. The full ferromagnetic hysteresis curve obtained at 2 K is shown in the inset of **Fig. 5.7(a)**, where it is evident that the remanence magnetization (~ 4.94 emu/g) and coercive field (~ 0.3 T) are strongly decreased with oxygen doping. As for undoped Nd₂NiO₄¹¹⁵, the remanence is ~ 15 emu/g and the coercive field is higher than 1 T at 4.5 K. The reduction of the coercive field could be associated with the decrease in magnetocrystalline anisotropy upon additional oxygen doping. The internal field acting on the Nd³⁺ ions due to Ni²⁺ ferromagnetic component is evaluated using the **Eq. (5.4)**¹¹⁵

$$M^0(T) = M_{Ni}^0 + \chi_{dif}(T)H_i^0 \quad (5.4)$$

Where H_i^0 is the internal field induced by the weak ferromagnetic component of Ni²⁺ magnetic moments and M_{Ni}^0 is the ferromagnetic component of magnetization from the Ni-sublattice. This relation is depicted in **Fig. 5.7(b)**, where a linear dependence between $M(T)$ and $\chi_{dif}(T)$ in the temperature range from $T = 40$ K down to 10 K is evident. The linear fit gives $M_{Ni}^0 = -0.08(4) \mu_B/f. u.$ and $H_i^0 = 1.12(8)$ T. In the following section, with a group theoretical analysis, we show that the weak ferromagnetic component of magnetization (M_{Ni}^0) points towards the crystallographic *c*-axis. Therefore, the internal magnetic field H_i^0 acting on the Nd³⁺ ions induced by this ferromagnetic component also points towards the crystallographic *c*-axis. The negative sign of M_{Ni}^0 indicates that the Nd-Ni interaction is antiferromagnetic. A similar scenario is also observed in undoped Nd₂NiO_{4.0} ($M_{Ni}^0 = -0.36 \mu_B/f. u.$ and $H_i^0 = 5.26$ T in Nd₂NiO_{4.0})¹¹⁵, although these values are strongly reduced with oxygen doping. To verify the direction dependence of the weak ferromagnetic component, magnetization measurements were performed on a single crystal of Nd₂NiO_{4.14}, which was prepared after reduction at high temperature separately. The inverse magnetic susceptibility data recorded in ZFC configuration are plotted in **Fig 5.8** for [001] and [110] directions. It is evident that the magnetic easy axis of the crystal being the [110] direction in the entire temperature range indicating favored orientation of the spins in the *ab*-plane. This conjecture is further established in the next section with magnetic structure analysis from neutron diffraction data. Furthermore, the magnetic ordering temperature of Ni-sublattice is increased to 56 K in the crystal and the sharp discontinuity is only observed in the inverse susceptibility data parallel to the *c*-axis. However, such a peak is not absent in the susceptibility data of *ab*-plane. This confirms two scenarios. First, the ferromagnetic component is parallel to the *c*-axis and second, the macroscopic magnetization is strongly sensitive to the weak ferromagnetic component appearing from the spin canting due to DM interactions in the LTT structure. Strong reduction of the ferromagnetic component in the oxygen-doped sample can be

attributed to the decrease of the DM interactions between in plane nearest neighbor Ni^{2+} ions. To a first approximation, the spin Hamiltonian can be described by¹¹⁵

$$\mathcal{H} = J_{\text{Ni-Ni}} \sum_{\text{NN}} \mathbf{S}_i^{\text{Ni}} \cdot \mathbf{S}_j^{\text{Ni}} + J'_{\text{Ni-Ni}} \sum_{\text{NNN}} \mathbf{S}_i^{\text{Ni}} \cdot \mathbf{S}_j^{\text{Ni}} + \mathbf{D}_{\text{Ni-Ni}} \sum_{\text{NN}} \mathbf{S}_i^{\text{Ni}} \times \mathbf{S}_j^{\text{Ni}} + J_{\text{Nd-Ni}} \sum_{\text{NN}} \mathbf{S}_i^{\text{Nd}} \cdot \mathbf{S}_j^{\text{Ni}} \quad (5.5)$$

where all the sums are extended to nearest neighbours, except for the second one which is extended to next nearest neighbours. $J_{\text{Ni-Ni}}$ and $\mathbf{D}_{\text{Ni-Ni}} [D_x, D_y, 0]$ stands for the in-plane symmetric and antisymmetric DM Ni-Ni superexchange interactions, respectively. $J'_{\text{Ni-Ni}}$ stands for the magnetic interactions between two adjacent NiO_2 planes along the c -axis, while $J_{\text{Nd-Ni}}$ is the isotropic symmetric antiferromagnetic Nd-Ni superexchange coupling constant (*cf.* Fig. 5.9(b)). In Eq. (5.5), the magnetocrystalline anisotropy and Nd-Nd superexchange terms are ignored for simplification. In a first order approximation, the magnitude of the antisymmetric exchange interaction is directly proportional to the displacement of $\text{O}_{\text{eq}2}$ atoms from the basal plane, i.e. largely depends on the angle α_2 as shown in Fig. 5.5(b) and further outlined in Fig. 5.9(c). Rietveld refinements of the NPD data of $\text{Nd}_2\text{NiO}_{4.11}$ revealed that α_2 is decreased by 2° at 2 K compared to the $\text{Nd}_2\text{NiO}_{4.0}$, which is consistent with the observed decrease in the magnitude of the ferromagnetic component. Therefore, our NPD and magnetization data reveals a strong modification in the DM interactions, allowing a spin canting, through the subtle change in the tilting pattern of NiO_6 octahedra of LTT structure with oxygen doping in $\text{Ln}_2\text{NiO}_{4+\delta}$ compounds.

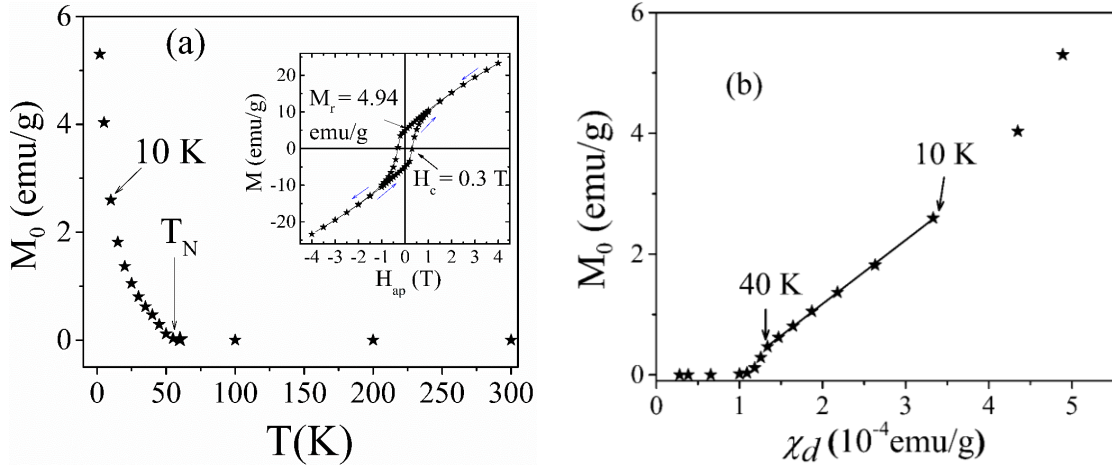


Figure 5.7 | Extracted parameters from magnetization data of $\text{Nd}_2\text{NiO}_{4.11}$. (a) Temperature dependence of $M_0(T)$, deduced from isothermal magnetization data. Néel temperature T_N is marked with an arrow. The inset presents the ferromagnetic hysteresis loop recorded at 2 K. (b) $M_0(T)$ vs χ_d curve as discussed in the text. A linear fit is made between 10-40 K to extract the ferromagnetic component M_{Ni}^0 and the internal magnetic field H_i^0 .

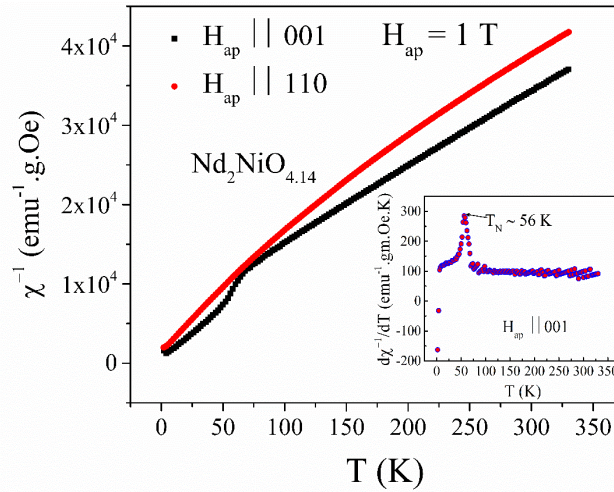


Figure 5.8 | Macroscopic magnetic susceptibility measured for $\text{Nd}_2\text{NiO}_{4.14}$ single crystal. Inverse magnetic susceptibility curves recorded in ZFC configuration with applied magnetic field parallel to the c -axis and [110] direction in a crystal of $\text{Nd}_2\text{NiO}_{4.14}$. The inset shows the first order derivative plot illustrating the magnetic ordering temperature.

5.3. Magnetic structure

Temperature dependent NPD data reveals the appearance of commensurate superstructure reflections below 50 K. These reflections can be indexed with a propagation vector $\mathbf{k} = (100)$ with respect to the tetragonal chemical unit cell. These reflections are related to the long-range magnetic ordering of Ni-sublattice. **Fig. 5.9(a)** shows the variation of the integrated intensity of (101) magnetic reflection with temperature. The (101) magnetic reflection is predominantly related to the contributions of Ni-magnetic moments. Therefore, the temperature evolution of (101) magnetic reflection confirms the magnetic ordering temperature of the Ni-sublattice around 50 K, in agreement with our dc magnetic susceptibility data. The magnetic ordering of the Nd-sublattice below 10 K is confirmed from the temperature evolution of NPD patterns. The (103) magnetic reflection mainly arises from the magnetic ordering of the Nd sublattice. We note that the (103) magnetic reflection is overlapped by the (112) nuclear Bragg peak as shown in the inset of **Fig. 5.10**. However, the nuclear structure factor of the (112) reflection is close to zero, and any structural transition at low temperature is excluded from the SXRPD data. Therefore, the sharp increase in the intensity of the (103) reflection between 2 and 10 K in the NPD data, as presented in the inset of Fig. 2(b), clearly suggests the magnetic ordering of the Nd-sublattice. Another indication of Nd^{3+} ordering can be inferred from the substantial increase in intensities of magnetic reflections at higher Q ($= 4\pi\sin\theta/\lambda \sim 2.51 \text{ \AA}^{-1}$) where the magnetic form factor of Ni^{2+} is low. Additional incommensurate superstructure reflections are also observed in the NPD data below 30 K. Potential origin of these incommensurate reflections are discussed in the next section.

We now discuss the commensurate magnetic structure of Nd₂NiO_{4.11}. The possible magnetic structures compatible with the $P4_2/ncm$ space group allowed by the (100) propagation vector are obtained by applying representation theory using the program *BasIreps* included in the *FullProf suite* program. The results are presented in the **Appendix B**. After checking all of the possible magnetic modes obtained with representation analysis, the ferromagnetic component allowed for Ni or Nd sites is only valid in the one-dimensional Γ_7 magnetic mode, corresponding to the Shubnikov space group $P4_2/nc'm'$.

The neutron diffraction pattern collected at 2 K on DMC was used to determine the commensurate magnetic structure. The NPD data was refined using the Γ_7 magnetic model combining with LTT structural model. The observed and calculated diffraction profiles are presented in **Fig. 5.10(a)** and the resulting magnetic structure is visualized in **Fig. 5.9(b)**. Refined magnetic parameters are listed in **table 5.1**. In the Γ_7 magnetic mode, the spin direction in the basal plane coincides with the [110] tilt axis of the NiO₆ octahedron of the LTT phase. Ni²⁺ and Nd³⁺ moments are slightly canted away from the basal plane towards the *c*-axis to produce a net effective magnetic moment. However, because of its small value, it could not be refined with our NPD data. Its existence ($\sim 0.08 \mu_B/\text{f. u}$) was, however, unambiguously determined by means of isothermal magnetization measurements as discussed in the previous section. Refined ordered magnetic moments of Ni and Nd sites are 1.14(8) μ_B and 1.63(5) μ_B at 2 K, respectively. The refined magnetic moments of the Ni²⁺ and Nd³⁺ ions are respectively 28% and 50% smaller than the values reported for the stoichiometric compound (ordered magnetic moments of the Ni²⁺ is 1.59 μ_B and of the Nd³⁺ is 3.2 μ_B at 1.5 K)¹¹². Please note that both, Ni²⁺ and Nd³⁺ ions are far from magnetic saturation even at 2 K in Nd₂NiO_{4.11}, as visible with the integrated intensity of (101) magnetic peak in **Fig. 5.9(a)**. A possible explanation of the reduced magnetic moment for the Ni-site could be deduced by considering the location of injected holes in the magnetic lattice due to oxygen doping. If the holes are Ni-site centered (that is Ni³⁺ with 3d⁷ electronic configuration), as in the case of site-centered stripes in La₂NiO_{4+δ}^{35,63}, the presence of Ni³⁺ ions will reduce the saturation magnetic moment of the Ni-site. However, if the holes are bond centered (that is Ni ions with electronic configuration (3d⁸ \underline{L})), i.e. occupying one of the equatorial oxygen site, as is the case of bond-centered stripes in La₂NiO_{4+δ}³⁵, the excess holes located at the oxygen sites cause the ferromagnetic coupling between the neighboring Ni²⁺ spins, which are in competition with the normal antiferromagnetic superexchange interaction. The resulting frustration will also reduce the ordered magnetic moment of the Ni-site. In contrast, the reduction of the Nd³⁺ magnetic moment is mainly due to changes in the crystalline electric field on the rare-earth site, because of double negatively charged O_{int} ions in tetrahedral sites. These interstitial oxygen atoms highly perturb the crystal-field levels of Nd³⁺ ions. A qualitative estimation of this effect is proposed in **Appendix E** from a simple point charge calculations revealing important changes in

the crystal-field levels of the J multiplet of the Nd^{3+} . Such a change strongly affects the saturated value of the Nd^{3+} magnetic moment.

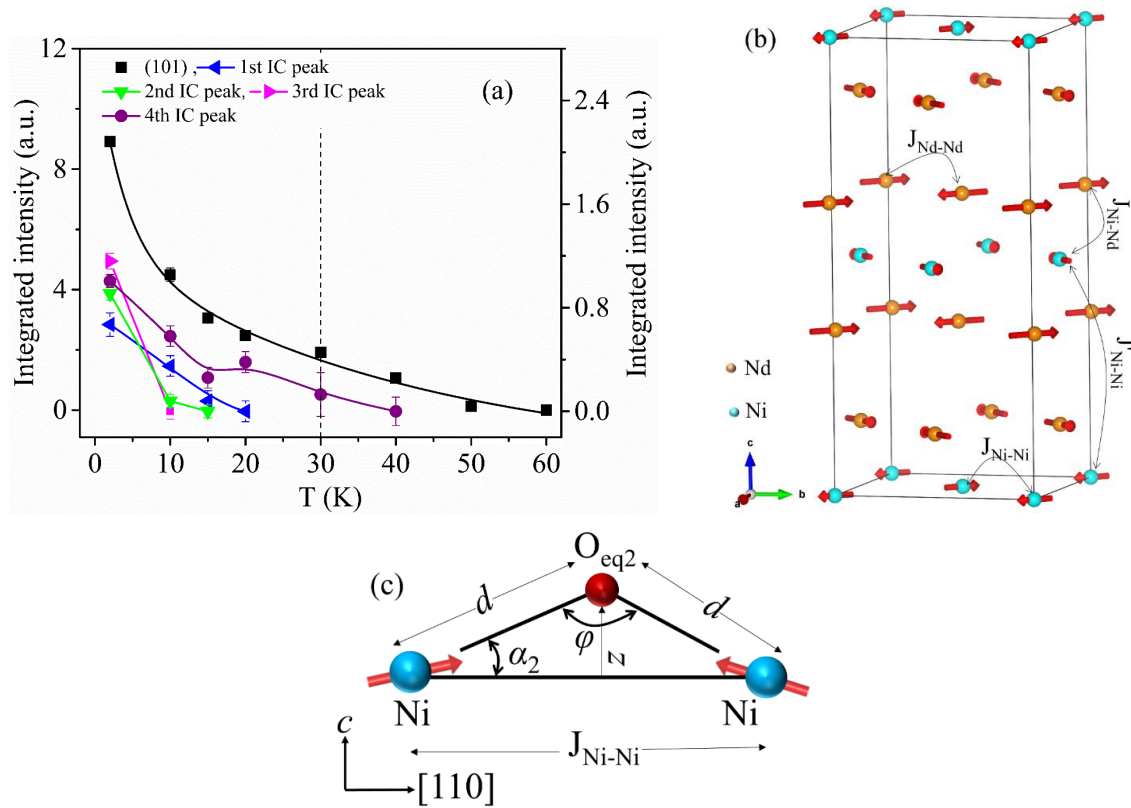


Figure 5.9 | Magnetic parameters obtained for $\text{Nd}_2\text{NiO}_{4.11}$ with powder neutron diffraction data. (a) Temperature evolution of integrated intensities of the (101) magnetic reflection (left side scale) and four intense incommensurate reflections (right side scale, IC1 to IC4) are plotted for $\text{Nd}_2\text{NiO}_{4.11}$ obtained with the NPD data. The vertical dashed line shows the temperature at which incommensurate reflections start to appear. (b) Commensurate antiferromagnetic structure of $\text{Nd}_2\text{NiO}_{4.11}$ compound in $P4_2/nc'm'$ Shubnikov space group. Only the Ni and Nd magnetic sites are shown. Ferromagnetic components of Ni and Nd moments along the c -axis are not shown for simplification. The in-plane antiferromagnetic superexchange $J_{\text{Ni-Ni}}$ occurs through Ni-O_{eq}-Ni bonds. The out of plane nearest neighbor Ni-Ni superexchange interaction $J_{\text{Ni-Ni}}^{\prime}$ occurs through bridging Nd, O_{ap} and O_{int} atoms. The $J_{\text{Ni-Nd}}$ superexchange interaction goes through the apical site. (c) Breaking of the rotational symmetry regarding the Ni-Ni axis due to the displacement of O_{eq2} atoms from the basal plane, which allows the DM interaction. Consequently, a weak ferromagnetic component appears parallel to the c -axis in the LTT phase. The superexchange angle (ϕ) and distance (d) are also shown.

In this context, it is important to point the influence of the observed structural changes due to the oxygen over-stoichiometry on magnetic superexchange interaction parameters i.e. $J_{\text{Ni-Ni}}$; the intra-plane symmetric antiferromagnetic Ni-Ni superexchange interaction and $J_{\text{Ni-Ni}}^{\prime}$; the

interplane Ni-Ni superexchange interaction (*cf.* **Fig. 5.9(b)**). The $J_{\text{Ni-Ni}}$ interaction predominantly depends on two parameters: the superexchange angle (ϕ) and the superexchange distance (d) (see **Fig. 5.9(c)**). The tilting angle of NiO₆ octahedron decreases with oxygen doping, therefore, ϕ changes from 158° to 163° and $d_{\text{Ni-O}_{\text{eq}2}}$ changes from 1.9668(6) Å to 1.9514(7) Å at 2 K. With these values, however, a relative increase in $J_{\text{Ni-Ni}}$ of 6% is expected on switching from Nd₂NiO_{4.0} to Nd₂NiO_{4.11}. 3D magnetic order appears mainly because of the interplane magnetic interaction $J'_{\text{Ni-Ni}}$, which essentially depends on the Ni-O_{ap} bond length and the distance between two nearest interplane apical oxygen atoms (O_{ap}-O_{ap}) through which interplane superexchange occurs. The expansion of the rock salt (Nd-O_{ap}) layer and the change in the Ni-O_{ap} bond length (only increased by 0.002 Å at 2 K) is not significant due to the incorporation of excess oxygen atoms. Therefore, only a negligible change in the $J'_{\text{Ni-Ni}}$ parameter is expected on switching from Nd₂NiO₄ to Nd₂NiO_{4.11}. It is evident that structural changes associated with oxygen doping cannot explain the observed reduction in 3D magnetic properties completely. Therefore, with our NPD study, we reveal that antiferromagnetic $J_{\text{Ni-Ni}}$ and $J'_{\text{Ni-Ni}}$ interactions are mainly influenced by the incorporated disorder in the magnetic lattice due to injected holes and not directly related to the interstitial oxygen atoms themselves.

In addition to the commensurate magnetic reflections, additional weak incommensurate reflections are observed at $T \leq 30$ K. In **Fig. 5.9(a)**, the integrated intensities of four intense incommensurate reflections (marked in the inset of **Fig. 5.10(b)**) as a function of temperature are outlined, as observed from the NPD data. The second and third incommensurate magnetic peaks appear below, whereas the first and fourth magnetic reflection appears above 10 K. However, the ordering temperature of excess oxygen atoms in these compounds had usually been found to be close to 300 K. The positions of these incommensurate reflections could, however, not be related to wave vectors associated to stripe magnetic order as reported for oxygen intercalated La₂NiO_{4+δ} compounds³². Another potential origin of these incommensurate reflections could arise from a 1D or 3D ordering of excess oxygen atoms. These incommensurate reflections could also be related with the long-range magnetic ordering of the Ni²⁺, Ni³⁺ and Nd³⁺ spins. A more dedicated single crystal neutron diffraction study has been performed to uncover the incommensurate phase detected in oxygen over-stoichiometric Nd₂NiO_{4.11}.

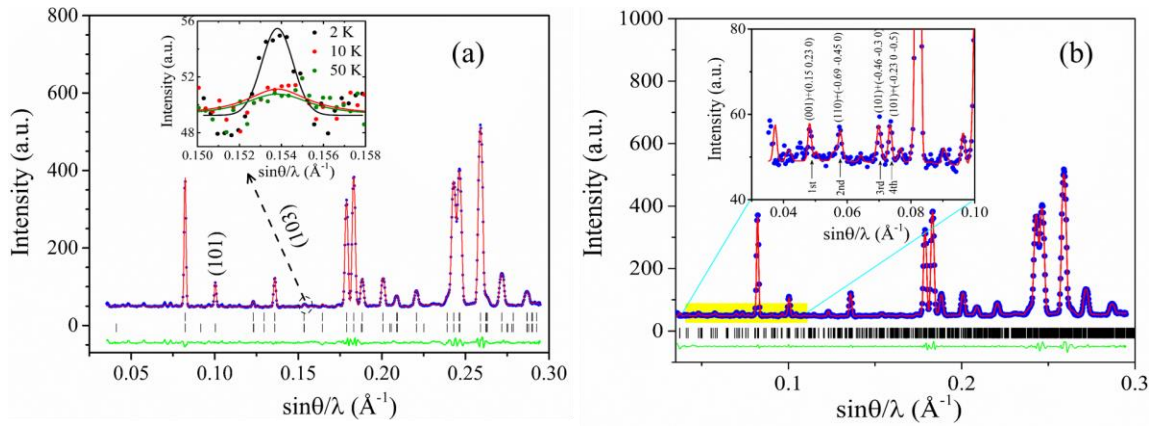


Figure 5.10 | Powder neutron diffraction patterns of $\text{Nd}_2\text{NiO}_{4.11}$ collected at 2 K. (a) Observed (blue circles), calculated (red line) and difference (green continuous line) patterns resulting from the Rietveld analysis of NPD data. Upper and lower row of ticks show the positions of structural and magnetic reflections, respectively. (b) A Le Bail fit of the 2 K NPD data with the q -vectors obtained from reciprocal space plane mapping illustrating the excess oxygen ordering. A magnified portion of the diffraction pattern is shown in the inset displaying the quality of the fit and validity of the q -vectors obtained from the plane mapping on the single crystal.

5.4. Excess oxygen ordering

To study the incommensurate phase and to perform neutron diffraction experiments, a large single crystal with mass 200 mg was prepared by annealing the as-grown crystal in dynamic vacuum at 1073 K for 6 h. The overall oxygen stoichiometry in the single crystal was found to be 4.09(1) with least-square refinement of the neutron diffraction data as discussed in the **section 5.5**. Thus, this single crystal is different from the crystal on which magnetization measurements were performed. The magnetic ordering temperature of the Ni-sublattice is ~ 48 K as obtained from the integrated intensities of (104) and (101) reflections as shown in **Fig. 5.11(a)** and **(b)**, respectively. The commensurate magnetic structure with propagation vector (100) was solved with least-square refinement from a set of integrated intensities of Bragg reflections recorded at 2 K. The refined magnetic structure is identical to the magnetic structure reported with powder diffraction data shown in **Fig. 5.9(b)**. The total magnetic moments for the Ni and Nd-sites are found to be 1.02(5) μ_B and 1.08(2) μ_B , respectively.

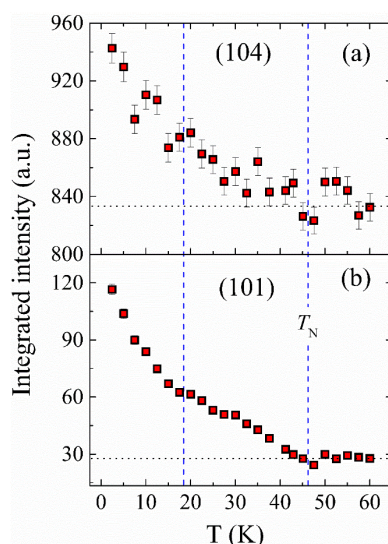


Figure 5.11 | Integrated intensities of (104) and (101) magnetic reflections as a function temperature. Data were recorded with neutron diffraction measurements on $\text{Nd}_2\text{NiO}_{4.09}$ single crystal. The magnetic ordering temperature of the Ni-sublattice is identified around 48 K while the polarization of Nd-sublattice starts to occur around 20 K.

To investigate the origin of the incommensurate phase, $(hk0)$ and $(h0l)$ reciprocal plane mappings were performed at 300 K, 55 K (just above the magnetic ordering) and at 2 K. In addition to the main structural Bragg reflections consistent with the $P4_2/ncm$ space group, additional superstructure reflections are found in the diffraction pattern at all the investigated temperatures as displayed in **Fig. 5.12-5.15**. These reflections are presumably due to long-range ordering of excess oxygens in the interstitial sites. Their intensities are significant and reach up to 2% with respect to the main structural Bragg spots signifying strong structural modulations even at 300 K. Thus, the room temperature single crystal data provides important insights on structural modulation, which has not been realized with powder diffraction at 300 K. In addition, single crystal data uncovers that excess oxygen atoms do not randomly occupy the $4b$ sites but a special ordering scheme exists in the LTT phase. In addition, impurity peaks from the NiO phase are also observed in all diffraction patterns (*cf.* **Fig. 5.12(a)**).

Furthermore, extra commensurate reflections such as (210), (105) and (103), which are extinct in the $P4_2/ncm$ space group, are also evidenced in all diffraction patterns. Presence of these reflections at 300 K indicates the fact that the true structural symmetry is possibly lower than $P4_2/ncm$. In this context, it is worth noting that commensurate reflections originating from charge ordering are also expected at these positions. However, in the presence of commensurate charge ordering, commensurate magnetic Bragg peaks at $(h \sim 0.5, 0, 0)$ positions are also expected, which are not observed in the diffraction pattern. Therefore, it is assumed that these reflections are most probably due to a lower structural symmetry. Furthermore, this assumption

is required as incommensurate oxygen superstructure reflections are also evidenced in the diffraction pattern related to these extinct Bragg peaks as we discuss next. No structural phase separation is observed in the single crystal in the investigated temperature range as confirmed by the ω -scans of nuclear Bragg peaks with high-resolution neutron diffraction measurements.

The experimental ($hk0$) plane at 2 K is presented in **Fig. 5.12(a)**. Incommensurate reflections up to fourth order are found in the diffraction pattern as shown by small arrows in the pattern. However, strong intensity modulation of these reflections made it difficult to identify the ordering vector and the order up to which they are present. To simplify this problem, a simulation program OxyPy was used to calculate such reciprocal planes, in particular the positions of different harmonics up to a certain order, with experimentally observed modulation vector(s). From ($hk0$) plane mapping, a modulation vector $q = 0.23a^* + 0.23b^*$ is immediately identified. A simple symmetry analysis (**Appendix B**) with the program *BasIreps* shows the presence of possible eight modulation vectors (each domain is represented by one of those eight modulation vectors) which are related by the symmetry of the underlying space group but structurally inequivalent. An example of such calculated map is shown in **Fig. 5.12(b)** with those eight modulation vectors: $q = \pm 0.15a^* \pm 0.23b^*$ and $\pm 0.23a^* \pm 0.15b^*$. An excellent agreement of the positions is found between the experimental and calculated maps at 2 K with superstructure reflections present up to fourth order. Presence of both sets of modulation vectors in the experimental data also confirms the tetragonal nature of the crystal system. All eight modulation vectors are present in the experimental data measured at all the temperatures. A magnified section of the ($hk0$) reciprocal plane is presented in **Fig. 5.13** for 2 K and 300 K data together with the calculated map. Presence of all eight modulation vectors are clearly evidenced at 2 K data. However, strong decrease in the intensities of these superstructure reflections is observed for 300 K data. An important finding of the simulation is that strong overlaps of intensities of different harmonics related to different Bragg peaks are realized only in the calculated map, which are difficult to be identified in the experimental data. Moreover, superstructure peaks related to extinct Bragg peaks like (210) are observed in the diffraction patterns. This also indicates that the structural symmetry is lower than $P4_2/ncm$.

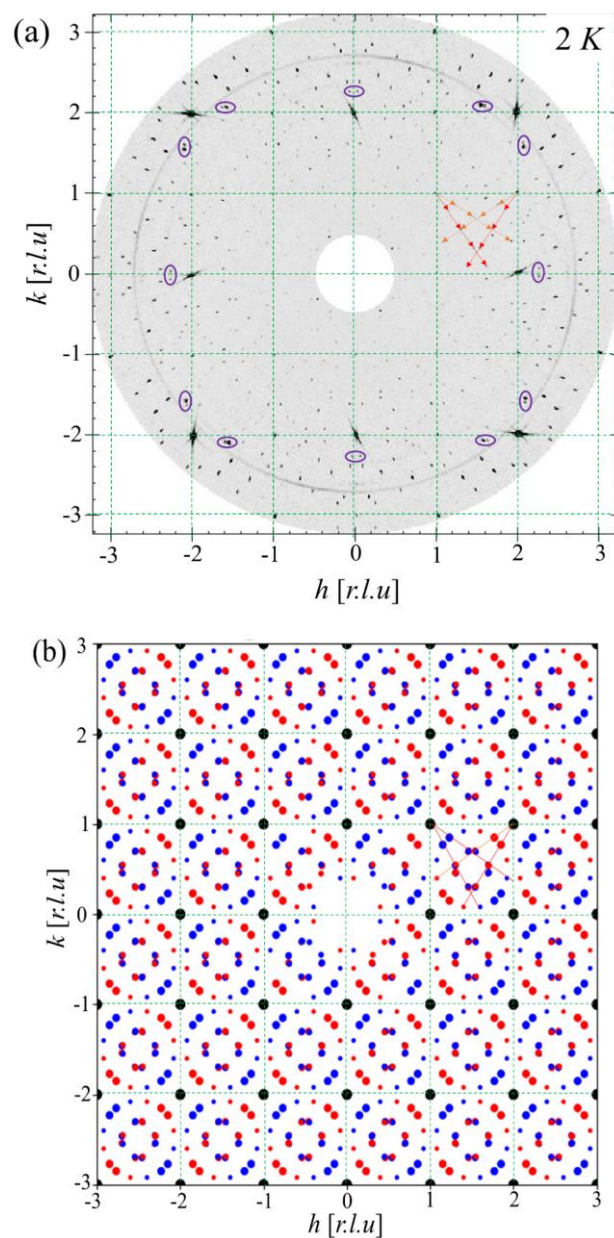


Figure 5.12 | Reciprocal space plane mapping of $\text{Nd}_2\text{NiO}_{4.11}$. (a) Experimentally measured ($hk0$) reciprocal plane with single crystal neutron diffraction on DMC ($\lambda = 2.4586(3)$ Å) at SINQ, PSI. Impurity NiO peaks are shown with circles. P-type lattice is shown with green dashed lines. Oxygen superstructure peaks up to 4th order are observed in the diffraction pattern as shown by small arrows. (b) Simulated ($hk0$) reciprocal plane corresponding to the wave vectors $q = \pm 0.15a^* \pm 0.23b^*$ in tetragonal $P4_2/ncm$ structure. Red and blue circles are used to define two domains in the tetragonal structure by exchanging a and b lattice parameters. The intensities of the superstructure peaks have been modeled arbitrarily. The size of the symbols decreases with increasing order number.

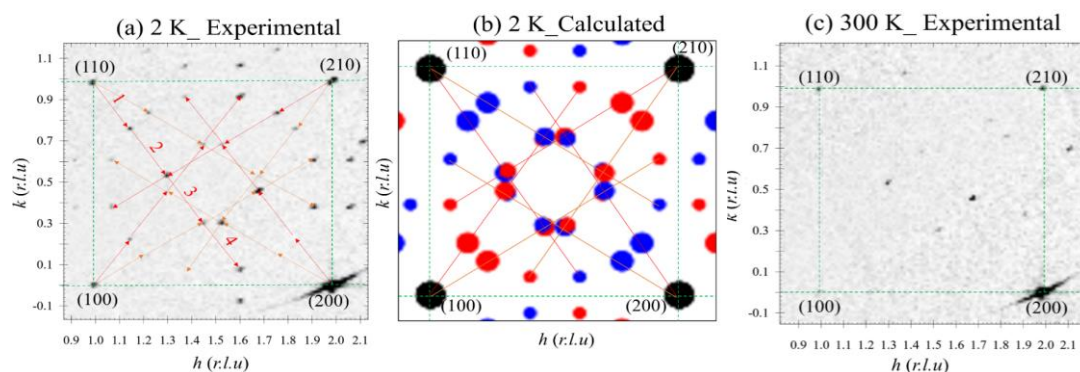


Figure 5.13 | Magnified section of the $(hk0)$ reciprocal plane. (a) Experimental data at 2 K illustrating the presence of oxygen superstructure peaks up to 4th order, (b) the simulated pattern with the observed wave vectors and (c) experimental pattern at 300 K.

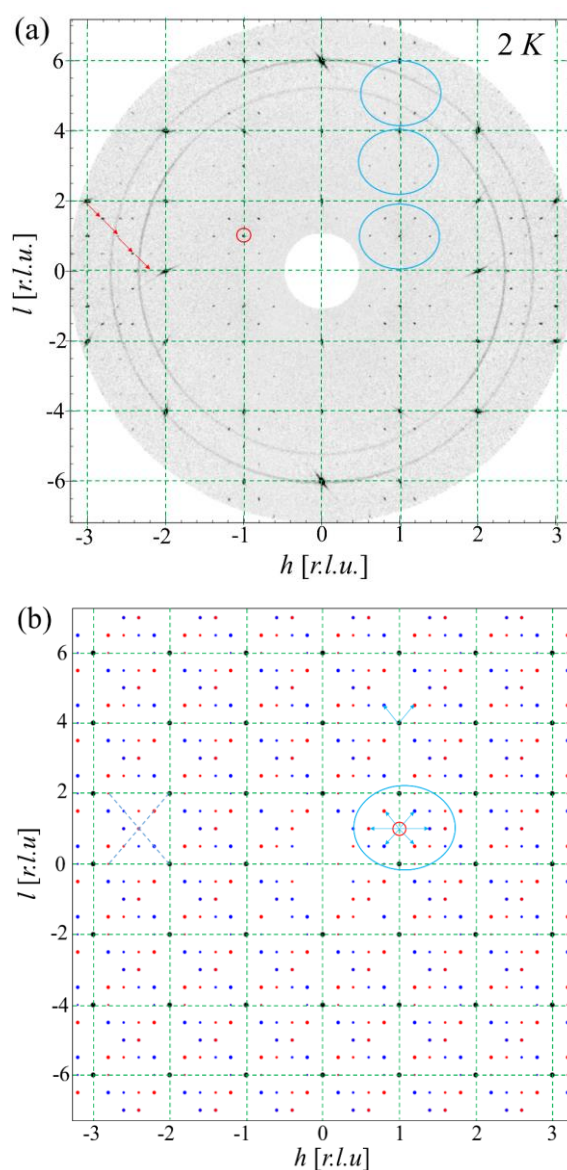


Figure 5.14 | $(h0l)$ reciprocal plane mapping of $\text{Nd}_2\text{NiO}_{4.11}$. (a) Experimentally measured with single crystal neutron diffraction on DMC ($\lambda = 2.4586(3)$ Å) at SINQ, PSI. Superstructure peaks up to 4th order are observed in the diffraction pattern as shown by small arrows. (b) Simulated $(h0l)$

reciprocal plane corresponding with modulation vectors $q = \pm 0.2a^* \pm 0.5c^*$ in tetragonal $P4_2/ncm$ structure. The intensities of the superstructure peaks have been modeled arbitrarily. The size of the symbols decreases with increasing order number.

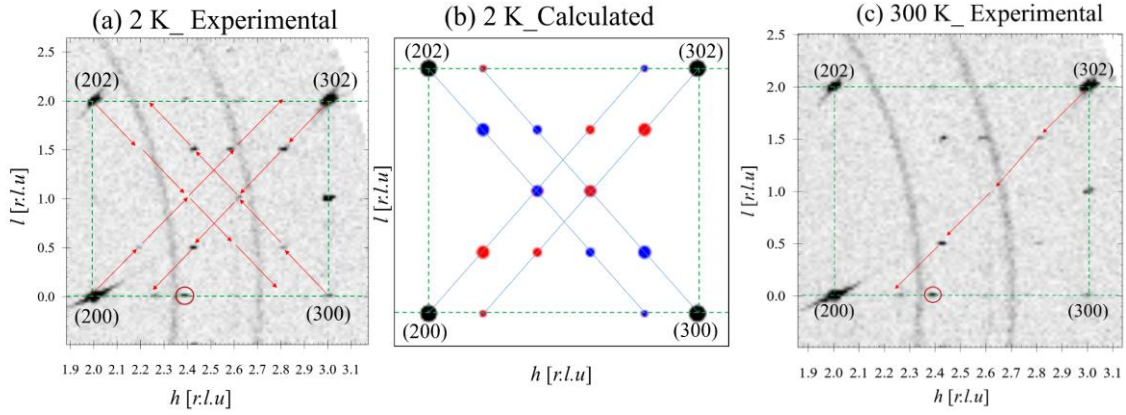


Figure 5.15 | Magnified section of the $(h0l)$ reciprocal plane. (a) Experimental data at 2 K displaying the presence of oxygen superstructure peaks up to 4th order at 2 K, (b) the simulated pattern with $q = \pm 0.2a^* \pm 0.5c^*$ and (c) experimental pattern at 300 K.

The reciprocal $(h0l)$ plane measured at 2 K is presented in **Fig. 5.14(a)**. It is found that superstructure peaks are arranged in such a way that it forms a hexagon around commensurate magnetic peaks of $(h0l)$ type with $l = \text{odd}$. Such arrangement of superstructure reflections could indicate the magnetic origin for these reflections. However, few of these reflections are already present at room temperature as shown in **Fig. 5.15 (c)**. From this observation, it is assumed that they are likely to be related with excess oxygen ordering. These superstructure peaks can be indexed with modulation vectors $q = \pm 0.2a^* \pm 0.5c^*$ (cf. **Appendix B**) as shown in **Fig. 5.15(a)** and **(c)**. Superstructure peaks up to fourth order exists in the diffraction pattern at both 2 K and 300 K. A simulated pattern with these modulation vectors up to fourth order is shown in **Fig. 5.14(b)**. A very good match is observed between the simulated and experimental patterns and most importantly, the hexagonal feature is retrieved with such simulation. However, with such ordering, hexagonal features are expected around each $(h0l)$ type reflection with $l = \text{odd}$ which of course are not observed in the experimental data. Nice agreement is only obtained for few selected zones as shown by green circles. Presence of these four modulation vectors in the $(h0l)$ plane also confirms the tetragonal symmetry of the crystal.

Specific cuts in reciprocal q -space are obtained at different temperatures through these superlattice reflections from the single crystal data and presented in **Fig. 5.16(a)** and **(b)**. It is evident that intensities of specific oxygen superstructure reflections like the first harmonic related to (-302) and (-110) Bragg reflections are strongly enhanced below the magnetic ordering

temperature. This is a hint of an improved correlation between the interstitials by the occurrence of the magnetic ordering. Excess oxygens are possibly still mobile even at a low temperature (~50 K) and the correlation between the interstitials are weak. As the superexchange interaction between two neighboring NiO₂ layers occurs through the interstitial sites (*cf.* **Fig. 5.9(b)**) and therefore, 3D commensurate magnetic ordering possibly freezes interstitials to their average positions, which consequently increases the correlation among them. This result also hints at strong spin-lattice coupling in nickelates.

Modulation vectors obtained from reciprocal plane mappings on the single crystal are used to fit the powder diffraction pattern obtained at 2 K for Nd₂NiO_{4.11}. Positions of most superstructure peaks, which are observed only below T_N are well explained by these modulation vectors as presented in **Fig. 5.10(b)**. Therefore, the presence of superlattice peaks in the powder data are also likely due to excess oxygen ordering and not attributable to the magnetic ordering. In this regard, it should be emphasized that the single crystal and powder data cannot exclude the possibility of any magnetic contribution on those specific superstructure peaks, which are enhanced below the magnetic ordering temperature. Therefore, polarized neutron diffraction and x-ray diffraction experiments on the single crystal must be conducted to recognize the true origin of these superstructure reflections by separating magnetic and nuclear contributions.

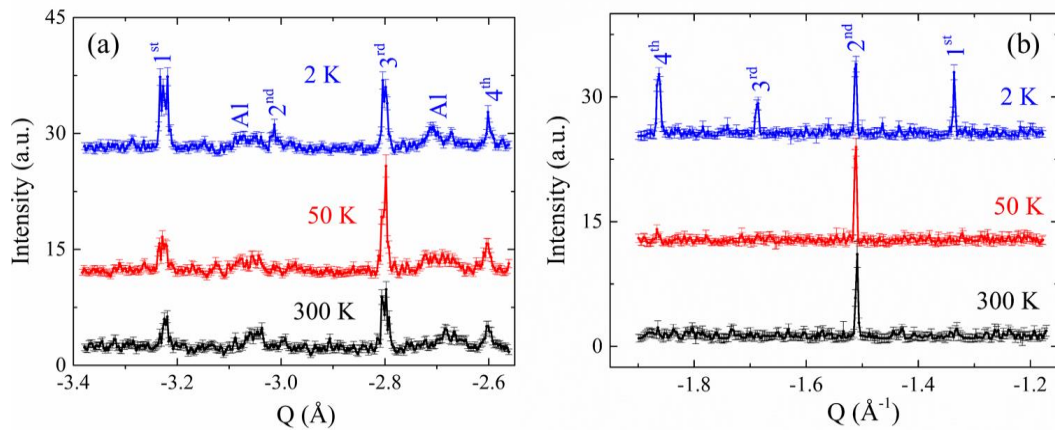


Figure 5.16 | Cuts through the oxygen superstructure peaks in $(hk0)$ and $(h0l)$ planes of Nd₂NiO_{4.09} as shown in Fig. 5.13 and Fig. 5.15. Evidence of oxygen superstructure peaks up to fourth order related to (a) (-302) and (b) (-110) Bragg reflections). A constant y-offset is used to plot the 50 K and 2 K data. Data were recorded on DMC ($\lambda = 2.4586(3)$ Å) at SINQ, PSI

5.5. Apical oxygen disorder

For a more detailed structural analysis, especially in view of a precise analysis of the effect of excess oxygen ordering on apical oxygen disorder, least-squares refinements were conducted of the integrated intensity data measured on a $\text{Nd}_2\text{NiO}_{4.09}$ single crystal at different temperatures. Results are summarized in **Table 5.2** and are in good agreement with those obtained from the powder diffraction study. Calculated and observed structure factors resulting from the least-square refinement of room temperature integrated intensity data is presented in **Fig. 5.17(a)**. The oxygen over-stoichiometry δ in the single crystal is refined to be 0.097(10). A detailed inspection of the apical oxygen atoms yields an occupancy corresponding to an overall stoichiometry of the apical site 1.71(2) at 55K, 1.80(1) at 300 K and 1.92(1) at 673 K i.e. 15%, 10% and 4% less than the stoichiometric occupation, respectively. While at the same time, the occupancies for the equatorial oxygen atoms correspond very closely to the ideal stoichiometry. The presumed under stoichiometry of the apical site is, however, not real but an artefact, related to strong and anharmonic distortions of the O_{ap} , which can no longer be described in a harmonic approach as turned out from the least-square refinements. The anisotropic thermal displacement parameters (ADPs) of apical oxygen atoms are plotted in **Fig. 5.17(b)** as a function of temperature. ADPs of apical oxygen atoms increases with temperature, however, U_{11} (and U_{22}) and U_{33} are pronouncedly non-linear. The large intercepts at 0 K cannot be attributed to the zero-point motions and therefore confirm the very large static disorder component of apical oxygen atoms.

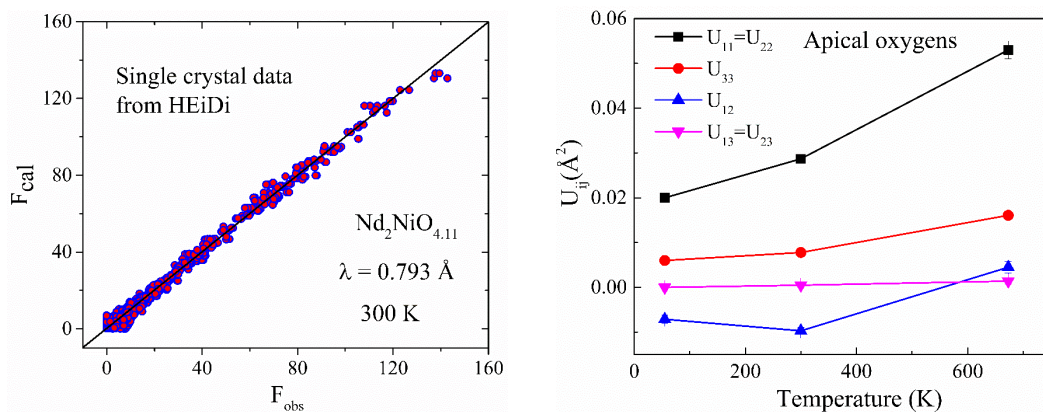


Figure 5.17 | Least-squares refinement results of neutron diffraction data recorded on $\text{Nd}_2\text{NiO}_{4.09}$ single crystal. (a) Observed versus calculated nuclear structure factors obtained with LTT structural model as shown in **Table 5.2** after correction for absorption and extinctions. (b) Thermal displacement parameters of apical oxygen atoms at different temperatures. Data were recorded on HEiDi ($\lambda = 0.793(1) \text{ \AA}$) at FRM II.

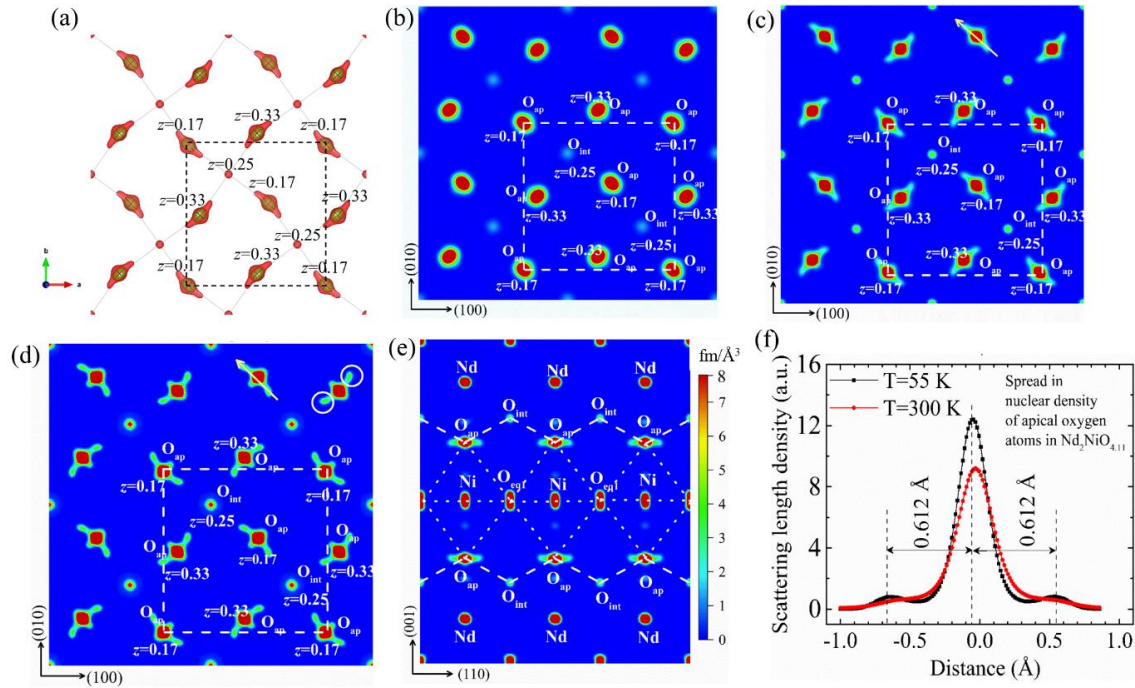


Figure 5.18 | MEM reconstructions of $\text{Nd}_2\text{NiO}_{4.11}$ obtained from neutron diffraction data. (a) Nuclear density iso-surfaces of apical and interstitial oxygen atoms at 300 K. Anisotropic thermal ellipsoids of apical oxygen atoms are also shown. (b) $2a \times 2b$ projection of nuclear density maps obtained by high-resolution neutron powder diffraction data at ambient and (c-d) by high-resolution single crystal neutron diffraction data at 55 K and 300 K, respectively. Cuts were made along the c -axis in the range of $0.16 \leq z \leq 0.34$. The tetragonal P -centered unit cell is marked with a dashed square. Positions of apical and interstitial oxygen atoms along the c -axis are indicated. (e) $[110]/[001]$ projection cut along the $[11\bar{0}]$ -direction in the range of $-0.25 \leq z \leq 0.25$ showing the oxygen diffusion $\text{O}_{\text{ap}}\text{-O}_{\text{int}}\text{-O}_{\text{ap}}$ pathway (white dashes) along the $[110]$ -direction obtained with single crystal neutron diffraction data at 300 K. Ni_6 -octahedra are indicated by white dotted lines. All color maps are plotted on the same scale as shown in (e). (f) Scattering densities of the apical oxygen atoms at different temperatures. Line cuts were made at 55 K and 300 K data through the apical oxygen atom along the $[110]$ -direction, the partial split positions of O_{ap} becomes evident at 55K. Data were recorded on HEiDi ($\lambda = 0.793(1)$ Å) at FRM II.

The crystal structure using harmonic displacement factors (probability 85%) is visualized in **Fig. 5.5**, while a more sophisticated data analysis using the Maximum Entropy Method (MEM) is given in **Fig. 5.18(a)-(e)** for 55 K and 300 K, also comparing to NPD data. MEM results corresponding to 673 K is shown **Fig. 5.19(a)-(c)**. The refinement results are given in **Table 5.2** and used for phasing the respective intensities for the Maximum Entropy analysis. It is evident that apical oxygen atoms are strongly displaced from their equilibrium positions in a way to allow a symmetrical expansion of the $\text{O}_{\text{int}}(\text{O}_{\text{ap}})_4$ tetrahedra both at 55 and 300 K (*cf.* **Fig. 5.18(a)**). Apical oxygen atoms

are displaced specifically along the tilting axis of the NiO₆ octahedron that changes by 90° at different layers along the *c*-axis. Such displacements of apical oxygens in two neighboring layers yield an increased O_{int}-O_{ap} distance of 2.76 Å at 55K, compared to only 2.15 Å when using the average structural model. The as obtained real O_{int}-O_{ap} distance of 2.76 Å corresponds very well to the expected O-O distance, taking into account an O²⁻ ionic radius of 1.4 Å according to Shannon¹¹⁷. These findings also indicate strong displacements of O_{ap} in the [110]-direction inside the rock salt layer, favoring an easy oxygen diffusion pathway between apical and vacant interstitial sites, which is in agreement with a theoretically predicted push-pull diffusion mechanism reported in^{20,24}. From a methodological aspect, it is also interesting to state that only high-resolution diffraction data of up to 0.9 Å⁻¹ allowed visualizing such important structural details, which do not emerge from the NPD data, obtained up to 0.66 Å⁻¹ only. It is noteworthy that a similar disorder scenario of the apical oxygen atoms has been reported for Pr₂NiO_{4.09} at room-temperature¹⁴ from single crystal neutron diffraction studies, suggesting this type of disorder to be a general feature in K₂NiF₄-type oxides^{25,60}. However, related O_{ap} displacements become much more obvious in Nd₂NiO_{4.11}, probably related to the lower ionic radius of Nd³⁺ (1.163 Å compared to 1.179 Å for Pr³⁺ in 9-fold coordination). The same argument can also be taken to explain the different transition temperatures for the orthorhombic to tetragonal phase transition of Pr₂NiO_{4.23} at 638 K and Nd₂NiO_{4.23} at 1003 K. **Fig. 5.18(f)** represents a 1D cut through the nuclear density maps at the apical oxygen atoms, showing precisely the temperature dependence of the apical oxygen disorder. Two localized nuclear density lobes, separated by a distance of 0.621 Å from the apical oxygen center along [110]-direction, are evident at 55 K. These two nuclear density lobes behave like splitted apical sites at 55 K that hints at large static component of disorder to the apical site, consistent with the results from harmonic refinements. However, with increasing temperature, a clear overlap of nuclear densities of these two lobes with the center occurs suggesting the movements related to the libration-mode of NiO₆-octahedra and an onset of phonon assisted oxygen diffusion process at 300 K. Therefore, oxygen diffusion mechanism close to room temperature involves important local structural distortions that resemble to a successively in- and exhaling behaviour of the involved empty and occupied tetrahedra along the diffusion pathway (*cf.* **Fig. 5.5(c)**). Further oxidation of this compound requires incorporation of excess oxygen atoms in those contracted tetrahedra i.e. into the 4*e* tetrahedral sites represented by blue spheres in **Fig. 5.5(c)**. However, as shown with difference Fourier maps and MEM analysis, the anisotropic displacement pattern of apical oxygen atoms at low temperature does not allow the incorporation of excess oxygens at these sites. Consequently, this compound with the LTT phase cannot be oxidized further at low temperature even with electrochemical methods as revealed by a recent in-situ neutron powder diffraction study¹⁴. In contrary, the MEM results (*cf.* **Fig. 5.19**) show a different scenario for the displacement pattern of apical oxygens at 673 K. At this temperature, the scattering densities of apical oxygens appear

more isotropic within the ab -plane. All $\text{O}_{\text{int}}\text{-(O}_{\text{ap}})_4$ tetrahedra look exactly identical and are in a dynamically disordered state due to strong thermal contributions. It seems that there is no effect of interstitials to the apical oxygen atoms. Accordingly, a thermally activated site-to-site oxygen hopping occurring is expected via regular apical and vacant interstitial sites at this temperature as proposed by Piovano et al.¹¹⁸. This scenario also indicates that an easy oxidation of the compound is highly likely at this temperature by inclusion of excess oxygens in all the tetrahedral sites.

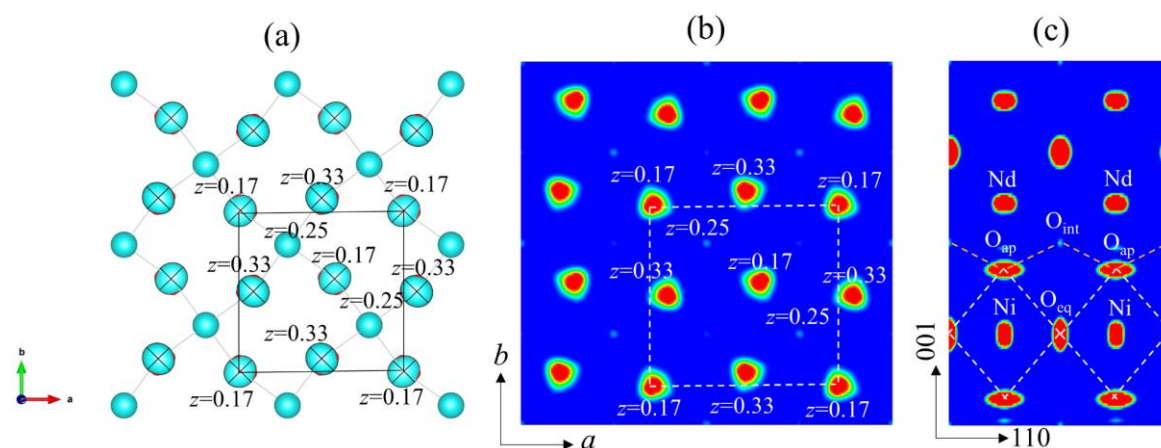


Figure 5.19 | MEM reconstructed nuclear scattering density of $\text{Nd}_2\text{NiO}_{4.11}$ obtained from single crystal neutron diffraction data collected at 673 K. Single crystal data were recorded on D9 ($\lambda = 0.837(1)$ Å) at ILL. (a) Thermal ellipsoids of apical and interstitial oxygen atoms are overlapped with their respective nuclear density iso-surfaces. (b) $2a \times 2b$ projection of nuclear density maps. Cuts were made along the c -axis in the range of $0.16 \leq z \leq 0.34$. The tetragonal P -centered unit cell is marked with a dashed square. Positions of apical and interstitial oxygen atoms along the c -axis are indicated. (c) $[110]/[001]$ projection cut along the $[110]$ -direction in the range of $-0.25 \leq z \leq 0.25$ showing the oxygen diffusion $\text{O}_{\text{ap}}\text{-O}_{\text{int}}\text{-O}_{\text{ap}}$ pathway (yellow dashes) along the $[110]$ -direction. NiO_6 -octahedra are indicated by white dashed lines. Colors maps are on the same scale as used in Fig. 5.18.

Table 5.2 | Least-square refinement results of single crystal neutron diffraction data obtained for the $Nd_2NiO_{4.09}$ compound on HEiDi at MLZ/FRM II, using a wavelength of $0.793(1)$ Å up to $\sin\theta_{\max}/\lambda = 0.9$ Å⁻¹. Refinements were carried out in $P4_2/nm$ space group. Thermal displacement parameters U_{ij} are given in Å².

Temperature		55 K	300 K	673 K
$a = b$	(Å)	5.4498(2)	5.4597(5)	5.4681(3)
c	(Å)	12.1536(6)	12.2027(4)	12.3198
	Occ.	1	1	1
Ni (4 <i>d</i>) (0 0 0)	$U_{11} = U_{22}$	0.0032(5)	0.0045(3)	0.0096(3)
	U_{33}	0.0073(6)	0.0132(5)	0.0290(4)
	U_{12}	-0.0005(2)	-0.0006(2)	-0.002(4)
	$U_{13} = U_{23}$	0.0003(2)	0.00049(18)	0.0068(9)
	Occ.	2	2	2
Nd (8 <i>i</i>) ($x x z$)	x	0.98904(19),	0.98967(15)	0.9933(7)
	z	0.36146(8)	0.36133(7)	0.36070(8)
	$U_{11} = U_{22}$	0.0070(5)	0.0105(4)	0.0215(4)
	U_{33}	0.0027(6)	0.0064(4)	0.0141(3)
	U_{12}	0.0011(3)	0.0015(2)	0.002(4)
	$U_{13} = U_{23}$	0.0007(2)	0.00035(17)	0.0036(7)
	Occ.	1.710(18)	1.800(15)	1.924(14)
O _{ap} (8 <i>i</i>) ($x x z$)	x	0.0421(4),	0.0413(3)	0.0394(5)
	z	0.17681(18)	0.17706(12)	0.17756(17)
	$U_{11} = U_{22}$	0.0200(9)	0.0287(7)	0.053(2)
	U_{33}	0.0060(9)	0.0078(7)	0.0161(7)
	U_{12}	-0.0071(9)	-0.0097(8)	0.0045(13)
	$U_{13} = U_{23}$	0.0000(3)	0.0005(3)	0.0014(7)
	Occ.	0.95(2)	0.96(1)	1
O _{eq1} (4 <i>a</i>) ($\frac{3}{4} \frac{1}{4} 0$)	$U_{11} = U_{22}$	0.0054(7)	0.0060(5)	0.014(4)
	U_{33}	0.0270(12)	0.0325(10)	0.100(10)
	U_{12}	0.0001(5)	0.0020(5)	0.006(3)
	Occ.	1.04(2)	1.005(15)	1
O _{eq2} (4 <i>e</i>) ($\frac{1}{4} \frac{1}{4} z$)	z	0.97690(17)	0.97828(13)	0.9857(2)
	$U_{11} = U_{22}$	0.0030(7)	0.0073(5)	0.019(4)
	U_{33}	0.0112(9)	0.0174(7)	0.014(5)
	U_{12}	0.0016(5)	-0.0029(5)	-0.008(3)
	Occ.	0.057(14)	0.097(10)	0.092(19)
O _{int} (4 <i>b</i>) ($\frac{3}{4} \frac{1}{4} \frac{1}{4}$)	U_{iso}	0.008(8)	0.014(3)	0.018(7)
no. of reflections	all	1121	1290	866
	unique	470	670	225
R_p (%)		6.54	5.37	4.49
wR_p (%)		10.46	7.76	10.77
R_{int} (%)		2.02	2.31	3.74

5.6. Conclusions

The crystal structure and magnetic properties of moderately oxygen doped Nd₂NiO_{4.11} were investigated in the temperature range of 2-673 K by employing single crystal and powder diffraction techniques combined with macroscopic magnetization measurements. This study leads to following conclusions:

- i. In the investigated temperature range, the compound crystallizes in a tetragonal structure with $P4_2/ncm$ space group (LTT phase) with excess oxygen atoms selectively occupy the $4b$ ($\frac{3}{4}$ $\frac{1}{4}$ $\frac{1}{4}$) interstitial sites, coordinated by four apical oxygen atoms. This finding is in accordance with the previously proposed crystal structure with DFT calculations on the parent La₂NiO_{4.125} compound.
- ii. A complex 3D ordering of excess oxygen atoms with superstructure reflections up to fourth order has been identified close to 300 K. Therefore, excess oxygens do not randomly occupy the $4b$ sites. Instead, a specific long-range ordering pattern of interstitials exists. The $P4_2/ncm$ model only explains the average structure of this compound without considering oxygen superstructure reflections. This result is also inconsistent with the 1D ordering model of excess oxygens originally observed for parent La₂NiO_{4+δ} with similar δ . Surprisingly, the interstitial correlations are strongly enhanced below the magnetic ordering temperature. This is a hint for a spin-lattice coupling in doped nickelates.
- iii. Structural analysis reveals large and anisotropic thermal displacement parameters for equatorial and apical oxygen atoms with a large static component of disorder. MEM results show strong anharmonic delocalization of the apical oxygen atoms, towards the nearest vacant $4b$ interstitial sites, related to the phonon assisted oxygen diffusion mechanism. Oxygen diffusion along the [110]-direction close to room temperature thus involves important local distortions of the respective tetrahedral sites, resembling to a successively in- and exhaling behaviour of the involved empty and occupied tetrahedra along the diffusion pathway. Such an anisotropic displacement pattern of apical oxygens at low temperature in the LTT phase allows to understand the origin of reduced oxygen mobility in the moderately oxygen doped phase. However, all tetrahedra become dynamically disordered and structurally equivalent at 673 K, which activates enhanced mobility at moderate temperatures.

- iv. Macroscopic magnetization measurements and neutron diffraction studies reveal long-range antiferromagnetic ordering of the Ni-sublattice at $T_N \sim 53$ K with a weak ferromagnetic component along the c -axis, while the long-range magnetic ordering of the Nd-sublattice occurs below 10 K. Temperature dependent neutron diffraction patterns show the appearance of a commensurate magnetic order at T_N with the propagation vector $\mathbf{k} = (100)$. In this way, the moderately doped Nd₂NiO_{4.11} system shows the coincidence of 3D ordering of interstitials and a commensurate magnetic order below 53 K that has never been observed in the parent La₂NiO_{4+δ} homologue.

Output

1. Results related to crystal structure (sections 5.1 and 5.5) and magnetic properties (sections 5.2 and 5.3) of Nd₂NiO_{4.11} as discussed in this chapter are published in *Phy. Rev. Mat.* 3, 083604 (2019).

Chapter 6

Modulated crystal structure, oxygen disorder, and incommensurate magnetic order in $\text{Nd}_2\text{NiO}_{4.23}$

The role of excess oxygen atoms is indisputably recognized in controlling the oxygen mobility and magnetic properties in layered Ruddlesden-Popper nickelates, as already observed for $\text{Nd}_2\text{NiO}_{4.11}$ (**chapter 5**). The present chapter focuses on the highly oxygen-doped $\text{Nd}_2\text{NiO}_{4.23}$. The incommensurately modulated crystal structure, strong apical oxygen disorder and the incommensurate antiferromagnetic spin order were investigated by high-resolution X-ray powder diffraction, polarized and unpolarized single crystal neutron diffraction studies together with macroscopic magnetization measurements.

The current chapter is organized as follows: the temperature evolution of the monoclinic phase is discussed in **section 6.1**. Based on these results, a temperature dependent structural phase diagram is proposed. Complex incommensurate ordering of excess oxygens and its influence on the apical oxygen disorder are presented in **section 6.2** from temperature dependent X-ray powder diffraction data and neutron diffraction data on single crystal. In **section 6.3**, the evidence of an antiferromagnetic order at $T_N \sim 150$ K and a magnetic field induced ferromagnetic type transition are reported from magnetic susceptibility and isothermal magnetization data on single crystal. Polarized and unpolarized neutron diffraction experiments on the single crystal suggest the presence of a unique and incommensurate static spin order in $\text{Nd}_2\text{NiO}_{4.23}$ as summarized in **section 6.4**.

6.1. Structural evolution with temperature

Room temperature synchrotron X-ray powder diffraction (SXRPD) data shows good crystalline quality and absence of impurity phases in the powder sample. The room temperature SXRPD pattern looks similar to that of the orthorhombic $Fmmm$ phase, as reported previously for the undoped Nd₂NiO_{4.23} compound^{18,55}. However, a closer inspection reveals subtle splitting of (hhl) -type Bragg reflections indicating the presence of monoclinic distortion in the crystal structure. High-resolution x-ray diffraction measurement on a laboratory diffractometer is used to uncover this monoclinic distortion at room temperature as discussed in **chapter 4** (*cf. inset of Fig. 4.6*). However, in the SXRPD data, extra superstructure reflections with intensities only about 0.5% compared to the strongest (113) structural Bragg peak are observed (*cf. Fig. 6.1*). Such superstructure reflections are likely to be related with the long-range ordering of excess oxygen atoms. The indexation of these superstructure reflections in the powder data is a complicated task as more than one modulation vector up to fourth order may exist, as discussed in the previous chapter for Nd₂NiO_{4.11}, which makes the routine modulation vector searching procedure ineffective. Therefore, a structural refinement considering these superstructure reflections could not be carried out. Instead, a Le-bail method was used to extract the lattice parameters at different temperatures to correlate the structural changes with associated excess oxygen ordering. The monoclinic $F112/m$ space group (a non-standard setting of $C112/m$ space group, no. 12) is used to fit the positions of main structural Bragg reflections in the SXRPD data. An excellent agreement is found between the experimental and calculated patterns as presented in **Fig. 6.1** for the 300 K data. The refined monoclinic unit cell parameters are $a = 5.37(3) \text{ \AA}$, $b = 5.43(1) \text{ \AA}$, $c = 12.35(1) \text{ \AA}$, $\alpha = \beta = 90^\circ$ and $\gamma = 90.071^\circ$. This monoclinic phase is abbreviated as “LTM” (Low Temperature Monoclinic) as previously introduced for Pr₂NiO_{4.22}⁵³. Temperature dependent SXRPD study shows no pronounced structural changes in the temperature range of 5-300 K with oxygen superstructure reflections remain fixed to their positions without any significant change in the intensities as displayed in **Fig. 6.2(a)**. However, a complex sequence of phase transition is observed in the temperature range of 300-873 K. It is evident from **Fig. 6.2(b)** that the intensities of these superstructure reflections start to change at temperature as low as 423 K and it is possible that modulation vectors also start to change at this temperature. At $T \sim 523 \text{ K}$, additional B-type weak reflections start to appear in the diffraction pattern and new set of $(00l)$ type reflections becomes evident close to the $(00l)$ type peaks of the primary monoclinic phase as shown in **Fig. 6.2(b)**. This confirms the appearance of a secondary phase and indicates the sign of a phase separation into oxygen-poor and oxygen-rich domains as the c -axis length strongly depends on the additional oxygen content δ . The refined secondary phase turns out to be orthorhombic $Bmab$ (LTO) as originally proposed for the stoichiometric Nd₂NiO_{4.0} at room temperature. However, the refined lattice parameters corresponding to the secondary phase are

much larger than the lattice parameters of the stoichiometric phase. Furthermore, the length of the *c*-axis corresponding to the secondary phase is approximately 1% less than the monoclinic phase. This indicates that the secondary phase has a reduced δ value. This biphasic region exists in a broad temperature range of 523-623 K. This biphasic region is likely due to miscibility gaps arising from strong correlations among the interstitials as originally observed for Sr doped La_{2-x}Sr_xNiO_{4+ δ} compounds by Hücker et al.¹¹⁹ Consequently, interstitials are mixed unevenly into oxygen-poor (the orthorhombic phase) and oxygen-rich (the monoclinic phase) domains. Usually, the oxygen-poor domains hold the maximum δ value of the bordering pure low- δ phase while the oxygen-rich domains take the minimum δ of the pure high- δ phase¹¹⁹. In this biphasic region, strong changes in intensity of superstructure reflections are observed. The phase coexistence region vanishes at 623 K (*cf.* **Fig. 6.2(c)**) and the primary monoclinic phase exists in the temperature range of 623 K < T < 783 K (*cf.* **Fig. 6.2(d)**). The number of oxygen superstructure reflections corresponding to the LTM phase remains constant in this range as shown in **Fig. 6.2(c)**. Another biphasic region has been observed in a narrow temperature region of 783 K < T < 803 K in which the primary monoclinic phase coexists with a high temperature tetragonal (HTT) phase. With increasing temperature, the volume fraction of the monoclinic phase gradually decreases while that related to the tetragonal phase continuously increases such that only the HTT phase remains at T \geq 813 K. In this HTT phase, no additional oxygen superstructure reflections are observed although the δ value at this temperature is close to 0.1. It is likely that at this temperature range, the interstitials become highly mobile and participate in the oxygen diffusion mechanism. Consequently, the correlations among them are completely lost, which explains the disappearance of these superstructure reflections. Therefore, an incommensurate-commensurate structural transition is observed at T \sim 813 K for the Nd₂NiO_{4.23} system associated with the complex 3D ordering of interstitials.

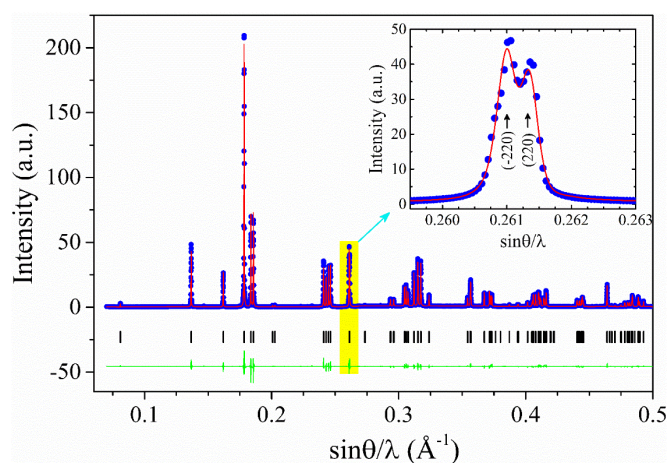


Figure 6.1 | An excerpt of the room temperature SXRPD pattern of Nd₂NiO_{4.23}. The data was collected at the Material Sciences beamline X04SA ($\lambda = 0.5646(1)$ Å) of SLS, PSI and analyzed with

Le-Bail method with monoclinic F112/*m* space group. The inset shows the splitting of the (220) Bragg reflection due to monoclinic distortion in the average crystal structure.

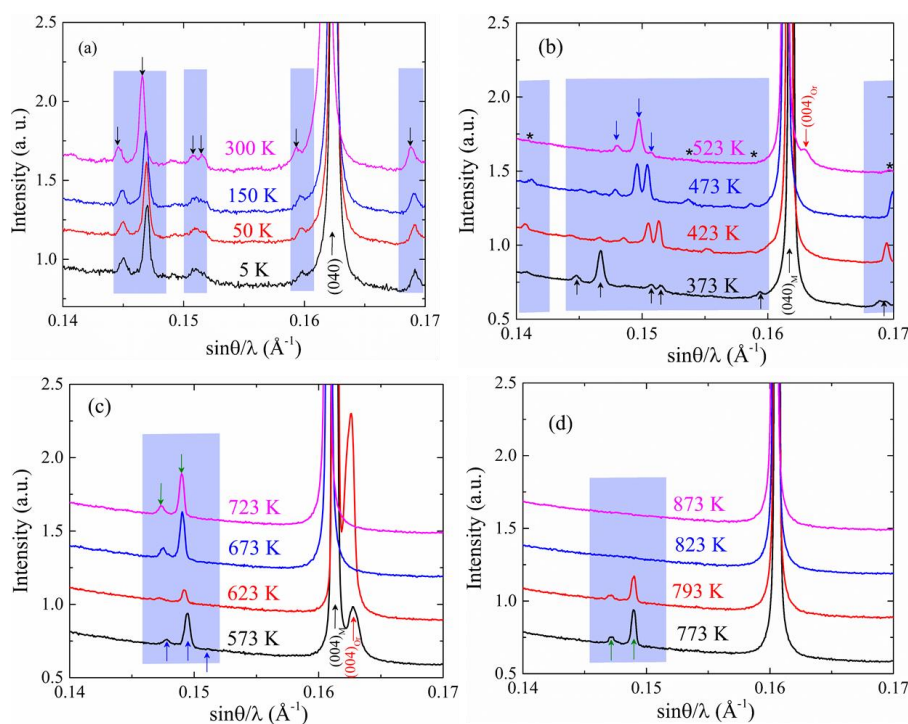


Figure 6.2 | Temperature evolution of oxygen superstructure reflections in the SXRPD data.

The data were collected at MSX04SA ($\lambda = 0.5646(1) \text{ \AA}$) of SLS, PSI. Blue shaded areas present oxygen superstructure reflections. A constant offset along the *y*-axis has been applied to plot the diffraction patterns at variable temperatures. Black, blue and olive arrows represent oxygen superstructure reflections in the monoclinic phase at temperatures $5 \text{ K} \leq T \leq 373 \text{ K}$, biphasic region at temperatures $523 \text{ K} \leq T \leq 623 \text{ K}$ and monoclinic phase at temperatures $623 \text{ K} \leq T \leq 803 \text{ K}$, respectively. The black arrow near $\sin\theta/\lambda = 0.163 \text{ \AA}^{-1}$ denotes $(004)_M$ peak for the monoclinic phase and red arrow represents the $(004)_{OR}$ peak corresponding to the orthorhombic phase. Stars in panel (b) show the superstructure reflections whose intensity strongly decreased on reaching from the monoclinic phase to the biphasic region.

To correlate the structural changes with interstitials ordering, temperature evolution of various lattice parameters were extracted and plotted in **Fig. 6.3(a)-(d)**. From the above discussion, five different temperature segments can be separated as follows: i) $5 \leq T \leq 523 \text{ K}$ (displayed by the light yellow color): the average crystal structure is LTM and *a*, *b* and *c* lattice parameters increase non-linearly with temperature and the distortion angle, referred by $\gamma-90^\circ$, decreases smoothly with the temperature. ii) $523 \leq T \leq 633 \text{ K}$ (displayed by the light orange color): A biphasic region containing the LTM and LTO phases is observed. In this regime, the monoclinic *a*-axis increases rapidly with temperature while the *b*-axis does not change significantly. The evolution of these parameters

respectively shows a maxima and minima at $T^* = 623$ K just below the phase boundary. The monoclinic c -axis initially increases and then starts to decrease with increasing temperature towards T^* while the distortion angle shows a sharp minima at T^* . Sharp anomalies at T^* perhaps indicate the temperature at which correlations between interstitials are partially lost and consequently, the miscibility gap disappears. iii) $643 \leq T \leq 783$ K (displayed by the light orange color): A single LTM phase exists. a , b and c -axes smoothly increase with temperature. Surprisingly, the distortion angle slightly increases initially and then sharply decreases with increasing temperature. iv) $793 \leq T \leq 803$ K (displayed by light green color): A biphasic region comprising the LTM and HTT phases is observed. The distortion angle of the monoclinic phase abruptly decreases toward zero approaching the phase boundary. v) $T \geq 813$ K (displayed by the white region): The HTT phase exists and all the cell parameters smoothly increase with increasing temperature. In contrast to the other cell parameters, the thermal evolution of the monoclinic unit cell volume does not show any anomaly in the investigated temperature range and smoothly transforms at each phase boundaries. The non-linear thermal evolution of the unit cell volume can be described by a quasi-harmonic Debye model as discussed in Eq. 5.1. This model represents well the observed temperature dependence of the unit-cell volume as shown by the thick orange line on top of experimental data in Fig. 6.3(d). The fitting parameters are $A = 0.0506(2)$ ($\text{\AA}/\text{K}$) and $\Theta_D = 541(10)$ K in a good agreement to the reported results on similar compounds¹²⁰. The observed temperature dependence indicates a strong phonon contribution to the thermal expansion.

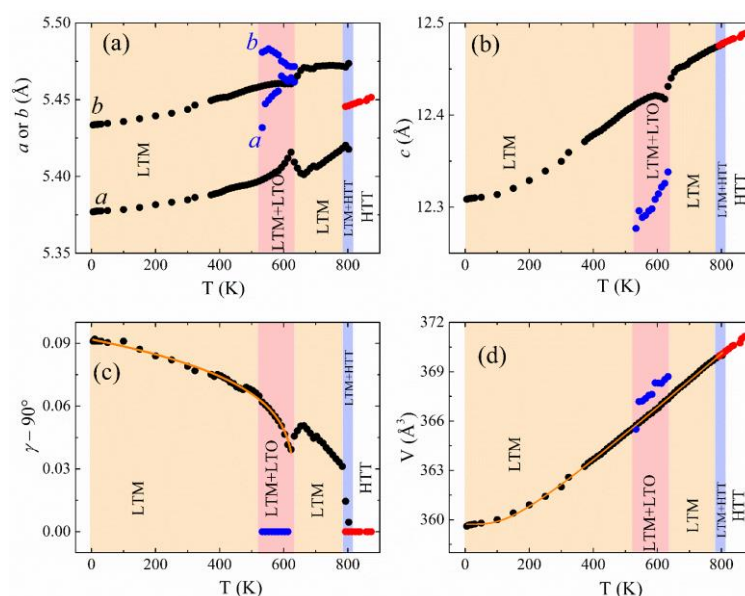


Figure 6.3 | Temperature evolution of different lattice parameters of Nd₂NiO_{4.23}. Evolution of (a) a and b -lattice parameters, (b) the c -lattice parameter, (c) the monoclinic distortion angle ($\gamma - 90^\circ$) and (d) the unit cell volume with temperature. Black, blue and red symbols define

respectively the monoclinic, orthorhombic and tetragonal phase. The data were collected at the MSX04SA ($\lambda = 0.5646(1) \text{ \AA}$) of SLS, PSI.

6.2. Ordering of excess oxygens

In order to search for modulation vectors related to the ordering of interstitials, neutron diffraction reciprocal maps were obtained at different temperatures on the as-grown Nd₂NiO_{4.23} single crystal on DMC. Sections of $(hk0)$ and $(h0l)$ planes are displayed in **Fig. 6.4(a)-(f)**. Presence of $h + k = 2n$ and $h + l = 2n$ type structural Bragg peaks confirm the F-centering of the lattice. In addition, extra superstructure reflections (as shown by red circles) are also observed confirming the presence of strong structural modulations associated with the ordering of excess oxygens, consistent with the X-ray powder diffraction data. Laue diffraction (**section 4.3.3**) and neutron diffraction data (**section 4.3.4**) reveal that the as-grown single crystal contains four structural twin domains. Two twins share a common $[110]$ axis while the other set of two twins shares the $[-110]$ axis as shown schematically in **Appendix C**. The presence of four twin domains along with the higher order modulation vectors did not allow to separate superstructure reflections corresponding to a single domain. Consequently, the correct modulation vectors could not be found with plane mappings even combining with a theoretical approach as discussed for Nd₂NiO_{4.11} in **chapter 5**. Nevertheless, these reciprocal plane mappings provide few important insights: The ordering vectors and the intensities of superstructure reflections are unchanged in between 2 K and 300 K in accordance with the powder data. At 450 K, few superstructure reflections are disappeared. However, the modulation vectors remain unaffected, which is also consistent with the powder data. Furthermore, reciprocal plane mappings reflect a complex 3D ordering of interstitials, which seems different from previously reported results on the La-based parent compounds²⁸. It turned out that only few superstructure reflections are observed in the neutron diffraction single crystal mappings compared to the single crystal x-ray data as presented in **Fig. 6.4(d)-(e)** for the $(h0l)$ plane. These unobserved reflections also add complications into the modulation vectors searching procedure. However, single crystal x-ray diffraction data are in accordance with our neutron data. It is found that superstructure reflections in the $(h0l)$ zone appear at $Q = (h \pm \Delta, 0, l \pm \Lambda)$ positions with both $h, l = \text{odd}$. For detailed analysis of these superstructure reflections, 1D-line cuts have been made at different temperatures. Typical q_h and q_l -cuts of such incommensurate satellite at $Q = (1 \pm \Delta, 0, 5 \pm \Lambda)$ reflects $\Delta \sim 0.25, \Lambda \sim 0.1$ are shown in **Fig. 6.5(a)-(b)**. Positions of these satellites suggest a unit cell that is four times larger along the a -axis and ten times larger along the c -direction compared to the F-type unit cell. Fitting of the oxygen superstructure reflection with a Lorentzian function convoluted with a Gaussian

instrumental resolution gives the in-plane and out-of-plane correlation lengths (associated to the oxygen ordering) of about 140(14) Å and 78(10) Å, respectively.

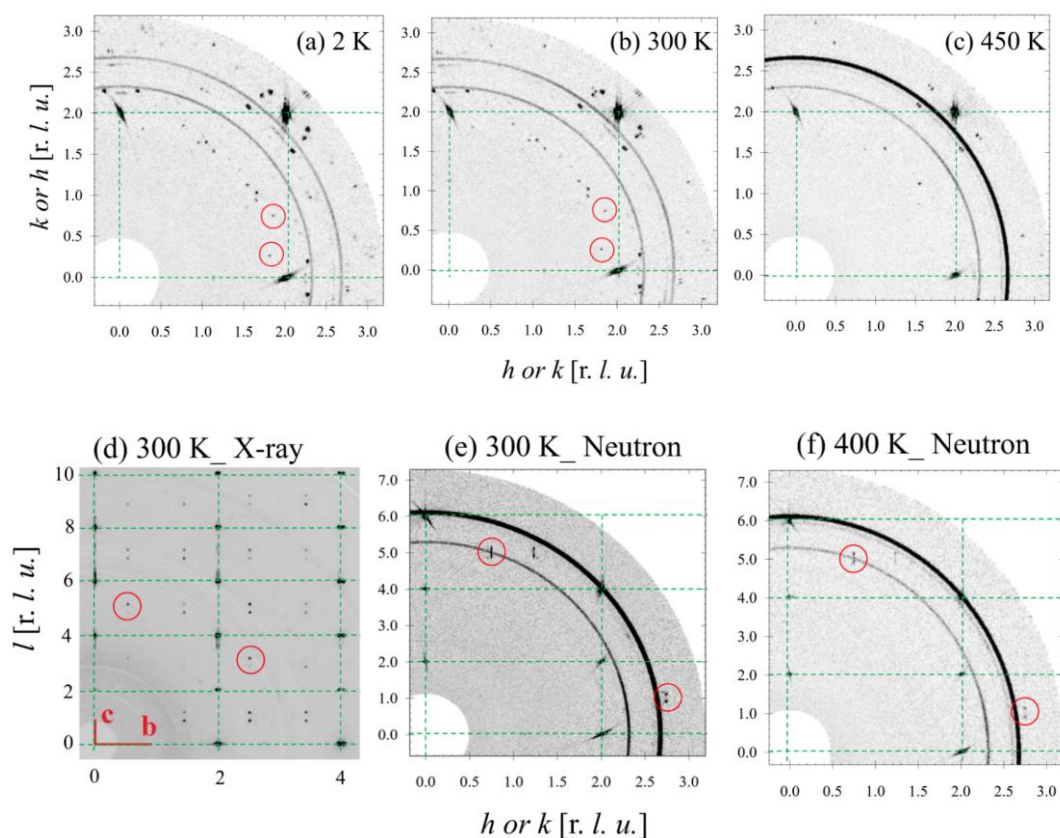


Figure 6.4 | 3D ordering of excess oxygen atoms in Nd₂NiO_{4.23} as obtained with reciprocal plane mapping. $(hk0)$ reciprocal plane obtained with single crystal neutron diffraction at (a) 2 K, (b) 300 K and (c) 450 K. $(h0l)$ reciprocal plane obtained with single crystal (d) X-ray diffraction at 300 K (taken from the reference¹²¹) and neutron diffraction at (e) 300 K and (f) at 400 K. Vertical and horizontal dashed lines show the basic F-type lattice. Red circles denote additional superstructure peaks from the excess oxygen ordering. Neutron data were recorded on DMC at SINQ, PSI ($\lambda = 2.4586(3)$ Å).

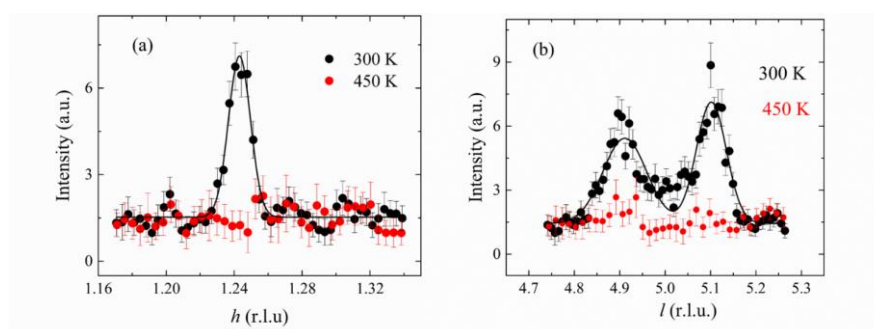


Figure 6.5 | Elastic q -cuts through the oxygen ordering reflections. A representative (a) q_h cut and (b) q_l -cut through the oxygen ordering reflection at $(h = 1.25 \ 0 \ l = 4.9)$ at 300 K and 450 K.

6.3. Apical oxygen disorder

To study the average crystal structure especially the influence of excess oxygens ordering on apical and equatorial oxygen displacement parameters, powder neutron diffraction (PND) experiments were carried out at 300 K and 2 K on HRPT. Structural refinements were performed with the orthorhombic $Fmmm$ space group instead of $F112/m$, as the resolution of HRPT is not enough to detect the subtle monoclinic distortion in $\text{Nd}_2\text{NiO}_{4.23}$. Structural parameters obtained with Rietveld refinements are presented in **Table 6.1** while excerpts of refined patterns are displayed in **Fig. 6.6(a) and (b)**. Structural refinements reveal that the anisotropic thermal ellipsoids of the equatorial oxygen atoms are extended along the c -axis while the apical oxygen atoms are strongly displaced in the ab -plane. In accordance with the x-ray data, large number of oxygen superstructure reflections has also been observed in the PND data. In addition to these superstructure peaks, one extra reflection (as shown by an arrow) is observed in the PND pattern collected at 2 K as shown in **Fig. 6.2(b)**. This additional reflection is likely due to a static magnetic order as discussed in **section 6.5** with single crystal data.

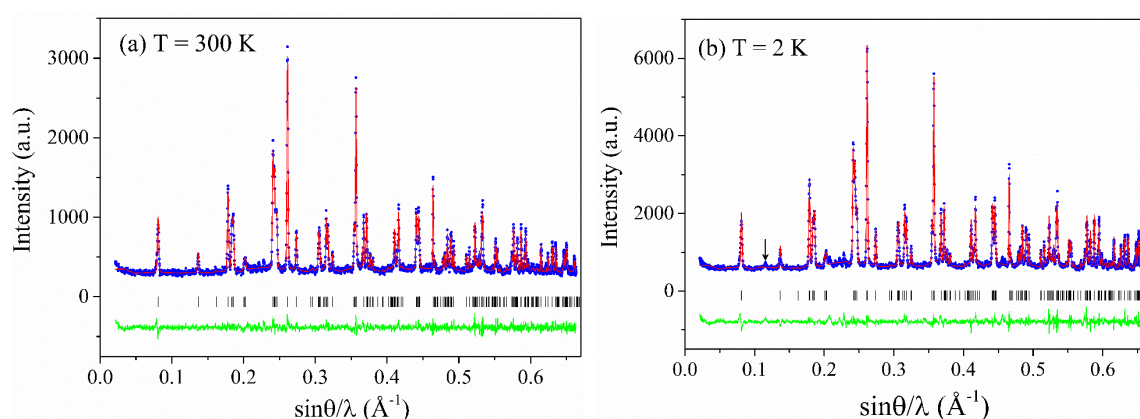


Figure 6.6 | Powder neutron diffraction patterns of $\text{Nd}_2\text{NiO}_{4.23}$. Observed (blue circles), calculated (red line) and difference (green continuous line) patterns resulting from Rietveld analysis of NPD data collected at (a) 300 K and (b) 2 K for $\text{Nd}_2\text{NiO}_{4.23}$ on HRPT ($\lambda = 1.494 \text{ \AA}$), SINQ, PSI. Ticks show the positions of nuclear Bragg reflections.

Table 6.1 | Refined structural parameters obtained from Rietveld refinements of powder neutron diffraction data recorded for the $\text{Nd}_2\text{NiO}_{4.23}$ compound. Data were collected on HRPT ($\lambda = 1.4940(2)$ Å) at SINQ, PSI. Space group: $Fmmm$. Thermal parameters U_{ij} are given in Å².

Temperature		2 K	300 K
a	(Å)	5.37499(5)	5.38461(5)
b	(Å)	5.43780(5)	5.44392(5)
c	(Å)	12.30670(11)	12.35047(13)
Ni (0 0 0)	Occ.	1	1
	U_{11}	0.0058(9)	0.0058(10)
	U_{22}	0.0027(9)	0.0072(11)
	U_{33}	0.0089(11)	0.0133(13)
Nd (0 0 z)	Occ.	2	2
	z	0.35889(14)	0.35922(15)
	U_{11}	0.0063(8)	0.0081(9)
	U_{22}	0.0126(9)	0.0115(9)
	U_{33}	0.0015(7)	0.0049(9)
O _{ap} (0 0 z)	Occ.	2	2
	z	0.1725(3)	0.1732(4)
	U_{11}	0.065(2)	0.070(3)
	U_{22}	0.144(4)	0.135(4)
	U_{33}	0.0051(13)	0.0070(14)
O _{eq} ($\frac{1}{4}$ $\frac{1}{4}$ 0)	Occ.	2	2
	U_{11}	0.0096(11)	0.0111(12)
	U_{22}	0.0058(11)	0.0045(11)
	U_{33}	0.0511(19)	0.050(2)
	U_{12}	0.0072(9)	0.0035(10)
O _{int} ($\frac{1}{4}$ $\frac{1}{4}$ $\frac{1}{4}$)	Occ.	0.23	0.23
	U_{iso}	0.033(9)	0.0360(4)
R_p (%)		20.3	23.3
wR_p (%)		18.0	19.0
R_{Bragg}		4.52	4.90

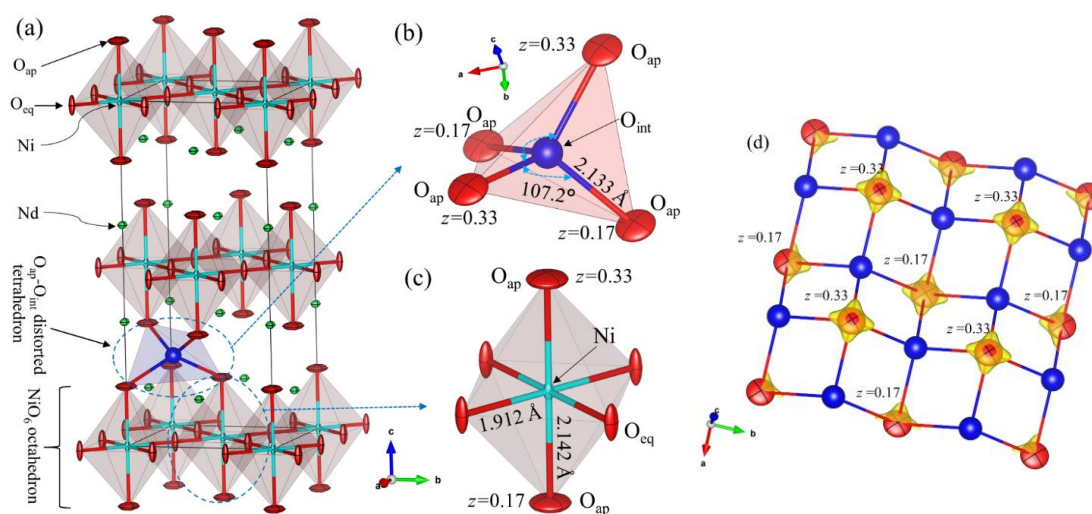


Figure 6.7 | Perspective presentation of the tetragonal unit cell of $\text{Nd}_2\text{NiO}_{4.23}$ in $F4/mmm$ space group. (a) The average crystal structure obtained with least-square refinement of room

temperature single crystal neutron diffraction data. Interstitial oxygen atoms (blue spheres) occupy the interstitial ($\frac{1}{4} \frac{1}{4} \frac{1}{4}$) Wyckoff site. Please note that on average only one out of eight interstitial sites in Nd₂NiO_{4.23} is filled the F-centered tetragonal unit cell. (b-c) represent magnified views of the O_{int}-(O_{ap})₄ tetrahedral cage and NiO₆ octahedra at 300 K, respectively. (d) Isosurfaces of apical and interstitial oxygen atoms obtained from MEM analysis of single crystal neutron diffraction data at 300 K. Thermal ellipsoids of apical and interstitial oxygens are also included.

For a more detailed structural analysis, especially in view of a precise analysis of the thermal displacement parameters for apical and equatorial oxygen atoms and their correlations with the ordering of interstitials, high-resolution single crystal neutron diffraction measurements were carried out at 20 K, 300 K, 673 K and 1023 K. From the intensity distribution of (*hh*0) type Bragg reflections, a volume fraction ratio of 38 (2): 38 (2): 12 (2): 12 (2) is extracted at room temperature for four twin domains. The incoherent superposition of intensity, from these four domain orientations causing multi-peak profiles of Bragg reflections, makes it difficult to integrate each subpeaks separately. Therefore, an averaging of total integrated intensities of (*hkl*) and (*khl*) type Bragg reflections allows the refining of the average crystal structure only in the tetragonal *F4/mmm* space group (*I4/mmm* in standard setting, space group no. 139) in spite of the real symmetry of the domains being still monoclinic. The least-square refinement results of the integrated intensity data are presented in **table 6.2**, while the *average crystal structure* is visualized in **Fig. 6.7**. The oxygen over-stoichiometry δ in the single crystal is evaluated to be 0.26(2) from the refinement of 300 K data, in close agreement with the value obtained with TGA analysis. It is important to note that with this δ value, approximately 12.5% interstitial sites are occupied. Calculated and observed structure factors resulting from the least-square refinement of room temperature integrated intensity data is presented in **Fig. 6.8(a)**. Structural refinements yield reduced occupancy for the apical site to what would be expected from the multiplicity of a crystallographic site while at the same time, the occupancies for the equatorial oxygen atoms correspond very closely to the ideal stoichiometry. The presumed under stoichiometry of the apical site is, however, not real but an artefact, related to strong and anharmonic displacements of apical oxygens, which can no longer be described in a harmonic approach as assumed in the least-square refinements and already observed for Nd₂NiO_{4.11} in chapter 5. The anisotropic thermal displacement parameters (ADPs) of apical oxygen atoms are plotted in **Fig. 6.8(b)** as a function of temperature. ADPs of apical oxygen atoms increases with temperature, however, U_{11} (and U_{22}) and U_{33} are pronouncedly non-linear. The large intercepts at 0 K cannot be attributed to the zero-point motions and therefore confirm the very large static disorder component of apical oxygen atoms. Absolute values of ADP parameters corresponding to the apical oxygens are enhanced by a factor 2-3 in Nd₂NiO_{4.23} compared to the moderately doped phase of Nd₂NiO_{4.11}.

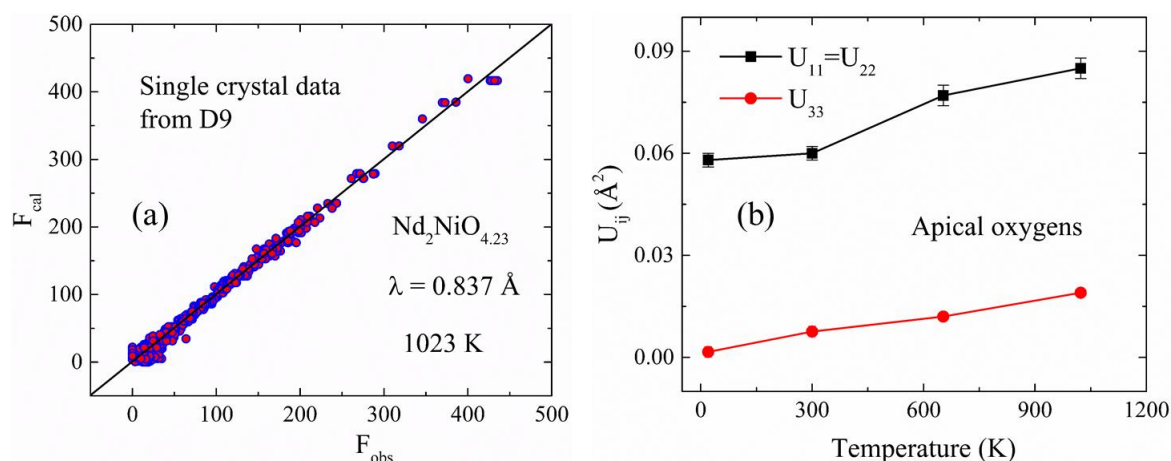


Figure 6.8 | Least-squares refinement results of neutron diffraction data recorded on $\text{Nd}_2\text{NiO}_{4.23}$ single crystal. (a) Observed versus calculated nuclear structure factors obtained with $F4/mmm$ structural model at 1023 K as shown in **Table 6.2** after correction for absorption and extinctions. (b) Thermal displacement parameters of apical oxygen atoms in $\text{Nd}_2\text{NiO}_{4.23}$ at different temperatures.

The disorder of apical and equatorial sites are further studied with maximum entropy (MEM) analysis. **Fig. 6.7(d)** depicts the nuclear scattering density isosurfaces for apical and interstitial oxygen atoms, obtained with MEM analysis of single crystal data at 300 K, along with anisotropic thermal ellipsoids of the apical oxygen atoms obtained with least-square refinement. It should be emphasized that the figure presents an average representation as only 12.5% interstitial sites (shown by blue sphered) are occupied. **Fig. 6.9** represents 2D nuclear density distributions for different structural sections obtained with MEM at different temperatures. A strong anharmonic contribution to the apical oxygen displacement is observed specifically along the [110]-direction with respect to the F-symmetry cell i.e. toward the nearest interstitial site as evidenced in the upper row of **Fig. 6.9** showing the ab -projection $0.14 \leq z \leq 0.28$. However, anharmonic type apical oxygen displacements are also observed at 20 K, which indicates a large static contribution to the apical oxygen disorder. This large static component is probably due to incommensurate structural modulations, representing on average the displacements of all apical oxygen atoms from their average positions. Scattering densities of apical oxygens are strongly enhanced at 300 K towards the [110] directions approximately with an outer perimeter of about 2 \AA . This strong enhancement of scattering density has partially dynamical origin as the incommensurate structural modulations remain fixed between 20 and 300 K, therefore, the static component should also be remain unchanged. The strong displacements of the apical oxygen atoms pointing towards the interstitial oxygen sites, highly favor an interstitial diffusion mechanism as shown by solid lines in the lower row of **Fig. 6.9**. It is evident that apical oxygen atoms at 300 K are displaced from their equilibrium positions in such a way that allows a symmetric increase of the $O_{\text{int}}-(O_{\text{ap}})_4$

tetrahedra. Such displacements of apical oxygens yield an increased O_{int}-O_{ap} distance of about 2.8 Å, instead of 2.15 Å for a non-distorted tetrahedron. These findings indicate an easy oxygen diffusion pathway between apical and vacant interstitial sites in the [110]-direction inside the rock salt layer, activated by strong displacements of apical oxygen atoms, and which is in agreement with a theoretically predicted push-pull diffusion mechanism reported in^{20,24}. Therefore, oxygen diffusion mechanism close to room temperature involves important local structural distortions that is far from rigid body configurations and resemble to a successively in- and exhaling behaviour of the involved empty and occupied tetrahedra along the diffusion pathway.

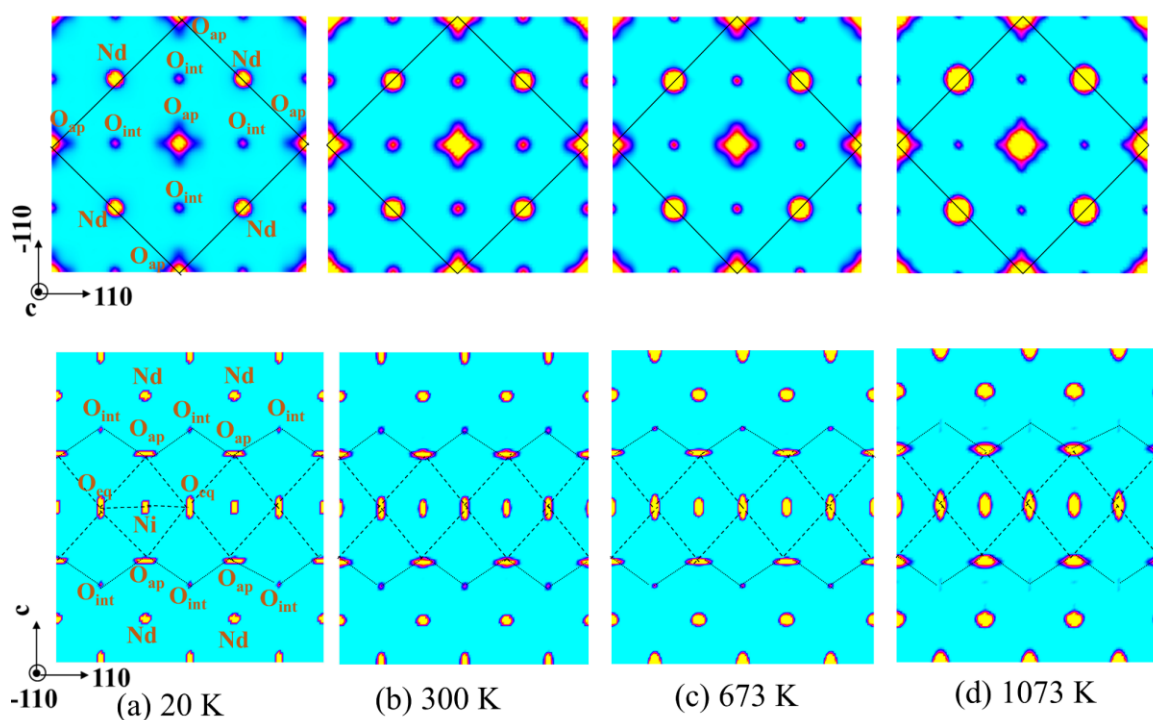


Figure 6.9 | Maximum entropy analysis of single crystal neutron diffraction data of Nd₂NiO_{4.23} obtained at (a) 20 K, (b) 300 K, (c) 673 K and (d) 1073 K. Single crystal data were recorded on ZEBRA ($\lambda=1.178(1)\text{\AA}$) at SINQ, PSI and on D9 ($\lambda=0.837(1)\text{\AA}$) at ILL. (Upper row) (110)-(-110) projection of 2D-nuclear density maps of particularly showing apical oxygen displacements toward closest interstitial site toward nearest interstitial site. Black continuous line outlines the F-centered unit cell. (Lower row) (110)-(001) projection of 2D-nuclear density map of displaying the O_{ap} - O_{int} - O_{ap} oxygen diffusion pathway along [110] direction.

In contrary, the MEM results at 673 K and 1073 K show a different scenario of displacement pattern for apical oxygens. At 673 K, incommensurate structural modulations are different to those at 300 K while no structural modulations exist at 1073 K. At 673 K, the scattering densities of apical oxygens appear more isotropic within the *ab*-plane with predominant dynamical

contributions signifying that interstitial oxygens no longer have significant influence on oxygen displacement parameters. Consequently, All O_{int}-(O_{ap})₄ tetrahedra are in a dynamically disordered state that enhances the oxygen mobility in this temperature range. It is important to note that the double-well potential behaviour of apical oxygens observed in Pr₂NiO_{4.25} at 673 K¹⁸, slightly above the orthorhombic-tetragonal phase transition, is proposed to be the origin of amplified oxygen mobility in the moderate temperature range as a diffusion pathway with a shallow potential is established between apical and interstitial vacancies. However, such behavior of apical oxygens is not observed in the present case for the Nd₂NiO_{4.23} compound likely due to the shift of the tetragonal phase transition temperature towards the higher temperature range (x-ray powder diffraction measurements confirm the structural transition at 813 K). This at least qualitatively explains the origin of reduced oxygen mobility in Nd-homologue in the moderate temperature range. The MEM results at 1073 K show complete isotropic nuclear scattering density distribution for apical oxygen atoms. This means that apical oxygens are almost freed from the octahedron. Consequently, they are expected to be highly mobile in this temperature range.

Table 6.2 | Structural parameters of the Nd₂NiO_{4.23} compound in *F4/mmm* space group obtained from least-square refinements of single crystal neutron diffraction data. Thermal parameters U_{ij} are given in Å². Single crystal data were recorded on ZEBRA ($\lambda=1.178(1)\text{Å}$) at SINQ, PSI and on D9 ($\lambda=0.837(1)\text{Å}$) at ILL.

Temperature		20 K	300 K	673 K	1023 K
$a = b$	(Å)	5.405(3)	5.417(2)	5.424(2)	5.441(9)
c	(Å)	12.3097(6)	12.3497(3)	12.4469(1)	12.5274(1)
	Occ.	1	1	1	2
Ni (0 0 0)	$U_{11} = U_{22}$	0.0025(6)	0.0041(5)	0.0086(4)	0.0118(3)
	U_{33}	0.0064(7)	0.0141(7)	0.0238(5)	0.0327(6)
	Occ.	2	2	2	2
Nd (0 0 z)	z	0.35980(12)	0.35965(11)	0.35933(8)	0.36016(9)
	$U_{11} = U_{22}$	0.0080(5)	0.0121(5)	0.0209(5)	0.0269(4)
	U_{33}	0.0025(7)	0.0066(7)	0.0122(4)	0.0157(4)
	Occ.	1.70(2)	1.74(2)	1.66(3)	1.82(2)
O _{ap} (0 0 z)	z	0.1728(2)	0.1735(3)	0.1735(2)	0.1759(2)
	$U_{11} = U_{22}$	0.058(2)	0.060(2)	0.077(3)	0.085(3)
	U_{33}	0.0016(16)	0.0076(15)	0.0120(10)	0.0190(10)

	Occ.	2.007(15)	1.985(14)	2.027(19)	2.026(15)
O _{eq} (¼ ¼ 0)	$U_{11} = U_{22}$	0.0044(8)	0.0065(7)	0.0165(7)	0.0216(5)
	U_{33}	0.0490(18)	0.0520(16)	0.0635(16)	0.0648(16)
	U_{12}	0.0004(7)	-0.0014(6)	-0.0061(5)	-0.0087(5)
O _{int} (¼ ¼ ¼)	Occ.	0.238(17)	0.252(16)	0.128(14)	0.112(17)
	U_{iso}	0.033(9)	0.036(8)	0.040(6)	0.046(16)
no. of	all	350	498	754	734
reflections	unique	90	91	246	238
R_p (%)		5.65	5.81	5.63	4.35
wR_p (%)		8.15	7.6	8.29	6.30
R_{int}		5.82	4.90	5.46	5.31
G.O.F		6.17	5.66	6.46	4.58

6.4. Magnetic susceptibility

DC Magnetic susceptibility measurements were performed on a pre-oriented single crystal by applying 1 T magnetic field parallel ($H_{ap} \parallel ab$, along [110] direction) and perpendicular ($H_{ap} \perp ab$, i.e. parallel to the c -axis) to the NiO₂ planes. Corresponding data will be referred as χ_{\parallel} , M_{\parallel} and χ_{\perp} , M_{\perp} , respectively. DC magnetic susceptibility curves are shown in **Fig. 6.10(a)** along with differential inverse magnetic susceptibility curves in **Fig. 6.10(b)**. No apparent anomaly is observed in χ as a function of temperature. However, three magnetic transitions could be identified from $d\chi/dT$ data. Two magnetic anomalies were observed in the $d\chi_{\parallel}/dT$ data. The first anomaly at $T_N \sim 148$ K is related to the magnetic transition of the Ni-sublattice and the second anomaly at 8 K, presumably related to the magnetic ordering of the Nd-sublattice. On the other hand, only one anomaly is observed around 16 K in the $d\chi_{\perp}/dT$ data. The 16 K anomaly is related to the reorientation of Ni magnetic moments along the c -axis as we discuss in the following section with neutron polarimetry experiments. The non-linear characteristic of the magnetic susceptibility below 150 K is predominantly due to the contribution of Nd³⁺ crystal field levels. In addition, very small magnetic anisotropy is observed between χ_{\parallel} and χ_{\perp} as shown in the insets of **Fig. 6.10(a)** and **6.10(b)** where the inverse magnetic susceptibilities and their difference are plotted, respectively. It is found that the crystallographic c -axis behaves as the magnetic easy-axis in the entire temperature range as evident from the inset of **Fig. 6.10(b)**. Fitting of the magnetic susceptibility curves were performed according to the Curie-Weiss law in the temperature range of 150-330 K. The fitted parameters are listed in **Table 6.3**. The negative Curie-Weiss temperature Θ confirms pronounced antiferromagnetic correlations at low temperature. Field dependent

isothermal magnetization curves are shown in **Fig. 6.10(c)** and differential magnetization curves are presented in **Fig. 6.10(d)**. At 300 K, the magnetization is linear with the field, an indication of paramagnetic response of the system. However, at low temperature below 10 K, field dependent magnetization curves, for both directions, become non-linear especially at high magnetic fields (> 3 T). Moreover, magnetization curves, along both directions, are far from the magnetic saturation even at 2 K with 9 T magnetic field. In addition, a sharp field induced magnetic transition is observed at $H_{ap} \sim 3.5$ T with the applied field parallel to the c -axis. The field dependent magnetic transition at 2 K is clearly noticeable in the differential magnetization curve in **Fig. 6.10(d)**.

Table 6.3 | Magnetic parameters obtained with from the fitting of ZFC magnetic susceptibilities data with Curie-Weiss law, $\chi(T) = \chi_0 + C/T + \theta$ in the temperature range of 150-330 K.

Crystallographic axis	χ_0 (emu. mol $^{-1}$)	C (emu. mol. K)	Θ (K)	μ_{eff}/μ_B
[001]	0.859×10^{-3}	3.888	-54.16	5.568
[110]	2.42×10^{-3}	2.735	-31.21	5.873

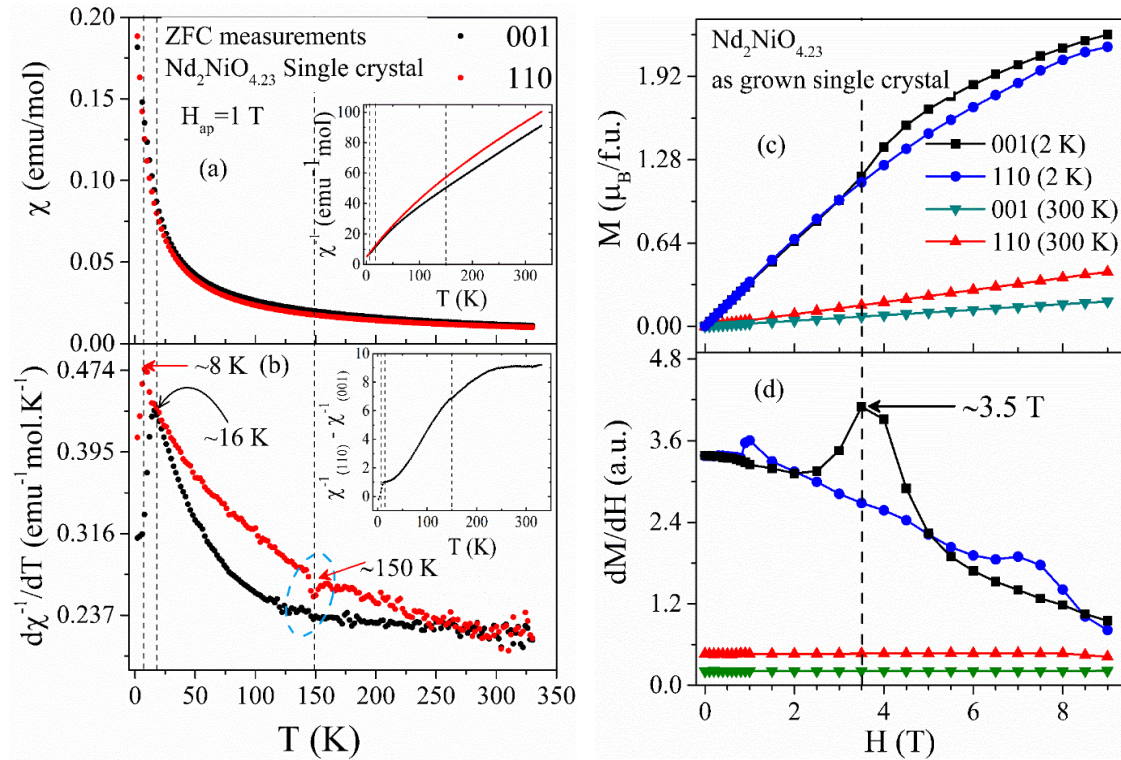


Figure 6.10 | Magnetization as a function of temperature and magnetic field of $\text{Nd}_2\text{NiO}_{4.23}$ single crystal. (a) DC magnetic susceptibility curves measured as a function of temperature in zero-field-cooled configuration for $\text{Nd}_2\text{NiO}_{4.23}$ single crystal with field parallel to [001] and [110] directions. The inset of panel (a) shows the inverse molar magnetic susceptibility curves as a function of temperature. Small anisotropy is observed in the 50-300 K range. (b) 1st order

temperature derivative of the inverse magnetic susceptibilities. The derivative curves confirm the onset of the magnetic transition around 148 K and spin reorientations at 16 K and 8 K. The inset of panel (b) shows the difference magnetic susceptibility plot in the temperature region 2-300 K showing that the crystallographic *c*-axis is the easy-axis in the whole temperature range. All magnetic transitions are marked with vertical dashed lines. (c) Isothermal *M* - *H* curves measured at 2 K and 300 K. (d) 1st order field derivative of magnetization curves indicating a field induced transition at $H_{ap} \sim 3.5$ T at 2 K when applied parallel to the *c*-axis.

6.5. Incommensurate magnetic order

6.5.1. Reciprocal plane mapping

Reciprocal plane mappings provide useful insights on the long-range ordering schemes of the interstitials as well as on the magnetic ordering at low temperature. The neutron powder diffraction study at 2 K already shows the evidence of magnetic ordering at low temperature in Nd₂NiO_{4.23}. This result is clearly inconsistent with a previously reported result in which no static magnetic order was observed for an oxidized sample⁵⁰. In order to search for magnetic propagation vectors, neutron diffraction plane mappings were performed on the pre-oriented Nd₂NiO_{4.23} single crystal at 2 K, 15 K and 300 K. Surprisingly, no additional reflections were observed in the (*hk*0) plane at 2 K compared to the 300 K data as shown in **Fig. 6.4(a)-(b)**. Mapped (*h*0*l*) reciprocal plane obtained at 2 K is shown in **Fig. 6.11(a)**. Sharp structural Bragg reflections are evidenced along with the superstructure peaks from the interstitials order. In addition, diffuse type superlattice reflections appear parallel to the reciprocal *l*-direction with approximate centering at (*h* ± ϵ , 0, *l*/2) positions with *h* and *l* being odd integer numbers i.e. 1, 3, 5...etc. and ϵ is the observed incommensurability. These reflections are not observed on the SXRPD data obtained at 5 K, most likely confirming their magnetic origin. A magnified portion of the 2 K reciprocal map is presented in **Fig. 6.11(b)** illustrating strong diffuse character of these superstructure reflections parallel to the reciprocal *l*-direction. In contrast, these diffuse incommensurate superstructure reflections are not present at 300 K map as shown in **Fig. 6.11(c)**. A representative *q_h*-cut at (*h*, 0, *l* = 1.5) reveals the incommensurability, $\epsilon \sim 0.36$ r.l.u. as illustrated in **Fig. 6.12(a)**, while the *q_l*-cut at (*h* = 0.64, 0, *l*) as presented in **Fig. 6.12(b)** shows the centering of these reflections approximately at $l = n/2$ with *n* being an odd integer number. Additionally, no temperature dependence in the modulus of ϵ is observed in the investigated temperature range. Moreover, the observed ϵ value is significantly less than the expected incommensurability ($n_h = 2\delta \sim 0.46$) for a stripe spin ordered phase, as previously ascribed for the Sr-doped La₂NiO_{4+ δ} compounds with similar hole concentration^{37,73}. Here it is worth to mention that superstructure

peaks due to stage-2 ordering of interstitials are also expected at the $(h, 0, l \pm 1/2)$ positions but with $h = \text{odd}$ and $l = \text{even integers}$ ²⁷. Therefore, the observed diffuse incommensurate superstructure peaks in our data are likely not due to stage-2 ordering of interstitials in Nd₂NiO_{4.23}. In the next section, we confirm that these diffuse superstructure reflections have magnetic origin. In-plane and out-of-plane magnetic correlation lengths are estimated from a fit of a satellite at $(0.64, 0, 1.5)$ with a Lorentzian function convoluted with a Gaussian type instrumental resolution function. Instrumental resolution parameters are obtained based on a fit of the nearest structural Bragg reflection at $(0, 0, 2)$ as twinning related broadening is absent for this reflection. The fitted Lorentzian widths are larger than the estimated resolution along both the reciprocal h and l -directions. In plane (ξ_{ab}) and out-of-plane (ξ_c) magnetic correlation lengths are estimated to be around 184(11) Å and 39(2) Å, respectively.

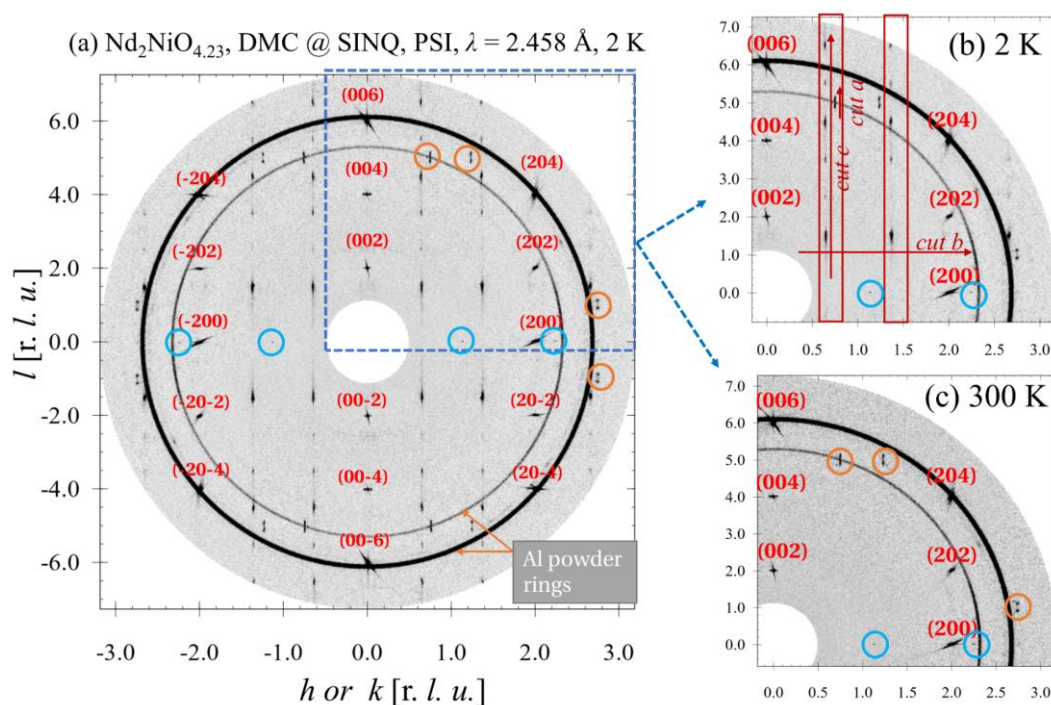


Figure 6.11 | $(h0l)$ reciprocal space plane mapping of Nd₂NiO_{4.23} crystal obtained on DMC at SINQ, PSI ($\lambda = 2.458$ Å). (a) Measured $(h0l)$ plane at 2 K. The structural Bragg reflections are marked with respective Miller indices (hkl) with regard to the average unit cell metric. Incommensurate superstructure reflections associated to the interstitials ordering are marked with brown circles. Al powder lines are from sample container visible in the mapping as circular rings. (b) and (c) are magnified views of the section of the reciprocal map as shown by blue dashed box in (a) measured at 2 K and 300 K, respectively. Presence of diffuse type incommensurate magnetic reflections are marked at 2 K with red boxes, which are not present at 300 K. The 1d line cuts are performed along reciprocal h and l directions as shown by arrows at 2 K data (panel b). Superstructure reflections marked with blue circles are also from interstitials ordering.

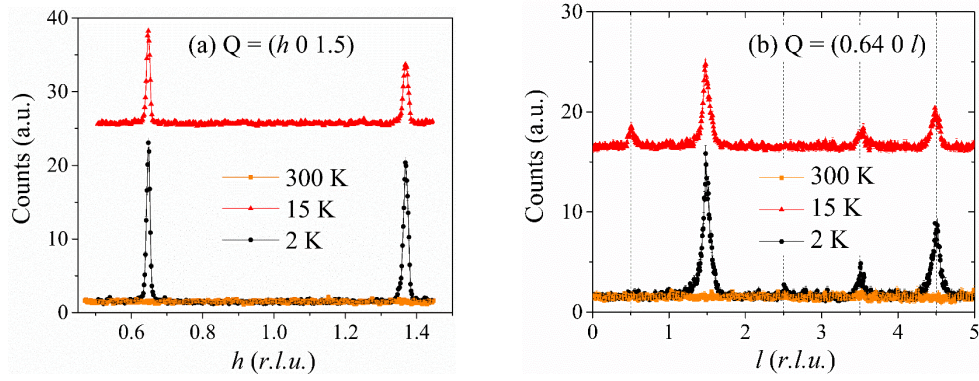


Figure 6.12 | Elastic q -cuts through the magnetic reflections obtained from $(h0l)$ reciprocal space plane mapping as shown in Fig.6.11. (a) A representative q_h -cut at $(h \ 0 \ l = 1.5)$ on the reciprocal plane mapping shows the evidence of incommensurate magnetic reflections with incommensurability $\epsilon \sim 0.36$. (c) A representative q_l -cut at $(h = 0.64 \ 0 \ l)$ shows the presence of magnetic peaks with centering at $l = n/2$ with n being an odd integer number. A magnetic transition can easily be identified between 2 and 15 K (see panel *b*).

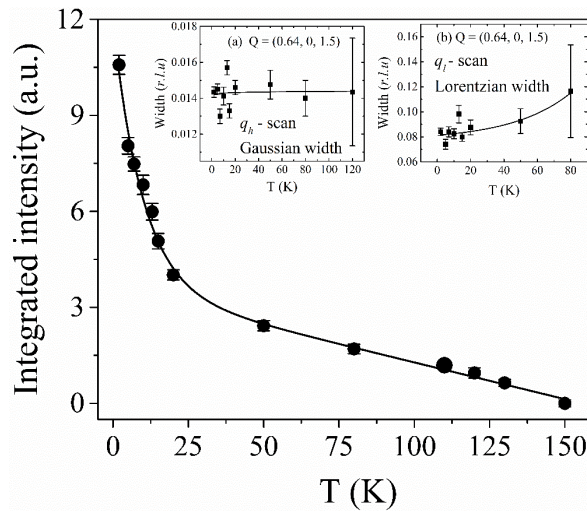


Figure 6.13 | Temperature dependence of the magnetic satellite at $Q = (0.64, 0, 4.5)$. The data was collected on EIGER at SINQ, PSI ($E_i = E_f = 14.86$ meV). Insets show the temperature dependence of widths of $(0.64, 0, 1.5)$ magnetic peak along reciprocal (a) h and (b) l -directions.

The temperature dependence of the $(0.64, 0, 4.5)$ peak is shown in **Fig. 6.13**. The integrated intensity is determined by fitting each q_h -scan by a Gaussian function with a constant background. Temperature evolution confirms the appearance of the incommensurate magnetic order below 150 K, in accordance to our DC magnetic susceptibility data. The integrated intensity of this peak smoothly increases with decreasing temperature from 150 K to 25 K and then rapidly increases below 20 K. This rapid increase is due to the polarization of Nd^{3+} in the internal

magnetic field from Ni²⁺ magnetic moments. In the insets of **Fig. 6.13(a)**, the temperature dependent widths along the reciprocal h and l directions of the magnetic satellite peak at (0.64, 0, 1.5) are presented. No pronounced change in the peak width is observed along the reciprocal h -direction with temperature. However, a small increase of the peak width is observed along the reciprocal l -direction with increasing temperature. This result suggests that the inter-plane magnetic correlations become weaker approaching the magnetic transition temperature.

6.5.2. Spherical neutron polarimetry

The origin of diffuse type incommensurate reflections (IC) was further investigated by spherical neutron polarimetry using the spin state of the incident and scattered neutrons. The polarization of a neutron beam is a statistical quantity defined as the expectation value of an ensemble of neutron spins. The spin direction of neutrons can be changed after a scattering event from a sample. This process is described by a (3×3) polarization matrix $P_{\alpha\beta}$, given by **Eq. (6.1)**. Thus, a spherical neutron polarimetry experiment consists of measuring all 18 elements in both spin-flip and non-spin-flip channels, $\sigma(\alpha, \beta)$ and $\sigma(\alpha, -\beta)$, respectively in 3D. The initial spin direction is defined by α and the final direction by β , such that,

$$P(\alpha, \beta) = \frac{\sigma(\alpha, \beta) - \sigma(\alpha, -\beta)}{\sigma(\alpha, \beta) + \sigma(\alpha, -\beta)} \text{ with } \alpha \text{ and } \beta: x, y, z \quad (6.1)$$

The polarization analysis neither sensitive to the magnetic form factor nor to the size of the magnetic moment since the polarization matrix is measured at a particular Q point and consists of normalized intensity as given by **Eq. (6.1)**. However, in practice, measuring magnetic Bragg peaks at larger $|Q|$ becomes difficult due to decrease of the magnetic form factor that consequently reduces the scattered intensity. In neutron polarimetry, a set of polarization axes is conventionally defined as follows: x -axis is parallel to Q , z -axis is perpendicular to the scattering plane and y -axis completes the right-handed coordinate system. In the (α, α) configuration, the neutrons with initial polarization along the α -direction strike the sample and detected with final polarization along the α -direction. Therefore, the detected intensity in the (α, α) configuration is from a physical process in which no reorientation of the neutron magnetic moment takes place such as nuclear scattering, which is in general termed as *non-spin-flip* (NSF) scattered intensity. Similarly, in the $(\alpha, -\alpha)$ configuration, the neutrons with initial polarization along α -direction hit the sample and detected with final polarization along negative α -direction. Therefore, neutrons with a phase change of π before and after the scattering event are detected in the $(\alpha, -\alpha)$ configuration, which is termed as *spin-flip* (SF) intensity. Thus, the intensity from the magnetic scattering is detected in the *spin-flip* channel, whereas the scattered intensity from a non-

magnetic process is not. Therefore, measuring a reflection in both *spin-flip* and *non-spin-flip* channels can independently separate the nuclear and magnetic contributions to a Bragg reflection.

To investigate the origin of IC superstructure reflections with polarimetry experiments, the single crystal was mounted in the (*h*0*l*) plane to access two intense superstructure reflections at (0.64, 0, 1.5) and (0.64, 0, 4.5). To make the following discussion simpler, we neglect the indexation due to twinning and index everything with respect to the (*h*0*l*) plane. Nevertheless, the following discussion is equally valid for the twinned (*okl*) plane. In **Fig. 6.14(a)**, a sketch of the (*h*0*l*) reciprocal plane observed with mapping at 2 K is presented. The conventional setting of the polarization axes is also shown in the figure; the *x*-*y* plane defines the (*h*0*l*) scattering plane with the *z*-axis out of the scattering plane i.e. the *z*-direction is parallel to the *b*-axis of the crystal. With this set up, typical ω -scans were performed at 2 K for both SF and NSF configurations. Typical scan profiles of (0.64, 0, 4.5) reflection are plotted in **Fig. 6.14(b)** for the (*x*, *x*) and (*x*, -*x*) configurations. Nearly ten times larger intensity is detected in the SF channel compared to the NSF channel. Hence, the polarimetry results indicate the magnetic origin of these IC reflections and doubling of the magnetic unit cell along the *c*-axis. Moreover, this observed magnetic phase largely differs with that associated with the stripe ordered state in nickelates. In a stripe ordered phase, magnetic reflections only appear at *integer values* along the reciprocal *l*-direction. Furthermore, the observed incommensurability ϵ along the *h*-direction is much smaller than the expected value (~ 0.46) for a stripe ordered phase with a similar hole concentration. In Sr-doped RP-nickelates (Ln_{2-x}Sr_xNiO_{4+ δ}), ϵ does not exactly follow the value of net hole concentration and the maximum of ϵ levels off at 0.44 for $x \geq 0.5$ ³⁷. We note that similar type of IC magnetic reflections were reported before for the La₂NiO_{4.152} compound with single crystal neutron diffraction³⁴. That study revealed the coexistence of IC magnetic peaks originating from a stripe magnetic order phase and from an unknown magnetic phase. The stripe ordered peaks appear at ($2m + l \pm \epsilon$, 0, *n*) positions with *m* and *n* integer numbers with $\epsilon \sim 0.3$. Additional IC magnetic peaks from the unknown magnetic phase appear at *l* = half integer numbers at the same *h* values where the stripe magnetic peaks appear. Since the peak widths of these IC reflections were resolution limited along the reciprocal *l*-direction, these peaks were assumed to be due to a certain long-range magnetic order. However, no magnetic model was proposed to account for these reflections. In our present study, the observed magnetic order is most likely similar to that corresponds to the unknown magnetic phase observed in La₂NiO_{4.152} single crystal. However, in the present case of Nd₂NiO_{4.23}, the magnetic peaks are strongly diffuse along the *c*-axis. In addition, in our sample, no superstructure reflections were observed that correspond to the stripe magnetic order.

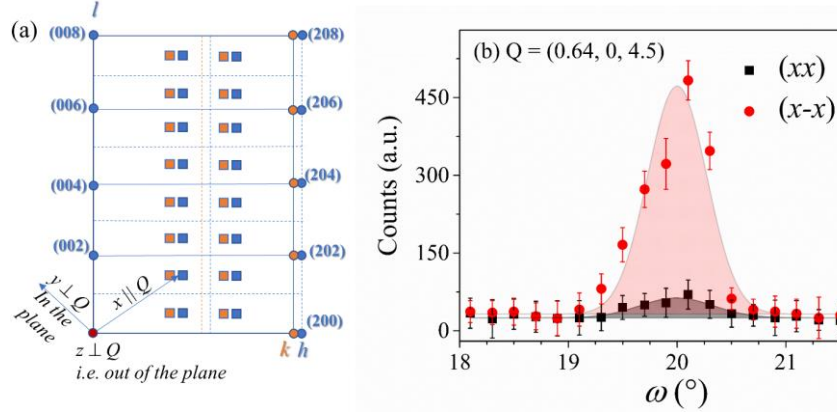


Figure 6.14 | Spherical neutron polarimetry measurements on $\text{Nd}_2\text{NiO}_{4.23}$ single crystal. (a) Idealized sketch of the reciprocal $(h0l)$ plane showing the positions of structural (circles) and magnetic (squares) Bragg peaks. Structural twin domains are largely exaggerated for clear observation. Two domains are presented with two different colors. With respect to the conventional axes labelling of neutron polarimetry, x is parallel to Q , z is perpendicular to Q and out of plane, y completes the right hand coordinate system. (b) Spin-flip $(x, -x)$ and non-spin-flip (x, x) intensities of $(0.64, 0, 4.5)$ reflection measured at 2 K on TASP at SINQ, PSI ($\lambda = 3.14 \text{ \AA}$) with MUPAD.

In this work, we attempt a group theoretical approach to find a magnetic model for the observed magnetic phase with least-square refinements of the integrated intensity data of a set of magnetic Bragg peaks combining with neutron polarization measurements. The positions of IC magnetic reflections in our data are represented by a magnetic propagation vector $\mathbf{k} = (0.64, 0, 0.5)$. The average structural symmetry of the paramagnetic phase is well represented by $Fmmm$ space group without taking into account the subtle monoclinic distortion in the crystal structure. Group theory can predict possible magnetic structures emanating from the paramagnetic group. The program BASIREPS was used to calculate the possible irreducible representations (IRs) valid with the propagation vector \mathbf{k} . The magnetic representation at the Ni and Nd sites with Wyckoff positions $4a$ and $8i$ can be decomposed into a direct sum of IRs as $\Gamma_{\text{mag}} = 1 \Gamma(1) + 2 \Gamma(2)$. The Nd site is split into two orbits related by a center of inversion. All calculated IRs are one-dimensional. The basis vectors ψ for different IRs are calculated using the projection operator technique. The spin distribution of the j -th atom can be expressed as the Fourier transform of the linear combination of basis vectors, such that for a single propagation wave vector,

$$S_j = \sum_n C_n \psi_n e^{ik \cdot r} + c. c. \quad 6.2$$

where the coefficients C_n can be complex, in general. Magnetic moments, for the Ni and Nd sites at (000) and $(00z)$ respectively, obtained from the basis function calculated for the $\Gamma(1)$ and $\Gamma(2)$

resolved along the crystallographic axes as $(0, \nu, 0)$ and $(u, 0, w)$, respectively. Magnetic structure refinements allows the determination of the free parameters u , ν and w experimentally. That means the magnetic moments are either pointing along the b -axis (i.e. in $\Gamma(1)$, hereafter denoted as G1 model) or lying on the ac -plane (i.e. in $\Gamma(2)$, hereafter denoted as G2). To check which model represents our data, least-square refinements of the single crystal neutron diffraction data were carried out. Integrated intensities of 18 magnetic reflections were collected with ω -scans with the crystal oriented on the $(h0l)$ reciprocal plane. In addition, integrated intensities of six structural Bragg reflections were collected to derive the scale factor for the magnetic structure analysis. A least-square fitting of the integrated intensity data were carried out with the G1 and G2 magnetic models. However, the refinements are not straightforward. First, an isotropic magnetic form factor of Ni²⁺ is used for the refinements, which is not true as Ni³⁺ ions are also present in the sample. Furthermore, the magnetic form factor strongly deviates from its isotropic character due to covalent bonds. Second, observed magnetic peaks are strongly diffuse. Therefore, the integrated of intensities with typical ω -scans contain certain systematic errors. Third, the number of structural and magnetic reflections used in the least-square refinements and polarization analysis is low. The absolute values of the magnetic moments obtained for Ni and Nd-sites may contain large errors. Consequently, the following discussion is semi-quantitative. Nevertheless, our measurements certainly suggest a unique magnetic order present in the strongly oxygen-doped systems of RE₂NiO_{4+ δ} .

It was found with least-square refinements that both G1 and G2 models provide a similar quality of fit to the observed integrated intensity data as shown in **Fig. 6.15(a)-(b)**. Nonetheless, the G1 model fits the data slightly better. The refined magnetic structures are visualized in **Fig. 6.15** and the refinements results are tabulated in **Table 6.4**. Now, we turn to neutron polarization analysis to find the correct magnetic structure. For that, complete polarization matrices (all 18 components) were recorded at 2 K for two magnetic satellites at $Q_1 = (0.64, 0, 1.5)$ and $Q_2 = (0.64, 0, 4.5)$. For the estimation of the neutron polarization efficiencies, polarization matrices were measured for two nuclear reflections at $(2, 0, 0)$ and $(0, 0, 2)$. Furthermore, a complete polarization matrix was recorded for a background point at $Q_3 = (0.68, 0, 1.4)$ at 2 K to eliminate the systematic errors. Intensities of few selected structural Bragg reflections were measured in both SF and NSF channels. This allows determination of polarization efficiency of the neutron beam that corresponds to 96%. The recorded matrix elements after background corrections for two magnetic satellites are presented in **Table 6.5**. We note that, for these satellites, $P(x, x) \neq P(y, y) \neq P(z, z)$ and both $P(x, x)$ and $P(y, y)$ are negative while $P(z, z)$ is positive and all the other elements are zero within statistics except the $P(y, z)$ for $(0.64, 0, 1.5)$. Referring to the polarization tensor in reference⁸⁴, these results reveal pure magnetic character of these reflections. However, the mixed term $P(y, z)$ for $(0.64, 0, 1.5)$ arises due to the interference effect between M^x and M^z components.

To determine which magnetic model is consistent with the observed polarization matrices, we have calculated the polarization matrices for these two magnetic satellites using both G1 and G2 magnetic models with the *MuFit* program assuming a single domain sample¹²². Calculated polarization matrices are presented in **Table 6.5**. It turns out that the G1 magnetic model is qualitatively in accordance with the observed polarimetry data. In contrast, the G2 model does not match the observed data at all and is excluded by the polarimetry method. However, the presence of the mixed term could not be explained by either magnetic model within the approximation of a single domain sample. The mix term may originate from the overlap of scattering intensities from different domains present in the crystal. In a multi-domain sample, both the cross section and the scattered polarization have to be calculated for each magnetic domain and summed up with weights proportional to the domain fraction. Blume¹²³ and Maleyev¹¹⁸ equations are strictly valid for a single domain sample and relates different elements of the polarization matrix with different scattering processes as outlined in reference⁸⁴. In the case of multi-domain sample, the scattering cross-section in Eq. (1) becomes $\sigma(\alpha, \beta) \rightarrow \sum_n f_n \sigma_n(\alpha, \beta)$, where the fraction of the n -th domain is given by f_n . Two possible types of domains can exist in our single crystal sample. The first possibility is the presence of structural twin domains. In the case of the $(h0l)$ plane, two structural twins are related by a four-fold rotation matrix about the c -axis. Incorporation of such structural twins in our calculation does not affect the mixing term at all. The other possibility is the presence of multiple magnetic domains. The most common types of magnetic domains are configuration K-domains and orientation S-domains. The scattered intensity at any particular Q is not affected by the presence of multiple K domains. Therefore, they are not included in our calculations. Orientation S-domains occur whenever a magnetic structure has lower symmetry than the configurational symmetry. S-domains can affect the mixing term and can depolarize the scattered beam. In the present case, two S-domains are created by the x - z mirror plane. However, inclusion of S-domains also does not produce the mix term. Another possible origin of the mix term could be the tilting of magnetic moments away from the b -axis into the ac -plane. Our test calculations indeed confirm the possibility that the magnetic interference term can be simulated only if the magnetic moments are slightly tilted away from b -axis into the ac -plane. In terms of symmetry, the tilting of the magnetic moments toward the ac -plane is not restricted and feasible with $\Gamma(3)$ representation. The $\Gamma(3)$ magnetic mode (hereafter denoted as G3 model) can be represented by the linear combination of G1 and G2 modes. Magnetic moments for the Ni and Nd sites obtained from the basis function calculated for the G3 mode resolved along the crystallographic axes as (u, v, w) where u, v and w are free parameters to be determined with refinements. The G3 model fits the data significantly better as presented in **Fig. 6.11(c)** and reveals a large magnetic component in the ac -plane. The least square refinement results are presented **Table 6.3**. With the G3 magnetic model, calculated polarization matrices for the satellite reflections at Q₁ and Q₂ that are in good

agreement ($\chi^2 = 7\%$) with the observed polarization matrices. In the final step, the fractions of the S-domains were refined to obtain the best fit ($\chi^2 = 4\%$) with the observed data. Fitted matrices are presented in **Table 6.4**. The resulting magnetic structure is visualized in **Fig. 6.15(c)**.

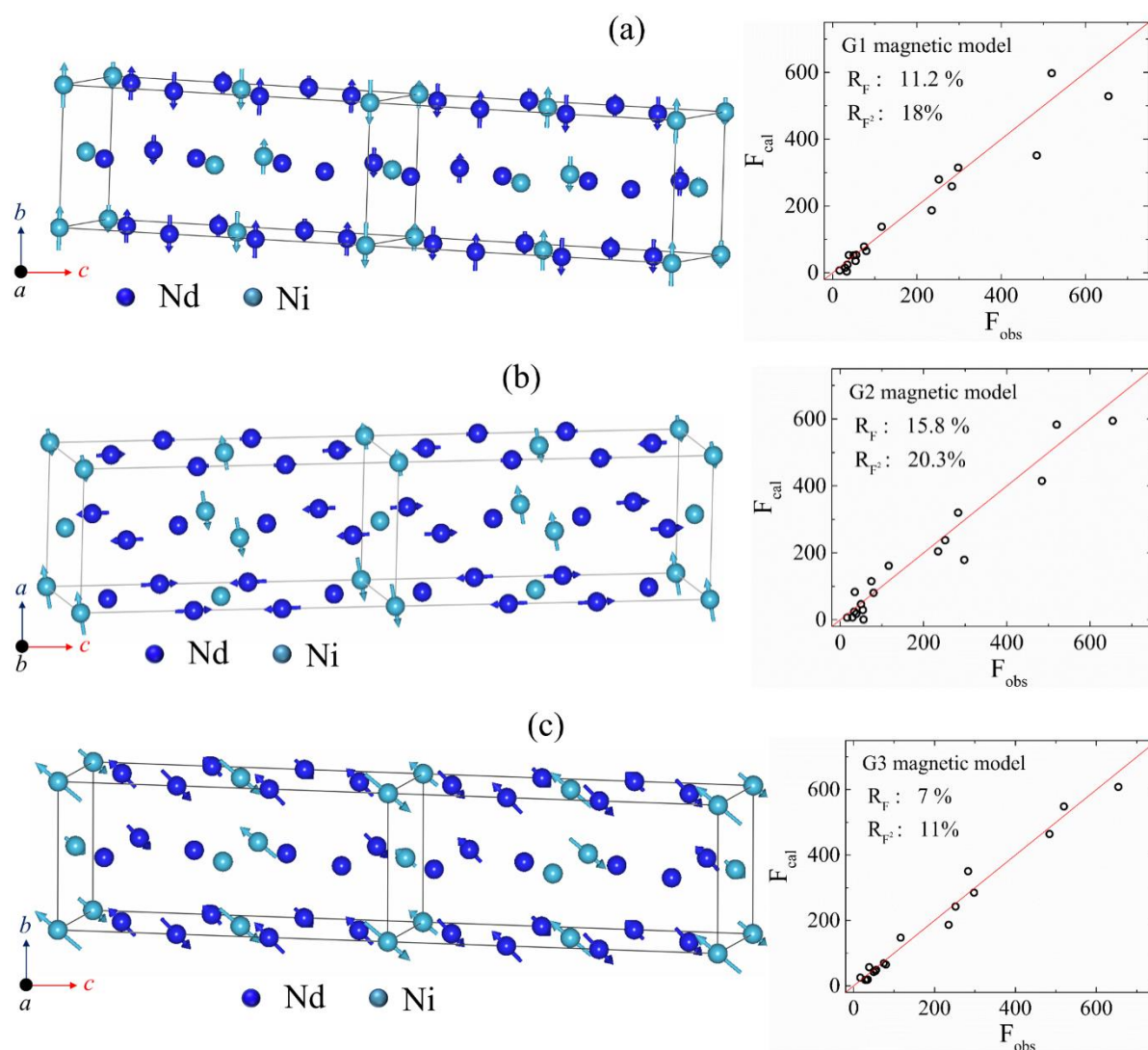


Figure 6.15 | Incommensurate magnetic structure of $\text{Nd}_2\text{NiO}_{4.23}$. Possible Magnetic structures are obtained with integrated intensity data. (a) G1 magnetic model with spins parallel to the b -axis. (b) G2 magnetic model with spins lying on the ac -plane. (c) G3 magnetic model with tilted spins from the b -axis into the ac -plane. In the right side, each figure presents a plot of the calculated versus observed structure factors resulting from the least-square refinements of integrated intensity data of magnetic reflections.

Now, we discuss the temperature evolution of the matrix elements obtained with neutron polarimetry experiments at $Q_1 = (0.64, 0, 1.5)$. Different matrix elements are plotted in **Fig. 6.16** as a function of temperature in the temperature range of 2-20 K. The matrix element $P(x, x)$ remains constant over the investigated temperature range. However, the matrix elements $P(y, y)$ and $P(z,$

z) increase sharply from -0.53(6) to -0.93(5) and 0.46(6) to 0.83(5), respectively with increasing temperature. The mix term $M_{mix} \sim P(y, z)$ simultaneously decreases from 0.50(6) to 0.06(6) with increasing temperature from 2 to 20 K. The temperature evolution suggests a reorientation of the magnetic moments between 2 and 20 K, possibly at 16 K as revealed previously with our magnetic susceptibility data parallel to the c -axis. The full polarization matrix recorded at 20 K is presented in **Table 6.4**. Comparison of the recorded matrix elements at 20 K with the calculated ones with the G1 magnetic model suggests that the magnetic moments are strictly pointing toward the b -axis at 20 K. Therefore, the ac -component of magnetic moment is lost in the rearrangement process that consequently produces an anomaly in the susceptibility data at 16 K. Since the magnetic ordering of the Nd-sublattice occurs around 8 K, the rearrangement process at 16 K is likely to be correlated with the Ni²⁺/Ni³⁺ magnetic moments. It is worth to point out that the Nd³⁺ ions follow the same magnetic representation as the Ni-ions below their magnetic ordering temperature at 8 K. What causes the spin rearrangement at 16 K of Ni-magnetic moments? We note that the onset of the magnetic order in the Nd-sublattice is induced by the combination of two effects as discussed for the undoped Nd₂NiO_{4.0} compound by Battle et al.¹¹⁵. At higher temperatures ~ 25 K as in the present case, the Nd-sublattice is under strong local exchange field from Ni²⁺/Ni³⁺ cations ($J_{Ni-Nd} > J_{Nd-Nd}$). Therefore, the intensity of magnetic reflection (*cf.* **Fig. 6.13**) rapidly increases due to the polarization of Nd³⁺ in this strong internal field. At lower temperature around 8 K, the cooperative ordering occurs when J_{Nd-Nd} becomes significant. We speculate that at $8 \text{ K} < T < 25 \text{ K}$, short-range magnetic order persists for the Nd-sublattice that in succession induces the magnetic rearrangement of the Ni-moments.

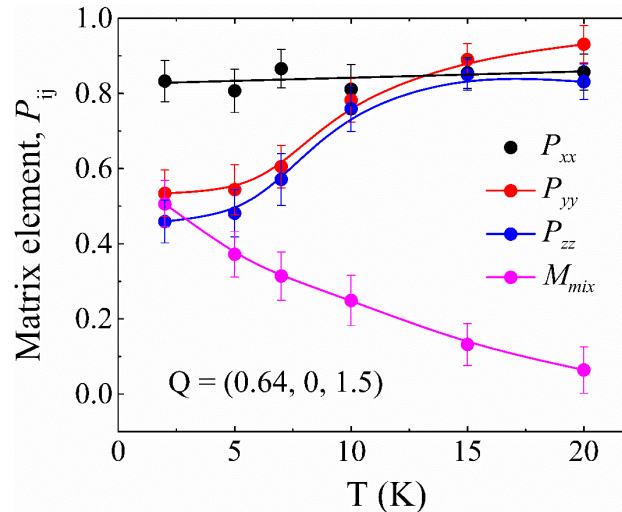


Figure 6.16 | Temperature evolution of polarization matrix elements. Polarization matrix elements were recorded for the (0.64, 0, 1.5) magnetic reflection. Measurements were performed on TASP at SINQ, PSI ($\lambda = 3.14 \text{ \AA}$) with MUPAD.

Table 6.4 | Least-square refinement results of the integrated intensity data obtained at 2 K. Magnetic models G1, G2 and G3 were used for least-square refinements.

	R_F (%)	R_F^2 (%)	Ni-site at (0, 0, 0)				Nd site at (0, 0, z)			
			μ_x (μ_B)	μ_y (μ_B)	μ_z (μ_B)	μ_{total} (μ_B)	μ_x (μ_B)	μ_y (μ_B)	μ_z (μ_B)	μ_{total} (μ_B)
G1 ν_1 : (010)	11.2	18	0	1.016	0	1.016	0	0.842	0	0.842
G2 ν_1 : (100) ν_2 : (001)	15.8	20.3	0.656	0	0.13	0.7	0.03	0	0.57	0.573
G3 ν_1 : (100) ν_2 : (010) ν_3 : (001)	7	11	0.44	0.95	1.03	1.48	0.46	0.78	0.62	1.09

Table 6.5 | Measured and calculated polarization matrices for (0.64, 0, 1.5) and (0.64, 0, 4.5) magnetic reflections at 2 K and 20 K. G1, G2 and G3 magnetic models were used for matrix elements calculations with MuFit program. Matrices are recorded with MUPAD on TASP at SINQ, PSI.

	$Q_1 = (0.64, 0, 1.5)$				$Q_2 = (0.64, 0, 4.5)$			
	Measured	Calculated			Measured	Calculated		
		G1 ($\chi^2 = 12\%$)	G2 ($\chi^2 = 73\%$)	G3 ($\chi^2 = 4\%$)		G1 ($\chi^2 = 12\%$)	G2 ($\chi^2 = 73\%$)	G3 ($\chi^2 = 4\%$)
2 K	-0.83(6), -0.12(6), 0.17(6) 0.12(6), -0.53(6), 0.42(6) 0.07(7), 0.50(6), 0.46(6)	-0.85, 0, 0 0, -0.85, 0 0, 0, 0.85	-0.85, 0, 0 0, 0.85, 0 0, 0, -0.85	-0.85, 0, 0 0, 0.85, 0.58 0, 0.58, -0.85	-0.77(4), 0.05(5), 0.10(5) -0.02(5), -0.71(5), -0.17(5) 0.13(5), -0.10(5), 0.68(4)	-0.85, 0, 0 0, -0.85, 0 0, 0, 0.85	-0.85, 0, 0 0, 0.85, 0 0, 0, -0.85	-0.85, 0, 0 0, 0.85, -0.18 0, -0.18, -0.85
20 K	-0.85(5), -0.06(6), 0.14(6) 0.11(6), -0.93(5), 0.06(6) 0.09(6), 0.03(6), 0.83(5)							

6.5.3. Magnetic field dependence

Inspired by the field dependent magnetization data (**Section 6.4**), a field dependence effect on the magnetic Bragg peaks was studied by neutron diffraction below 10 K with applied magnetic field $H_{ap} \parallel c$ -axis. In **Fig. 6.17**, we plot the influence of external magnetic field and temperature on the intensity of the magnetic satellite at (0.64, 0, 2.5). This particular magnetic peak is weak compared to the other satellites and appears only below $T \sim 8$ K and then rapidly increases with decreasing temperature down to 2 K. Such temperature dependence implies that this particular magnetic satellite could directly be related to the ordering of Nd^{3+} ions. Upon application of the magnetic field $\parallel c$ -axis i.e. perpendicular to the NiO_2 -planes, strong decrease in the peak intensity is observed with $H_{ap} \geq 3.5$ T and $T \leq 8$ K, in fine agreement to our field dependent macroscopic magnetization data. The peak intensity decreases by 40% upon the application of magnetic field of 5.5 T at 2 K. The l -scan profiles of the magnetic peak is presented in the inset of **Fig. 6.17** for $H_{ap} = 0$ and 5.5 T. In strong contrast, the intense magnetic satellite peak at (0.64, 0, 1.5) does not show any magnetic field induced effect at any temperatures. If the reduction in the intensity upon application of magnetic field is due to the decrease either in magnetic volume fraction or in the ordered magnetic moments, this should affect the all the magnetic peaks at all values of the out of plane wave vector l . Therefore, the field-induced effect observed here is probably due to the strong contribution of Nd^{3+} magnetic moments on the magnetic structure factor of the magnetic satellite at (0.64, 0, 2.5) and the rotation of Nd^{3+} magnetic moments under the magnetic field. However, the neutron diffraction data is not enough to prove this speculation and quantify the change in the magnetic structure in presence of magnetic field.

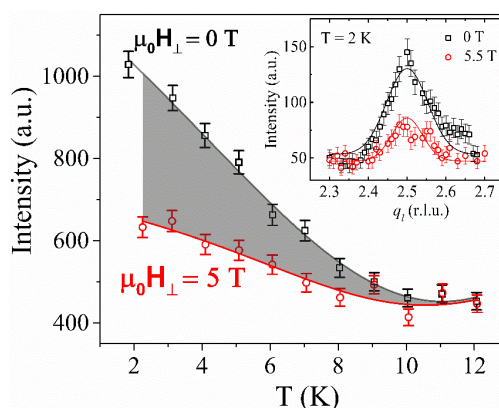


Figure 6.17 | Magnetic field and temperature dependence of the (0.64, 0, 2.5) magnetic peak. Evolution of peak top intensity with temperature without and with applied magnetic field of 5 T. Magnetic field is applied parallel to the crystallographic c -axis i.e. perpendicular to the NiO_2 planes. Measurements were performed at RITA II at SINQ, PSI ($E_i = E_f = 3.4$ meV). The inset shows the magnetic field dependence of peak profile of the corresponding reflection at 2 K. Solid lines are only guide to the eyes.

6.6. Conclusions

The crystal structure, apical oxygen disorder, interstitials and spin ordering are investigated for the Nd₂NiO_{4.23} compound in the temperature range of 2-1073 K. We conclude that

- (i) A complex phase transitions sequence has been revealed for Nd₂NiO_{4.23} in the investigated temperature range. Strong structural modulations corresponding to the 3D ordering of excess oxygens are observed in both powder and single crystal diffraction data. The average crystal structure could well be described by a monoclinic unit cell metric with F112/*m* space group symmetry. The monoclinic to tetragonal structural phase transition occurs at 813 K.
- (ii) Strong anisotropic thermal displacement of apical oxygen atoms toward nearest vacant interstitial sites are found. The modulus of thermal displacement parameters are largely increased, on an absolute scale, compared to the moderately doped Nd₂NiO_{4.11} phase. In addition, diffuse type systematic anharmonic local displacements of the apical oxygen atoms are observed induced by oxygen interstitials, which are expected to be important prerequisite to have oxygen mobility in RE₂NiO_{4+δ} oxides close to room temperature.
- (iii) Ni²⁺ spins are antiferromagnetically ordered at low temperature with T_N ~ 150 K while the magnetic ordering of the Nd³⁺ ions is detected below 10 K. The incommensurate magnetic structure is characterized by the magnetic satellites at (*h* ± *ε*, 0, *l*/2) with *h* and *l* being odd integer numbers with *ε* ~ 0.36. Combining neutron polarization analysis with group theory, a magnetic model is proposed. It quantitatively explains the positions and intensities of these incommensurate peaks. At 2 K, both Ni and Nd moments are tilted away in the *ac*-plane from the *b*-axis. However, a magnetic transition at 16 K suppresses the *ac*-component of the magnetization such that spins strictly point towards the *b*-axis at T > 16 K. Furthermore, a weak magnetic field dependence is observed when the applied field is parallel to the *c*-axis below 10 K. The observed magnetic phase seems substantially different from a stripe ordered phase observed in Sr-doped La-based RP-Nickelates with similar hole concentration.

Output

1. A manuscript containing the results related to crystal structure (sections 6.1 and 6.3) and magnetic structure (sections 6.5.1 and 6.5.3) of Nd₂NiO_{4.23} is under preparation.

Chapter 7

Investigations on crystal structure and magnetic properties of Sr-doped $\text{Nd}_{2-x}\text{Sr}_x\text{NiO}_{4+\delta}$

In recent years, Sr-doped $\text{RE}_2\text{NiO}_{4+\delta}$ compounds are extensively studied because of their remarkable physical properties resulting from the subtle interplay of lattice, charge and spin degrees of freedom. Sr^{2+} randomly replaces RE^{3+} in the chemical unit cell and injects holes in the NiO_2 planes³⁵. These holes segregate in array of parallel regions forming charge stripes separating antiferromagnetically ordered domains, which are essentially undoped. Neighboring antiferromagnetic domains have an antiphase relationship. These charge stripes run diagonal to the Ni-O-Ni bonds⁶⁸. Our TGA analyses (**sec. 4.1.2**) reveal that all $\text{Nd}_{2-x}\text{Sr}_x\text{NiO}_{4+\delta}$ samples are oxygen over-stoichiometric in the range of $0.1 \leq x \leq 0.7$. However, the δ value strongly depends on the Sr concentration. These excess oxygens occupy regular tetrahedral interstitial site inside the RE_2O_2 layers and strongly modify structural and magnetic properties of these compounds as discussed in chapter 5 and chapter 6. In this chapter, structural, thermodynamic and magnetic properties of Sr and oxygen codoped samples of $\text{Nd}_{2-x}\text{Sr}_x\text{NiO}_{4+\delta}$ system with $0.1 \leq x \leq 0.7$ are investigated in the temperature range of 2-800 K.

The present chapter is organized as follows. Distinct structural phases of (Sr, O)-codoped samples of $\text{Nd}_{2-x}\text{Sr}_x\text{NiO}_{4+\delta}$ system as revealed by synchrotron X-ray diffraction measurements are reported in **section 7.1**. Based on these results, a structural phase diagram is proposed for the $\text{Nd}_{2-x}\text{Sr}_x\text{NiO}_{4+\delta}$ system. The ordering of interstitials and its effect on the apical oxygen disorder is reported in **section 7.2**. The significance of excess oxygens on low temperature oxygen mobility is drawn from these results comparing with purely oxygen samples. Results of macroscopic magnetic properties and specific heat measurements are reported in **section 7.3** and **section 7.4**, respectively. Powder and single crystal neutron diffraction measurements displaying complex charge and spin ordering in $x = 0.5$ are summarized in **section 7.5**.

7.1. Structural phase diagram of Nd_{2-x}Sr_xNiO_{4+δ}

Room temperature synchrotron x-ray diffraction patterns of the Sr-doped powder samples show sharp structural Bragg peaks reflecting high quality of these samples. All the samples were found to be single phased with K₂NiF₄ type structure (*cf.* **Fig. 7.1**). No secondary phase was detected in any powder samples except a small amount of unreacted NiO. In the following, before presenting the SXRPD data, a short summary of allowed and extinct structural Bragg reflections is presented that allows identifying different phases appearing at different Sr content x , excess oxygen content δ and temperature T .

In the following discussion, (hkl) indexation is referred to the HTT structure with $F4/mmm$ space group. The LTO phase with $Bmab$ space group, in which the NiO₆ octahedrons rotate antiferrodistortively around the [100] direction, is characterized by a splitting of (hkl) type reflections with $h \neq k$ like (200)/(020) and (515)/(155). Moreover, superlattice reflections such as (212) or (012) are also present, attributable to the long-range coherent NiO₆ octahedral tilt pattern. In the LTT phase, the octahedral tilt axis changes to the [110]-direction. The tilt axis alternates by 90° in adjacent NiO₂ layers. In this LTT phase with $P4_2/ncm$ space group, the splitting of (hkl) type reflections is absent for $h \neq k$ but the superlattice reflections like (212) and (012) still exist. A biphasic region comprising of LTO-LTT phases can be identified by the coexistence of split and non-split (hkl) reflections with $h \neq k$ due to different lattice constants of the LTO and LTT phases. In the LTLO phase with $Pccn$ symmetry, the tilt axis is lying on the basal plane in between [100] and [110], shows a similar but reduced orthorhombicity compared to the LTO phase. The LTLO phase is observed neither for the undoped Nd₂NiO_{4.0} nor for any Sr/O-doped compounds at any temperature as discussed below. The LTO' phase with $Fmmm$ symmetry is similar to the LTO phase. However, no superstructure reflections are present in the diffraction pattern due to large disorder in the octahedron tilt pattern, and the orthorhombic splitting is less than in the LTO phase. The structural distortions in the LTM phase with $F112/m$ space group are identical to the LTO' phase. However, an additional splitting of $(hh0)$ type reflections is present in the LTM phase. In the HTT phase with $F4/mmm$ symmetry, no coherent long-range tilt pattern of NiO₆ octahedron is present. Thus, superlattice reflections such as (212) and (012) are absent in the HTT phase. However, short-range octahedral tilt correlations may still exist due to local lattice distortion associated with the excess oxygen and Sr dopants. The biphasic region comprised of LTT and HTT phases can be identified from the splitting of the $(00l)$ reflections due to the large difference in the absolute values of the c -axis lattice parameters. Furthermore, the c -axis lattice parameter is also different for the LTO and LTO' phases.

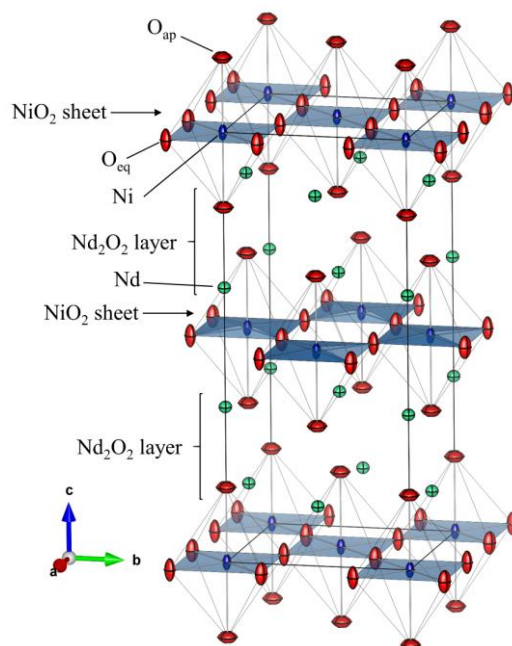


Figure 7.1 | Schematic representation of the anisotropic layered crystal structure of $\text{Nd}_{2-x}\text{Sr}_x\text{NiO}_{4+\delta}$ system. The crystal structure was obtained from the refinement of high-resolution x-ray powder diffraction data of $x = 0.5$ at 300 K. The layered structure consists of alternating NiO_2 sheets and rock salt Nd_2O_2 layers along the c -axis.

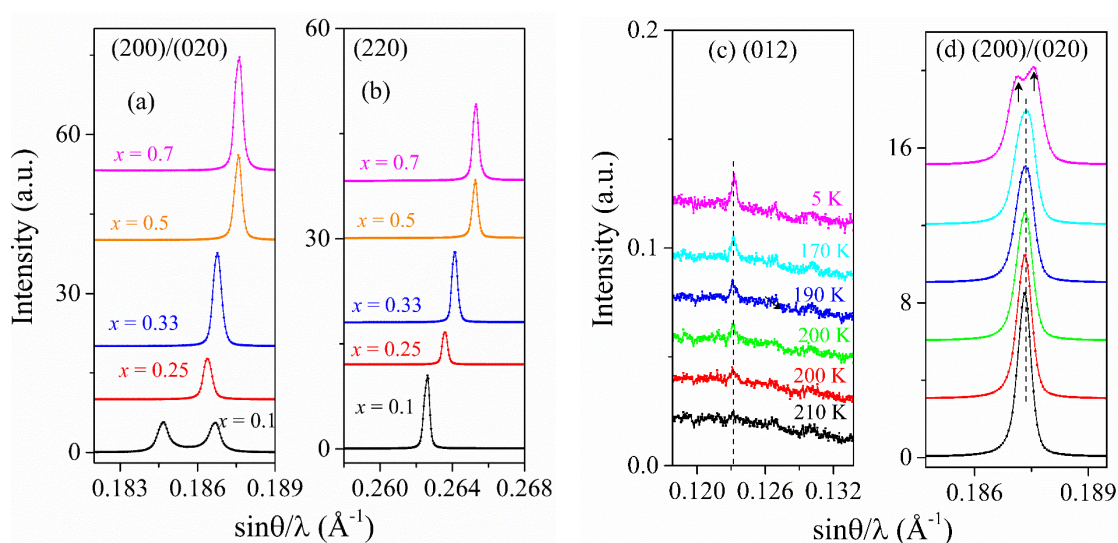


Figure. 7.2 | Excerpts of room temperature synchrotron powder patterns of $\text{Nd}_{2-x}\text{Sr}_x\text{NiO}_{4+\delta}$ system as a function of Sr-content. Measurements were performed on MS-X04SA at SLS with $\lambda = 0.6208(1)$ Å. Profiles of (a) (200)/(020) and (b) (220) reflections showing LTO' to HTT phase transformation at room temperature as a function of x . Profiles of (c) (012) and (d) (200)/(020) Bragg reflections with decreasing temperature confirming HTT to LTO phase transition in $x = 0.5$.

Synchrotron x-ray diffraction patterns collected at room temperature for Nd_{2-x}Sr_xNiO_{4+δ} system are shown in **Fig. 7.2** where few characteristic reflections are presented to distinguish different structural phases. In the present study, no biphasic region is observed in any powder samples at any Sr content x and temperature T . For $x = 0.1$, $(h00)/(0k0)$ reflections (**Fig. 7.2(a)**) are split into two reflections, though, the splitting of $(hh0)$ type reflections are absent. These observations suggest orthorhombic LTO' type crystal structure for $x = 0.1$. The LTO' phase is observed only for oxygen doped samples with high excess oxygen content $\delta \sim 0.23$. Therefore, the observation of the LTO' phase for $x = 0.1$ with $\delta \sim 0.11$ is puzzling and perhaps indicates that even $\delta \sim 0.11$ is enough to destroy the long-range tilting pattern of NiO₆ octahedron in Nd_{1.9}Sr_{0.1}NiO_{4+δ}. A HTT phase is observed for $x \geq 0.25$, as the splitting of main structural Bragg reflections vanishes and superstructures reflections such as $(012)/(212)$ are absent in powder diffraction patterns collected at room temperature. The LTT phase was not detected for any Sr-doped samples at any temperature since the required δ value was not close enough in the prepared powder samples. Therefore, this SPXRD study reveals sequence of structural transitions as a function of Sr-doping at RT. With increasing Sr concentration, the structural transformation from LTM (for $x = 0$ and $\delta = 0.23$ as discussed in **chapter 6**) to LTO' occurs at $x \sim 0.1$ and LTO' to HTT phase transition occurs in between 0.1 and 0.25. This observation is in accordance with the reported results by Arbuckle et al.¹²⁴. In addition to the structural Bragg reflections, additional incommensurate (IC) superstructure reflections are also observed in the diffraction patterns of $x = 0.1, 0.25$ and 0.33 . Observed IC superstructure reflections (*cf.* **Fig. 7.8**) are qualitatively identical in all these samples and absent for $x = 0.5$ and 0.7 compounds. The superstructure reflections at first sight appeared to be from long-range ordering of excess oxygen atoms. However, as discussed in the next section (section 7.2), they are from an intergrowth phase.

All the SXRPD patterns collected at room temperature were analyzed by Rietveld method. Representative refinement patterns are presented in **Fig. 7.3** for reference. For all refinements, the occupancies of all atoms were fixed to the ideal composition. The additional oxygen content was fixed as determined by TGA analysis. Positional and thermal parameters of all atoms were refined without any constraints. Thermal displacement parameters have been refined anisotropically within the harmonic approximation. Refinement results for $x = 0.5$ are tabulated in **Table 7.1** while for other samples they are tabulated in **Appendix D**. The refined room temperature crystal structure of $x = 0.5$ is displayed in **Fig. 7.1**. Extracted lattice parameters and bond lengths at room temperature are shown in **Figs. 7.4(a)** and **7.4(b)**, respectively. The c -axis lattice parameter increases with the Sr-content with a maximum at $x = 0.5$ and then decreases for $x > 0.5$. On the other hand, the a - and b -axis lattice parameters decrease monotonically with increasing Sr-content until $x \sim 0.5$ and then remains almost constant for $x > 0.5$. At the same time,

the Ni-O_{eq} bond length follows a similar variation as the *a*- or *b*-lattice parameters while the Ni-O_{ap} bond length replicates the evolution of the *c*-axis. These structural changes strongly signify a modification in the Ni orbital state with Sr-doping. In undoped $\text{Nd}_2\text{NiO}_{4.0}$, Ni^{2+} ions ($3d^8$) are in the high-spin state with two electrons occupying the e_g orbital and one electron placed in each $d_{x^2-y^2}$ and $d_{z^2-r^2}$ orbital. As pointed out earlier in previous studies that doped holes due to the Sr-doping first enters into the $d_{x^2-y^2}$ orbital up to $x \sim 0.5$ and then into the $d_{z^2-r^2}$ orbital for $x \geq 0.5$ ^{36,124}. Therefore, with increasing Sr-concentration, the density of Ni^{3+} site ($3d^7$, in low-spin state) with unoccupied $d_{x^2-y^2}$ orbital increases until $x \sim 0.5$. Consequently, the *a*- and *c*-axis lattice parameters start to decrease and increase, respectively up to $x \sim 0.5$. This displays the presence of a strong electron-phonon coupling in the e_g orbital systems with K_2NiF_4 -type structure⁶³. This result alludes that the electrons and holes in $d_{x^2-y^2}$ orbital form the stripe and checkerboard charge ordering on the NiO_2 planes. However, the increase in Nd/Sr-O_{ap} bond length with increasing x is completely due to continuous substitution of smaller Nd^{3+} ions with larger Sr^{2+} ions in $\text{Nd}_{2-x}\text{Sr}_x\text{NiO}_{4+\delta}$.

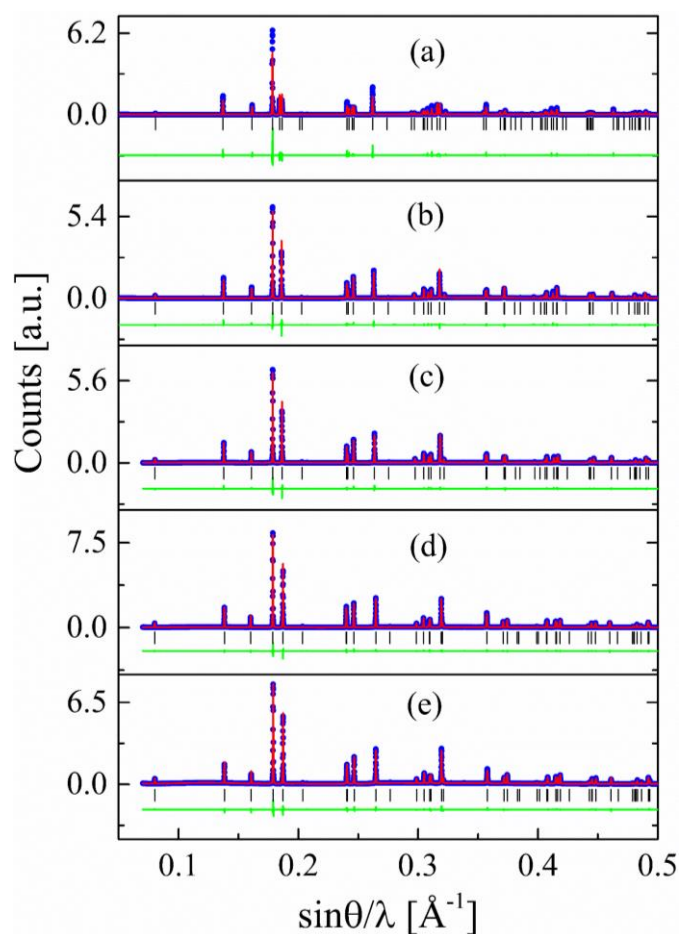


Figure 7.3 | Representative Rietveld fits of synchrotron powder diffraction data of $\text{Nd}_{2-x}\text{Sr}_x\text{NiO}_{4+\delta}$ compounds collected at 300 K on MS-X04SA at SLS with $\lambda = 0.6208(1)$ Å. Refinements of powder data collected on (a) $x = 0.1$ (LTO'), (b) $x = 0.25$ (HTT), (c) $x = 0.33$ (HTT), (d) $x = 0.5$

(HTT) and (e) $x = 0.7$ (HTT). Closed blue symbols represent the experimental data, solid red lines are the models, and solid green lines represent the differences. Vertical black lines mark the positions of structural Bragg peaks.

Table 7.1 | First two columns tabulate the Rietveld refinement results obtained with synchrotron x-ray powder diffraction data at 300 K and 5 K for $Nd_{1.5}Sr_{0.5}NiO_{4.06}$. Data were collected on MS-X04SA at SLS with $\lambda = 0.6208(1)$ Å. The last column corresponds to the least-square refinement of single crystal neutron diffraction data obtained at 300 K for $Nd_{1.5}Sr_{0.5}NiO_{4.05}$ on ZEBRA ($\lambda = 1.178(1)$ Å) at SINQ, PSI.

Temperature		5 K	300 K	300 K
a	(Å)	5.330606(10)	5.343186(4)	5.3494(2)
b	(Å)	5.343928(11)	5.343186(4)	5.3494(2)
c	(Å)	12.43804(2)	12.489749(10)	12.4735(7)
	Occ.	1	1	1
Ni (0 0 0)	U_{11}	0.0053(4)	0.00826(8)	0.0074(5)
	U_{22}	0.0096(4)	0.00826(8)	0.0014(5)
	U_{33}	0.0072(3)	0.01255(17)	0.0112(6)
	U_{13}	-0.0042(14)	-	-
	Occ.	2	2	2
Nd or Sr ($x x z$)	x	0	0	0
	y	-0.0037(3)	0	0
	z	0.36137(3)	0.361207(13)	0.36077(9)
	U_{11}	0.00528(11)	0.01137(3)	0.0141(5)
	U_{22}	0.00929(15)	0.01137(3)	0.0141(5)
	U_{33}	0.00625(10)	0.00941(5)	0.0055(6)
	Occ.	2	2	1.892(17)
O_{ap} ($x x z$)	x	0	0	0
	y	0.023(3)	0	0
	z	0.1754(2)	0.17446(13)	0.17445(14)
	U_{11}	0.0116(17)	0.0278(6)	0.0291(10)
	U_{22}	0.022(5)	0.0278(6)	0.0291(10)
	U_{33}	0.0083(14)	0.0088(7)	0.0074(10)
	U_{13}	0.014(3)	-	-
	Occ.	2	2	1.934(15)
O_{eq} ($1/4 1/4 z$)	z	-0.0095(9)	0	0
	U_{11}	0.017(2)	0.0116(5)	0.0047(7)
	U_{22}	0.0003(16)	0.0116(5)	0.0047(7)
	U_{33}	0.010(4)	0.0224(9)	0.0142(9)
	U_{12}	-0.0024(10)	-0.0035(6)	-0.0020(5)
R_p (%)		11.9	8.73	4.8
wR_p (%)		14	9.40	5.41
R_{exp}		2.36	2.06	2.94

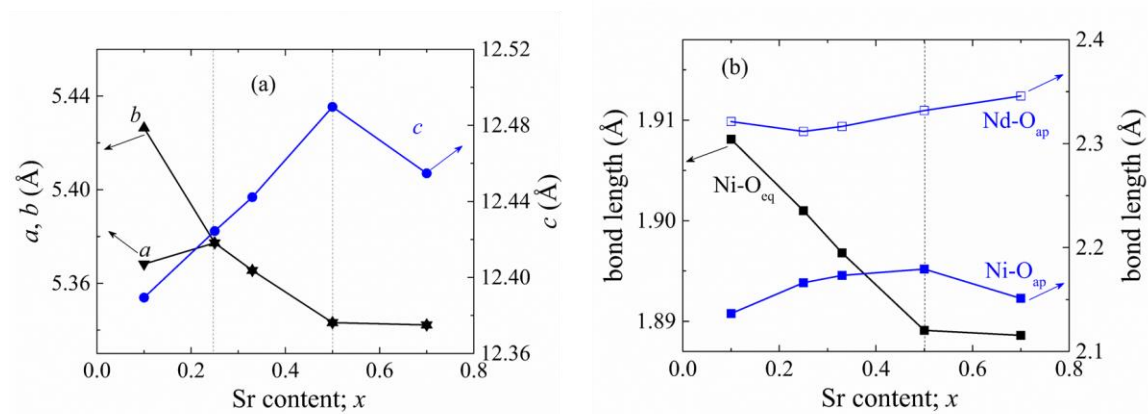


Figure 7.4 | Evolution of (a) Lattice parameters and (b) Bond lengths obtained from Rietveld refinements of powder diffraction data recorded at room temperature for $\text{Nd}_{2-x}\text{Sr}_x\text{NiO}_{4+\delta}$ compounds on MS-X04SA at SLS with $\lambda = 0.6208(1)$ Å.

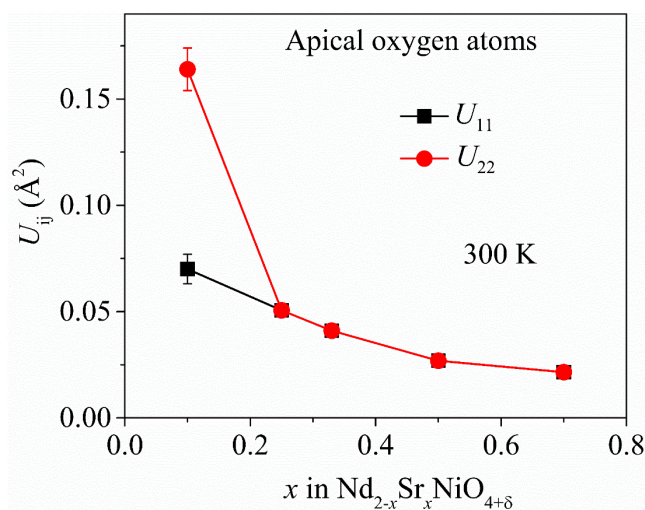


Figure 7.5 | Variation of anisotropic thermal displacement parameters of apical oxygen atoms in $\text{Nd}_{2-x}\text{Sr}_x\text{NiO}_{4+\delta}$. Thermal displacement parameters are obtained from Rietveld refinement of synchrotron x-ray powder diffraction data at room temperature. Measurements were performed on MS-X04SA at SLS with $\lambda = 0.6208(1)$ Å.

In addition to the rich electronic properties, $\text{RE}_{2-x}\text{Sr}_x\text{NiO}_{4+\delta}$ compounds also possess oxide ion conductivity close to room temperature. A phonon mediated oxygen diffusion mechanism occurring through the apical and vacant interstitial site is proposed for these compounds close to room temperature. In **chapters 5 and 6**, the evidence of phonon assisted oxygen diffusion mechanism is observed for oxygen doped $\text{Nd}_2\text{NiO}_{4+\delta}$ phases. It is shown that the excess oxygens play a crucial role on the oxygen mobility by inducing important shifts to the apical oxygen atoms toward nearest vacant interstitial sites. Therefore, anisotropic thermal displacement parameters

of apical oxygen atoms provides important measure of the oxygen mobility occurring close to room temperature. For all samples, thermal ellipsoids of apical oxygen atoms are highly anisotropic with components mainly along the ab -plane (see Fig. 7.1 for $x = 0.5$). Fig. 7.5 presents the evolution of in-plane thermal displacement parameters (U_{11} and U_{22}) of apical oxygen atoms as a function of Sr-content at room temperature. U_{11} and U_{22} parameters, on an absolute scale, strongly decrease with Sr-doping compared to the pure oxygen doped phases, as discussed in chapters 5 and 6. Moreover, in-plane displacement parameters are strongly suppressed with increasing Sr-content. This strong decrease in U_{11} and U_{22} is directly correlated with the less amount of intercalated oxygen atoms with increasing Sr-content. This result suggests that the release of excess oxygen atoms due to Sr-doping pins the apical oxygen atoms to the lattice. Thus, pure O-doped compounds are expected to be better oxide ion conductors than pure Sr-doped compounds close to room temperature, consistent with previous experimental findings^{125–127}.

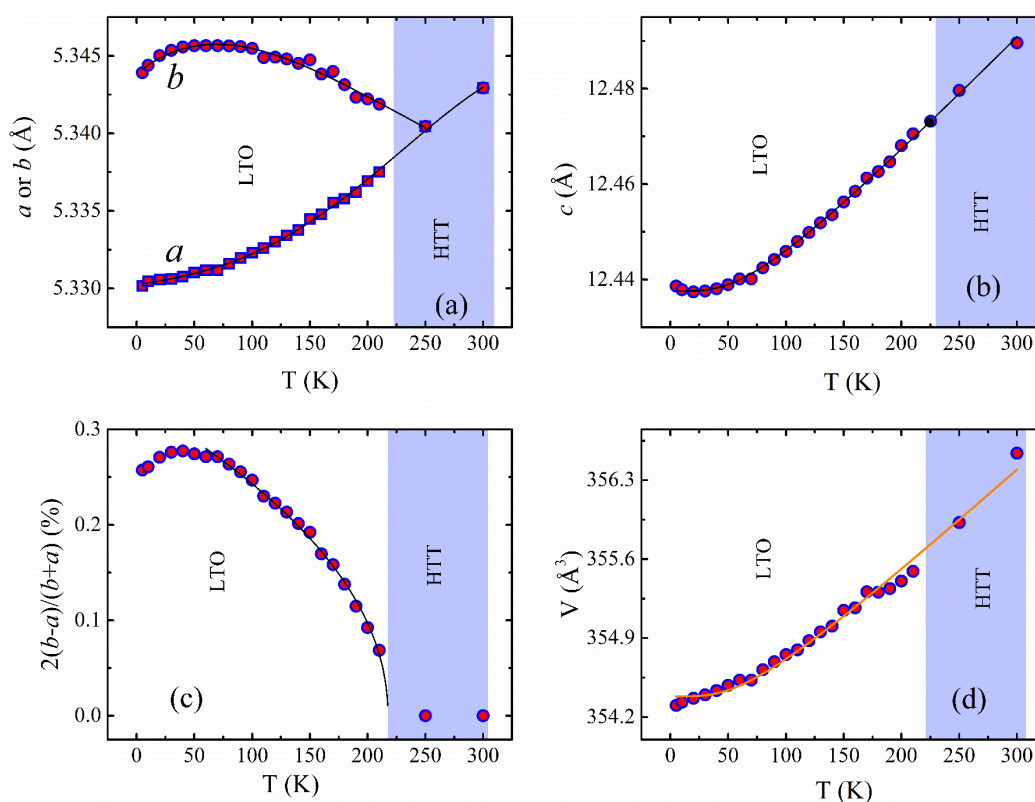


Figure 7.6 | Structural parameters obtained for $\text{Nd}_{1.5}\text{Sr}_{0.5}\text{NiO}_{4+\delta}$ with synchrotron x-ray powder diffraction. Thermal evolution of (a) the a - and b -axis, (b) the c -axis, (c) orthorhombicity and (d) the unit cell volume (V). HTT region is shown by blue shaded area. Powder data were collected on MS-X04SA at SLS with $\lambda = 0.6208(1)$ Å.

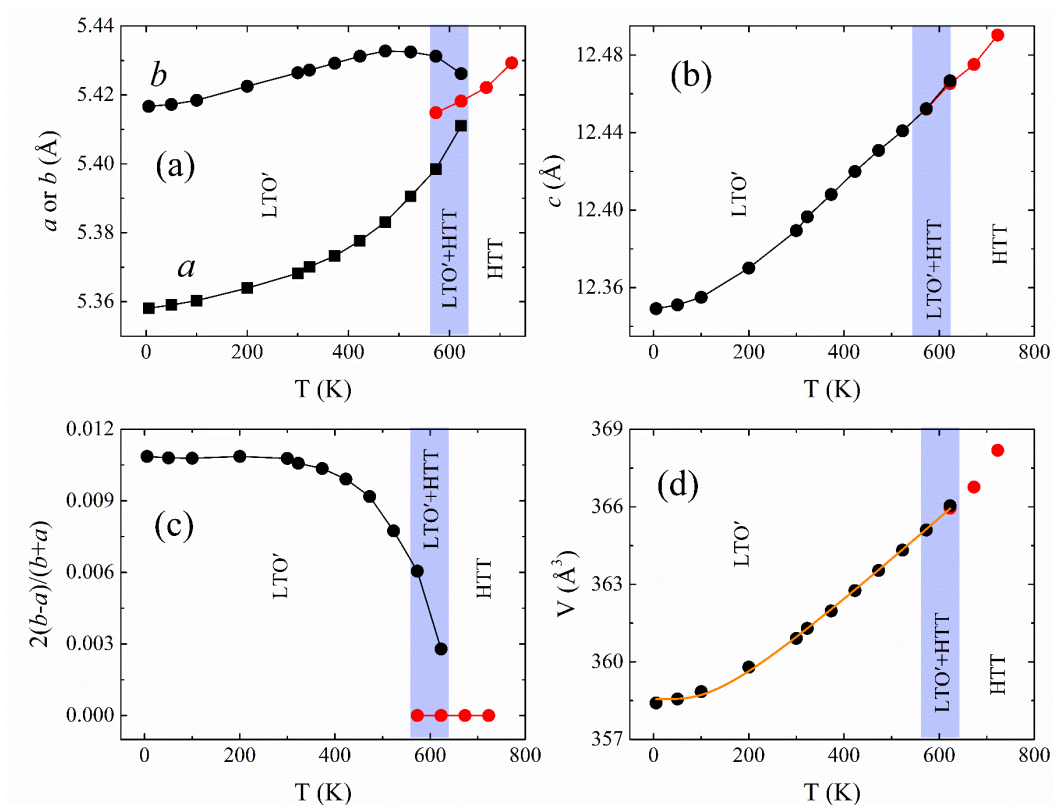


Figure 7.7 | Structural parameters obtained for $\text{Nd}_{1.9}\text{Sr}_{0.1}\text{NiO}_{4+\delta}$ with synchrotron x-ray powder diffraction. Thermal evolution of (a) the a - and b -axis, (b) the c -axis, (c) orthorhombicity and (d) the unit cell volume (V). A biphasic region comprising of LTO' and HTT phases is shown by blue shaded area. Powder data were collected on MS-X04SA at SLS with $\lambda = 0.6208(1)$ Å.

No structural transition is observed for any sample with decreasing temperature down to 5 K except for the $x = 0.5$ compound. A structural phase transition from HTT to LTO in $x = 0.5$ is distinguished by the appearance of (012) structural Bragg peak (Fig. 7.2(c)) and orthorhombic splitting in $(h00)/(0k0)$ type Bragg reflections (Fig. 7.2(d)) below $T \sim 210$ K. This structural transition is likely due to increasing mismatch between Nd- O_{ap} and Ni- O_{eq} bond lengths with decreasing temperature that induces a coherent tilting pattern of NiO_6 octahedron around the [100] direction. The structural transition is second order as previously reported for $\text{La}_2\text{NiO}_{4+\delta}$ ⁴⁶. To study the structural changes as a function of temperature, various lattice parameters are extracted from the SXRPD data and plotted in Figs. 7.6(a)-(d) as a function of temperature. With increasing the temperature in the LTO phase, both a - and b -lattice parameters initially increases up to 50 K. Consequently, the orthorhombicity, referred by $2(b - a)/(b + a)$, also increases up to 50 K as shown in Fig. 7.6(c). In this temperature range, the c -axis lattice parameter almost remains fixed (cf. Fig. 7.6(b)) while the unit cell volume smoothly increases (cf. Fig. 7.6(d)). With the increasing temperature from 50-210 K, a - and c -lattice parameters increases while the b -lattice parameter decreases significantly approaching the transition temperature. Consequently,

the orthorhombicity sharply decreases in this temperature range and drops to zero at the structural transition temperature (~ 210 K). The non-linear thermal evolution of the unit cell volume can be described by a quasi-harmonic Debye model as discussed in **Eq. 5.1**. This model represents well the observed temperature dependence of the unit-cell volume as shown by a thick orange line on top of the experimental data in **Fig. 7.6(d)**. The fitting parameters for Nd_{1.5}Sr_{0.5}NiO_{4+δ} are found to be $A = 0.027(7)$ (Å/K) and $\Theta_D = 248(31)$ K. Crystal structure of $x = 0.1$ at high temperature is also studied by x-ray diffraction. The temperature evolution of various lattice parameters are plotted in **Figs. 7.7(a)-(d)**. A complex sequence of the phase transition is observed with increasing temperature. In the temperature range of 5-550 K i.e. in the LTO' phase, a -, b - and c -lattice parameters and the unit cell volume (V) smoothly increase with increasing temperature. However, the orthorhombicity only slightly decreases in this temperature range. A phase coexisting region is observed in between 550 K-650 K as shown by blue shaded area in **Figs. 7.7(a)-(d)**. In this biphasic region, the b -lattice parameter smoothly decreases with increasing temperature and therefore, the orthorhombicity approaches sharply toward zero. The non-linear variation of the unit cell volume is fitted with the Debye law as expressed in **Eq. (5.1)**. The obtained fitting parameters are $A = 0.049(1)$ (Å/K) and $\Theta_D = 532(38)$ K for Nd_{1.9}Sr_{0.1}NiO_{4+δ}.

7.2. Excess oxygen ordering and apical oxygen disorder

Now, we turn to the IC superstructure reflections, which are observed for Sr doping with $x = 0.1$, 0.25, 0.33. **Fig. 7.8** shows typical IC satellite reflections that are observed in the SXRPD data. For comparison, as discussed in **section 6.2**, the IC superstructure reflections observed for Nd₂NiO_{4.23} ($x = 0$) due to 3D ordering of excess oxygen atoms are also presented. The intensities of these reflections are only about 0.1% with respect to the strongest (113) structural Bragg reflection. No significant changes in intensities of these satellites are observed with decreasing temperature down to 5 K. The presence of IC satellites in the Sr-doped samples ($0.1 \leq x \leq 0.33$) possibly indicate the existence of analogous structural modulations from the ordering of excess oxygen atoms as in the case of $x = 0$. In this case, a clear transition in the ordering pattern of excess oxygens is expected on moving from $x = 0$ to $x = 0.1$, 0.25 and 0.33 as clearly less satellite reflections are observed for Sr-doped samples. However, positions of these IC reflections remain invariant as a function of x at RT. It is found that for $x = 0.1$, first two IC satellite peaks (*cf.* **Fig. 7.8(a)**) can satisfactorily be indexed as $(0, 1, 2 \pm \Delta)$ with $\Delta \sim 0.1$. This Δ value indicates possible 1D ordering of excess oxygens along the c -axis with a stage-10 order²⁷. However, the positions of these satellites could not be fitted with such staging model for other two Sr-doped samples with $x = 0.25$ and 0.33. In addition, the high temperature SXRPD data of $x = 0.1$ shows no thermal evolution of

these reflections with increasing temperature and persist even after LTO' to HTT structural transition at $T \sim 673$ K. This observation is in strong contrast with that of the $x = 0$ compound in which concomitant evolution of the oxygen ordering reflections with structural changes is evidenced with increasing temperature from 300 K to 900 K. Furthermore, if these IC satellites are due to additional O-ordering, then they are expected to appear strongly in the PND data, as neutrons are highly sensitive to oxygen atoms compared to x-rays. Surprisingly, IC satellites are absent (or very weak to detect) in the PND data for Sr-doped compounds as shown in **Figs. 7.13(a)** and **7.13(b)** for $x = 0.25$ and 0.33 , respectively. Furthermore, the positions of IC reflections in these Sr-doped samples at any temperature can satisfactorily be described by an impurity phase from $\text{Sr}_2\text{Nd}_8(\text{SiO}_4)_6\text{O}_2$ with hexagonal crystal structure ($P6_3/m$ with lattice parameters $a = b = 9.577$ Å and $c = 7.117$ Å at room temperature¹²⁸). Therefore, it is likely that these IC reflections in Sr-doped samples are from an impurity phase rather than staging order of the excess oxygen atoms. In this context, it is worth to mention that staging order of excess oxygen atoms is suppressed by a small amount of Sr doping in $\text{La}_{2-x}\text{Sr}_x\text{NiO}_{4+\delta}$ systems as revealed by previous synchrotron X-ray powder diffraction data¹¹⁹. It was proposed that the Coulomb interactions with the Sr ions prevent the interstitial oxygen ions to form the staging order. In strong contrast, isostructural $\text{La}_{2-x}\text{Sr}_x\text{CuO}_{4+\delta}$ samples with $0 \leq x \leq 0.09$ show staging peaks below RT as confirmed with single crystal X-ray diffraction²⁹. Therefore, to answer this puzzle, single crystal x-ray/neutron diffraction measurements on $\text{Nd}_{2-x}\text{Sr}_x\text{NiO}_{4+\delta}$ samples are essential.

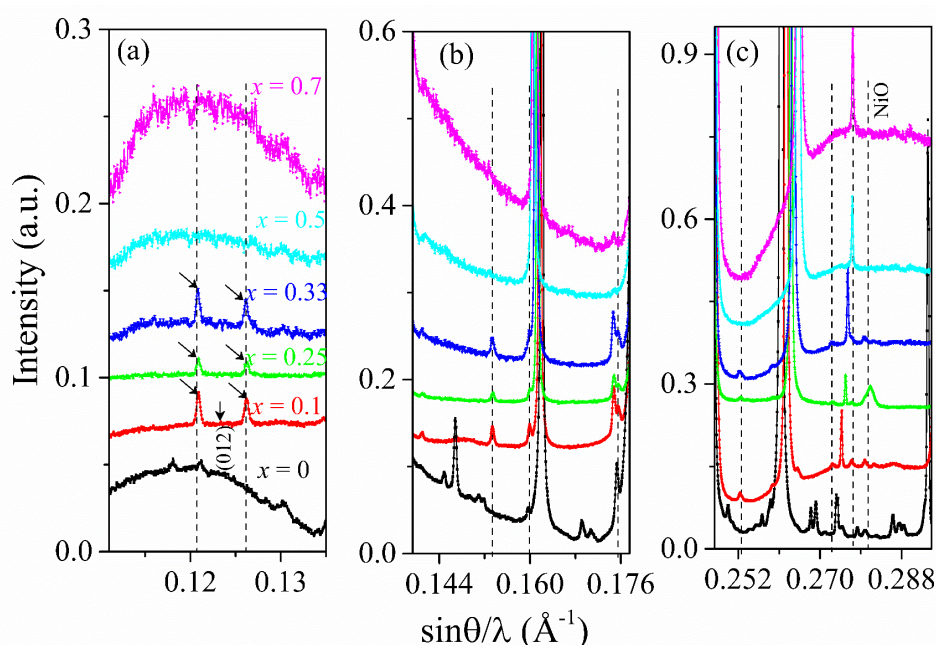


Figure 7.8 | Typical incommensurate satellite reflections observed with synchrotron x-ray powder diffraction at room temperature in $\text{Nd}_{2-x}\text{Sr}_x\text{NiO}_{4+\delta}$. Vertical dashed lines represent position of these satellites present in Sr-doped samples. Powder data were collected on MS-X04SA at SLS with $\lambda = 0.6208(1)$ Å.

For a more detailed structural analysis, especially in view of a precise analysis of apical oxygen disorder in absence of ordering of interstitials, least squares refinements were conducted of the integrated intensity data measured on a $\text{Nd}_{1.5}\text{Sr}_{0.5}\text{NiO}_{4.05}$ single crystal at room temperature. Results are presented in **Table 7.1** and in good agreement with those obtained from the powder diffraction study. A detailed inspection of the apical oxygen atoms yields an occupancy corresponding to an overall stoichiometry of the apical site 1.89(1) at 300 K i.e. only 6% less than the stoichiometric occupation, respectively. While at the same time, the occupancies for the equatorial oxygen atoms correspond very closely to the ideal stoichiometry. The presumed under stoichiometry of the apical site is, however, not real but an artefact as discussed in chapter 5 and chapter 6 for $\text{Nd}_2\text{NiO}_{4.11}$ and $\text{Nd}_2\text{NiO}_{4.23}$ respectively, related to strong and anharmonic distortions of the O_{ap} , which can no longer be described in a harmonic approach as turned out from the least-square refinements. The crystal structure using harmonic displacement factors is visualized in **Fig. 7.1**, while a more sophisticated data analysis using the Maximum Entropy Method (MEM) is given in **Figs. 7.9(a)-(c)** 300 K. The apical oxygen isosurface obtained with MEM analysis is shown in **Fig. 7.9(a)** along with anisotropic thermal ellipsoids obtained from refinements. Isotropic nature of nuclear scattering densities of apical oxygen atoms at 300 K shows that apical oxygens are pinned to the lattice due to absence of interstitial oxygens in the nearest vacant sites as shown by dashed circles. Therefore, no additional displacements of apical oxygens are observed at room temperature towards the vacant interstitial sites (*cf.* **Fig. 7.9(b)**). These findings indicate absence of strong displacements of O_{ap} in the [110]-direction inside the rock salt layer as shown in **Fig. 7.9(c)**, which are observed for oxygen doped compounds. Absence of such diffusion pathway extremely reduces the oxygen diffusion in Sr-doped compounds close to room temperature. However, a thermally activated site-to-site oxygen hopping occurring is expected via regular apical and vacant interstitial sites at high temperature.

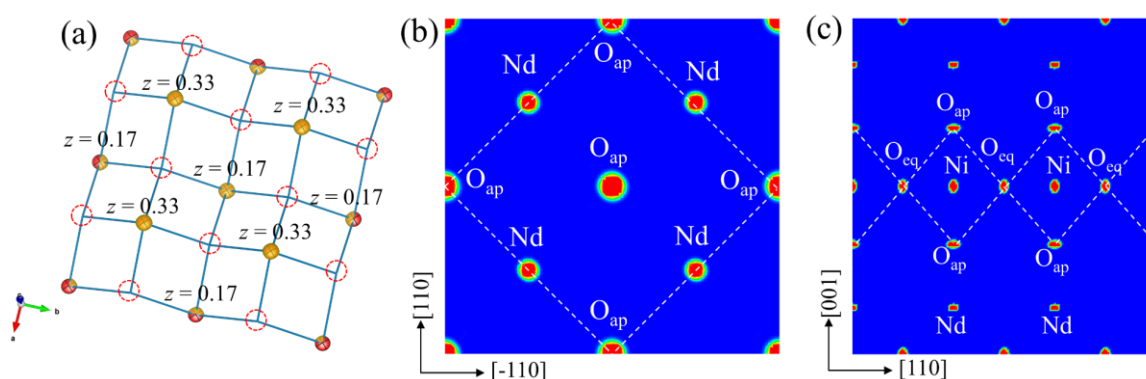


Figure 7.9 | Maximum entropy results obtained with single crystal neutron diffraction data at 300 K of $\text{Nd}_{1.5}\text{Sr}_{0.5}\text{NiO}_{4.05}$. Measurements were performed on ZEBRA at SINQ, PSI with $\lambda = 1.178(1)$ Å. (a) Isosurfaces of apical oxygen atoms obtained with MEM. Thermal ellipsoids of apical oxygens are also included. Positions of interstitial oxygen atoms, which are not present in

this case, are denoted by dashed circles. (a) (110)-(-110) projection of 2D-nuclear density maps from $0.12 \leq z \leq 0.28$. White dashed line outlines the F-centered unit cell. (c) (110)-(001) projection of 2D-nuclear density map in the range of $0.45 \leq y \leq 0.55$ displaying the absence of O_{ap} - O_{int} - O_{ap} oxygen diffusion pathway along the [110] direction. Dashed lines show NiO₆ octahedrons.

7.3. Macroscopic magnetization

Macroscopic DC magnetic susceptibility curves for members of the Nd_{2-x}Sr_xNiO_{4+δ} system are presented in **Fig. 7.10** as a function of temperature in the range of 2-330 K. For comparison, magnetic susceptibility curve measured on as-grown powder sample of Nd₂NiO_{4.23} ($x = 0$) is also included. The decrease in the absolute value of the magnetic susceptibility with increasing Sr content x is evident due to progressive replacement of paramagnetic Nd³⁺ ions by diamagnetic Sr²⁺ ions. No long-range magnetic order is observed down to 2 K in any of the magnetic susceptibility curves except a broad anomaly around $T \sim 16$ K corresponding to $x \geq 0.33$. The 16 K anomaly was previously denoted as an onset of antiferromagnetic order related to Nd³⁺ ions¹²⁹. However, recent neutron scattering and magnetization measurements on single crystals reveal that the 16 K peak is a Schottky type anomaly due to lifted degeneracy of the ground state doublet of the Nd³⁺ ions¹³⁰. In addition, an upturn is noticed around $T \sim 5$ K for $x \geq 0.25$ likely to be related with Nd³⁺ ordering. It was previously proposed that incorporated holes due to Sr/O-doping destroy 3D long-range magnetic ordering and incommensurate quasi-2D stripe magnetic order appears. In **chapter 6**, single crystal neutron diffraction and magnetization measurements show the evidence of long-range incommensurate magnetic order below 150 K in Nd₂NiO_{4.23}. However, evidence of such ordering is absent in the magnetic susceptibility curve recorded for our powder sample. It is possible that the anomaly corresponding to quasi-2D magnetic ordering is weak, thus strong paramagnetic contribution of Nd³⁺ ions possibly masks such anomaly in the susceptibility data of the powder samples. The temperatures where stripe magnetic ordering is observed with previous neutron diffraction measurements are marked with arrows in our susceptibility data for all the members^{73,130}. An ideal Curie-Weiss type behavior is evident in the temperature range of 200-330 K. Magnetic susceptibility curves become non-linear below 100 K, which are attributable to the crystal field splitting of Nd³⁺ ground state (⁴I_{9/2}). The magnetic susceptibility strongly depends on the relative population of these levels at different temperatures. The susceptibility data in the temperature range of 200-330 K was fitted to the Curie-Weiss law given as $\chi = \chi_0 + C/(T + \Theta)$, where C and Θ are the Curie constant and Weiss temperature, respectively. The temperature independent term χ_0 can be due to a combination of Pauli paramagnetism, Van Vleck paramagnetism, and core diamagnetism. The Curie constants and Weiss temperatures for all the samples were determined from a least-square fitting. Fitted

magnetic parameters are listed in **Table 7.2**. Negative Weiss temperatures for all the compositions indicate dominant antiferromagnetic correlations at low temperature. Furthermore, a weak increase in the absolute value of Weiss temperature is observed with increasing Sr-concentration owing to the loss of extra oxygens with Sr-doping. The Θ values obtained for the Nd_{2-x}Sr_xNiO_{4+δ} system in the present study are smaller than the values in previously reported results on the similar compounds¹²⁴. The spread in the Θ values reported by different authors could possibly be due to minor difference in the excess oxygen content in the powder samples. As these samples are non-metallic, the Pauli paramagnetic contribution is expected to be very small and the core diamagnetic contribution is estimated to be around 0.1×10^{-3} emu. mol⁻¹. Therefore, the temperature independent term is mainly dominated by the Van Vleck contribution resulting Nd³⁺ crystal field levels and from Ni²⁺ ions. **Table 7.2** lists calculated effective magnetic moments μ_{eff} from the Curie constants. The system is composed of two magnetic sublattices formed by Nd³⁺ and Ni²⁺/Ni³⁺ ions, and assuming that they can be treated as non-interacting systems of isolated spins (which is true at $T \geq 10$ K), a simple dilution law enables the evaluation of the effective magnetic moments of Nd and Ni-sites as follows:

$$\mu_{eff}^2 = (2 - x)\mu_{eff}^2(Nd) + \mu_{eff}^2(Ni) \quad (7.1)$$

The linear fit gives $\mu_{eff}(Nd^{3+}) = 3.14\mu_B$ and $\mu_{eff}(Ni) = 2.54\mu_B$ for the Nd_{2-x}Sr_xNiO_{4+δ} system. The effective magnetic moment of the Nd-site is 13% smaller than the known value ($3.62\mu_B$) while the small value of $\mu_{eff}(Ni)$ compared with $3.9\mu_B$ observed in octahedral symmetry is mainly due to the presence of small fraction of nickel ions in Ni³⁺ state ($S = 1/2$, $\mu_{eff} = 1.73\mu_B$). The 5 K anomaly observed in the susceptibility data is possibly due to the long-range magnetic ordering of Nd³⁺ ions. For undoped Nd₂NiO_{4.0}, the long-range magnetic order for rare earth ions occurs around $T \sim 11$ K⁵⁰. It was proposed that the long-range magnetic order in the Nd sublattice strongly sensitive to the amount of oxygen non-stoichiometry δ and the Sr content x , which is consistent with the absence of the magnetic order in Nd_{2-x}Sr_xNiO_{4+δ} for $x \leq 0.25$ where $\delta \geq 0.09$ ¹²⁴. The long-range magnetic order in the Nd sublattice depends on the relative strengths of two local exchange fields J_{Ni-Nd} and J_{Nd-Nd} . When $J_{Ni-Nd} > J_{Nd-Nd}$, which is true at relatively higher temperatures, the strong local fields originating from the polarization of Ni²⁺ ions prevent long-range static magnetic order in the rare earth lattice. However, J_{Nd-Nd} becomes dominant at lower temperatures ($T \sim 5$ K), setting up the magnetic order in the rare earth lattice. The isothermal magnetization curves recorded for Nd_{1.5}Sr_{0.5}NiO_{4.06} are shown in **Fig. 7.11**. At low temperature, magnetization curves become non-linear due to contribution of Nd³⁺ magnetic moments. No ferromagnetic components have been observed down to 2K.

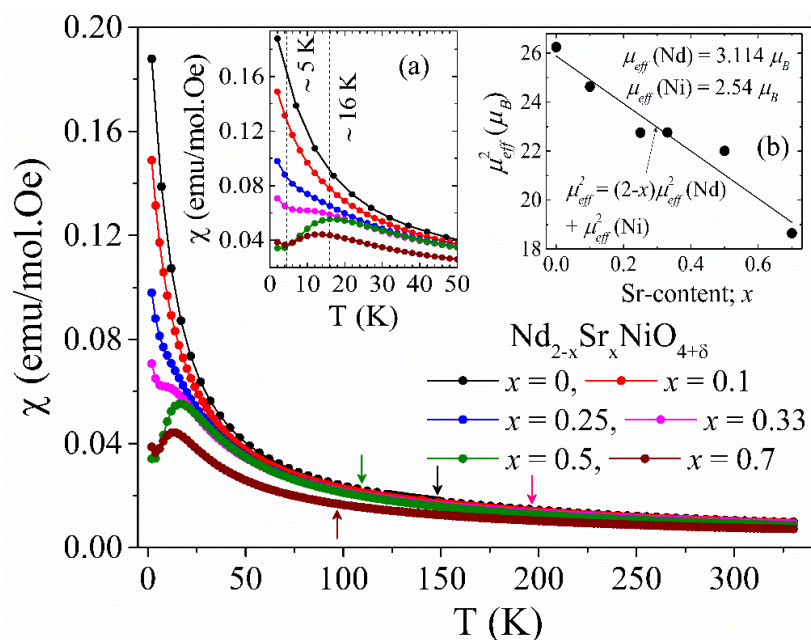


Figure 7.10. Magnetic susceptibility curves for members of the $\text{Nd}_{2-x}\text{Sr}_x\text{NiO}_{4+\delta}$ system as a function of temperature. The arrows mark magnetic ordering temperatures detected by previous investigations. (a) Low temperature portion of the susceptibility curves showing the Schottky anomaly around $T \sim 16$ K and the Nd ordering around $T \sim 5$ K. (b) Total effective magnetic moments as a function of Sr-content. A linear fit is made following a dilution law (see text) of two non-interacting magnetic sublattices to evaluate the effective magnetic moments of Nd and Ni sites.

Table 7.2 | Least-square fitting results of the DC magnetic susceptibility data of $\text{Nd}_{2-x}\text{Sr}_x\text{NiO}_{4+\delta}$ compounds in the temperature range of 200-330 K with the Curie-Weiss law.

Sr-content x	Excess oxygen content δ	χ^0 (emu/mol. Oe)	μ_{eff} (μ_B)	Θ (K)	G (K)
0	0.23(2)	0.001	5.125	-44.63	-
0.1	0.09(2)	0.00118	4.9632	-43.59	-
0.25	0.08(2)	0.00127	4.77	-42.24	24.84
0.33	0.04(2)	0.00148	4.771	-43.74	16.56
0.5	0.06(2)	0.00107	4.6913	-37.99	16.51
0.7	0.00(2)	9.87E-4	4.318	-53.34	16.56

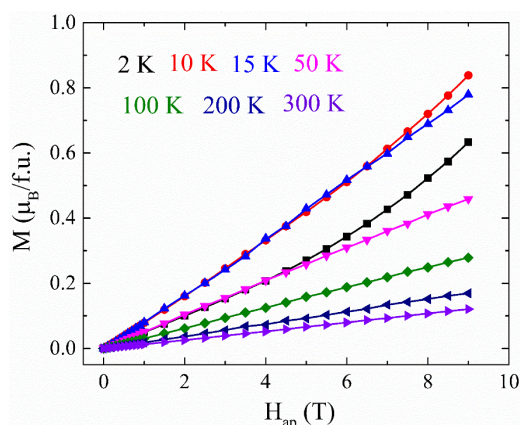


Figure 7.11 | Isothermal magnetization curves of the $\text{Nd}_{1.5}\text{Sr}_{0.5}\text{NiO}_{4.06}$ compound. Magnetization measurements were recorded on powder sample with increasing field in the range of 0-9 T.

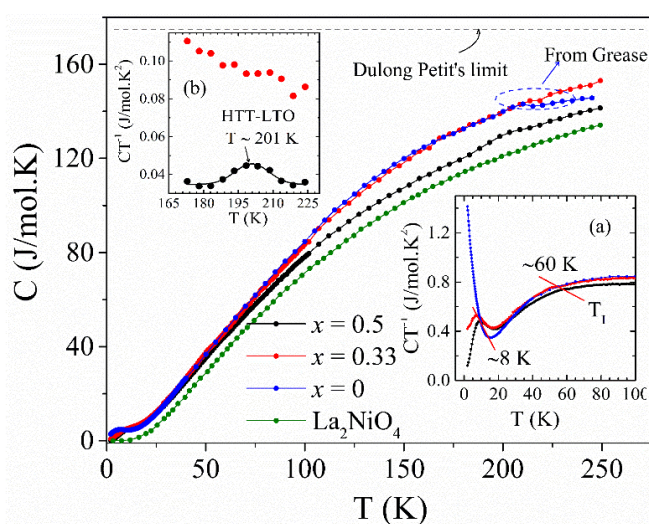


Figure. 7.12 | Variation of specific heat as a function of temperature measured for $\text{Nd}_{2-x}\text{Sr}_x\text{NiO}_{4+\delta}$ system. Specific heat data of La_2NiO_4 is also plotted to separate the lattice and magnetic contributions. The inset (a) CT^{-1} vs T plot showing the anomaly at T_1 and the presence of Schottky peak around 8 K. (b) ΔC vs T plot illustrating the presence of second order HTT to LTO phase transition around 200 K for $x = 0.5$.

7.4. Specific heat

Specific heat measurements were carried out for detailed examination of the magnetic ordering and Schottky anomaly arising at low temperature. In **Fig. 7.12**, the specific heat data of $\text{Nd}_{2-x}\text{Sr}_x\text{NiO}_{4+\delta}$ is plotted for the samples with $x = 0, 0.33$ and 0.5 along with the specific heat data of the $\text{La}_2\text{NiO}_{4.0}$ sample from the reference¹³¹ to separate the pure lattice contribution. A broad

hump is observed at $T_S \sim 210$ K for $x = 0.5$ due to a 2nd order HTT to LTO structural transition, consistent to the x-ray powder data. In contrast, the corresponding anomaly is not observed for other samples in the temperature range of 2- 300 K. In addition, no anomaly is observed in the specific heat data at temperatures at which charge and spin ordering are expected. Another small anomaly is observed at T_I in the CT^{-1} vs T curve only for $x = 0.33$ and 0.5 systems as shown in the inset (a) of **Fig. 7.12**. The anomaly at T_I shifts from 53 K to 60 K with increasing x from 0.33 to 0.5. It should be noted that no structural rearrangement is observed for the $x = 0.33$ system in our SXRPD data. Therefore, a structural transition at T_I is excluded. Furthermore, with the susceptibility data, it is found that the Nd-sublattice orders only around 5 K. Therefore, only minor changes in the spin structure of the stripe ordered phase at this temperature is expected to occur. The amount of an additional change in the specific heat at T_I is very small. Therefore, the occurrence of any long-range ordering at T_I can also be excluded. Recently, with specific heat measurements on single crystal data similar results were obtained Ikeda et al.¹³⁰. The anomaly at T_I is observed only in the stripe region ($x \leq 0.5$), and disappeared in the checkerboard (CB) region ($x > 0.5$). Therefore, the anomaly at T_I is supposed to be an intrinsic feature of a stripe ordered region for the Nd-system. With decreasing temperature, a clear broad Schottky-type peak in the CT^{-1} vs T curve is clearly observed for the Nd-systems except for the $x = 0$. This anomaly possibly associated to the Nd magnetic moments since this anomaly is not present for the La-system. Indeed, the magnetic entropy associated with this peak approximately reaches $R \ln 2$ up to 50 K. It suggests the splitting of the degenerate Kramers doublet of Nd^{3+} into two singlets at low temperature. This could be due to acting of strong exchange field on Nd^{3+} ions from ordered Ni^{2+} magnetic moments that lifts the degeneracy of the Nd^{3+} ground state doublets. In **Appendix D**, a simple point charge calculations show that strong molecular field from Ni^{2+} magnetic ions with strength about 5.2 T parallel to the c -axis is sufficient to destroy the ground state degeneracy of magnetic Nd^{3+} ions for all the systems. However, Schottky peak is absent in the susceptibility data of $x =$ and 0.1. The splitting energy G of the Nd^{3+} ground-state doublet can be evaluated from both specific heat and magnetic susceptibility data as presented in **Appendix D**. The energy gap of G between two singlets for a two-level system, the maximum of the Schottky peak appears in the specific heat data at temperature T_m such that $G = 2.399 \times T_m$. The corresponding peak in the magnetic susceptibility data will appear at T_{mag} so that $G = 1.543 \times T_{mag}$ and in the differential magnetic data it will appear at T'_{mag} so that $G = 2.703 \times T'_{mag}$. In this way, the splitting energy G is evaluated and tabulated in **table 7.2**. The evaluated G values obtained with specific heat data and susceptibility data coincide reasonably and are consistent with the previously reported results¹³⁰. Finally, we note that the Schottky type peak is absent/not distinguished for the members of $Nd_{2-x}Sr_xNiO_{4+\delta}$ system where $\delta \geq 0.09$ i.e. for $x = 0, 0.1$ and 0.25 systems. This behavior could be explained by the fact that the splitting energy G is connected with the exchange magnetic field (H_i) thus on the strength of the J_{Nd-Ni} superexchange interaction. It is certain that the presence of

excess oxygen atoms in the interstitial sites induces severe structural distortions, which largely influence the local field acting on Nd^{3+} ions and weakens the $J_{\text{Nd-Ni}}$ superexchange interaction. Furthermore, a weak Sr-content dependence is noticeable in the value of the splitting energy. Thereby, the Sr-content dependence of G suggests the change of the orbital state at $x = 0.5$. This behavior is previously attributed to the switching of orbital state of Ni^{3+} ions in which the doped hole enters from $d_{x^2-y^2}$ -orbital to the $d_{3z^2-r^2}$ -orbital at the border of the stripe and CB regions i.e. at $x = 0.5$ as reported by Ikeda et al.¹³⁰

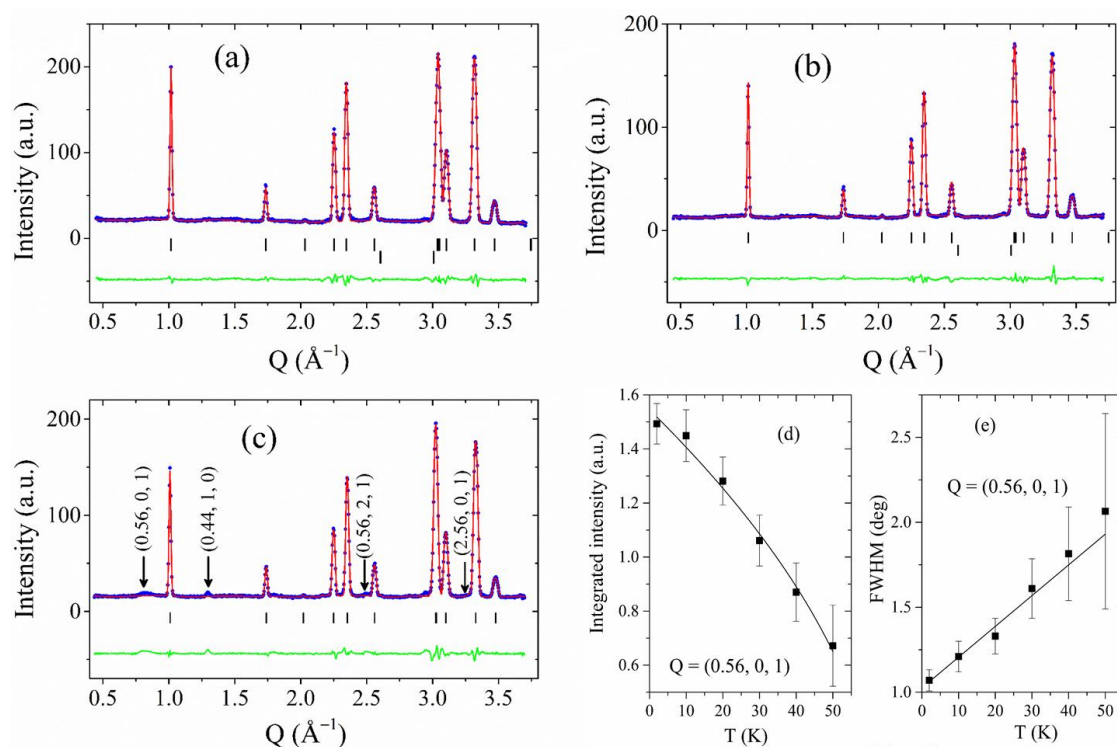


Figure 7.13 | Powder neutron diffraction patterns of $\text{Nd}_{2-x}\text{Sr}_x\text{NiO}_{4+\delta}$ system collected at 2 K on DMC ($\lambda = 2.4586(3)$ \AA) at SINQ, PSI. PND pattern of (a) $x = 0.25$, (b) $x = 0.33$ and (c) $x = 0.5$. Blue filled circles, Red continuous lines, Green lines and Black bars represent observed, calculated, difference diffraction patterns and structural Bragg reflections, respectively. Stripe magnetic peaks are marked with arrows in (c). Evolution of (d) integrated intensity and Full width at half-maximum of $(0.56, 0, 1)$ magnetic reflection as a function of temperature in $\text{Nd}_{1.5}\text{Sr}_{0.5}\text{NiO}_{4+\delta}$.

7.5. Spin and charge ordering in $\text{Nd}_{1.5}\text{Sr}_{0.5}\text{NiO}_{4+\delta}$

PND data sets were collected for the $\text{Nd}_{2-x}\text{Sr}_x\text{NiO}_{4+\delta}$ system with $x = 0.25$ ($\delta = 0.08(2)$), 0.33 ($\delta = 0.04(2)$) and 0.5 ($\delta = 0.06(2)$) at 300 K and 2 K. Typical PND patterns are presented in Fig. 7.13 for $x = 0.25$, 0.33 and 0.5 . At 300 K, PND patterns of these compounds are well characterized by the HTT structure in accordance with the SXRPD data. However, with decreasing temperature, weak

and diffuse type stripe magnetic peaks appear in the diffraction pattern. For all samples, stripe magnetic ordering peaks are noticeable in the 2 K patterns. However, for $x = 0.25$ and 0.33 , stripe magnetic peaks are extremely weak and barely discernible from the background even at 2 K. The stripe magnetic peaks are characterized by the wave vector $Q_{SO} = Q_{AF} \pm (\epsilon, 0, 0)$ where $Q_{AF} = (1, 0, 0)$ is the antiferromagnetic wave vector observed for the undoped compound. Our PND data reveals $\epsilon \sim 0.44$ for $x = 0.5$. The diffuse magnetic reflection at $Q \sim 0.84 \text{ \AA}^{-1}$ is indexed as $(0.56, 0, 1)$ and the second, somewhat less-broad magnetic peak at $Q \sim 1.29 \text{ \AA}^{-1}$ is indexed as $(0.44, 1, 0)$. The diffuse character of the first magnetic peak could be explained by weak inter-plane stripe correlations along the c -axis. In contrast, the second magnetic peak to the instrumental resolution is likely due to strong intra-plane superexchange interaction. The temperature dependencies of the integrated intensity and full width at half maximum (FWHM) of the $(0.56, 0, 1)$ magnetic reflection are plotted in **Figs. 7.13(d) and 7.13(e)**, respectively. The observed FWHM is about twice that of a nearest structural Bragg peak at 2 K. The FWHM of the diffuse magnetic peak roughly increases in linearly with increasing temperature and the reflection becomes barely detectable at $T > 50$ K. This suggests that the inter-plane stripe correlation remarkably weakens on approaching the transition temperature. In comparison, the second magnetic peak persists at $T > 50$ K. However, the existence of magnetic peaks with propagation vector $(\frac{1}{2}, \frac{1}{2}, \frac{1}{2})$ from the NiO impurity phase partially falls on top of this second reflection, which restricts us to perform further analysis of the magnetic structure. Though, an attempt was made to fit the temperature evolution of the integrated intensity of the diffuse magnetic peak with a power law of type $I = I_0 (T_c - T)^\beta$. From the least square fitting, a $T_c \sim 62$ K and the critical exponent $\beta \sim 0.54(12)$ is extracted. The extracted T_c value is very close to the observed unknown anomaly in the specific heat data. However, the exponent value β is much larger than expected values for 2D/3D Ising systems. Therefore, the anomaly in specific heat data possibly does not correspond to a real magnetic transition but rather resembles to a spin rearrangement or to a change in magnetic correlations. The magnetic correlation length is extracted by fitting the line shape of the $(0.56, 0, 1)$ magnetic reflection as a convolution of a Gaussian type instrumental resolution function and a Lorentzian. In order to obtain an analytical expression for the resolution function, the structural $(0, 0, 2)$ Bragg peak at $Q = 1.02 \text{ \AA}^{-1}$ was fitted to a Gaussian function. The Lorentzian function has the form

$$L(Q) = 1/(Q^2 + \xi^{-2}) \quad (7.2)$$

where ξ is the magnetic correlation length and Q is the wave vector. This Lorentzian corresponds to a 3D Ornstein-Zernike correlation function in direct space of the form ¹³²

$$S(R) = R^{-2} \exp(-R/\xi) \quad (7.3)$$

This analysis yields a correlation length or magnetic domain dimension of 18(3) Å at 2 K, in agreement with previously reported results¹²⁹, and is approximately three unit cells in the *ab*-plane and 1.5 unit cells along the *c*-axis. For $x = 0.25$ and 0.33 samples, stripe magnetic ordering peaks are also observed but they are too weak to extract any useful information.

Inspired by the results obtained with powder neutron diffraction on $x = 0.5$ sample, this compound was further investigated by single crystal neutron diffraction. A summary of expected positions of different stripe and checkerboard type charge and magnetic ordering peaks at reciprocal space are presented in **Figs. 7.14(a)** and **7.14(b)**. F-type structural Bragg reflections appear in the $(h, k, 0)$ and $(h, 0, l)$ zones with $h + k = 2n$ and $h + l = 2n$ with $n =$ integer numbers. Below the HTT-LTO structural phase transition, additional structural Bragg peaks appear at $(0, k, l)$ positions with $k + l = \text{odd}$. However, due to the presence of structural domains, B-type reflections also appear on the $(h0l)$ zone at $h + l = \text{odd}$. F-type and B-type structural Bragg reflections are represented by blue and green filled circles, respectively. Stripe magnetic ordering reflections appear on the $(hk0)$ zone at positions $(h \pm \epsilon, 0, 0)$ or at $(h, \pm\epsilon, 0)$ with $h =$ odd integers where ϵ is the magnetic incommensurability. A first set of magnetic reflections appears for stripes propagating parallel to the *b*-direction in the real space whereas the second set of magnetic reflections appear with a stripe propagation along the *a*-axis. Similarly, stripe magnetic peaks will also appear at $(0, k \pm \epsilon, 0)$ and $(\pm\epsilon, k, 0)$ positions for same two magnetic domains with $k =$ odd integer numbers. These stripe magnetic reflections are shown by filled triangles in **Fig. 7.14(a)** and two different colors are used to represent these two magnetic domains. The stripe type charge ordering reflections will appear at $(h \pm 2\epsilon, k, 0)$ and $(h, k \pm 2\epsilon, 0)$ with h and $k =$ odd integer numbers. Charge ordering peaks are shown by squares in **Fig. 7.14(a)**. Checkerboard commensurate charge ordering reflections are expected at reciprocal-lattice positions around $(h, k, 0)$ with $h + k = \text{odd}$. The magnetic cell, in real space, is two times larger than the unit cell corresponding to the charge ordering due to an antiphase relationship between two magnetic domains across the charge ordered domain walls. The stripe magnetic ordering peaks appear in the $(h0l)$ zone at reciprocal points at $(h \pm \epsilon, 0, l)$ with $h =$ odd and $l =$ any integer numbers and stripe charge ordering peaks will appear at $(h \pm 2\epsilon, 0, l)$ with $h =$ even and $l =$ odd integers. Whereas, checkerboard type charge ordering peaks appear at reciprocal points $(h, 0, l)$ positions with $h =$ odd and $l =$ odd.

Experimentally measured $(hk0)$ and $(h0l)$ reciprocal planes with neutron diffraction on DMC at 2 K are shown in **Fig. 7.15(a)** and **Fig. 7.15(b)**, respectively. In addition to the structural Bragg reflections (Miller indices are marked for F-structural Bragg reflections and B-type structural

Bragg reflections are shown by green circles), existence of checkerboard type commensurate charge ordering superstructure reflections and stripe type magnetic ordering reflections is observed on both planes. Surprisingly, stripe charge ordering peaks are absent in both zones likely due to their weak intensities. Stripe magnetic peaks are denoted by blue circles in the (hk0) zone while charge ordering peaks are shown by purple circles. Stripe spin ordering peaks are strongly diffuse along the reciprocal l -direction signifying weak correlations between the nearest neighbour NiO₂ planes along the c -axis in the real space. This displays the quasi-2D magnetic properties of these systems.

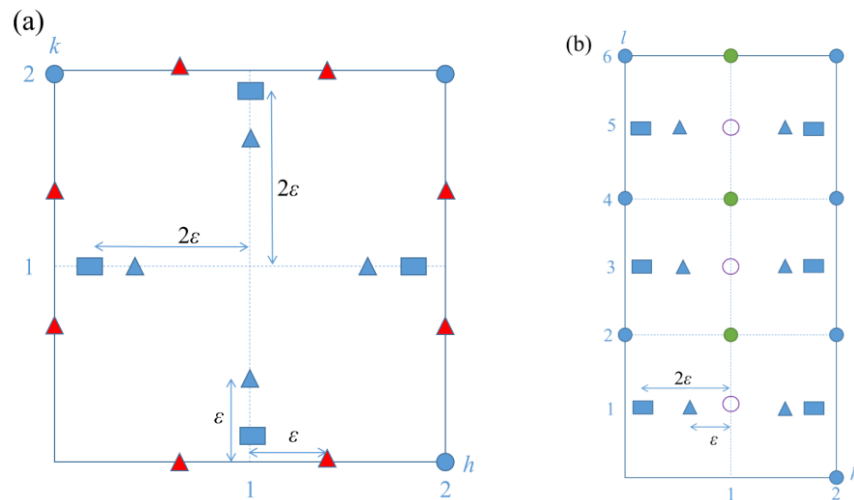


Figure 7.14 | Idealized sketches of reciprocal planes showing the positions of structural Bragg reflections, spin and charge ordering reflections in Nd_{1.5}Sr_{0.5}NiO_{4.0}. Sketch of the (a) reciprocal $(hk0)$ and (b) $(h0l)$ plane. Blue circles represent structural Bragg reflections for the $F4/mmm$ unit cell while green circles denote the B-type superstructure reflections. Triangles show the expected positions of stripe magnetic peaks with $\epsilon \sim 0.46$. Blue and red triangles represent two different magnetic domains. Squares denote the expected positions of incommensurate stripe charge ordering peaks. Open circles on $(h0l)$ zone show the commensurate checkerboard charge ordering peaks.

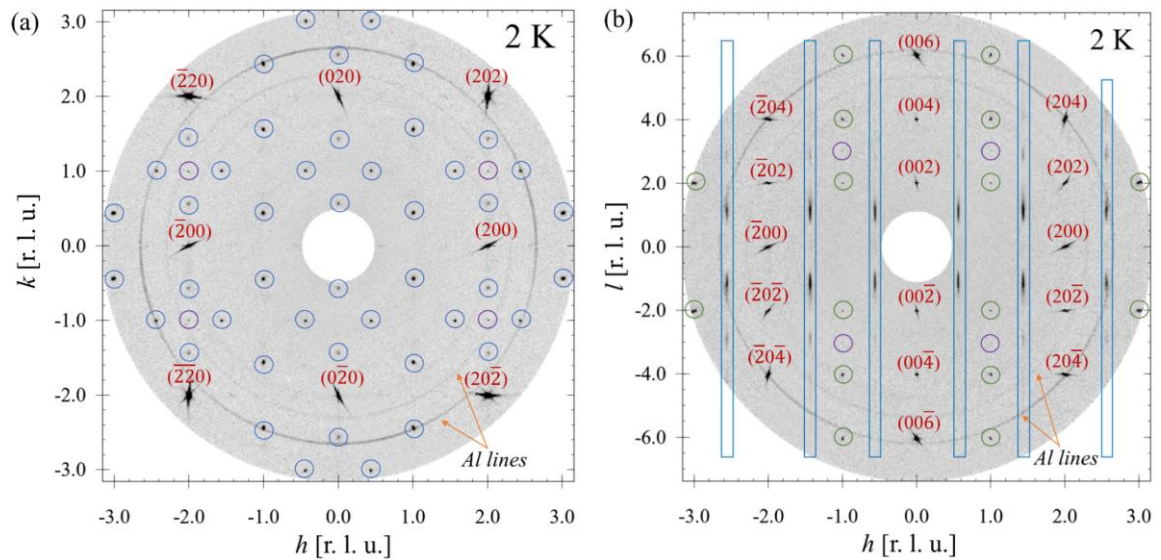


Figure 7.15 | Neutron diffraction reciprocal plane mappings of as-grown $\text{Nd}_{1.5}\text{Sr}_{0.5}\text{NiO}_{4.06}$ single crystal. (a) Measured $(hk0)$ and (b) $(h0l)$ reciprocal planes at 2 K on DMC at SINQ, PSI ($\lambda = 2.4586(3)$ Å). Miller indices of F-type structural reflections are mentioned. Blue circles represent structural Bragg reflections for the $F4/mmm$ unit cell while green circles denote the B-type superstructure reflections. Blue circles show stripe magnetic peaks with $\epsilon \sim 0.44$. Elongated blue squares on $(h0l)$ plane denote diffuse character of stripe magnetic peaks parallel to the c -axis. Circles in purple color show the commensurate checkerboard charge ordering peaks.

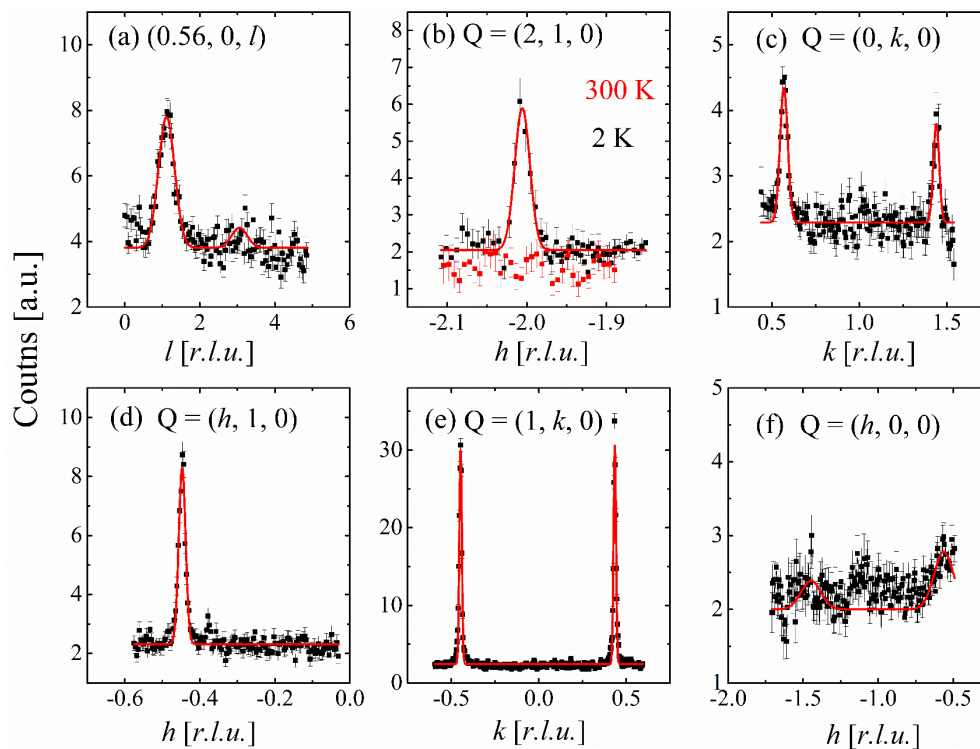


Figure 7.16 | Cuts in q -space through the spin and charge ordering superstructure reflections observed for $\text{Nd}_{1.5}\text{Sr}_{0.5}\text{NiO}_{4.06}$ single crystal at 2 K (Fig. 7.15). (a) l -dependence of the stripe spin

order at (0.56, 0, *l*), (b) Checkerboard charge ordering reflection at (2, 1, 0). Elastic *q*-cuts through stripe spin ordering reflections at (c) (0, *k*, 0), (d) (*h*, 1, 0), (e) (1, *k*, 0) and (f) at (*h*, 0, 0).

Fig. 7.16 shows several *q*-cuts of the charge and spin superlattice peaks observed on the (*hk*0) and (*h*0*l*) planes at 2 K. From the reciprocal plane mappings, the magnetic incommensurability ϵ is found to be ~ 0.44 which remains constant below the stripe magnetic ordering temperature at 95 K. **Fig. 7.16(a)** shows the *q_l* cut along the reciprocal *l*-direction through the stripe magnetic peak at (0.56, 0, *l*). Two diffuse peaks appear at around *l* = 1 and 3 at 2 K. This strongly signifies that the stripe spin order in neighboring NiO₂ layers is antiferromagnetically correlated. The intensity of the peak at *l* = 3 is strongly suppressed compared to the peak at *l* = 1. In addition, stripe magnetic peaks at *l* = 5 and 7 are barely discernible. Considering the magnetic form factor only, this behavior suggests that the moments are presumably aligned along the *c*-axis as in the case of Nd_{1.7}Sr_{0.3}NiO₄⁷⁴. To determine in plane and out of plane correlation lengths, stripe magnetic peak profile of (0.56, 0, 1) reflection was fitted to a Lorentzian function convoluted with Gaussian instrumental resolution. In plane and out of plane stripe correlation lengths are found to be 114(2) Å and 16(3) Å at 2 K, respectively. Obtained out of plane correlation length is in accordance with that estimated from the powder data. However, in plane correlation length is approximately seven times larger revealing quasi-2D magnetic behavior of these systems. The commensurate (2, 1, 0) checkerboard charge-ordering peak is shown in **Fig. 7.16(b)**. Neutrons are not directly sensitive to charges. However, the electronic charge ordering creates structural change in the local NiO₆ building blocks (**Fig. 7.17**). It appears as a Ni-O bond disproportionation or as breathing type distortions. In case of Ni-site centered charge ordering, octahedra containing the Ni²⁺ ions expands (**7.17(b)**) whereas octahedra containing the Ni³⁺ ions contracts largely because of their different ionic radii, i.e., the effective radius of Ni²⁺ (0.69 Å in six-fold coordination) is larger than Ni³⁺ (0.56 Å in six-fold coordination with low-spin state). Neutrons are sensitive to these structural modulations caused by charge ordering. The in-plane charge correlation length is determined by fitting the profile of a charge order peak (2, 1, 0) as shown in **Fig. 7.16(b)** to a Lorentzian function convoluted with the Gaussian instrumental resolution. The correlation length for the checkerboard charge order is determined to be 56(6) Å at 2 K. Both the correlation length and integrated intensities remain fixed until 200 K. The checkerboard commensurate charge order vanishes Between 200 K and 300 K. This is in strong contrast to the homologous La_{1.5}Sr_{0.5}NiO_{4.0} system in which checkerboard charge order persists until 480 K⁷³. The present neutron diffraction data is not enough to disclose the exact checkerboard charge ordering temperature but it is certainly below 300 K. Strong suppression of the checkerboard charge ordering temperature could possibly be due to excess oxygens in the present case. It is noted that estimated charge and magnetic correlation lengths are very close to the literature values reported for La_{1.5}Sr_{0.5}NiO₄⁷³ and La_{1.5}Sr_{0.5}CoO₄¹³³. **Figs. 7.16(c)-(f)** show the cuts through

the different stripe magnetic peaks in the $(hk0)$ zone along the reciprocal h and k directions. Stripe magnetic peaks at $(0, \pm 0.44, 0)$ and $(\pm 0.56, 1, 0)$ are almost similar in intensities whereas magnetic peaks at $(1, \pm 0.56, 0)$ and $(\pm 0.44, 0, 0)$ are not. The stripe magnetic peaks at $(\pm 0.44, 0, 0)$ are hardly observed at 2 K (**Fig. 7.16(f)**). This is likely due to the different volume fractions of stripe magnetic domains running parallel to the a - and b - axis in the real space. In addition, in the LTO phase below 245 K (see **Appendix D**), two structural twins are formed with non-equivalent volume fractions. Furthermore, strong anisotropic extinction effect is observed in the LTO phase of the crystal (**Appendix D**). Combination of all these effects probably make the stripe magnetic peak at $(\pm 0.44, 0, 0)$ barely distinguishable.

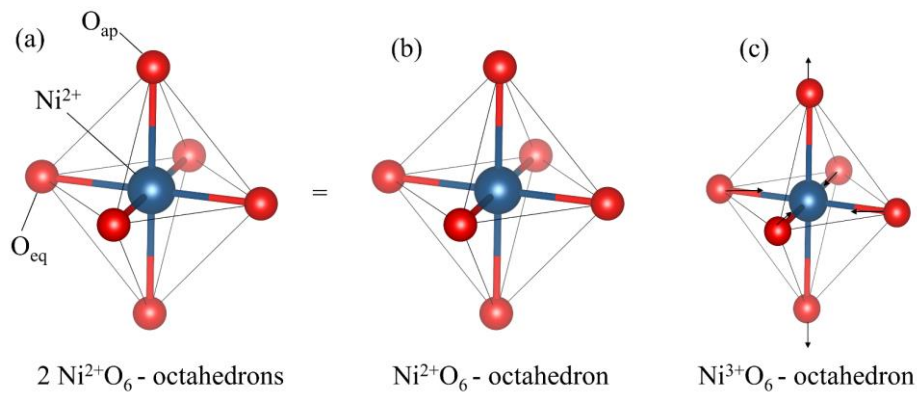


Figure 7.17 | Illustration of the effect of Ni-cite centered charge ordering on local NiO₆ octahedral distortion. (a) All octahedra are equivalent before the charge ordering. Charge ordering results into two non-equivalent Ni sites with 2+ and 3+ valence states, respectively. Charge transfer between Ni-sites causes one octahedron to dilate (b) and the other octahedron to contract (c), resembling a “breathing” mode of the NiO₆ octahedrons. In the contracted octahedra, arrows represent the directions of apical and equatorial oxygen displacements.

Next, the ordering process of the charge and spin are discussed for the Nd_{1.5}Sr_{0.5}NiO_{4.06} crystal. For the O-doped La₂NiO_{4+δ} samples, for hole concentration (n_h) between 1/4 and 1/3, ϵ is often locked at a rational value given by $\epsilon = (m + n)/(4m + 3n)$ because the commensurate $\epsilon = 1/4$ and $1/3$ stripe orders are mostly stable³⁵. For oxygen doping with hole concentration within $1/4 \leq n_h \leq 1/3$, the interstitial oxygen ordering introduces the competition between these two stable charge ordering patterns. Similarly for Sr-doped La_{2-x}Sr_xNiO_{4+δ} systems with $1/3 \leq n_h \leq 1/2$, the most two stable charge order configurations are those with $\epsilon = 1/3$ and $1/2$. Therefore, the ϵ can be expressed by a similar relation as $\epsilon = (n + m')/(3n + 2m')$ for $n_h \geq 1/3$ ³⁷. This formula implies that any ϵ value in the region between 1/3 and 1/2 can be expressed by a charge discommensuration picture in which a stripe pattern with $\epsilon = 1/3$ is embedded after every m' checkerboard units with $\epsilon = 1/2$. Therefore, the above formula reduces as $(1 + 3)/(3 \times 1) + (2 \times 3)$ for the present case with $\epsilon \sim 0.44$. Thus, embedding one stripe pattern with $\epsilon \sim 1/3$ after every

three checkerboard units allows to explain the observed incommensurability as originally proposed for La_{1.5}Sr_{0.5}NiO_{4.0}⁷³. To explain this, charge and spin ordering in NiO₂ planes are presented in **Figs. 7.18(a)** and **7.18(b)** for $\epsilon = 1/3$ and $1/2$, respectively by considering the Ni-site centered charge stripes. For $\epsilon \sim 1/3$, the charge ordering unit cell (light blue dashed line) is $3/2$ times along one of the axis of chemical unit cell (black dashed lines) and the magnetic unit cell (red dashed line) is twice larger than the charge ordered unit cell. Similarly, for $\epsilon \sim 1/2$, the charge ordered unit cell is identical to the chemical unit cell and the magnetic cell is two times larger along one of the axis of the chemical cell. In **Figs. 7.19(a)** and **7.19(b)**, 1D projections (along the a -axis) of these ordering schemes are presented without equatorial oxygens. The stripe order is represented by repetition of Ni³⁺-Ni²⁺(\uparrow)-Ni²⁺(\downarrow)-Ni³⁺ matrix where arrows represent the spin direction on Ni²⁺ sites. The width of the charge ordering cell is $3/2 a$ and the corresponding width of the magnetic unit cell is $3a$. The checkerboard charge order ($\epsilon \sim 1/2$) consists of a matrix of Ni³⁺-O-Ni²⁺(\uparrow). The widths of the charge and spin ordered unit cells of this pattern becomes a and $2a$, respectively as illustrated in **Fig. 7.19(a)**. Subsequently, a discommensuration is introduced into such pattern to obtain $\epsilon = 0.44$. For this, a stripe charge ordered unit cell of size $3a/2$ containing one hole is inserted after every three checkerboard units. Inserted hole at each discommensuration region occupies either the Ni site or an equatorial oxygen site as shown in **Fig. 7.19(c)** and **Fig. 7.19(d)**, **respectively**. It should be noted that for oxygen centered charge stripe a small ferromagnetic component is expected near to the charged ordered domain walls because of Ni²⁺ - Ni²⁺ superexchange interaction. A diffraction study alone cannot differentiate whether a hole occupies a Ni site or an oxygen site in the discommensuration region.

The likely scenario for the coexistence of checkerboard charge ordering and stripe spin ordering can be proposed as follows as originally proposed for the La_{1.5}Sr_{0.5}NiO₄ system⁷³. For the checkerboard charge ordered state, a unique superexchange (J_1) interaction between Ni²⁺ and Ni²⁺ ions exists across the charge ordered domain walls as shown in **Fig. 7.18(b)**. By contrast, for the stripe ordered state as shown in **Fig. 7.18(a)**, two different Ni²⁺-Ni²⁺ superexchange interactions are present; one (J_0) inside the inside the antiferromagnetic domain and another (J_1) across the charge ordered domain walls while the Ni²⁺-hole-Ni²⁺ ferromagnetic superexchange interactions are introduced about by the O-centered charge stripes additionally. Inelastic studies show that in the stripe-ordered state with $x = 1/3$ sample of Nd_{2-x}Sr_xNiO₄, two exchange constants $J_0 = 14$ meV and $J_1 = 7$ meV³⁶. On the other hand, the energy scale of the magnetic excitations is about 40-60 meV in the checkerboard region. Thus, the exchange interactions for stripe ordered phases are much stronger than in the checkerboard type order. Consequently, spin-exchange interactions allow the formation of a stripe order due to an energy gain compared to the checkerboard order. Small polarons are created through the electron-phonon coupling at high temperature at which spin interactions disappeared due to thermal fluctuations. The Coulomb

interactions between these polarons allow the formation of checkerboard charge order. The spin correlation develops with decreasing temperature and a large energy gain of the Ni^{2+} - Ni^{3+} bonds stabilizes the stripe order by introducing holes into the checkerboard pattern⁷³. Although the checkerboard order is favored by charges, it is further disfavored by the spin-exchange interactions. The latter favors the incommensurate ordering and results to the coexistence of the commensurate and stripe ordered regions at low temperatures in $\text{Nd}_{1.5}\text{Sr}_{0.5}\text{NiO}_{4.06}$.

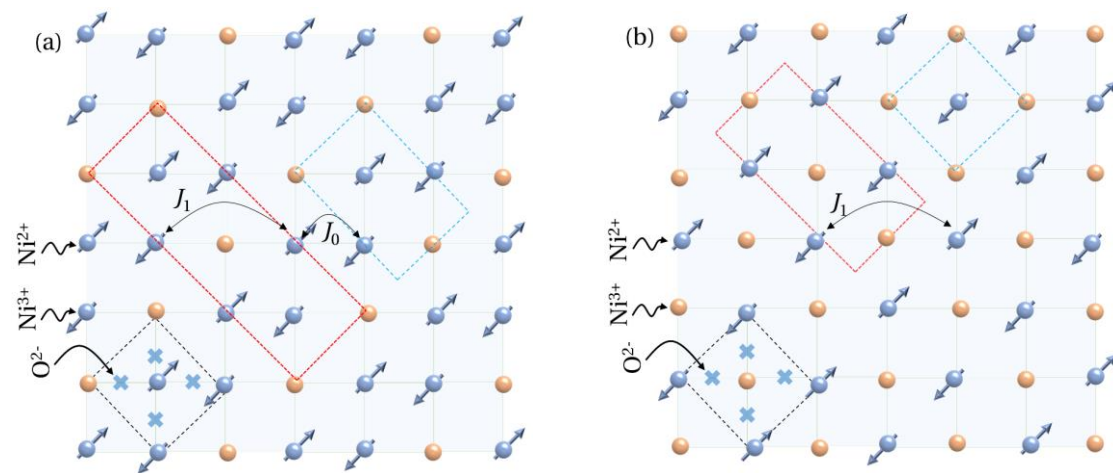


Figure 7.18 | Idealized sketch of the NiO_2 plane showing spin and charge ordering. (a) Ni-site centered stripe type charge ordering with $\epsilon = 1/3$, thus referring to 3 times larger magnetic unit cell (red dashed line) and 1.5 times larger charge ordering cell (light blue dashed line) compared to the chemical unit cell (black dashed line). (b) Checkerboard type charge ordering with $\epsilon = 1/2$ with 2 times larger magnetic unit cell. Note that in stripe order both intra- (J_0) and inter (J_1) stripe superexchange interactions are possible while only the later (J_1) is possible in checkerboard charge order.

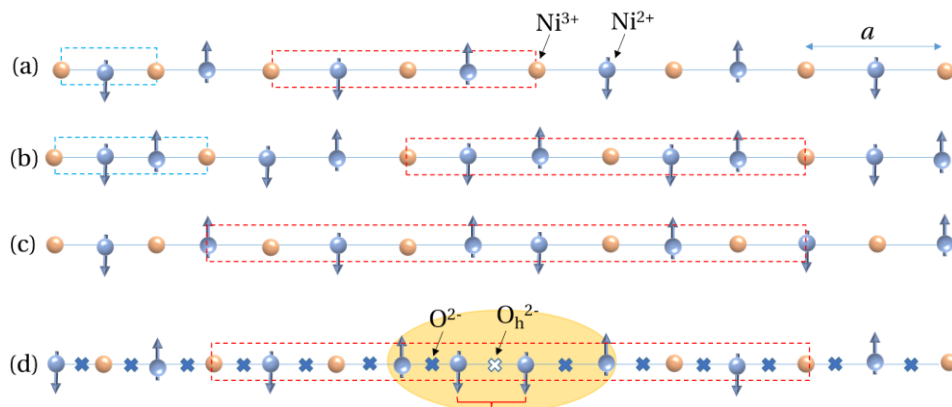


Figure 7.19 | One-dimensional projection (along the a -axis in this case) of the spin and charge ordering unit cell. (a) Checkerboard charge order with $\epsilon = 1/2$, (b) Stripe charge order with $\epsilon = 1/3$, (c) a charge discommensuration picture where three site centered checkerboard patterns (with $\epsilon = 1/2$) are repeated with one site centered stripe pattern (with $\epsilon = 1/3$) that gives $\epsilon = 4/9 \sim$

0.44 as observed for $x = 0.5$. (d) Same as (c) but with bond centered stripe pattern in which hole is located in the oxygen site (O_h^{2-}). A small ferromagnetic component is expected in case of bond centered stripes as shown by second bracket in (d).

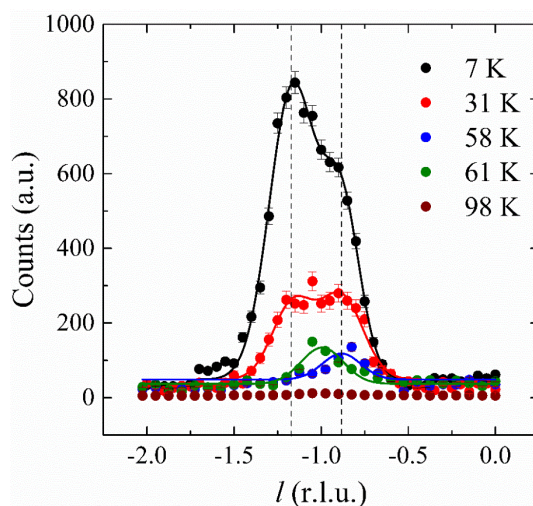


Figure 7.20 | Elastic q_l cuts through the stripe magnetic peak at $(0.56, 0, l)$ at different temperatures. Neutron diffraction measurements are performed on the high-resolution single crystal neutron diffractometer ZEBRA ($\lambda = 2.30 \text{ \AA}$) at SINQ, PSI. Scans at $T \leq 58 \text{ K}$ are fitted with two Gaussians and for $T \geq 61 \text{ K}$ are fitted with a single Gaussian as shown by solid lines.

The most intriguing result is obtained from the elastic q -scans along the reciprocal l -direction through the stripe magnetic peaks performed at different temperatures as shown in **Fig. 7.20**. Scans were performed on a high-resolution single crystal neutron diffractometer ZEBRA ($\lambda = 2.30 \text{ \AA}$) at SINQ, PSI. For stripe magnetic ordering, magnetic peaks should appear at $l = \text{integer values}$. However, $l = \text{even}$ peaks are much weaker than the $l = \text{odd}$ reflections, as observed in the present case. However, high-resolution l -scan at $(0.56, 0, l)$ shows the presence of two sub-reflections. To extract the peak positions, the peak profiles are fitted with two Gaussian lines. These sub-peaks are found to be centered at $l = 0.88$ and $l = 1.16$. These peaks are slightly asymmetric with respect to the center at $l = 1$. The deviations are possibly due to a small misalignment of the crystal as well as the temperature dependence of the c -axis length. However, the peak positions roughly can be expressed at $1-1/6$ and $1+1/6$ positions. Thus, from the splitting, it can be inferred that a long-range stacking order of stripes is developed along the c -axis with a period of $6c$. The splitting in l remains constant up to 58 K . However, the intensities of these two reflections strongly change in between 7 K and 58 K . Finally, these two reflections merge into a single reflection at $l = 1$ at 61 K corresponding to the loss or a qualitative change in the long-range stripe correlations along the c -axis. This single peak remains centered at $l = 1$ up to the magnetic ordering temperature.

7.6. Conclusions

A detailed study on structural, magnetic and thermodynamic properties of Nd_{2-x}Sr_xNiO_{4+δ} system with $0.1 \leq x \leq 0.7$ is presented as a function of temperature. This study led to following conclusions:

- (i) All air-prepared samples of Nd_{2-x}Sr_xNiO_{4+δ} contain significant amount of excess oxygens exist. However, no phase separation is observed in any powder samples. A complex sequence of structural phase transition is evidenced from high-resolution x-ray powder diffraction study. At 300 K, the system shows an orthorhombic (LTO) to a tetragonal (HTT) structural transition at $x \sim 0.22$. In addition, a HTT to LTO phase transition occurs for the $x = 0.5$ compound around 210 K. The unusual evolutions of the a - and c -lattice parameters and the Ni-O_{ap}/Ni-O_{eq} bond lengths as a function of the Sr-content signify electronic instabilities due to changes in the orbital state of the Ni ions and a strong electron-lattice coupling characteristic of the e_g orbital systems with K₂NiF₄-type structure.
- (ii) The additional oxygen content δ monotonically decreases from 0.11 to zero in as-prepared samples with the increasing Sr content x from 0.1 to 0.7. However, no evidence of the long-range ordering of excess oxygens is observed possibly due to the Coulomb interaction between the oxygen interstitials and the Sr defects, and the reduced NiO₆ octahedral tilt angle by Sr doping. Due to absence of interstitial oxygen ordering, apical oxygens are pinned to their positions without pronounced displacements to the nearest vacant interstitial sites. Consequently, oxygen mobility close to room temperature is strongly suppressed in the Sr-doped compounds compared to the oxygen-doped samples.
- (iii) A coexistence of a checkerboard-type commensurate charge order and incommensurate stripe-type spin order is evidenced in Nd_{1.5}Sr_{0.5}NiO_{4.06}. The charge ordering temperature decreases from 480 K to below 300 K due to presence of excess oxygens. While the stripe magnetic ordering sets ~ 95 K. The magnetic incommensurability is found to be $\epsilon \sim 0.44$ without any change down to 2 K. The observed incommensurability is explained by a charge discommensuration picture in which three checkerboard charge ordered unit cell is embedded with one stripe charge ordering pattern with $\epsilon = 1/3$. This result shows the evidence of robustness of the stripe order suggesting the importance of the interactions between spins and charges in the Sr-doped nickelate system. In addition, a sudden change magnetic correlation between the NiO₂ planes along the c -axis is observed

around 60 K that coincides with the anomaly on specific heat data. This point should be addressed in future studies.

Conclusions and Outlook

8.1. Conclusions

In conclusion, the oxygen and Sr-doping dependence of crystal structure, apical oxygen disorder, interstitial oxygen ordering, spin and charge ordering were investigated in layered Ruddlesden-Popper $\text{Nd}_{2-x}\text{Sr}_x\text{NiO}_{4+\delta}$ employing high resolution X-ray and neutron diffraction studies combined with macroscopic magnetic measurements. High quality poly- and single crystal samples were prepared with well-defined oxygen stoichiometry by solid-state reaction and floating zone techniques at high temperature, respectively.

In **chapter 5**, the results obtained for the moderately oxygen doped $\text{Nd}_2\text{NiO}_{4.11}$ phase are summarized. The compound crystallizes in LTT structure with tetragonal $P4_2/nm$ space group. However, the real crystal structure is far more complex and incommensurate due to 3D ordering of excess oxygen atoms in the temperature range of 2-700 K. We could evidence that the extra oxygen atoms selectively occupy the regular interstitial $4b$ Wyckoff site with site symmetry $\bar{4}$ only. Thereby, approximately one-half out of four tetrahedral sites are statistically occupied in $\text{Nd}_2\text{NiO}_{4.11}$. Occupied tetrahedra show a repulsive $\text{O}_{\text{int}}\text{-O}_{\text{ap}}$ interaction, leading to a symmetrical increase of the $\text{O}_{\text{int}}(\text{O}_{\text{ap}})_4$ tetrahedra, while the $\text{O}_{\text{int}}\text{-O}_{\text{ap}}$ distance reaches 2.76 Å, instead of 2.15 Å when taking into account the average structure. Oxygen diffusion along the [110]-direction thus involves important local distortions of the respective tetrahedral sites, resembling to a successively in- and exhaling behavior of the involved occupied and empty tetrahedra along the diffusion pathway. Such a mechanism is different from a rigid $\text{O}_{\text{int}}(\text{O}_{\text{ap}})_4$ configuration and the associated structural changes of the tetrahedral sites considerably reduces any oxygen mobility in the $P4_2/nm$ phase, compared to the disordered phase at high temperatures (~ 700 K) where all tetrahedra become dynamically activated and structurally equivalent. *This fact partially*

explains why the intermediate phase could not be oxidized at room temperature with electrochemistry. Moreover, strong anharmonic displacements of the apical oxygen atoms towards the nearest vacant interstitial sites are observed, induced by the presence of interstitial oxygen atoms. Such anharmonic behavior of the apical oxygen atoms was interpreted to be an important prerequisite for low temperature oxygen mobility in K_2NiF_4 type non-stoichiometric oxides close to room temperature. The magnetic structure of $Nd_2NiO_{4.11}$ at 2 K is antiferromagnetic with the propagation vector (100) with spins pointing parallel to the [110] directions, similar to the magnetic structure of undoped $Nd_2NiO_{4.0}$ at 2 K. The Ni-sublattice orders antiferromagnetically at 53 K showing a weak ferromagnetic component along the c -axis, explained in terms of strong DM interaction related to the tilt mode of NiO_6 octahedron in the LTT phase, while the Nd-sublattice orders only below 10 K. *Thus, the commensurate magnetic order coexists with 3D ordering of excess oxygen atoms in $Nd_2NiO_{4.11}$, which has never been observed in La-derivatives. Therefore, the conjecture that the 3D ordering of excess oxygen atoms and incommensurate magnetic ordering develops at the same oxygen content δ , as established in $La_2NiO_{4+\delta}$, does not hold in the present case.* The magnetic ordering at 53 K strongly influences the ordering of excess oxygen atoms as a large increase in the intensities of oxygen superstructure reflections are observed. This suggests a strong coupling between spins ordering and the underlying crystal lattice in nickelates, which was predicted long before with mean-field analyses of the single band Hubbard model.

In **chapter 6**, the crystal structure and magnetic properties are reported for the oxygen over-stoichiometric $Nd_2NiO_{4.23}$ phase in the temperature range of 2-1100 K. The fundamental difference between the $Nd_2NiO_{4.23}$ and $Nd_2NiO_{4.11}$ phases is that in the former compound all $O_{int}(O_{ap})_4$ tetrahedra are disordered even at low temperature, as compared to the selective disordered scheme observed in the later compound. Strong anisotropic thermal displacements of apical oxygen atoms are found towards the nearest vacant interstitial sites along the [110] directions. The modulus of thermal displacement parameters, on an absolute scale, are largely increased compared to the moderately doped $Nd_2NiO_{4.11}$ and stoichiometric $Nd_2NiO_{4.0}$ phases. In addition, diffuse systematic anharmonic local displacements of the apical oxygen atoms are observed induced by oxygen interstitials that are related to specific low energy phonon modes as simulated previously with DFT calculations. They are important prerequisites to realize oxygen mobility close to room temperature. With increasing temperature, these apical oxygen displacements are largely enhanced, however, become more isotropic in the ab -plane compared to the anisotropic nature at room temperature. *Furthermore, a double-well potential of apical oxygen atoms pointing towards interstitial vacancy sites allowing amplified oxygen mobility at moderate temperature, as observed in iso-structural $Pr_2NiO_{4.25}$ phase at 673 K, is absent in the present case. This might explain why the Pr-based compounds show higher oxygen mobility*

compared to the Nd-based derivatives in the moderate temperature range. In Nd₂NiO_{4.23}, Ni-spins antiferromagnetically order below T ~ 150 K while the magnetic contribution of Nd³⁺ is detected below 10 K. The incommensurate magnetic structure is characterized by magnetic satellites at ($h \pm \epsilon, 0, l/2$) with h and l being odd integer numbers with magnetic incommensurability, $\epsilon \sim 0.36$. A weak magnetic field dependence is observed when the magnetic field is parallel to the c -axis (perpendicular to the NiO₂ planes). The observed incommensurate magnetic phase can be explained by a 3D magnetic model in Ni and Nd spins are antiferromagnetically correlated in neighboring planes, which is substantially different from that of a stripe-type magnetic phase usually found in moderately O-doped and Sr-doped La-based RP-nickelates.

In **chapter 7**, a detailed study on structural, magnetic and thermodynamic properties of Nd_{2-x}Sr_xNiO_{4+δ} system with $x = 0.1, 0.25, 0.33, 0.5$ and 0.7 is presented as a function of temperature. In air prepared samples, the oxygen content δ value monotonically decreases from 0.11 to 0 with increasing Sr content from 0.1 to 0.7. *No phase separation exists in these samples in contrast to the La_{2-x}Sr_xNiO_{4+δ} system in which phase separation occurs at $\delta \sim 0.01$.* We showed that a structural transformation from LTO' to HTT occurs as a function of x at $x = 0.25$. In addition, the $x = 0.1$ system shows a structural transformation from LTO' to HTT at 473 K. In addition, we have interestingly found the evidence of a LTO phase below 210 K in the $x = 0.5$ compound. *One important finding of this work is that no long-range ordering of interstitial oxygen atoms is observed in these compounds even with high oxygen contents δ .* This is mainly due to the Coulomb interaction between the oxygen interstitials and the Sr defects, and the reduction of the octahedral tilt angle with Sr doping. Structure analysis reveals a large decrease in the absolute values of thermal displacement parameters of apical oxygen atoms signifying a strong decrease of apical site disorder with Sr-doping. *Therefore, strong decrease in oxygen mobility is expected at moderate temperatures in Sr-doped compounds compared to the O-doped phases, which indeed is observed experimentally.* The evolution of the c -axis lattice constant takes a local maximum at $x = 0.5$, suggesting that the doped hole first goes into the $d_{x^2-y^2}$ orbital up to $x = 0.5$ and subsequently into the $d_{3z^2-r^2}$ orbital for $x > 0.5$. Macroscopic magnetic susceptibility and specific heat measurements show the presence of a Schottky-like peak associated to the splitting of degenerate ground-state Kramer's doublet of Nd³⁺ moments into two singlets at low temperature. The strong exchange field acting on Nd³⁺ ions from ordered Ni moments lifts the degeneracy of the Nd³⁺ ground-state doublet. The splitting energy increases in the stripe region ($x \leq 0.5$) up to $x = 0.5$, while slightly decreases in the CB region ($x \geq 0.5$). An interesting scenario is observed with single crystal neutron diffraction study on the Nd_{1.5}Sr_{0.5}NiO_{4.06} compound. In the LTO phase, a commensurate checkerboard charge order is formed at T_{CO} ~ 180 K, which induces a breathing-mode type distortion of NiO₆ octahedron. However, a stripe type magnetic order is observed at T_{SO} ~ 95 K with $\epsilon \sim 0.46$. Such an incommensurability for $m_h = 0.5$ can be explained in terms of a

charge disproportionation picture which was originally introduced for $\text{Nd}_{1.5}\text{Sr}_{0.5}\text{NiO}_{4.06}$ compound. *Interestingly, the stripe type magnetic phase and checkerboard type charge order coexists below T_{SO} . However, stripe charge order peaks are not observed down to 2 K.* We have shown that the anomalies in the specific heat curves of $x = 0.33$ and 0.5 at $T \sim 60$ K, that has been a long-standing puzzle, are not related to any structural changes or spin rearrangements, *rather related to the stacking of spin stripes in the neighboring NiO_2 planes (along the c -axis) that abruptly changes around this temperature.*

8.2. Outlook

The current work answered multiple questions related to the structural and magnetic phases of O- and Sr-doped $\text{Nd}_2\text{NiO}_{4+\delta}$ compounds, however, few still remain unanswered for which further measurements are required. In the following, I have listed few of them, which are interesting but difficult to deal with at the same time.

a. Single crystal X-ray diffraction to characterize the incommensurate crystal structure

3D ordering of excess oxygen atoms is revealed with both powder and single crystal X-ray and neutron diffraction measurements for O-doped compounds. The incommensurate vectors related to the ordering excess oxygen atoms are revealed with neutron diffraction reciprocal space plane mapping in the present work. However, all the structure refinements were carried out using an average structural model and the real structural refinements were not carried, as the correct integrated intensities could not be obtained from such reciprocal space plane mappings. Therefore, single crystal X-ray and neutron diffraction measurements need to be carried out to extract correct integrated intensities of such superlattice peaks with high precision so that an incommensurate structural refinement could be undertaken. The new DMC diffractometer at SINQ, PSI with its wide 2D detector could play an important role to achieve this goal.

b. Magnetic structure of $\text{Nd}_2\text{NiO}_{4.23}$ under applied magnetic field

Macroscopic field dependent magnetization measurements show a field driven ferromagnetic like transition in $\text{Nd}_2\text{NiO}_{4.23}$ at the applied field of 3.5 T when applied parallel to the c -axis i.e. perpendicular to the NiO_2 planes below 10 K. This was initially supposed to the Nd^{3+} ordering at this temperature. With single crystal neutron diffraction, we have also confirmed such an effect

of the magnetic field; however, the change in magnetic structure under the field is not completely understood as we have observed.

c. Single crystal X-ray/neutron diffraction to verify the ordering of excess oxygen atoms in Sr-doped compounds

In the present work, synchrotron powder diffraction studies were undertaken to unravel the structural phase diagram of Sr-doped $\text{Nd}_{2-x}\text{Sr}_x\text{NiO}_{4+\delta}$ phases as a function of temperature. For $x = 0.1, 0.25$ and 0.33 , few additional superstructure reflections were observed which could not be indexed with any known impurity phases. They were primarily assumed as the superstructure peaks related to the 1D ordering of excess oxygen atoms. However, their temperature evolution raises questions about such origin. Therefore, to recognize the origin of such superstructure reflections indisputably, a combined synchrotron x-ray and neutron diffraction measurements must be carried out on single crystals.

d. Anomaly in the specific heat around 60 K for $\text{Nd}_{1.5}\text{Sr}_{0.5}\text{NiO}_{4+\delta}$ and $\text{Nd}_{1.67}\text{Sr}_{0.33}\text{NiO}_{4+\delta}$.

One of the long-lasting problems in the magnetic structure of $\text{Nd}_{2-x}\text{Sr}_x\text{NiO}_{4+\delta}$ with $x = 0.33$ and 0.5 is the anomaly in the specific heat curves around 60 K^{130} , which shifts towards higher temperature with increasing x . This anomaly was initially thought to be the structural rearrangements occurring at this temperature. However, our XRD measurements exclude such possibilities. We also exclude any change in the charge-ordering pattern around this temperature. Furthermore, neutron diffraction study performed on the $\text{Nd}_{1.5}\text{Sr}_{0.5}\text{NiO}_{4+\delta}$ single crystal in the present work demonstrates that this anomaly could be due to change in the stacking disorder or rearrangement of spin stripes along the c -axis. In addition, it is surprising to evidence this effect only in $x = 0.33$ and 0.5 as the underlying crystal symmetry is completely different at such temperature. The former compound exists in the tetragonal HTT phase while the later compound crystallizes in LTO phase with $Bmab$ space group. Therefore, further neutron diffraction measurements are required to unravel the stacking pattern in both systems.

In addition to these incomplete works, in the following I have listed some suggestions for future investigations on this compound and related compounds of this family to reach further understanding:

a. Spectroscopy to detect the presence of Ni³⁺ if any there is any in the oxygen doped samples

One of the fundamental questions related to oxygen and Sr doping in rare earth Ruddlesden-Popper type nickelates is “how the charge transfer mechanism occurs with doping”. Is it same in the case of Sr and O-doping? What is the valence state of Ni-ions in both systems? Are they same or different depending on the doped chemical (Sr or O)? In Sr-doped compounds, both stripe and checkerboard type charge orderings are observed indicating localization of injected holes in NiO₂ planes either on the equatorial site (bond centered) or on the Ni-site (site-centered). Furthermore, there are spectroscopic evidences confirming intercalation of holes in the Ni-site in both O and Sr-doped systems in a similar way⁶². However, in the present work, we have found two different magnetic ground states for O-doped and Sr-doped systems that are expected to be iso-electronic. Such observation raises the question about the charge compensation mechanism in O and Sr-doped systems. Therefore, spectroscopic studies are required to highlight this issue.

b. Crystal field levels as a function O and Sr-doping

Studying the macroscopic magnetic properties of a system can reveal the nature and temperature of spin and charge ordering at low temperature. However, with magnetic rare earth ions in a system as in the present case with Nd³⁺ ions, it may not be easy to extract such information because of the strong contribution of different crystal field levels of magnetic rare earth ions below a certain temperature that will hinder any unusual behavior of Ni-site. Therefore, a good knowledge of the crystal field levels of Nd³⁺ is required to understand the magnetic properties of these systems. As evidenced in this work, the arrangement of ligands is completely different for an O-doped compound with a Sr-doped system and preliminary calculations show strong changes in the crystal field levels with the introduction of excess oxygen atoms in the interstitial sites. Therefore, an experimental work devoted to this subject is essential. This is very demanding as numerous samples with known chemical concentrations of Sr or excess oxygens have to be prepared and analyzed.

c. Strain dependent ab-initio calculation to study the apical oxygen atoms

DFT calculations predicted the oxygen migration barriers in perovskite oxides under tensile strain and compressive strain^{134,135}. They demonstrated that tensile strain could be used to enhance the oxygen diffusion coefficient (by a factor of 10) by reducing migration barriers for oxygen diffusion compared to the unstrained conditions. Previous MD based positional recurrence maps calculated for apical oxygen atoms already provided insights on the oxygen diffusion mechanism at low temperature. However, no strain dependent study was undertaken

with such calculations. It is interesting to map out the nuclear density of the apical oxygen atoms in such strained condition. This is important towards applications where doping variations may be present especially in thin films.

d. Growing thin films with tensile strain and oxygen diffusion coefficient

Extensive efforts have been devoted in the past years to understand the role of epitaxial strain on oxygen migration mechanism and the formation of oxygen defects in ABO₃ perovskite oxides by growing thin films on various substrates. In contrast, only few similar studies are conducted for RP oxides. It was shown that the larger δ in tensile-strained Nd₂NiO_{4+ δ} thin films could enhance the oxygen diffusion coefficient relative to those of compressive-strained Nd₂NiO_{4+ δ} thin films¹³⁶. It is of particular interest to experimentally determine the oxygen diffusion coefficient at moderate temperature range with impedance spectroscopy or by isotopic exchange and compare these values with the previously obtained results from single crystal measurements.

e. Measuring oxygen conductivity with terahertz spectroscopy in rare earth nickelates at low temperature

Measuring ionic conductivity ($\sim 1 \text{ S.cm}^{-1}$) at room temperature is a difficult task, as conventional spectroscopic techniques do not allow this. Moreover, the measurements at elevated temperatures include also the electronic counterpart and extrapolation of the measured conductivity to the room temperature results in very small conductivity. Terahertz spectroscopy is one of the innovative and sophisticated technique that allows measuring ionic conductivity with large precision¹³⁷, thus provides a wealth of information unavailable from conventional techniques, and has been applied to various solid electrolyte materials recently. It also reflects the microscopic motion of the ion just before hopping to an unoccupied site. DFT based MD simulations already have shown that oxide ion diffusion in Nd₂NiO_{4+ δ} compounds occur on a time scale of about 40 ps close to room temperature. Therefore, terahertz spectroscopy can be used to measure the ionic conductivity of these systems at temperature as low as 300 K where the system is an insulator and no electronic contributions appear.

Appendix A

Properties of selected ions and stability of the $\text{RE}_{2-x}\text{Sr}_x\text{NiO}_{4+\delta}$ family

Table A.1 | Shannon ionic radii (r), coherent neutron scattering length (b_{coh}), and effective magnetic moment (μ_{eff}) of some selected ions of $\text{RE}_{2-x}\text{Sr}_x\text{NiO}_{4+\delta}$ family¹¹⁷.

Atoms	r (Å)	b_{coh} (fm)	μ_{eff} (μ_B)	Atoms	r (Å)	b_{coh} (fm)	μ_{eff} (μ_B)
La^{3+}	1.216	8.24	0.0	O^{2-}	1.4	5.803	0.0
Pr^{3+}	1.179	4.58	3.58	Ni^{2+}	0.69	10.3	2.83
Nd^{3+}	1.163	7.69	3.63	Ni^{3+}	0.6	10.3	3.87
Sm^{3+}	1.132	0.80-1.65i	0.84	Sr^{2+}	1.31	7.02	0.0

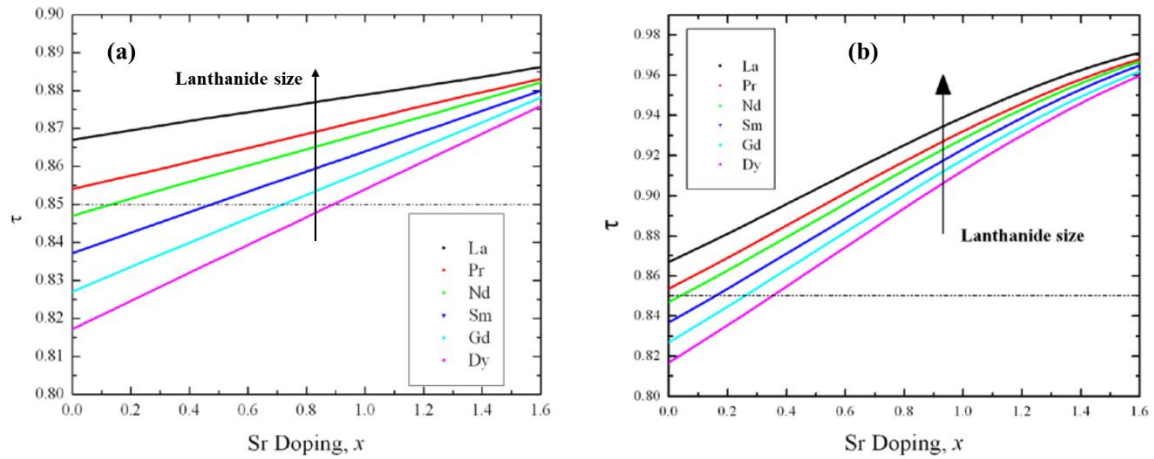


Figure A.1 | Plot of the tolerance factor as a function of Sr doping. The dashed line indicates the lower stability limit. (a) Without and (b) with taking out into account the change in the valence state of Ni ions with doping¹³⁸.

From the **Fig. A. 1**, the calculated tolerance factor (τ) as a function of x in $\text{RE}_{2-x}\text{Sr}_x\text{NiO}_{4+\delta}$ using the Shannon ionic radii given in **table A-1**, it appears that only Sr-doped La and Pr nickelates can be synthesized across the entire doping range. However, single-phase $\text{Nd}_2\text{NiO}_{4.0}$ can be synthesized successfully even at the lower stability limit. For the lanthanides smaller than Nd, it is clear that the doping size with Sr is smaller.

Appendix B

Group theoretical analyses of possible magnetic structures

a. The case of $\text{Nd}_2\text{NiO}_{4.11}$ with $P4_2/ncm$ space group

The possible magnetic structures compatible with the crystal symmetry are obtained by applying the representation theory. The little group G_k is a subset of symmetry elements within the paramagnetic space group $G_0(P4_2/ncm)$, which leaves the propagation wave vector invariant under the unitary transformation matrix M . In the present case for $\mathbf{k} = (1\ 0\ 0)$, the little group contains all elements of G_0 , which are listed in **Table A.2**. It is convenient to transform the representation of G_k into irreducible representations (IRs) which are orthogonal to one another. The character table of G_k is shown in **Table A.3**. The magnetic representation at the Ni and Nd sites can be decomposed into a direct sum of irreducible representations as following:

$$\begin{aligned}\Gamma_{\text{mag}}(\text{Ni}) &= 1\ \Gamma_1 + 2\ \Gamma_3 + 1\ \Gamma_5 + 2\ \Gamma_7 + 3\ \Gamma_{10} \\ \Gamma_{\text{mag}}(\text{Nd}) &= 1\ \Gamma_1 + 2\ \Gamma_2 + 2\ \Gamma_3 + 1\ \Gamma_4 + 1\ \Gamma_5 + 2\ \Gamma_6 + 2\ \Gamma_7 + 1\ \Gamma_8 + 3\ \Gamma_9 + 3\ \Gamma_{10}\end{aligned}$$

All IRs are one-dimensional, except Γ_9 and Γ_{10} , which are two-dimensional. The spin distribution of the j -th atom can be expressed as the Fourier transform of the linear combination of basis vectors, such that for a single propagation wave vector \mathbf{k} ,

$$S_j = \sum_n C_n V_n e^{-i\mathbf{k}\cdot\mathbf{r}_j} + c.c.,$$

where the coefficients C_n can, in general, be complex. There are four Ni (0 0 0) atoms and eight Nd ($x\ x\ z$) atoms within the primitive unit cell. They are Ni₁ (0 0 0), Ni₂ (1/2 1/2 0), Ni₃ (0 1/2 1/2), Ni₄ (1/2 0 1/2). Nd atoms are Nd₁ (x, x, z), Nd₂ ($-x+1/2, -x+1/2, z$), Nd₃ ($-x, x+1/2, -z+1/2$), Nd₄ ($x+1/2, -x+1/2, -z+1/2$), Nd₅ ($x+1/2, x+1/2, -z$), Nd₆ ($-x, -x+1/2, -z$), Nd₇ ($x, -x+1/2, z+1/2$) and Nd₈ ($-x+1/2, x, z+1/2$). The basis vectors belonging to each irreducible representation are presented in **Table A.4**.

Table A.2 | Symmetry operators of space group $P4_2/nm$ showing explicitly the rotational part, IT notation as listed in the International Tables of Crystallography.

Symbol	IT notation	Symbol	IT notation
g ₁	1	g ₉	-1 0,0,0
g ₂	2 1/4,1/4,z	g ₁₀	<i>n</i> (1/2,1/2,0) <i>x,y,0</i>
g ₃	2 (0,1/2,0) 0,y,1/4	g ₁₁	<i>c</i> <i>x</i> ,1/4, <i>z</i>
g ₄	2 (1/2,0,0) <i>x</i> ,1/2,1/4	g ₁₂	<i>c</i> 1/4, <i>y,z</i>
g ₅	2 (1/2,1/2,0) <i>x,x,0</i>	g ₁₃	<i>m</i> <i>x</i> ,- <i>x</i> +1/2, <i>z</i>
g ₆	2 (-1/2,1/2,0) <i>x</i> ,- <i>x</i> +1/2,0	g ₁₄	<i>m</i> <i>x,x,z</i>
g ₇	4- (0,0,1/2) 1/4,1/4, <i>z</i>	g ₁₅	-4- -1/4,1/4, <i>z</i> ; -1/4,1/4,1
g ₈	4+ (0,0,1/2) 1/4,1/4, <i>z</i>	g ₁₆	-4+ 1/4,-1/4, <i>z</i> ; 1/4,-1/4,1

Table A.3 | Irreducible representations of the space group $P4_2/nm$ with $\mathbf{k} = (1\ 0\ 0)$. The final column gives the magnetic space group of each 1D IR in the Belov-Neronova-Smirnova notation.

Γ	g_1	g_2	g_3	g_4	g_5	g_6	g_7	g_8	g_9	g_{10}	g_{11}	g_{12}	g_{13}	g_{14}	g_{15}	g_{16}	M.S.G
1	1	1	1	1	1	1	1	1	1	1	1	1	1	1	1	1	$P4_2/nm$
2	1	1	1	1	1	1	1	1	-1	-1	-1	-1	-1	-1	-1	-1	$P4_2/n'c'm'$
3	1	1	1	1	-1	-1	-1	-1	1	1	1	1	-1	-1	-1	-1	$P4'_2/nm'$
4	1	1	1	1	-1	-1	-1	-1	-1	-1	-1	-1	1	1	1	1	$P4'_2/n'c'm$
5	1	1	-1	-1	1	1	-1	-1	1	1	-1	-1	1	1	-1	-1	$P4'_2/nc'm$
6	1	1	-1	-1	1	1	-1	-1	-1	-1	1	1	-1	-1	1	1	$P4'_2/n'cm'$
7	1	1	-1	-1	-1	-1	1	1	1	1	-1	-1	-1	-1	1	1	$P4_2/nc'm'$
8	1	1	-1	-1	-1	-1	1	1	-1	-1	1	1	1	1	-1	-1	$P4_2/n'cm$
9	1 0	-1 0	1 0	-1 0	0 1	0 1	0 -1	0 -1	0 1	-1 0	-1 0	1 0	0 -1	0 1	0 1	0 -1	---
	0 1	0 -1	0 -1	0 1	1 0	-1 0	1 0	-1 0	0 -1	0 1	0 1	0 -1	-1 0	1 0	-1 0	1 0	
10	1 0	-1 0	1 0	-1 0	0 1	0 1	0 -1	0 -1	0 1	1 0	-1 0	1 0	-1 0	0 1	0 -1	0 -1	---
	0 1	0 -1	0 -1	0 1	1 0	-1 0	1 0	-1 0	0 1	0 -1	0 -1	0 1	1 0	-1 0	1 0	-1 0	

Table A.4 | Basis vectors corresponding of the Ni and Nd atoms. The notation for the direction is $[e_x e_y e_z]$; e_z is parallel to the c -axis axis and e_x and e_y are in the basal plane parallel to the a - and b -axis, respectively.

IRs	Basis vectors	Ni ₁ , Nd ₁	Ni ₂ , Nd ₂	Ni ₃ , Nd ₃	Ni ₄ , Nd ₄	Nd ₅	Nd ₆	Nd ₇	Nd ₈
Γ_1	V_1^1	$[1 \bar{1} 0]$	$[\bar{1} 1 0]$	$[\bar{1} \bar{1} 0]$	$[1 1 0]$	$[\bar{1} 1 0]$	$[1 \bar{1} 0]$	$[\bar{1} \bar{1} 0]$	$[1 1 0]$
	V_2^1	$[1 1 0]$	$[\bar{1} \bar{1} 0]$	$[\bar{1} 1 0]$	$[1 \bar{1} 0]$	$[1 1 0]$	$[\bar{1} \bar{1} 0]$	$[1 \bar{1} 0]$	$[\bar{1} 1 0]$
Γ_2	V_2^2	$[0 0 1]$	$[0 0 1]$	$[0 0 \bar{1}]$	$[0 0 \bar{1}]$	$[0 0 \bar{1}]$	$[0 0 \bar{1}]$	$[0 0 1]$	$[0 0 1]$
	V_3^1	$[1 1 0]$	$[\bar{1} \bar{1} 0]$	$[\bar{1} 1 0]$	$[1 \bar{1} 0]$	$[\bar{1} \bar{1} 0]$	$[1 1 0]$	$[\bar{1} 1 0]$	$[1 \bar{1} 0]$
Γ_3	V_3^2	$[0 0 1]$	$[0 0 1]$	$[0 0 \bar{1}]$	$[0 0 \bar{1}]$	$[0 0 1]$	$[0 0 1]$	$[0 0 \bar{1}]$	$[0 0 \bar{1}]$
	V_4^1	$[1 \bar{1} 0]$	$[\bar{1} 1 0]$	$[\bar{1} \bar{1} 0]$	$[1 1 0]$	$[1 \bar{1} 0]$	$[\bar{1} 1 0]$	$[1 1 0]$	$[\bar{1} \bar{1} 0]$
Γ_4	V_5^1	$[1 \bar{1} 0]$	$[\bar{1} 1 0]$	$[1 1 0]$	$[\bar{1} \bar{1} 0]$	$[\bar{1} 1 0]$	$[1 \bar{1} 0]$	$[1 1 0]$	$[\bar{1} \bar{1} 0]$
Γ_5	V_6^1	$[1 1 0]$	$[\bar{1} \bar{1} 0]$	$[1 \bar{1} 0]$	$[\bar{1} 1 0]$	$[1 1 0]$	$[\bar{1} \bar{1} 0]$	$[\bar{1} 1 0]$	$[1 \bar{1} 0]$
	V_6^2	$[0 0 \bar{1}]$	$[0 0 \bar{1}]$	$[0 0 \bar{1}]$	$[0 0 \bar{1}]$	$[0 0 \bar{1}]$	$[0 0 \bar{1}]$	$[0 0 \bar{1}]$	$[0 0 \bar{1}]$
Γ_6	V_7^1	$[1 1 0]$	$[\bar{1} \bar{1} 0]$	$[1 \bar{1} 0]$	$[\bar{1} 1 0]$	$[1 1 0]$	$[\bar{1} \bar{1} 0]$	$[\bar{1} 1 0]$	$[1 \bar{1} 0]$
	V_7^2	$[0 0 1]$	$[0 0 1]$	$[0 0 1]$	$[0 0 1]$	$[0 0 1]$	$[0 0 1]$	$[0 0 1]$	$[0 0 1]$
Γ_7	V_8^1	$[1 \bar{1} 0]$	$[\bar{1} 1 0]$	$[1 1 0]$	$[\bar{1} \bar{1} 0]$	$[1 \bar{1} 0]$	$[\bar{1} 1 0]$	$[\bar{1} \bar{1} 0]$	$[1 1 0]$
	V_9^1	$[1 0 0]$	$[1 0 0]$	$[\bar{1} 0 0]$	$[\bar{1} 0 0]$	$[\bar{1} 0 0]$	$[\bar{1} 0 0]$	$[1 0 0]$	$[1 0 0]$
Γ_8	V_9^2	$[0 1 0]$	$[0 1 0]$	$[0 1 0]$	$[0 1 0]$	$[0 \bar{1} 0]$	$[0 \bar{1} 0]$	$[0 \bar{1} 0]$	$[0 \bar{1} 0]$
	V_9^3	$[0 0 1]$	$[0 0 \bar{1}]$	$[0 0 \bar{1}]$	$[0 0 1]$	$[0 0 1]$	$[0 0 \bar{1}]$	$[0 0 1]$	$[0 0 \bar{1}]$
Γ_9	V_9^4	$[0 \bar{1} 0]$	$[0 \bar{1} 0]$	$[0 1 0]$	$[0 1 0]$	$[0 1 0]$	$[0 1 0]$	$[0 \bar{1} 0]$	$[0 \bar{1} 0]$
	V_9^5	$[\bar{1} 0 0]$	$[\bar{1} 0 0]$	$[\bar{1} 0 0]$	$[\bar{1} 0 0]$	$[1 0 0]$	$[1 0 0]$	$[1 0 0]$	$[1 0 0]$
Γ_{10}	V_9^6	$[0 0 \bar{1}]$	$[0 0 1]$	$[0 0 \bar{1}]$	$[0 0 1]$	$[0 0 \bar{1}]$	$[0 0 1]$	$[0 0 1]$	$[0 0 \bar{1}]$
	V_{10}^1	$[1 0 0]$	$[1 0 0]$	$[\bar{1} 0 0]$	$[\bar{1} 0 0]$	$[1 0 0]$	$[1 0 0]$	$[\bar{1} 0 0]$	$[\bar{1} 0 0]$
Γ_{10}	V_{10}^2	$[0 1 0]$	$[0 1 0]$	$[0 1 0]$	$[0 1 0]$	$[0 1 0]$	$[0 1 0]$	$[0 1 0]$	$[0 1 0]$
	V_{10}^3	$[0 0 1]$	$[0 0 \bar{1}]$	$[0 0 \bar{1}]$	$[0 0 1]$	$[0 0 \bar{1}]$	$[0 0 1]$	$[0 0 \bar{1}]$	$[0 0 1]$

V_{10}^4	[0 1 0]	[0 1 0]	[0 $\bar{1}$ 0]	[0 $\bar{1}$ 0]	[0 1 0]	[0 1 0]	[0 $\bar{1}$ 0]	[0 $\bar{1}$ 0]
V_{10}^5	[1 0 0]	[1 0 0]	[1 0 0]	[1 0 0]	[1 0 0]	[1 0 0]	[1 0 0]	[1 0 0]
V_{10}^6	[0 0 1]	[0 0 $\bar{1}$]	[0 0 1]	[0 0 $\bar{1}$]	[0 0 $\bar{1}$]	[0 0 1]	[0 0 1]	[0 0 $\bar{1}$]

b. Symmetry related modulation vectors for excess oxygen ordering in the LTT phase

The modulation vector found from the $(hk0)$ reciprocal plane mapping related to one domain is $k = (0.23, 0.15, 0)$. This k is not equivalent to $-k$, the extended little group is $G(k, -k)$. The symmetry operations following the k -vectors constitute the co-set decomposition $G[G_k]$. The star of k is formed by the following eight vectors that can be obtained after applying symmetry elements of LTT phase as listed in **Table A.2** of **Appendix B**. These modulation vectors are symmetry related but structurally inequivalent. On the right side of each modulation vector, symmetry operations are indicated.

$$\begin{aligned}
 k_1 &= (0.23, 0.15, 0); \text{ symmetry elements } g_1, g_{10} \\
 k_2 &= (-0.23, -0.15, 0); \text{ symmetry elements } g_2, g_9 \\
 k_3 &= (0.15, -0.23, 0); \text{ symmetry elements } g_3, g_{13} \\
 k_4 &= (-0.23, 0.15, 0); \text{ symmetry elements } g_4, g_{14} \\
 k_5 &= (-0.15, 0.23, 0); \text{ symmetry elements } g_5, g_{11} \\
 k_6 &= (0.23, -0.15, 0); \text{ symmetry elements } g_6, g_{12} \\
 k_7 &= (-0.15, -0.23, 0); \text{ symmetry elements } g_7, g_{16} \\
 k_8 &= (0.15, 0.23, 0); \text{ symmetry elements } g_8, g_{15}
 \end{aligned}$$

The modulation vector found from the $(h0l)$ reciprocal plane mapping related to one domain is $K = (0.2, 0, 0.5)$. This K is not equivalent to $-K$, the extended little group is $G(k, -k)$. The star of K is formed by the following four vectors as obtained by the application of symmetry operations of the LTT phase. On $(h0l)$ plane, only two of them could be observed.

$$\begin{aligned}
 k_1 &= (0.2, 0, 0.5) \text{ is equivalent to } k'_1 = (0.2, 0, -0.5); \text{ symmetry elements } g_1, g_6, g_{10}, g_{12} \\
 k_2 &= (-0.2, 0, 0.5) \text{ is equivalent to } k'_2 = (-0.2, 0, -0.5); \text{ symmetry elements } g_2, g_4, g_9, g_{14} \\
 k_3 &= (0, 0.2, 0.5) \text{ is equivalent to } k'_3 = (0, 0.2, -0.5); \text{ symmetry elements } g_3, g_7, g_{13}, g_{16} \\
 k_4 &= (0, -0.2, 0.5) \text{ is equivalent to } k'_4 = (0, -0.2, -0.5); \text{ symmetry elements } g_5, g_8, g_{11}, g_{15}
 \end{aligned}$$

Appendix C

Twining in as-grown $\text{Nd}_2\text{NiO}_{4+\delta}$ single crystal

The given discussion below provides a short overview on twinning appear during the growth of $\text{RE}_2\text{MO}_{4+\delta}$ single crystals at high temperature. Most of the results presented below are already summarized by Paulus et al.⁶⁰, Braden et al.¹³⁹ and Dréau et al.¹⁰⁴. Twin domains in these oxides appear during the cooling after the crystal growth when the crystal passes through the HTT to LTO' phase transition temperature¹³⁹. Such a phase transition is induced by a cooperative tilt of the NiO_6 octahedra occurring to releases structural strains. They are referred as transformation twins and in this case, different domains are microscopically intergrown. Depending on the orientations of the basal plane of different twin domains sharing a common c -axis, only two or four domains are possible to form in the bulk. The structural modifications lead to the tilting of octahedra either parallel to the a -axis (consequently, $a_{\text{LTO}'} > b_{\text{LTO}'}$) or parallel to the b -axis (consequently, $b_{\text{LTO}'} > a_{\text{LTO}'}$). The phase transition occurs simultaneously at different locations of the crystal during cooling. However, the tilts cannot propagate fast enough to form a single domain with a given tilt pattern of the octahedron. Two symmetry elements; the $(110)_{\text{LTO}'}$ and $(-110)_{\text{LTO}'}$ diagonal mirror planes are lost due to twin domain formation below the transition temperature. These two symmetry operations constitute the elements of the twin law^{25,60}. The loss of each mirror plane generates two twins, *i.e.* two twin domains are formed if one mirror is lost, and four twin domains appear if both mirrors are lost. The twinning is non-merohedral type since the twin elements belong neither to the point group nor to the crystal system below the transition temperature. However, it is of pseudo-merohedral type due to small orthorhombicity that results into partial overlapping of Bragg reflections. Due to the transition, the four-fold axis parallel to the c -axis is reduced to a two-fold. The two sets of twins are related by this four-fold axis. Consequently, when four twin domains are present, the reciprocal lattice consisting of superimposition of each twin lattice is symmetrical by 90° rotation around the c -axis. Thus, the reciprocal pattern can be averaged in a unique tetragonal unit-cell with $F4/mmm$ space group as shown in **Fig. A.2**. Depending on the values of a - and b -lattice parameters, the splitting angle is given by⁶⁰

$$\Delta = \tan^{-1}(b/a) - \tan^{-1}(a/b) \quad (\text{A.1})$$

The angular separation is given by Δ for $(h00)$ and $(0k0)$ reflections, while it corresponds to 2Δ for $(hh0)$ reflections. The nuclear Bragg reflections consist of two sub-reflections in the case of two twins. These sub-reflections are well resolved or partially overlapped depending on 2θ . However, $(-hh0)$ and $(h-h0)$ reflections are perfectly overlapped when the (110) mirror plane is lost and $(hh0)$ and $(-h-h0)$ reflections are completely overlapped if the (-110) mirror plane vanishes. In the case of four twin domains, each Bragg reflection consists of four sub-reflections, except the $(\pm h\pm h0)$ reflections, which split into three subpeaks (two of the four are exactly overlapped).

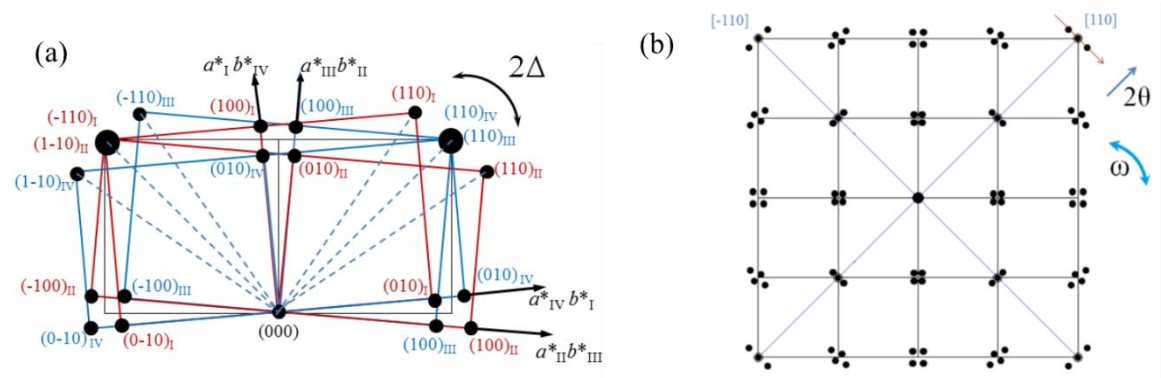


Figure A.2 | (a) Twinning scheme for the as-grown $\text{Nd}_2\text{NiO}_{4.23}$ single crystal with the loss of both $[110]$ and $[-110]$ mirror planes, resulting in four twin individuals. (b) Idealized reciprocal $(hk0)$ plane with four twin individuals with the c -axis perpendicular to the diffraction plane. The figure is taken from the reference¹⁰⁴.

The Δ value can be obtained experimentally with x-ray or neutron diffraction by performing conventional ω -scans of $(h00)$ and $(hh0)$ nuclear Bragg reflections by mounting the crystal with $(hk0)$ plane as the scattering plane. Δ is independent to both miller indices and wavelength. In case of as-grown $\text{Nd}_2\text{NiO}_{4.23}$ single crystal, we have found the evidence of four twin domains from the ω -scan of (220) and (-220) reflections as shown in **Fig. A.3**. However, deduction of integrated intensities of each Bragg reflection corresponding to each twin domain is a tough task due to the pseudo-merohedral twinning. Consequently, the intensities of Bragg reflections are integrated together and indexed with a single tetragonal structural model. However, this simplified data treatment process only allows the average structure solution in $F4/mmm$ space group with pseudo tetragonal unit-cell when the true symmetry of the domains is $Fmmm$ or $F112/m$.

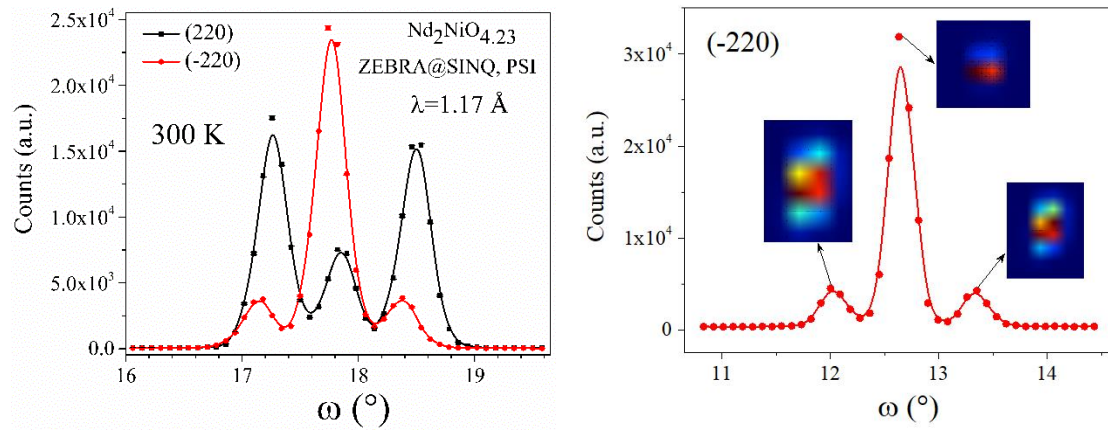


Figure A.3 | (left) Neutron diffraction ω -scan profiles of the (220) and (-220) Bragg reflections of as-grown $\text{Nd}_2\text{NiO}_{4.23}$ single crystal. Scans were performed at 300 K on ZEBRA at SINQ, PSI. The ratio of twin volumes is 38:38:12:12 as obtained from the integrated intensity of each peak. (right) Color map representation of intensity distribution of different twin individuals as observed in the 2D detector during the ω -scan of (-220) reflection on D9 at ILL.

Appendix D

Point charge calculations of crystal field levels of Nd³⁺ with Mcphase

Complex interplay between localized $4f$ moments of the Nd³⁺ ions and the antiferromagnetically correlated NiO₂ planes in Nd_{2-x}Sr_xNiO_{4+δ} gives rise to interesting magnetic properties at low temperatures ($T < 100$ K). The electronic states of these rare earth ions play a key role in understanding the microscopic origin of these effects. The electronic energy levels of rare earth ions are mainly determined by the spin-orbit coupling. Furthermore, the electric potential from the neighboring ions i.e. the local crystalline electric field (CEF) determines the splitting of the lowest J -multiplet, which mainly determines the magnetic properties of the system at any given temperature.

The electronic ground state of Nd³⁺ from Hund's rule gives the electron configuration as [Xe].4f⁶ which gives $S = 3/2$, $L = 6$ and $J = 9/2$. In the spectroscopic notation, the ground state is given by $^4I_{9/2}$ ¹⁴⁰. The multiplet separation between $J = 9/2$ and $J = 11/2$ is about 1800 cm⁻¹ (0.22 eV), and thus higher multiplets should not be neglected at room temperature¹⁴⁰. However, the correction term after including the higher multiplets adds only about 3% to the susceptibility at room temperature according to Frank et al.¹⁴¹. The ground state of Nd³⁺ is a half integer. According to Kramers theorem, the spatial degeneracy of this state cannot be lifted only by the electric field. Consequently, the minimum degeneracy of each level will be two and will show the Zeeman effect of the first and higher orders. Therefore, in the absence of a magnetic field, the ten levels ($2J+1=10$) of Nd³⁺ for $J = 9/2$ constitute five degenerate levels. In presence of a cubic crystalline field, these ten levels would split into three levels, with the upper two being doubly degenerate. There would be further splitting if the point symmetry is lower than cubic¹⁴². It is well known for rare earth compounds that the magnetic susceptibility deviates at low temperature from the Curie law. This is predominantly due to the contributions of the crystalline electric fields from surrounding ions. The fundamental expression for the magnetic susceptibility is¹⁴⁰

$$\chi = -\frac{N}{H} \frac{\sum \frac{\partial W}{\partial H} e^{-W/kT}}{\sum e^{-W/kT}} \quad (\text{A.2})$$

where H is the magnetic field, N is Avogadro's number, and W is the energy of the electronic states in the presence of the magnetic field. The summation in **eq. A.2** runs over all the energy levels. The dominant contribution to the susceptibility comes from the energy levels, which are lying in the range of kT and the contribution of the other levels that are far from kT is negligible. Each RE^{3+} ion is under an electric field determined by the surrounding atoms and the splitting energy depends on the crystal structure and the local environments around the RE^{3+} ion. Therefore, to account the magnetic properties of these systems at low temperature knowledge of the CEF is essential.

In undoped $\text{Nd}_2\text{NiO}_{4.0}$, each Nd^{3+} ion is coordinated by nine oxygen atoms (*cf.* **Fig. A.4**)-five of them are equatorial oxygen atoms from NiO_2 plane and other four are the apical oxygen atoms in the Nd_2O_2 plane. The stoichiometric $\text{Nd}_2\text{NiO}_{4.0}$ crystallizes with the LTO type structure at room temperature, and undergoes an LTO-LTT transition at 130 K. To a first approximation, the point symmetry of the Nd^{3+} site belongs to the tetragonal point group $4mm$ (C_{4v}), as in $\text{Nd}_{2-x}\text{Sr}_x\text{NiO}_{4+\delta}$ with $x \geq 0.25$. However, due to tilting of the NiO_6 octahedra the actual site symmetry is lowered to the monoclinic point group m (C_{1h}). **Fig. A. 4(a)** shows the distribution of nearest-neighbour oxygen ions around the Nd^{3+} site in the point group m . **Fig. A. 4(b)** shows the ligands distribution in the case of the oxygen doped $\text{Nd}_2\text{NiO}_{4.23}$ sample with the LTO' structure. In this case, statistically one extra interstitial oxygen (O_{int}) is present near to the Nd^{3+} ion with a bond distance of about 2.366 Å. This extra oxygen atom with charge $-2e$, as confirmed with the neutron diffraction experiments, largely perturbs the crystalline electric fields of the Nd^{3+} ions thus modifying the low temperature magnetic properties for oxygen-doped phases. The ligands distribution around Nd^{3+} in the HTT structure of Sr-doped samples with $x \geq 0.25$ can be illustrated as in the LTO' case without the interstitial oxygen atom.

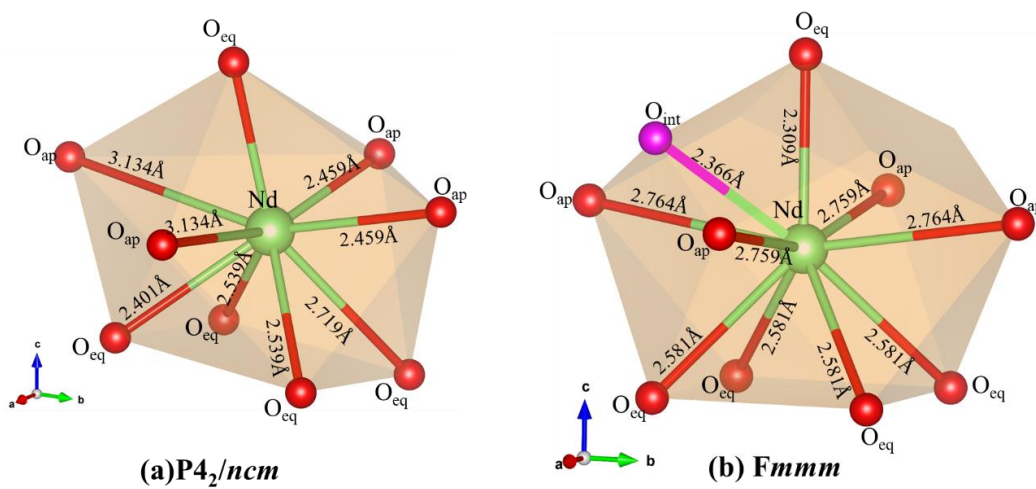


Figure A.4 | Representation of NdO polyhedra showing the change of local environment around Nd^{3+} ions in (a) stoichiometric LTT phase of $\text{Nd}_2\text{NiO}_{4.0}$ and (b) excess oxygen intercalated LTO'

phase of Nd₂NiO_{4.23} at 300 K. Different bond distances are indicated as obtained from neutron powder diffraction study.

In the following, we have calculated single ion crystal field levels of Nd³⁺ with a simple point charge model by taking into account the nearest neighbours oxygen atoms only. The primary idea of this calculation is to describe, at least qualitatively, the changes in the crystalline electric field as a function of structural changes induced by Sr and oxygen doping. It should be emphasized that the point charge model is used only to understand the *relative changes* in the CEF levels qualitatively. An *absolute* calculation can only be performed after inclusion of combined effects from distant neighbours, higher order J -multiplets, screening, and bond delocalization. For the calculation of crystal field levels, we have used the singleion package of the program Mcphase¹⁴³. The following magnetic Hamiltonian H was treated for Nd³⁺:

$$H = \sum_{n,lm} B_l^m O_{lm}(J^n) - \frac{1}{2} \sum_{nn'} J(nn') J^n J^{n'} - \sum_n g_j \mu_B J^n H \quad (\text{A.3})$$

The first term describes the crystal field (Stevens Operators O_m^l), the second term the magnetic exchange interaction, the third the Zeeman energy if an external magnetic field is applied. In these simple calculations, no magnetic exchange interaction was considered between the rare earth ions, which is also very weak.

Tables A.5-8 lists the energy levels calculated for single Nd³⁺ ion for these structures considering divalent oxide ions with charge -2e. These calculations were performed with the axes of local crystal field as $y \parallel b$, $z \parallel (a \times b)$ and x normal to y and z . A reasonable agreement is observed between the calculated and experimentally determined values of crystal field levels for the stoichiometric Nd₂NiO_{4.0} compound. Change in the structural distortion strongly influences the splitting energy of crystal field levels. Additional oxygen atoms in the interstitial sites strongly perturb the CEF scheme in the Nd₂NiO_{4.23} system. However, in each case, the degenerate ground state of Nd³⁺ ion is split into two levels with separation of 1.5 meV due to the applied magnetic field of magnitude 5 T parallel to the c -axis. The splitting results into a Schottky type anomaly in both the specific heat and magnetic susceptibility data as observed in this thesis work. The magnetic field appears from the internal magnetic field created by Ni magnetic moments in the NiO₂ planes. From the specific heat of stoichiometric compound¹⁴⁴ it was found that the internal magnetic field is acting on the Nd³⁺ spins along the c -axis of magnitude 5.2 T, as observed here numerically with the simple point charge model.

Table A.5 | Crystal field levels of Nd³⁺ ion at 2 K in the LTT phase of Nd₂NiO_{4.0}.

Without field energy levels (meV)	With field of 5.2 T <i>c</i> -axis energy levels (meV)	Experimentally determined energy levels (meV) ¹⁴⁴
0	0	0
0	1.19	1.5
8.85	8.59	6.89
8.85	10.3	6.89
26.45	26.7	24.13
26.45	27.39	24.13
36.54	36.75	38
36.54	37.52	38
54.42	54.99	49
54.42	55.07	49

Table A.6 | Crystal field levels of Nd³⁺ ion at 2 K in the HTT phase of Nd_{1.67}Sr_{0.33}NiO₄.

Without field energy levels (meV)	With field of 5.2 T <i>c</i> -axis energy levels (meV)
0	0
0	1.99
30.59	30.81
30.59	32.35
36.82	37.48
36.82	38.13
54.81	55.71
54.81	55.92
57.11	58
57.11	58.11

Table A.7 | Crystal field levels of Nd³⁺ ion at 2 K in the LTO phase of Nd_{1.5}Sr_{0.5}NiO₄.

Without field energy levels (meV)	With field of 5.2 T <i>c</i> -axis energy levels (meV)
0	0
0	1.97
26.09	26.41
26.09	27.74
38.63	39.19
38.63	40.05
55.54	56.34
55.54	56.72
59.6	60.4
59.6	60.78

Table A.8 | Crystal field levels of Nd³⁺ ion at 2 K in the LTO' phase of Nd₂NiO_{4.23}.

Without field and without interstitial energy levels (meV)	Without field and with interstitial energy levels (meV)	With field of 5.2 T c-axis energy levels (meV)
0	0	0
0	0	1.37
25.47	67.26	67.29
25.47	67.26	68.56
29.03	99.66	100.05
29.03	99.66	100.63
45.75	122.76	123.14
45.75	122.76	123.75
45.96	149.12	149.69
45.96	149.12	149.93

Calculation of splitting energy of ground state doublet of magnetic Nd³⁺ ions from specific heat and magnetic susceptibility data

The magnetization (M) of a paramagnet in a magnetic field (H) is defined by Langevin's expression and given by

$$M = N\mu \tanh\left(\frac{\mu H}{kT}\right) \quad (\text{A.4})$$

In a field H, the energy (E) of the magnetic moment of the body is MH. Therefore, the specific heat is given by

$$C = dE/dT = \left(N\mu^2 H^2 / kT^2\right) \text{sech}^2\left(\mu H / kT\right) \quad (\text{A.5})$$

The splitting of energy levels will be defined by $G = 2\mu H$ and in the temperature unit it is G/k . Then the equation (A.5) is defined by,

$$C = Nk \left(G^2 / 4T^2\right) \text{sech}^2(G/2T) \quad (\text{A.6})$$

Thus, the molar susceptibility is defined by,

$$C_{molar} = R \left(\frac{G^2}{4T^2} \right) \text{sech}^2(G/2T) \quad (\text{A.7})$$

Furthermore, $\text{sech}(x) = \frac{2}{e^x + e^{-x}}$ which leads equation (A.7) to the following form,

$$C_{molar} = R \left(\frac{G^2}{T^2} \right) \frac{e^{G/T}}{(1 + e^{G/T})^2} \quad (\text{A.8})$$

The equation (A.8) defines the molar specific heat of a paramagnetic substance in a magnetic field H , which separates energy levels by $2\mu H$ with equal degeneracy. For, non-equivalent degeneracy, the equation (A.8) will come as

$$C_{molar} = R \left(\frac{\varepsilon}{T} \right)^2 \frac{g_0/g_1 e^{\varepsilon/T}}{(1 + g_0/g_1 e^{\varepsilon/T})^2} \quad (\text{A.9})$$

The maximum of the specific heat will occur at temperature; T_m where $dC_{molar}/dT = 0$.

At T_m ,

$$e^{G/T_m} = \frac{G/T_m + 2}{G/T_m - 2} \quad (\text{A.10})$$

The solution gives $G/T_m = 2.3995$. Therefore, the maximum in the specific heat curve will give

$$G = 2.3995 T_m \quad (\text{A.11})$$

Following the equation (A.4), the magnetic susceptibility of the paramagnet can be defined by

$$\chi = dM/dH = \left(\frac{N\mu^2}{kT} \right) \text{sech}^2 \left(\frac{\mu H}{kT} \right) \quad (\text{A.12})$$

$$= \left(\frac{N\mu^2}{kT} \right) \text{sech}^2(G/2T) = \left(\frac{N\mu^2}{kT} \right) \frac{e^{G/T}}{(1 + e^{G/T})^2} \quad (\text{A.13})$$

$$\mu = \mu_{eff} = \sqrt{J(J+1)} g_j \mu_B \quad (\text{A.14})$$

The maximum of magnetic susceptibility will occur at $T = T_{max}$ where $\frac{d\chi}{dT} = 0$

At $T = T_{max}$,

$$e^{\frac{G}{T_{max}}} = \frac{\frac{G}{T_{max}} + 1}{\frac{G}{T_{max}} - 1} \quad (\text{A.15})$$

The solution gives $\frac{G}{T_{max}} = 1.5434$. Therefore, the peak in the specific heat curve will give

$$G = 1.5434 T_{max} \quad (\text{A.16})$$

The differential magnetic susceptibility is given by $\frac{d\chi}{dT}$. The maximum in the differential susceptibility will be appearing at $T = T_{\chi,max}$ where $\frac{d^2\chi}{dT^2} = 0$.

At $T = T_{\chi,max}$,

$$\frac{e^{\frac{G}{T_{\chi,max}}} - 2}{e^{\frac{G}{T_{\chi,max}}} + e^{-\frac{G}{T_{\chi,max}}}} = \frac{1}{x} + \frac{1}{2} \quad (\text{A.17})$$

The solution of equation (A.17) gives $\frac{G}{T_{\chi,max}} = 2.7032$. Therefore, the position of the maximum in the differential susceptibility curve correspond to

$$G = 2.7032 T_{\chi,max} \quad (\text{A.18})$$

Structural parameters obtained from Rietveld refinements of synchrotron X-ray powder diffraction patterns of $Nd_{2-x}Sr_xNiO_{4+\delta}$

Table A.9 | Rietveld refinement results obtained with synchrotron x-ray powder diffraction data at 5 K, 300 K and 723 K for $x = 0.1$.

Temperature		5 K	300 K	723 K
Space group		<i>Fmmm</i>	<i>Fmmm</i>	<i>F4/mmm</i>
<i>a</i>	(Å)	5.330606(10)	5.426466(15)	5.42925(2)
<i>b</i>	(Å)	5.343928(11)	5.426466(15)	5.42925(2)
<i>c</i>	(Å)	12.43804(2)	12.38931(4)	12.49030(5)
Ni (0 0 0)	Occ.	1	1	1
	U_{11}	0.0053(4)	0.0061(4)	0.00790(15)
	U_{22}	0.0096(4)	0.0087(5)	0.00790(15)
	U_{33}	0.0072(3)	0.0151(5)	0.0227(3)
Nd (0 0 <i>z</i>)	Occ.	2	2	2
	<i>z</i>	0.36137(3)	0.35956(3)	0.359883(16)
	U_{11}	0.00528(11)	0.01185(14)	0.01931(7)
	U_{22}	0.00929(15)	0.01638(16)	0.01931(7)
	U_{33}	0.00625(10)	0.00800(11)	0.00978(8)
O _{ap} (0 0 <i>z</i>)	Occ.	2	2	2
	<i>z</i>	0.1754(2)	0.1708(5)	0.1775(2)
	U_{11}	0.0116(17)	0.067(6)	0.0770(18)
	U_{22}	0.022(5)	0.132(9)	0.0770(18)
	U_{33}	0.0083(14)	0.006(3)	0.0183(16)
O _{eq} (¼ ¼ 0)	Occ.	2	2	2
	U_{11}	0.017(2)	0.0068(19)	0.0132(8)
	U_{22}	0.0003(16)	0.009(2)	0.0132(8)
	U_{33}	0.010(4)	0.054(4)	0.065(2)
	U_{12}	-0.0024(10)	-0.0038(15)	-0.0094(10)
R_p (%)		11.9	10.8	9.93
wR_p (%)		14	12.5	12.7
R_{exp}		2.36	1.13	3.57

Table A.10 | Rietveld refinement results obtained with synchrotron x-ray powder diffraction data at 5 K and 300 K for $x = 0.25$.

Temperature		5 K	300 K
Space group		<i>F4/mmm</i>	<i>F4/mmm</i>
<i>a</i>	(Å)	5.368213(7)	5.377172(7)
<i>b</i>	(Å)	5.368213(7)	5.377172(7)
<i>c</i>	(Å)	12.379715(20)	12.424015(19)
Ni (0 0 0)	Occ.	1	1
	U_{11}	0.00628(12)	0.00933(15)
	U_{22}	0.00628(12)	0.00933(15)
	U_{33}	0.0080(2)	0.0154(3)

Nd (<i>0 0 z</i>)	Occ.	2	2
	<i>z</i>	0.360530(19)	0.36041(2)
	<i>U</i> ₁₁	0.00766(5)	0.01295(6)
	<i>U</i> ₂₂	0.00766(5)	0.01295(6)
	<i>U</i> ₃₃	0.00429(5)	0.00805(7)
<i>O</i> _{ap} (<i>0 0 z</i>)	Occ.	2	2
	<i>z</i>	0.1784(3)	0.1766(3)
	<i>U</i> ₁₁	0.0480(18)	0.064(2)
	<i>U</i> ₂₂	0.0480(18)	0.064(2)
	<i>U</i> ₃₃	0.0075(13)	0.0126(17)
<i>O</i> _{eq} ($\frac{1}{4} \frac{1}{4} 0$)	Occ.	2	2
	<i>U</i> ₁₁	0.0113(8)	0.0175(10)
	<i>U</i> ₂₂	0.0113(8)	0.0175(10)
	<i>U</i> ₃₃	0.0281(20)	0.034(2)
	<i>U</i> ₁₂	-0.0023(10)	-0.0120(12)
<i>R</i> _p (%)		16.3	16.0
<i>wR</i> _p (%)		19.2	21.1
<i>R</i> _{exp}		4.41	5.83

Table A.11 | Rietveld refinement results obtained with synchrotron x-ray powder diffraction data at 5 K and 300 K for $x = 0.33$.

Temperature		5 K	300 K
Space group		F4/ <i>mmm</i>	F4/ <i>mmm</i>
<i>a</i>	(Å)	5.357551(7)	5.365499(6)
<i>b</i>	(Å)	5.357551(7)	5.365499(6)
<i>c</i>	(Å)	12.396384(20)	12.442430(15)
Ni (<i>0 0 0</i>)	Occ.	1	1
	<i>U</i> ₁₁	0.0086(2)	0.01031(14)
	<i>U</i> ₂₂	0.0086(2)	0.01031(14)
	<i>U</i> ₃₃	0.0097(4)	0.0153(3)
Nd (<i>0 0 z</i>)	Occ.	2	2
	<i>z</i>	0.36095(3)	0.360846(17)
	<i>U</i> ₁₁	0.00936(6)	0.01338(5)
	<i>U</i> ₂₂	0.00936(6)	0.01338(5)
	<i>U</i> ₃₃	0.00574(8)	0.00925(6)
<i>O</i> _{ap} (<i>0 0 z</i>)	Occ.	2	2
	<i>z</i>	0.1752(3)	0.17542(19)
	<i>U</i> ₁₁	0.0487(17)	0.0490(11)
	<i>U</i> ₂₂	0.0487(17)	0.0490(11)
	<i>U</i> ₃₃	0.0048(15)	0.0095(11)
<i>O</i> _{eq} ($\frac{1}{4} \frac{1}{4} 0$)	Occ.	2	2
	<i>U</i> ₁₁	0.0071(9)	0.0110(7)
	<i>U</i> ₂₂	0.0071(9)	0.0110(7)
	<i>U</i> ₃₃	0.032(2)	0.0360(16)
	<i>U</i> ₁₂	-0.0054(11)	-0.0054(8)
<i>R</i> _p (%)		15.8	11.2

$wR_p(\%)$		18.2	13.2
R_{exp}		1.65	1.42

Table A.12 | Rietveld refinement results obtained with synchrotron x-ray powder diffraction data at 5 K and 300 K for $x = 0.7$.

Temperature		5 K	300 K
Space group		$F4/mmm$	$F4/mmm$
a	(Å)	5.334490(7)	5.342185(6)
b	(Å)	5.334490(7)	5.342185(6)
c	(Å)	12.40442(2)	12.454785(15)
Ni (0 0 0)	Occ.	1	1
	U_{11}	0.00568(12)	0.00698(11)
	U_{22}	0.00568(12)	0.00698(11)
	U_{33}	0.0069(2)	0.0099(2)
Nd (0 0 z)	Occ.	2	2
	z	0.36113(2)	0.361118(19)
	U_{11}	0.00687(4)	0.01059(4)
	U_{22}	0.00687(4)	0.01059(4)
	U_{33}	0.00906(8)	0.01221(8)
O_{ap} (0 0 z)	Occ.	2	2
	z	0.1731(3)	0.17162(16)
	U_{11}	0.0127(6)	0.0174(6)
	U_{22}	0.0127(6)	0.0174(6)
	U_{33}	0.0174(14)	0.0097(10)
O_{eq} ($\frac{1}{4}$ $\frac{1}{4}$ 0)	Occ.	2	2
	U_{11}	0.0092(6)	0.0108(6)
	U_{22}	0.0092(6)	0.0108(6)
	U_{33}	0.0152(13)	0.0130(10)
	U_{12}	-0.0025(8)	-0.0010(7)
$R_p(\%)$		15.4	12.4
$wR_p(\%)$		19.0	12.1
R_{exp}		3.83	2.23

Phase transition in $Nd_{1.5}Sr_{0.5}NiO_{4+\delta}$ single crystal

The tetragonal (HTT) to orthorhombic (LTO) structural phase transition in the single crystal of $Nd_{1.5}Sr_{0.5}NiO_{4+\delta}$ was studied by neutron diffraction on ZEBRA ($\lambda = 2.30 \text{ \AA}$) at SINQ, PSI. For that, integrated intensity of B-type structural Bragg peak was measured with decreasing temperature from 300 K to 7 K. It was observed that the intensity of the (014) peak start to appear just below 250 K and sharply increases down to 180 K and then remains fixed until 7 K. From this temperature evolution, the structural phase transition temperature is identified to be around 245 K as shown in **Fig. A.5**. The phase transition temperature in the single crystal is higher than in the powder sample (212 K). This is likely due to different δ in the powder and single crystal samples. Inset of **Fig. A.5** show the ω -scan profiles of (2-20) Bragg reflection at 300 K and 7 K. At 300 K, in the tetragonal phase, only one reflection exists. However, in the orthorhombic phase, the (2-20) Bragg reflection splits into two subpeaks. This is an indication of the presence of two twin domains in the volume of the single crystal in the LTO phase. To extract the peak positions, the peak profiles are fitted with two Gaussian lines. It is found that the center of two peaks is separated by 0.34° in ω . This value is in accordance with the expected value ($\sim 0.3^\circ$) calculated from lattice parameters ($a = 5.330606(10) \text{ \AA}$ and $b = 5.343928(11) \text{ \AA}$) at 7 K. The intensity distribution of the sub peaks show 53:47 volume fraction ratio of two domains.

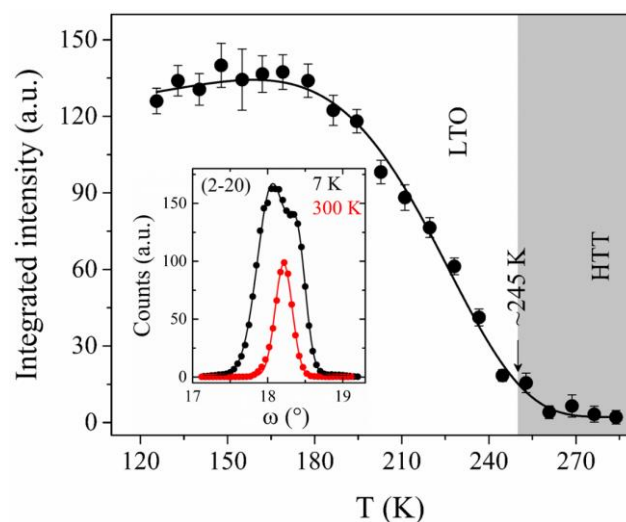


Figure A.8.5 | Integrated intensity of B-type (014) structural Bragg reflection as a function of temperature. Measurements were performed on ZEBRA ($\lambda = 2.30 \text{ \AA}$) at SINQ, PSI. Inset shows the profiles of (2-20) structural Bragg peak measured at 7 K and 300 K.

References

- (1) Gerhardt, M. R. Solid-oxide Fuel Cells: Using familiar fuel in a new way, Available at: <http://sitn.hms.harvard.edu/flash/2015/solid-oxide-fuel-cells-using-familiar-fuel-in-a-new-way/>.
- (2) Kilner, J. A.; Burriel, M. Materials for Intermediate-Temperature Solid-Oxide Fuel Cells. *Annu. Rev. Mater. Res.* **2014**, *44* (1), 365–393.
- (3) Wan, T.; Zhang, L.; Du, H.; Lin, X.; Qu, B.; Xu, H.; Li, S.; Chu, D. Recent Developments in Oxide-Based Ionic Conductors: Bulk Materials, Nanoionics, and Their Memory Applications. *Crit. Rev. Solid State Mater. Sci.* **2018**, *43* (1), 47–82.
- (4) Skinner, S. J.; Kilner, J. A. Oxygen Ion Conductors. *Mater. Today* **2003**, *6* (3), 30–37.
- (5) Kilner, J. A. Fast Oxygen Transport in Acceptor Doped Oxides. *Solid State Ionics* **2000**, *129* (1), 13–23.
- (6) Tuller, H. L. Oxygen Ion Conduction and Structural Disorder in Conductive Oxides. *J. Phys. Chem. Solids* **1994**, *55* (12), 1393–1404.
- (7) Singhal, S. C. Solid Oxide Fuel Cells for Stationary, Mobile, and Military Applications. *Solid State Ionics* **2002**, *152–153*, 405–410.
- (8) Paulus, W.; Schober, H.; Eibl, S.; Johnson, M.; Berthier, T.; Hernandez, O.; Ceretti, M.; Plazanet, M.; Conder, K.; Lamberti, C. Lattice Dynamics To Trigger Low Temperature Oxygen Mobility in Solid Oxide Ion Conductors. *J. Am. Chem. Soc.* **2008**, *130* (47), 16080–16085.
- (9) Routbort, J. L.; Rothman, S. J.; Flandermeyer, B. K.; Nowicki, L. J.; Baker, J. E. Oxygen Diffusion in $\text{La}_{2-x}\text{Sr}_x\text{CuO}_{4-y}$. *J. Mater. Res.* **1988**, *3* (1), 116–121.
- (10) Boehm, E.; Bassat, J. M.; Dordor, P.; Mauvy, F.; Grenier, J. C.; Stevens, P. Oxygen Diffusion and Transport Properties in Non-Stoichiometric $\text{Ln}_{2-x}\text{NiO}_{4+\delta}$ Oxides. *Solid State Ionics* **2005**.
- (11) Boehm, E.; Bassat, J.-M.; Steil, M. C.; Dordor, P.; Mauvy, F.; Grenier, J.-C. Oxygen Transport Properties of $\text{La}_2\text{Ni}_{1-x}\text{Cu}_x\text{O}_{4+\delta}$ Mixed Conducting Oxides. *Solid State Sci.* **2003**, *5* (7), 973–981.
- (12) Kilner, J. A.; C.K.M. Shaw. Mass Transport in $\text{La}_2\text{Ni}_{1-x}\text{Co}_x\text{O}_{4+\delta}$ Oxides with the K_2NiF_4 Structure. *Solid State Ionics* **2002**, *154–155*, 523–527.
- (13) Munnings, C.; Skinner, S.; Amow, G.; Whitfield, P.; Davidson, I. Oxygen Transport in the LaNiCoO System. *Solid State Ionics* **2005**, *176* (23–24), 1895–1901.
- (14) Ceretti, M.; Wahyudi, O.; André, G.; Meven, M.; Villesuzanne, A.; Paulus, W. (Nd/Pr) $_2\text{NiO}_{4+\delta}$: Reaction Intermediates and Redox Behavior Explored by in Situ Neutron Powder Diffraction during Electrochemical Oxygen Intercalation. *Inorg. Chem.* **2018**, *57* (8), 4657–4666.
- (15) Bhavaraju, S.; DiCarlo, J. F.; Scarfe, D. P.; Yazdi, I.; Jacobson, A. J. Electrochemical Intercalation of Oxygen in $\text{Nd}_2\text{NiO}_{4+x}$ ($0 \leq x \leq 0.18$) at 298 K. *Chem. Mater.* **1994**, *6* (11), 2172–2176.
- (16) Bassat, J.; Burriel, M.; Wahyudi, O.; Castaing, R.; Ceretti, M.; Veber, P.; Weill, I.; Villesuzanne, A.; Grenier, J.; Paulus, W.; et al. Anisotropic Oxygen Diffusion Properties in $\text{Pr}_2\text{NiO}_{4+\delta}$ and $\text{Nd}_2\text{NiO}_{4+\delta}$ Single Crystals. *J. Phys. Chem. C* **2013**, *117* (50), 26466–26472.
- (17) Perrichon, A.; Piovano, A.; Boehm, M.; Zbiri, M.; Johnson, M.; Schober, H.; Ceretti, M.; Paulus, W. Lattice Dynamics Modified by Excess Oxygen in $\text{Nd}_2\text{NiO}_{4+\delta}$: Triggering Low-Temperature Oxygen Diffusion. *J. Phys. Chem. C* **2015**, *119* (3), 1557–1564.
- (18) Ceretti, M.; Wahyudi, O.; Cousson, A.; Villesuzanne, A.; Meven, M.; Pedersen, B.; Bassat, J. M.;

- Paulus, W. Low Temperature Oxygen Diffusion Mechanisms in $\text{Nd}_2\text{NiO}_{4+\delta}$ and $\text{Pr}_2\text{NiO}_{4+\delta}$ via Large Anharmonic Displacements, Explored by Single Crystal Neutron Diffraction. *J. Mater. Chem. A* **2015**, *3* (42), 21140–21148.
- (19) Villesuzanne, A.; Paulus, W.; Cousson, A.; Hosoya, S.; Le Dréau, L.; Hernandez, O.; Prestipino, C.; Ikbél Houchati, M.; Schefer, J. On the Role of Lattice Dynamics on Low-Temperature Oxygen Mobility in Solid Oxides: A Neutron Diffraction and First-Principles Investigation of $\text{La}_2\text{CuO}_{4+\delta}$. *J. Solid State Electrochem.* **2011**, *15* (2), 357–366.
- (20) Chroneos, A.; Parfitt, D.; Kilner, J. A.; Grimes, R. W. Anisotropic Oxygen Diffusion in Tetragonal $\text{La}_2\text{NiO}_{4+\delta}$: Molecular Dynamics Calculations. *J. Mater. Chem.* **2010**, *20* (2), 266–270.
- (21) Cleave, A. R.; Kilner, J. A.; Skinner, S. J.; Murphy, S. T.; Grimes, R. W. Atomistic Computer Simulation of Oxygen Ion Conduction Mechanisms in La_2NiO_4 . *Solid State Ionics* **2008**, *179* (21–26), 823–826.
- (22) Tealdi, C.; Ferrara, C.; Mustarelli, P.; Islam, M. S. Vacancy and Interstitial Oxide Ion Migration in Heavily Doped $\text{La}_2\text{-xSr}_x\text{CoO}_{4+\delta}$. *J. Mater. Chem.* **2012**, *22* (18), 8969–8975.
- (23) Kushima, A.; Parfitt, D.; Chroneos, A.; Yildiz, B.; Kilner, J. A.; Grimes, R. W. Interstitialcy Diffusion of Oxygen in Tetragonal $\text{La}_2\text{CoO}_{4+\delta}$. *Phys. Chem. Chem. Phys.* **2011**, *13* (6), 2242–2249.
- (24) Parfitt, D.; Chroneos, A.; Kilner, J. A.; Grimes, R. W. Molecular Dynamics Study of Oxygen Diffusion in $\text{Pr}_2\text{NiO}_{4+\delta}$. *Phys. Chem. Chem. Phys.* **2010**, *12* (25), 6834–6836.
- (25) Le Dréau, L.; Prestipino, C.; Hernandez, O.; Schefer, J.; Vaughan, G.; Paofai, S.; Perez-Mato, J. M.; Hosoya, S.; Paulus, W. Structural Modulation and Phase Transitions in La_2CoO_4 .14 Investigated by Synchrotron X-Ray and Neutron Single-Crystal Diffraction. *Inorg. Chem.* **2012**, *51* (18), 9789–9798.
- (26) Demourgues, A.; Weill, F.; Darriet, B.; Wattiaux, A.; Grenier, J. C.; Gravereau, P.; Pouchard, M. Additional Oxygen Ordering in “ $\text{La}_2\text{NiO}_{4.25}$ ” ($\text{La}_8\text{Ni}_4\text{O}_{17}$). II. Structural Features. *Journal of Solid State Chemistry*. 1993, pp 330–338.
- (27) Tranquada, J. M.; Kong, Y.; Lorenzo, J. E.; Buttrey, D. J.; Rice, D. E.; Sachan, V. Oxygen Intercalation, Stage Ordering, and Phase Separation in $\text{La}_2\text{NiO}_{4+\delta}$ with $0.05 \leq \delta \leq 0.11$. *Phys. Rev. B* **1994**, *50* (9), 6340–6351.
- (28) Hiroi, Z.; Obata, T.; Takano, M.; Bando, Y.; Takeda, Y.; Yamamoto, O. Ordering of Interstitial Oxygen Atoms in $\text{La}_2\text{NiO}_{4+\delta}$ Observed by Transmission Electron Microscopy. *Phys. Rev. B* **1990**, *41* (16), 11665–11668.
- (29) Ray, P. J.; Andersen, N. H.; Jensen, T. B. S.; Mohottala, H. E.; Niedermayer, C.; Lefmann, K.; Wells, B. O.; Zimmermann, M. v.; Udby, L. Staging Superstructures in High-Tc Sr/O Codoped $\text{La}_2\text{-xSr}_x\text{CuO}_{4+y}$. *Phys. Rev. B* **2017**, *96* (17), 174106.
- (30) Fine, S. M.; Greenblatt, M.; Simizu, S.; Friedberg, S. A. Effect of Nominal Composition on the Superconductivity in $\text{La}_2\text{CuO}_{4-y}$. *Phys. Rev. B* **1987**, *36* (10), 5716–5718.
- (31) Dabrowski, B.; Jorgensen, J. D.; Hinks, D. G.; Pei, S.; Richards, D. R.; Vandervoort, K. G.; Crabtree, G. W.; Vanfleet, H. B.; Decker, D. L. $\text{La}_2\text{MO}_{4+\delta}$ (M=Cu, Ni, Co): Phase Separation and Superconductivity Resulting from Excess Oxygen Defects. In *Superconductivity and Applications*; Springer US: Boston, MA, 1990; pp 379–387.
- (32) Tranquada, J. M.; Buttrey, D. J.; Sachan, V.; Lorenzo, J. E. Simultaneous Ordering of Holes and Spins in $\text{La}_2\text{NiO}_{4.125}$. *Phys. Rev. Lett.* **1994**, *73* (7), 1003–1006.

- (33) Tranquada, J. M.; Buttrey, D. J.; Lorenzo, J. E.; Sachan, V. Ordering of Holes and Spins in La_2NiO_4 .125 and $\text{La}_{1.8}\text{Sr}_{0.2}\text{NiO}_4$. *Phys. B Phys. Condens. Matter* **1995**, 213–214 (C), 69–71.
- (34) Yamada, K.; Omata, T.; Nakajima, K.; Endoh, Y.; Hosoya, S. Incommensurate Magnetic Correlations in La_2NiO_4 .125. Magnetic Phase Diagram and Two-Dimensional Hole-Order. *Phys. C Supercond. its Appl.* **1994**, 221 (3–4), 355–362.
- (35) Wochner, P.; Tranquada, J. M.; Buttrey, D. J.; Sachan, V. Neutron-Diffraction Study of Stripe Order in $\text{La}_2\text{NiO}_{4+\delta}$ with $\delta = 2/15$. *Phys. Rev. B* **1998**, 57 (2), 1066–1078.
- (36) Ikeda, Y.; Suzuki, S.; Nakabayashi, T.; Yoshizawa, H.; Yokoo, T.; Itoh, S. Inelastic Neutron Scattering Study of Stripe and Overdoped Checkerboard Ordering in Layered Nickel Oxide $\text{Nd}_{2-x}\text{Sr}_x\text{NiO}_4$. *J. Phys. Soc. Japan* **2016**, 85 (2), 023701.
- (37) Yoshizawa, H.; Kakeshita, T.; Kajimoto, R.; Tanabe, T.; Katsufuji, T.; Tokura, Y. Stripe Order at Low Temperatures in $\text{La}_{2-x}\text{Sr}_x\text{NiO}_4$ with $0.289 \leq x \leq 0.5$. *Phys. Rev. B* **2000**, 61 (2), R854–R857.
- (38) Zhang, H. L.; Wu, X. S.; Chen, C. S.; Liu, W. Excess Oxygen Ordering in the $\text{La}_2\text{NiO}_{4+\delta}$ System Studied by Low-Frequency Internal Friction. *Phys. Rev. B* **2005**, 71 (6), 064422.
- (39) Goldschmidt, V. M. Die Gesetze Der Krystallochemie. *Naturwissenschaften* **1926**, 14 (21), 477–485.
- (40) Lemanov, V. V. Improper Ferroelastic SrTiO_3 and What We Know Today about Its Properties. *Ferroelectrics* **2002**, 265 (1), 1–21.
- (41) Megaw, H. D. Origin of Ferroelectricity in Barium Titanate and Other Perovskite-Type Crystals. *Acta Crystallogr.* **1952**, 5 (6), 739–749.
- (42) Knafo, W.; Meingast, C.; Boris, A. V.; Popovich, P.; Kovaleva, N. N.; Yordanov, P.; Maljuk, A.; Kremer, R. K.; Löhneysen, H. V.; Keimer, B. Ferromagnetism and Lattice Distortions in the Perovskite YTiO_3 . *Phys. Rev. B* **2009**, 79 (5), 054431.
- (43) Guo, R.; Cross, L. E.; Park, S.-E.; Noheda, B.; Cox, D. E.; Shirane, G. Origin of the High Piezoelectric Response in $\text{PbZr}_{1-x}\text{Ti}_x\text{O}_3$. *Phys. Rev. Lett.* **2000**, 84 (23), 5423–5426.
- (44) Ruddlesden, S. N.; Popper, P. New Compounds of the K_2NiF_4 Type. *Acta Crystallogr.* **1957**, 10 (8), 538–539.
- (45) Bednorz, J. G.; Müller, K. A. Possible High T_c Superconductivity in the Ba-La-Cu-O System. *Zeitschrift für Phys. B Condens. Matter* **1986**, 64 (2), 189–193.
- (46) Rodríguez-Carvajal, J.; Fernández-Díaz, M. T.; Martínez, J. L. Neutron Diffraction Study on Structural and Magnetic Properties of La_2NiO_4 . *J. Phys. Condens. Matter* **1991**, 3 (19), 3215–3234.
- (47) M. T. Fernández-Díaz, J. Rodríguez-Carvajal, J. L. Martínez, G. Fillion, F. Fernández, R. Saez-Puche. Structural and Magnetic Phase Transitions in Pr_2NiO_4 . *Zeitschrift für Phys. B Condens. Matter* **1991**, 82 (2), 275–282.
- (48) Fernández-Díaz, M. T.; Martínez, J. L.; Rodríguez-Carvajal, J. High-Temperature Phase Transformation of Oxidized $\text{R}_2\text{NiO}_{4+\delta}$ (R=La, Pr and Nd) under Vacuum. *Solid State Ionics* **1993**, 63–65 (C), 902–906.
- (49) Buttrey, D. J.; Sullivan, J. D.; Shirane, G.; Yamada, K. Influence of Oxygen Nonstoichiometry on Structure and Magnetism in $\text{Pr}_2\text{NiO}_{4+\delta}$. *Phys. Rev. B* **1990**, 42 (7), 3944–3951.
- (50) Rodríguez-Carvajal, J.; Fernández-Díaz, M. T.; Martínez, J. L.; Fernández, F.; Saez-Puche, R. Structural Phase Transitions and Three-Dimensional Magnetic Ordering in the Nd_2NiO_4 Oxide.

- Europhys. Lett.* **1990**, *11* (3), 261–268.
- (51) Sullivan, J. D.; Buttrey, D. J.; Cox, D. E.; Hriljac, J. A Conventional and High-Resolution Synchrotron X-Ray Diffraction Study of Phase Separations in $\text{Pr}_2\text{NiO}_{4+\delta}$. *J. Solid State Chem.* **1991**, *94* (2), 337–351.
- (52) Frayret, C.; Villesuzanne, A.; Pouchard, M. Application of Density Functional Theory to the Modeling of the Mixed Ionic and Electronic Conductor $\text{La}_2\text{NiO}_{4+\delta}$: Lattice Relaxation, Oxygen Mobility, and Energetics of Frenkel Defects. *Chem. Mater.* **2005**, *17* (26), 6538–6544.
- (53) Broux, T.; Prestipino, C.; Bahout, M.; Paofai, S.; Elkaïm, E.; Vibhu, V.; Grenier, J.-C.; Rougier, A.; Bassat, J.-M.; Hernandez, O. Structure and Reactivity with Oxygen of $\text{Pr}_2\text{NiO}_{4+\delta}$: An in Situ Synchrotron X-Ray Powder Diffraction Study. *Dalt. Trans.* **2016**, *45* (7), 3024–3033.
- (54) Ishikawa, K. Crystal Structure of $\text{Nd}_2\text{NiO}_{4.08}$. *Solid State Ionics* **2014**, *262*, 682–686.
- (55) Ishikawa, K.; Metoki, K.; Miyamoto, H. Orthorhombic-Orthorhombic Phase Transitions in $\text{Nd}_2\text{NiO}_{4+\delta}$ ($0.067 \leq \delta \leq 0.224$). *J. Solid State Chem.* **2009**, *182* (8), 2096–2103.
- (56) Hücker, M.; Zimmermann, M. V.; Klingeler, R.; Kiele, S.; Geck, J.; Bakehe, S. N.; Zhang, J. Z.; Hill, J. P.; Revcolevschi, A.; Buttrey, D. J.; et al. Unidirectional Diagonal Order and Three-Dimensional Stacking of Charge Stripes in Orthorhombic $\text{Pr}_{1.67}\text{Sr}_{0.33}\text{NiO}_4$ and $\text{Nd}_{1.67}\text{Sr}_{0.33}\text{NiO}_4$. *Phys. Rev. B - Condens. Matter Mater. Phys.* **2006**, *74* (8), 1–12.
- (57) Le Toquin, R.; Paulus, W.; Cousson, A.; Dhahenne, G.; Revcolevschi, A. Interstitial and Apical Oxygen Order-Disorder in $\text{La}_2\text{CoO}_{4+\delta}$ Observed by Single-Crystal Neutron and X-Ray Diffraction. *Phys. B Condens. Matter* **2004**, *350* (1-3 SUPPL. 1), 269–272.
- (58) Minervini, L.; Grimes, R. W.; Kilner, J. A.; Sickafus, K. E. Oxygen Migration in $\text{La}_2\text{NiO}_{4+\delta}$. *J. Mater. Chem.* **2000**, *10* (10), 2349–2354.
- (59) Piovano, A.; Perrichon, A.; Boehm, M.; Johnson, M. R.; Paulus, W. Positional Recurrence Maps, a Powerful Tool to de-Correlate Static and Dynamical Disorder in Distribution Maps from Molecular Dynamics Simulations: The Case of $\text{Nd}_2\text{NiO}_{4+\delta}$. *Phys. Chem. Chem. Phys.* **2016**, *18* (26), 17398–17403.
- (60) Paulus, W.; Cousson, A.; Dhahenne, G.; Berthon, J.; Revcolevschi, A.; Hosoya, S.; Treutmann, W.; Heger, G.; Le Toquin, R. Neutron Diffraction Studies of Stoichiometric and Oxygen Intercalated La_2NiO_4 Single Crystals. *Solid State Sci.* **2002**, *4* (5), 565–573.
- (61) Tranquada, J. M. Stripe Correlations of Spins and Holes in Cuprates and Nickelates. *Ferroelectrics* **1996**, *177* (1), 43–57.
- (62) Tan, Z.; Heald, S. M.; Cheong, S.-W.; Cooper, A. S.; Moodenbaugh, A. R. Nature of Hole Doping in Nd_2NiO_4 and La_2NiO_4 . Comparison with La_2CuO_4 . *Phys. Rev. B* **1993**, *47* (18), 12365–12368.
- (63) Uchida, M.; Yamasaki, Y.; Kaneko, Y.; Ishizaka, K.; Okamoto, J.; Nakao, H.; Murakami, Y.; Tokura, Y. Pseudogap-Related Charge Dynamics in the Layered Nickelate $\text{R}_2\text{-XSr}_x\text{NiO}_4$ ($X \sim 1$). *Physical Review B - Condensed Matter and Materials Physics*. 2012.
- (64) Brown, P. J.; Hayden, S. M.; Lander, G. H.; Zaretsky, J.; Stassi, C.; Metcalf, P.; Honig, J. M. Observation of Incommensurate Two-Dimensional Magnetic Correlations in $\text{La}_{1.8}\text{Sr}_{0.2}\text{NiO}_4$. *Phys. B Condens. Matter* **1992**, *180–181*, 380–382.
- (65) Poilblanc, D.; Rice, T. M. Charged Solitons in the Hartree-Fock Approximation to the Large-U

- Hubbard Model. *Phys. Rev. B* **1989**, 39 (13), 9749–9752.
- (66) Vergés, J. A.; Louis, E.; Lomdahl, P. S.; Guinea, F.; Bishop, A. R. Holes and Magnetic Textures in the Two-Dimensional Hubbard Model. *Phys. Rev. B* **1991**, 43 (7), 6099–6108.
- (67) Zaanen, J.; Littlewood, P. B. Freezing Electronic Correlations by Polaronic Instabilities in Doped La₂NiO₄. *Phys. Rev. B* **1994**, 50 (10), 7222–7225.
- (68) Tranquada, J. M.; Sternlieb, B. J.; Axe, J. D.; Nakamura, Y.; Uchida, S. Evidence for Stripe Correlations of Spins and Holes in Copper Oxide Superconductors. *Nature* **1995**, 375 (6532), 561–563.
- (69) Shinomori, S.; Okimoto, Y.; Kawasaki, M.; Tokura, Y. Insulator–Metal Transition in La₂-XSr_xNiO₄. *J. Phys. Soc. Japan* **2002**, 71 (3), 705–708.
- (70) Ishizaka, K.; Taguchi, Y.; Kajimoto, R.; Yoshizawa, H.; Tokura, Y. Charge Ordering and Charge Dynamics in Nd₂-XSr_xNiO₄ (0.33 ≤ x ≤ 0.7). *Phys. Rev. B* **2003**, 67 (18), 184418.
- (71) Yoshizawa, H.; Kakeshita, T.; Kajimoto, R.; Tanabe, T.; Katsufuji, T.; Tokura, Y. Stripe Order at Low Temperatures in La₂-XSr_xNiO₄ with 0.289 ≤ x ≤ 0.5. *Phys. Rev. B* **2000**, 61 (2), R854–R857.
- (72) Babkevich, P.; Freeman, P. G.; Enderle, M.; Prabhakaran, D.; Boothroyd, A. T. Direct Evidence for Charge Stripes in a Layered Cobalt Oxide. *Nat. Commun.* **2016**, 7 (1), 11632.
- (73) Kajimoto, R.; Ishizaka, K.; Yoshizawa, H.; Tokura, Y. Spontaneous Rearrangement of the Checkerboard Charge Order to Stripe Order in La_{1.5}Sr_{0.5}NiO₄. *Phys. Rev. B* **2003**, 67 (1), 014511.
- (74) Kobayashi, R.; Yoshizawa, H.; Matsuda, M.; Kajimoto, R.; Ishizaka, K.; Tokura, Y. Neutron Diffraction Study of Parasitic Nd-Moment Order in the Checkerboard-Type Phase Nd_{1.3}Sr_{0.7}NiO₄. *J. Phys. Soc. Japan* **2015**, 84 (6), 064711.
- (75) Tranquada, J. M.; Axe, J. D.; Ichikawa, N.; Nakamura, Y.; Uchida, S.; Nachumi, B. Neutron-Scattering Study of Stripe-Phase Order of Holes and Spins in La_{1.48}Nd_{0.4}Sr_{0.12}CuO₄. *Phys. Rev. B* **1996**, 54 (10), 7489–7499.
- (76) Bragg, W. H.; Bragg, W. L. The Reflection of X-Rays by Crystals. *Proc. R. Soc. A Math. Phys. Eng. Sci.* **1913**, 88 (605), 428–438.
- (77) Wilson, C. C. *Single Crystal Neutron Diffraction From Molecular Materials*; Series on Neutron Techniques and Applications; WORLD SCIENTIFIC, 2000; Vol. 2.
- (78) Fischer, H. E.; Barnes, A. C.; Salmon, P. S. Neutron and X-Ray Diffraction Studies of Liquids and Glasses. *Reports Prog. Phys.* **2006**, 69 (1), 233–299.
- (79) Cullity, B. D.; Stock, S. R. *Elements of X-Ray Diffraction.*; Pearson Education UK, 2013.
- (80) Willis, B. T. M. (Bertram T. M.; Carlile, C. J. (Colin J. . *Experimental Neutron Scattering*; Oxford University Press, 2009.
- (81) Squires, G. L. *Introduction to the Theory of Thermal Neutron Scattering*; Cambridge University Press: Cambridge, 2012.
- (82) Chatterji, T. *Neutron Scattering from Magnetic Materials*; Elsevier, 2006.
- (83) Schweizer, J. Polarized Neutrons and Polarization Analysis. In *Neutron Scattering from Magnetic Materials*; Elsevier, 2006; pp 153–213.
- (84) Janoschek, M.; Klimko, S.; Gähler, R.; Roessli, B.; Böni, P. Spherical Neutron Polarimetry with MuPAD. *Phys. B Condens. Matter* **2007**, 397 (1–2), 125–130.
- (85) TASP: Cold Neutron Triple-axis spectrometer, Available at: <https://www.psi.ch/sinq/tasp/tasp>.

- (86) Willmott, P. R.; Meister, D.; Leake, S. J.; Lange, M.; Bergamaschi, A.; Böge, M.; Calvi, M.; Cancellieri, C.; Casati, N.; Cervellino, A.; et al. The Materials Science Beamline Upgrade at the Swiss Light Source. *J. Synchrotron Radiat.* **2013**, *20* (5), 667–682.
- (87) Rodríguez-Carvajal, J. Recent Advances in Magnetic Structure Determination by Neutron Powder Diffraction. *Phys. B Phys. Condens. Matter* **1993**, *192* (1–2), 55–69.
- (88) Fischer, P.; Frey, G.; Koch, M.; Konnecke, M.; Pomjakushin, V.; Schefer, J.; Thut, R.; Schlumpf, N.; Burge, R.; Greuter, U.; et al. High-Resolution Powder Diffractometer HRPT for Thermal Neutrons at SINQ. *Phys. B Condens. Matter* **2000**, *276–278*, 146–147.
- (89) Schefer, J.; Fischer, P.; Heer, H.; Isacson, A.; Koch, M.; Thut, R. A Versatile Double-Axis Multicounter Neutron Powder Diffractometer. *Nucl. Instruments Methods Phys. Res. Sect. A Accel. Spectrometers, Detect. Assoc. Equip.* **1990**, *288* (2–3), 477–485.
- (90) Cold Neutron Powder Diffractometer DMC, Available at: <https://www.psi.ch/sinq/dmc/>.
- (91) HRPT: High-Resolution Powder Diffractometer for Thermal Neutrons, Available at: <https://www.psi.ch/en/sinq/hrpt>.
- (92) MATLAB, Available at: <https://www.mathworks.com/products/matlab.html>.
- (93) ZEBRA: Thermal Single Crystal Diffractometer, Available at: <https://www.psi.ch/sinq/zebra/>.
- (94) Meven, M.; Sazonov, A. HEiDi: Single Crystal Diffractometer at Hot Source. *J. large-scale Res. Facil. JLSRF* **2015**, *1*, A7.
- (95) D9:Hot neutron four-circle diffractometer, Available at: <https://www.ill.eu/users/instruments/instruments-list/d9/>.
- (96) Collins, D. M. Electron Density Images from Imperfect Data by Iterative Entropy Maximization. *Nature* **1982**, *298* (5869), 49–51.
- (97) Sakata, M.; Sato, M. Accurate Structure Analysis by the Maximum-entropy Method. *Acta Crystallogr. Sect. A* **1990**, *46* (4), 263–270.
- (98) Momma, K.; Ikeda, T.; Belik, A. A.; Izumi, F. Dysnomia, a Computer Program for Maximum-Entropy Method (MEM) Analysis and Its Performance in the MEM-Based Pattern Fitting. *Powder Diffr.* **2013**, *28* (3), 184–193.
- (99) Clegg, W.; Blake, A. J.; Cole, J. M.; Evans, J. S. O.; Main, P.; Parsons, S.; Watkin, D. J. *Crystal Structure Analysis*; Oxford University Press, 2009; Vol. 9780199219.
- (100) Petříček, V.; Dušek, M.; Palatinus, L. Crystallographic Computing System JANA2006: General Features. *Zeitschrift für Krist.* **2014**, *229* (5), 345–352.
- (101) Momma, K.; Izumi, F. VESTA: A Three-Dimensional Visualization System for Electronic and Structural Analysis. *J. Appl. Crystallogr.* **2008**, *41* (3), 653–658.
- (102) Momma, K.; Izumi, F. VESTA 3 for Three-Dimensional Visualization of Crystal, Volumetric and Morphology Data. *J. Appl. Crystallogr.* **2011**, *44* (6), 1272–1276.
- (103) Wahyudi, O.; Ceretti, M.; Weill, I.; Cousson, A.; Weill, F.; Meven, M.; Guerre, M.; Villesuzanne, A.; Bassat, J.-M.; Paulus, W. Growth of High Quality Single Crystals of Strontium Doped (Nd,Pr)-Nickelates, Nd₂-XSr_xNiO_{4+δ} and Pr₂-XSr_xNiO_{4+δ}. *CrystEngComm* **2015**, *17* (33), 6278–6285.
- (104) Dréau, L. Le. Phase Transitions and Oxygen Ordering in La₂CoO_{4+δ} and (T, T')-La₂CuO₄: Single Crystal Growth and Structural Studies Using Synchrotron and Neutron Diffraction Methods, 2011.

- (105) Wahyudi, O. Exploring Oxygen Mobility in (Pr/Nd)₂NiO_{4+δ}: Single Crystal Growth, Isotopic Exchange Depth Profiling and Structural Characterization by X-Ray, Neutron and Electron Diffraction, 2011.
- (106) *Handbook of Crystal Growth*; Dhanaraj, G., Byrappa, K., Prasad, V., Dudley, M., Eds.; Springer Berlin Heidelberg: Berlin, Heidelberg, 2010.
- (107) Equipment, Solid State Chemistry, Available at: <https://www.psi.ch/en/lmx-ssc/equipment>.
- (108) Basic Demonstration of OrientExpress for orienting a single crystal from a single Laue Photograph, Available at: <http://www.ccp14.ac.uk/tutorial/lmgp/orientexpress.html>.
- (109) QLaue, Available at: <https://sourceforge.net/projects/qlaue/>.
- (110) ORION: Test Diffractometer, Available at: <https://www.psi.ch/en/sinq/orion>.
- (111) MORPHEUS: Two-axes neutron diffractometer & reflectometer, Available at: <https://www.psi.ch/de/sinq/morpheus>.
- (112) Rodríguez-Carvajal, J.; Fernández-Díaz, M. T.; Martínez, J. L.; Fernández, F.; Saez-Puche, R. Structural Phase Transitions and Three-Dimensional Magnetic Ordering in the Nd₂NiO₄ Oxide. *Europhys. Lett.* **1990**, *11* (3), 261–268.
- (113) Freeman, P. G.; Christensen, N. B.; Prabhakaran, D.; Boothroyd, A. T. The Temperature Evolution of the Out-of-Plane Correlation Lengths of Charge-Stripe Ordered La_{1.725}Sr_{0.275}NiO₄. *J. Phys. Conf. Ser.* **2010**, *200* (1), 012037.
- (114) Kiyama, T.; Yoshimura, K.; Kosuge, K.; Ikeda, Y.; Bando, Y. Invar Effect of SrR: Itinerant Electron Magnetism of Ru Electrons. *Phys. Rev. B - Condens. Matter Mater. Phys.* **1996**, *54* (2), R756–R759.
- (115) Batlle, X.; Obradors, X.; Martnez, B. Magnetic Interactions, Weak Ferromagnetism, and Field-Induced Transitions in Nd₂NiO₄. *Phys. Rev. B* **1992**, *45* (6), 2830–2843.
- (116) Obradors, X.; Batlle, X.; Rodriguez-Carvajal, J.; Martnez, J. L.; Vallet, M.; González-Calbet, J.; Alonso, J. Magnetic Transitions in Nd₂NiO₄. *Phys. Rev. B* **1991**, *43* (13), 10451–10454.
- (117) Shannon, R. D. Revised Effective Ionic Radii in Halides and Chalcogenides. *Acta Cryst. A* **1976**, *32* (5), 751–767.
- (118) Syromyatnikov, A. V.; Maleyev, S. V. Nuclear-Magnetic Interference in the Inelastic Scattering of the Polarized Neutrons in a Dipolar Ferromagnet. *Phys. B Condens. Matter* **2001**, *297* (1–4), 82–86.
- (119) Hücker, M.; Chung, K.; Chand, M.; Vogt, T.; Tranquada, J. M.; Buttrey, D. J. Oxygen and Strontium Codoping of La₂NiO₄: Room-Temperature Phase Diagrams. *Phys. Rev. B - Condens. Matter Mater. Phys.* **2004**, *70* (6), 1–10.
- (120) Wu, G.; Neumeier, J. J.; Ling, C. D.; Argyriou, D. N. Temperature Evolution of the Crystal Structure of La₂-XSr_xNiO₄ (X= 1/4 and 1/3) as Revealed through Neutron Powder Diffraction. *Phys. Rev. B* **2002**, *65* (17), 174113.
- (121) Perrichon, A. Etude Des Mécanismes de Diffusion Des Ions Oxydes à Température Ambiante Dans Nd₂NiO_{4+δ}, 2015.
- (122) Poole, A.; Roessli, B. Analysis of Neutron Polarimetry Data Using MuFit. *J. Phys. Conf. Ser.* **2012**, *340*, 012017.
- (123) Blume, M. Polarization Effects in the Magnetic Elastic Scattering of Slow Neutrons. *Phys. Rev.* **1963**, *130* (5), 1670–1676.
- (124) Arbuckle, B. W.; Ramanujachary, K. V.; Zhang, Z.; Greenblatt, M. Investigations on the Structural,

- Electrical, and Magnetic Properties of Nd₂-XSr_xNiO_{4+δ}. *J. Solid State Chem.* **1990**, *88* (1), 278–290.
- (125) Li, Z.; Haugsrud, R.; Norby, T. Oxygen Bulk Diffusion and Surface Exchange in Sr-Substituted La₂NiO_{4+δ}. *Solid State Ionics* **2011**, *184* (1), 42–46.
- (126) Boehm, E.; Bassat, J. M.; Dordor, P.; Mauvy, F.; Grenier, J. C.; Stevens, P. Oxygen Diffusion and Transport Properties in Non-Stoichiometric Ln₂-XNiO_{4+δ} Oxides. *Solid State Ionics* **2005**, *176* (37–38), 2717–2725.
- (127) Li, Z.; Haugsrud, R.; Smith, J. B.; Norby, T. Transport Properties and Defect Analysis of La_{1.9}Sr_{0.1}NiO_{4+δ}. *Solid State Ionics* **2009**, *180* (26–27), 1433–1441.
- (128) Masubuchi, Y.; Higuchi, M.; Katase, H.; Takeda, T.; Kikkawa, S.; Kodaira, K.; Nakayama, S. Oxide Ion Conduction in Nd_{9.33}(SiO₄)₆O₂ and Sr₂Nd₈(SiO₄)₆O₂ Single Crystals Grown by Floating Zone Method. *Solid State Ionics* **2004**, *166* (1–2), 213–217.
- (129) Greedan, J. E.; Liu, G.; Arbuckle, B. W.; Ramanujachary, K. V.; Greenblatt, M. Neutron Diffraction Studies of the Crystal and Magnetic Structure of Nd_{1.5}Sr_{0.5}NiO₄. *J. Solid State Chem.* **1992**, *97* (2), 419–426.
- (130) Ikeda, Y.; Suzuki, S.; Nakabayashi, T.; Yoshizawa, H.; Yokoo, T.; Itoh, S. Transport and Thermodynamic Studies of Stripe and Checkerboard Ordering in Layered Nickel Oxides R₂-XSr_xNiO₄ (R = La and Nd). *J. Phys. Soc. Japan* **2015**, *84* (2), 1–5.
- (131) Boothroyd, A. T.; Longmore, A.; Castro, M.; Burriel, R.; Eccleston, R. S. The Magnetic States of R³⁺ in R₂NiO₄ (R = Pr, Nd). **1997**, *9* (May), 2275–2294.
- (132) Lin, Y. P.; Greedan, J. E.; O'Reilly, A. H.; Reimers, J. N.; Stager, C. V.; Post, M. L. Defect Ordering in YBa₂Cu₃O_{6.5} and YBa₂Cu₃O_{6.6}: Synthesis and Characterization by Neutron and Electron Diffraction. *J. Solid State Chem.* **1990**, *84* (2), 226–236.
- (133) Zaliznyak, I. A.; Hill, J. P.; Tranquada, J. M.; Erwin, R.; Moritomo, Y. Independent Freezing of Charge and Spin Dynamics in La_{1.5}Sr_{0.5}CoO₄. *Phys. Rev. Lett.* **2000**, *85* (20), 4353–4356.
- (134) Aidhy, D. S.; Liu, B.; Zhang, Y.; Weber, W. J. Strain-Induced Phase and Oxygen-Vacancy Stability in Ionic Interfaces from First-Principles Calculations. *J. Phys. Chem. C* **2014**, *118*, 42.
- (135) Fronzi, M.; Cereda, S.; Tateyama, Y.; De Vita, A.; Traversa, E. Ab Initio Investigation of Defect Formation at ZrO₂-CeO₂ Interfaces. *Phys. Rev. B* **2012**, *86*, 85407.
- (136) Tsvetkov, N.; Lu, Q.; Chen, Y.; Yildiz, B. Accelerated Oxygen Exchange Kinetics on Nd₂NiO_{4+δ} Thin Films with Tensile Strain along C-Axis. *ACS Nano* **2015**, *9* (2), 1613–1621.
- (137) Morimoto, T.; Nagai, M.; Minowa, Y.; Ashida, M.; Yokotani, Y.; Okuyama, Y.; Kani, Y. Microscopic Ion Migration in Solid Electrolytes Revealed by Terahertz Time-Domain Spectroscopy.
- (138) Chung, K. Investigation of the Structure and Properties of Lanthanum Strontium Nickel Oxide, 2008.
- (139) Braden, M.; Heger, G.; Schweiss, P.; Fisk, Z.; Gamayunov, K.; Tanaka, I.; Kojima, H. Characterization and Structural Analysis of Twinned La₂-xSr_xCuO_{4±δ} Crystals by Neutron Diffraction. *Phys. C Supercond.* **1992**, *191* (3–4), 455–468.
- (140) Penney, W. G.; Schlapp, R. The Influence of Crystalline Fields on the Susceptibilities of Salts of Paramagnetic Ions. I. The Rare Earths, Especially Pr and Nd. *Phys. Rev.* **1932**, *41* (2), 194–207.
- (141) Frank, A. Temperature Variation of the Magnetic Susceptibility, Gyromagnetic Ratio, and Heat Capacity in Sm⁺⁺⁺ and Eu⁺⁺⁺. *Phys. Rev.* **1932**, *39* (1), 119–129.

- (142) Puche, R. S.; Norton, M.; White, T. R.; Glaunsinger, W. S. Magnetic Properties of the Semiconducting Lanthanide Cuprates Ln_2CuO_4 and Their Interpretation: Evidence for a New Series of Planar Copper Antiferromagnets. *J. Solid State Chem.* **1983**, *50* (3), 281–293.
- (143) Rotter, M. Using McPhase to Calculate Magnetic Phase Diagrams of Rare Earth Compounds. *J. Magn. Mater.* **2004**, *272–276*, E481–E482.
- (144) Castro, M.; Burriel, R. Phase Transitions and Crystal-Field Levels in Nd_2NiO_4 . *Thermochim. Acta* **1995**, *269–270*, 523–535.

Acknowledgements

I am very grateful to the many people for helping and supporting me to bring this PhD thesis work to its completion. My deepest thanks to **Prof. Dr. Werner Paulus** not only for introducing me in this project but also for his guidance, valuable suggestions and motivations throughout this thesis work. My heartfelt thanks to my supervisor **Prof. Dr. Christian Ruegg** for his unique guidance, suggestions and advice throughout this thesis work. My sincere thanks and gratitude to my thesis advisors **Dr. Lukas Keller** and **Dr. Jürg Schefer** for their intellectual ideas, guidance, support and motivation at each step of this thesis work. I am also extremely grateful to them for their constructive criticism, which were essential in the course of this thesis, without them this work would have been a distant reality.

My special thanks to **Dr. Monica Ceretti** and **Dr. Ekaterina Pomjakushina** who devoted their valuable time to help me during the preparations of high quality poly- and single crystal samples that were used in this thesis work.

I would also like to thank the many instrument scientists at the SINQ, SLS, FRM II and ILL, particularly **Dr. Oksana Zaharko**, **Dr. Denis Cheptiakov**, **Dr. Bertrand Roessli**, **Dr. Uwe Stuhr**, **Prof. Dr. Christof Niedermayer**, **Dr. Antonio Cervellino**, **Dr. Martin Meven** and **Dr. Rodriguez Velamazan Jose Alberto** for their help with X-ray and neutron diffraction experiments. I am grateful to **Dr. Bertrand Roessli** for insightful discussions on the data treatment of spherical neutron polarimetry. I would like to thank **Dr. Andrea Testino** for her contributions in high temperature X-ray data collection. I would also like to thank **Dr. Tian Shang** for his efforts during the measurements on PPMS and MPMS.

Along with these, people I would like to also thank are post-docs and researchers for their good company that made my time working at PSI enjoyable. In this respect, I would like to thank **Dr. Saumya Mukherjee**, **Dr. Emmanuel Canevet**, **Dr. Romain Sibille**, **Dr. Fei Li**, **Dr. Shang Gao**, **Dr. Daniel Mazzone**, **Dr. Dariusz Jakub Gawryluk**, **Dr. Juan Mora**, **Guratinder Kaur**, **Alexandra Turrini**. Thanks and appreciation to the helpful colleagues **Dr. Avishek Maity** and **Dr. Rajesh Dutta** for their support and helpful discussions. I want to give special thanks to **Knupp Pamela** for her support and official arrangements from the start of this thesis work.

Finally, I would like to thank **my family members** for their patience, love, support, encouragement and understanding during these 4 years.

Curriculum Vitae

PERSONAL INFORMATION

Last name	Maity
First name	Sumit
Middle name	Ranjan
Date of birth	5 th April 1991
Place of birth	Biju, West Bengal, India
Nationality	Indian

EDUCATION

September 2015 – Present	Ph.D. degree in Physics Laboratory for Neutron scattering and Imaging (LNS), Paul Scherrer Institute (PSI) and Department of Physics, University of Genève, Switzerland Supervisors: Dr. Lukas. Keller, Dr. Juerg. Schefer, Prof. Dr. Christian Rugg
September 2014 – September 2015	Master in Material Science (2 nd year) Erasmus Mundus MaMaSELF Technical University of Munich, Munich, Germany Supervisors: Prof. Dr. Winfried Petry and Dr. Martin Meven
September 2013 – August 2014	Master in Material science (1 st year) Erasmus Mundus MaMaSELF University of Montpellier, Montpellier, France. Supervisor: Prof. Dr. Werner Paulus
August 2011 – August 2013.	Master of Science in Physics Indian Institute of Technology Madras, Chennai, India. Supervisor: Prof. Dr. MS. Ramachandra Rao
May 2008 – May 2011.	Bachelor of Science in Physics. Midnapore College, West Bengal, India.

PUBLICATIONS

- Sumit Ranjan Maity, Monica Ceretti, Lukas Keller, Jürg Schefer, Tian Shang, Ekaterina Pomjakushina, Martin Meven, Denis Sheptyakov, Antonio Cervellino, Werner Paulus, *Structural disorder and magnetic correlations induced by excess oxygens in Nd₂NiO_{4.11}*, *Phys. Rev. Materials* **3**, 083604 (2019).
- Sumit Ranjan Maity, Monica Ceretti, Lukas Keller, Jürg Schefer, Werner Paulus, *Interstitial oxygen and spin ordering in Nd₂NiO_{4+δ}* (to be submitted)
- Sumit Ranjan Maity, Monica Ceretti, Lukas Keller, Jürg Schefer, Werner Paulus, *Evidence of incommensurate magnetic order in highly oxygen doped Nd₂NiO_{4.23}* (in preparation).

CONFERENCE PRESENTATIONS

- **MLZ conference: Neutrons for energy, 18-22 July 2016, Poster presentation:** Effect of doping and temperature on oxygen disorder in Pr₂NiO_{4+δ} explored by single crystal neutron diffraction.
Abstract and results available at: Acta Cryst A. (2016). A72, s287 (doi: 10.1107/S2053273316095681)
- **European crystallography meeting (ECM 30), 28 August-3 September 2016, Poster presentation:** Crystal structure and apical oxygen disorder in Nd₂NiO_{4+δ} explored by neutron diffraction.
- **International Union of Crystallography (IUCR 2017), 21-28 August 2017, Oral presentation:** Neutron diffraction studies of apical oxygen disorder in Nd₂NiO_{4+δ}.
Abstract and results available at: Acta Cryst A: Foundations and Advances 73(a2):C1426-C1426, DOI: 10.1107/S2053273317081505
- **European crystallography meeting (ECM 31), 22-27 August 2018, Oral presentation:** Neutron diffraction studies of apical oxygen disorder and incommensurate magnetic order in Nd₂NiO_{4+δ}
- **Swiss Society of Crystallography, 12 September 2018, Oral presentation:** Incommensurate crystal structure and magnetism in oxygen doped Nd₂NiO_{4+δ}
- **European Crystallographic Meeting (ECM32), 18-23 August 2019, Poster presentation:** Structural disorder and magnetic correlations driven by oxygen doping in Nd₂NiO_{4.11}